STUDY OF R. F. PLASMA PROBES AND ITS APPLICATION TO THE ROCKET AND SATELLITE OBSERVATIONS(Dissertation_全文)

AUTHOR(S):

Ejiri, Masaki

STUDY OF R. F. PLASMA PROBES AND ITS APPLICATION TO THE ROCKET AND SATELLITE OBSERVATIONS

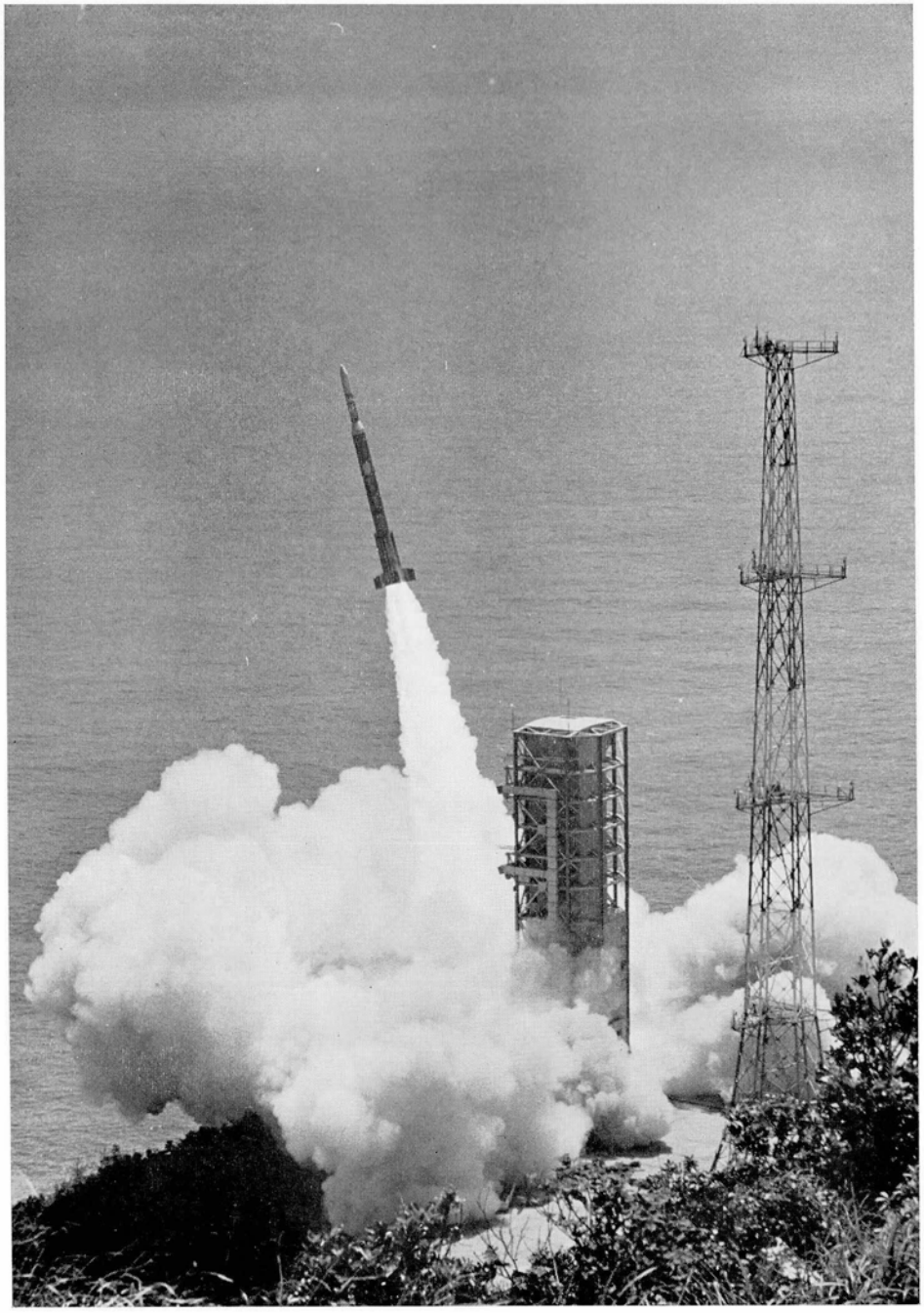

M–4S型 4 号機の発射 (1972–8–19)

STUDY OF R. F. PLASMA PROBES AND ITS APPLICATION TO THE ROCKET AND SATELLITE OBSERVATIONS

by

Masaki EJIRI

JUNE 1973

Institute of Space and Aeronautical Science
University of Tokyo
Tokyo, Japan

ACKNOWLEDGEMENTS

The author wishes to express his thanks to Prof. Tatsuzo Obayashi for his valuable instruction and guidance on this work and offer of opportunities of rocket and satellite experiments. Sincere thanks are also due to Prof. Ken-ichi Maeda and Prof. Iwane Kimura for their continual advices and encouragements.

The author is indebted to Dr. Hiroshi Oya who provided the original motivation of taking up the ionospheric study, especially the gyro-plasma probe and plasma diagnostics, and helped him to fulfil this investigation. The author is grateful to Prof. Kunio Hirao, Prof. Toru Ogawa, Prof. Susumu Kato, Dr. Tomizo Ito, Dr. Toshihiko Dote, Dr. Atsuhiro Nishida, and Dr. Koichiro Tsuruda for their helpful discussions and many suggestions. Many thanks are also due to his colleagues at the Institute of Space and Aeronautical Science, University of Tokyo, the Ionosphere Research Laboratory, Kyoto University, and the Radio Research Laboratories, especially to Messrs. Takehiko Aso, Kozo Morita, Nobuyoshi Yokobori and Osamu Furuta who have participated in the experiment of gyro-plasma probe onboard the spacecraft REXS, and also to Messrs. Hirotaka Mori, Satoru Kozima, and Yuzo Watanabe for their contributions to the experiments and numerical works.

It should be acknowledged that the successful operation of REXS satellite and the rocket experiments are due to the collaborative work of many scientists and engineers who have participated in the Mu 4S-4 experiment and the Radio Exploration Satellite "REXS", and the rocket observation projects, which have been supported by the Institute of Space and Aeronautical Science, University of Tokyo. The orbital data for this satellite were made available through the courtesy of the National Space Development Agency of Japan, and the data of ionograms during the rocket flight were supplied by the Radio Research Laboratories.

The space plasma simulation chamber experiment and the pre-flight simulation test of instruments were carried out under supervision of the Space Plasma Investigation Committee. The data processing and

analysis were performed by the digital computer (model HITAC 5020F) at the Computer Center, ISAS, University of Tokyo.

The experiments of laboratory plasma in section 3.2 and 3.4, Chapter III, are co-operative studies with Dr. Toshihiko Dote, and Messrs. Shigeru Miyazaki, Takehiko Aso, and Hirotaka Mori. Prof. Iwane Kimura and Mr. Tetsuo Tomimoto for the VLF Doppler methods, and Mr. Hirotaka Mori for the Langmuir Probe and the two-wire probe, took charge of measuring electron densities using each method in the rocket experiments of Kappa 9M-35 and 38 in section 5, Chapter IV. The instrumentation of plasma probes for rocket and satellite experiments were made possible with the co-operation of Messrs. Shinji Urimoto, Hiroyuki Yamaki, and Makoto Abe of the Meisei Electric Co. Ltd. The author also acknowledges the heartly efforts of these coworkers, and expresses his gratitude to Mrs. Hiroko Maezawa for her typewriting of this thesis.

PREFACE

The thesis is concerned with the study of radio-frequency plasma probes which have been developed to measure the electron density in space and laboratory plasmas; a word of "plasma" is used to designate the forth state of matter — high temperature gaseous state in which an appreciable number of the gas atoms are ionized. The most appropriate parameters to describe the physical properties are the electron density and temperature.

Recent years have witnessed an explosive development of space sciences, since space vehicles — artificial satellites and sounding rockets as well as manned spacecrafts — have made it possible to probe directly in its place and to give us a great deal of information on the conditions and properties of the upper atmosphere surrounding the earth and also of other planets, the sun, and stars.

The earth's upper atmosphere, for purposes of this study, extends upward in altitude from levels of 50 km or so, the whole region of significant ionization produced primarily by the solar radiation being termed the ionosphere. The percentage of ionization tends to increase with increasing height, although the absolute concentration of electrons exhibits a layered structure associated with different photoionization and recombination processes. The structure and its behaviour of the ionosphere have been revealed by measuring the electron density in the D, E and F region and above with in-situ plasma probes carried on rocket or satellite vehicles. The most useful technique in measuring the electron density is the gyro-plasma probe, a kind of the frequency scanning impedance probe, which was initiated by H. Oya in 1964.

The critical survey of existing probe techniques has been made, in order to find their most proper application to the electron density measurements in space and laboratory plasmas. The Langmuir probe has long been regarded as the most appropriate probe technique since I. Langmuir and H. Mott-Smith first examined the current-voltage characteristics of a metalic probe in a discharged tube in 1924. However, there has been known some difficulties in the Langmuir probe technique itself in

measuring the electron density in a tenuous (low density) plasma such as an ionospheric plasma. The most serious problem for such a d.c. plasma probe is to keep the probe surface extremely clean to avoid contamination. The r.f. plasma probes are free from such contamination, but one must clarify the complicated behaviors of frequency response of an antenna and various plasma resonance phenomena in a magneto-active plasma. The frequency response of the impedance of an antenna in the magneto-ionic environment is of interest from both theoretical and experimental viewpoints. For theoretical plasma physicists it poses basic problems in electromagnetic theory and boundary value problem, while for experimental researchers it is of practical use to diagnose the environmental plasmas as well as to make an efficient space communication.

The instrumentation of rocket-borne and satellite-borne probe systems must be carefully designed to have optimum conditions of electrical, mechanical, and thermal systems. The instrument should be subjected to pre-flight test of electrical and mechanical performances under various phases of the spacecraft mission, and also it is desirable that the operational functions of the probe system are confirmed in the space simulation laboratory plasma. Since the observed data are transmitted to the ground station through the telemetry system, onboard data processings including the automatic detection system are, sometimes, required in order to encode the observed analog data.

In this thesis, r.f. plasma probes such as gyro-plasma probe, mutual impedance probe, and capacitance probe are studied and are applied to the measurements of electron densities in the laboratory plasma as well as in the space plasma using sounding rockets and the satellite. The ionospheric observations with r.f. plasma probes, the earlier studies on the electron density variation in the ionosphere, and also the theoretical background on the r.f. plasma probes are reviewed in Chapter I.

Chapter II is devoted to the system description of r.f. plasma probes and the theoretical investigation of the ion sheath formation around the body in a plasma. The space vehicle in the ionospheric

plasma is surrounded by the ion sheath and, therefore, r.f. response of the ion sheath is essential in the experiment of plasma probes.

In Chapter III, the laboratory experiment of r.f. plasma probes is described. Using a apparatus of the vacuum chamber with plasma sources for simulating the space plasma, behaviors of r.f. plasma probes are examined under various plasma conditions. The comparison of electron density measurements by r.f. and d.c. plasma probes was carried out and a good agreement of measured electron densities in the range from about 10^4 cm^{-3} to 10^6 cm^{-3} has been obtained with gyro-plasma probe and Langmuir probe methods. In the Langmuir probe experiment, the contamination on the probe surface was carefully removed by ion bombardment and space potential was precisely determined by the r.f. method. As for the mutual impedance probe, the frequency response of the received signal intensity is very complicated because of the excitation of Bernstein mode waves. The effect on the probe measurement was originaly found by our experiment.

In Chapter IV, sounding rocket experiments with r.f. plasma probes are dealt with. The electron density profiles in the ionosphere in the altitude range from about 70 km to 2000 km were successfully obtained using sounding rockets S 210-6 and 8, Kappa 8-15, Kappa 9M-35, 38 and 41, and Lambda 3H-5 and 6, which were launched from Kagoshima Space Center from 1969 to 1973. Various plasma resonance effects on the antenna impedance have been discovered in these experiments. The comparisons between r.f. plasma probe, VLF Doppler method, Langmuir probe, and two-wire probe were carried out in the sounding rocket experiments of Kappa 9M-35 and 38. The comparisons of various probe methods revealed sources of error and gave increased confidence in measurements. The capacitance probe was used for the measurement of electron densities in the lower ionosphere where the gyro-plasma probe is not applicable due to collisional damping of the plasma resonance.

The Radio Exploration Satellite REXS "DENPA" was launched on August 19, 1972, with the Mu 4S-4 rocket from Kagoshima Space Center. The REXS project team has been organized since 1967 to build a scientific satellite to observe ionospheric and magnetospheric phenomena. Chapter

V gives the detailed description of the gyro-plasma probe (IPS) which was installed in the spacecraft REXS to measure the antenna impedance as a function of frequency over a wide range which includes the various plasma resonances. The IPS instrument onboard the spacecraft was successfully operated and measured values of all the observational items were acquired.

In the last Chapter VI, results obtained by the gyro-plasma probe onboard the spacecraft REXS are presented. The global electron density profile is deduced from measured upper hybrid resonance frequencies in the altitude range from about 250 km to 6500 km. The geomagnetic latitude variation of the electron density profile in the topside ionosphere is examined, compared with the results of the topside sounder satellites Alouette I and II. The observed enhancements of electron densities in the middle latitude towards the equatorial region are attributed to the equatorial anomally. The antenna impedance values are also investigated and the photoemission effect on the impedance value of an antenna in a tenuous plasma has been clarified. The measured lower hybrid resonance frequencies give the effective ion mass. The structure and the dynamics in the topside ionosphere are discussed on the basis of these experimental results.

LIST OF ILLUSTRATIONS

1-1 Normal electron distributions at the extremes of the sunspot cycle; (a) daytime and (b) night time (after W. B. Hanson[112]). 5

1-2 The electron density versus altitude in the D region for typical normal conditions, sudden ionospheric disturbances, polar cap absorption, and auroral absorption (after R. E. Bourdeau[124]). 8

1-3 The electron density profiles; (a) daytime and (b) nighttime (after K. Maeda[127,137]). 10

1-4 The electron density profiles for summer in the F1 region (after K. Maeda[158]). 13

1-5 The electron density versus the magnetic dip angle at various altitudes for the F region at local noon. The average peak electron density N_mF2 is given by the top curve (after S. A. Croom et al.[192]). 18

1-6 Contours of electron density at constant real hights above ground for Singapore, 10:00 local time. The real heights above ground (km) are indicated on the curves and the field line calculated from magnetic dip is drawn in (after J. W. King et al.[60]). 18

1-7 Contours of constant electron density scale height. The values in km are indicated on the curves (after J. W. King et al.[60]). 19

1-8 Contours of electron density as a function of latitude (in degree) and height (in unit of scale height). The electron density values (in unit of 10^5 cm^{-3}) are indicated on the curves. The dashed line represents the geomagnetic field line and the dotted line is the locus of points of maximum density at fixed height (after E. N. Bramley and M. Peart[186]). 20

1-9 A vector plot of electron fluxes (the equatorial fountain). Magnetic field lines are shown every

	200 km (after W. B. Hanson and R. J. Moffett[187]).	20
1-10	Averaged latitudinal and local-time behaviour of the electron density N_e (a) and temperature T_e (b), at 1000 km near 1965 vernal equinox (after L. H. Brace et al.[66]).	23
1-11	Relative electron and ion densities along a line of force as a function of the temperature-modified geopotential height z and the vertical altitude scale h. η, η_2, and η_3 are the density ratios of the electrons, the He^+, and the H^+ ions with respect to the O^+ ions (after J. J. Angerami and J. O. Thomas[208]).	24
1-12	Plasma density distributions along magnetic field line, whose apex in the equatorial plane is at L = 5 R_e, are shown for a diffusive equilibrium, and collisionless or ion-exosphere model, as well as for R^{-3} and R^{-4} power law models (after S. J. Bauer[212]).	25
1-13	Electron number density profile deduced from the upper hybrid resonance noise observed by IMP-6 (after R. R. Shaw and D. A. Gurnett[221]).	26
1-14	Equivalent electrical circuits of the specific admittance $y_\perp$ and $y_\parallel$ of cold plasma.	39
1-15	Equivalent electrical circuits of the total specific admittance y of sheath region (denoted by a suffix s) and plasma, ions being neglected.	40
1-16	Equivalent electrical circuit of the specific admittance $y_\perp^W$ of warm plasma.	41
1-17	Typical record of antenna admittance versus frequency (Kappa 8-15 rocket on Jan. 9, 1969).	42
2-1	Block diagram of rocket borne gyro-plasma probe system.	47
2-2	Typical example of antenna network circuit. The capacitance bridge with an antenna comprises the four capacitor arms; C_0, C_0, Ct, Cr and the variable capacitor	

MC601Y. 48

2-3 (a) Amplitude measuring circuit conversion-scale at 0.85 MHz. (b) Phase measuring circuit characteristic at IF frequency, 100 kHz. 49

2-4 (a) Simulation of amplitude by pure capacitance (1~3000 pF). (b) Simulation of amplitude and phase variation by L-C-R resonance circuit (L = 50 μH, C = 37 pF, R = 10 kΩ). (c) Simulation of amplitude variation; resonance damping due to R (L = 25 μH, C = 35 pF, R = ∞, 10 k, 7.5 k, 5.1 k, 3.0 k, 1.0 kΩ), and lower trace shows the reference frequency marker. 50

2-5 Deviation of electron density (α*) due to the gain difference of two EFT amplifiers (β*) and the normalized stray capacitance (Δ/C_{p0}). 52

2-6 Collisional damping of resonance and resonance frequency shift. Dots indicate minimum points of normalized probe capacitance. 53

2-7 Deviation of electron density due to electron-neutral collision; solid lines for constant f_p, and dashed lines for constant f_ν/f_p.

2-8 Prolate spherical coordinate system. 55

2-9 Normalized probe capacitance. D indicates the e-hold distance of electron density gradient, and L is the length of cylindrical probe. 56

2-10 Deviation of electron density due to density gradient in the μ direction. 57

2-11 Damping of resonance and resonance frequency shift due to the inhomogeneity of applied magnetic field. The cylindrical probe length 62 cm, z_0 = 1 cm, and B_{00} = 4.6 gauss. Three curves are corresponding to the magnetic field gradient; the parameters of B_0 [gauss·m] are (a) 1×10^{-4}, (b) 4.5×10^{-2}, and (c) 9×10^{-2}. 59

2-12 Capacitance of parallel plates in warm plasma. 60

2-13 Block diagram of self and mutual impedance measurement

	system. T1, T2, T3 are transmitting antennas and R receiving antenna.	61
2-14	Rocket borne instruments. (a) Lambda 3H-5 (four whip antennas with 130 cm in length and one vertical antenna with 60 cm in length); (b) Lambda 3H-6 (two whip antennas with 160 cm in length).	61
2-15	Block diagram of mutual impedance system.	62
2-16	Equivalent circuit for mutual impedance probe system.	63
2-17	Received signal intensity as a function of frequency. f_p = 3 MHz, f_H = 1.18 MHz, f_ν = 0.05 MHz, and T_e = 1000°K. Probe distance is 0.1 m, and C_{p0} = 10 pF, C_{pmo} = 5 pF, C_{st} = 1 pF, C_{mt} = 0.5 pF, and M' = 0.25 μH. Sheath capacitance is assumed to be 30 pF.	64
2-18	Circuit diagram of the Hartley-type oscillator.	65
2-19	System block diagram of the capacitance probe onboard S 210-6 sounding rocket.	66
2-20	Hartley oscillator; (a) a.c. equivalent of Hartley oscillator and (b) representation as the four terminal network.	68
2-21	Index of stability of Hartley-type oscillator versus conductance of the capacitor. (C = 30 pF, L_1 = 3 μH, L_2 = 0.33 μH, g_i = 20 μmho, g_f = 9.2 mmho (3SK28G)). k is a coupling factor of L_1 and L_2.	69
2-22	Normalized capacitance Λ versus probe potential.	74
2-23	Change in floating potential due to applied r.f. potential.	76
2-24	Change in quasi-equilibrium floating potential due to applied r.f. potential. (T_e = 1000°K, N_0 = 1 × 10^5 cm^{-3}, ion monocular weight AA = 25, and V_a = 1.0 volt).	78
2-25	Change in body's potential; frequency 1.0 MHz.	79
3-1	System of space plasma simulation chamber.	82
3-2	Pressure versus vacuum pumping sequence.	83
3-3	Back diffusion type plasma gun.	84
3-4	Electron density versus plate current. Argon plasma	

is produced by the back diffusion type plasma gun with tantalum metal cathodes (filament current 170 A and grid G1 current 50 mA); (a) grid G2 current 60 mA and G.P. the gas pressure, and (b) gas pressure 5.0 × 10^{-3} torr. and I_{G2} the grid G2 current. 85

3-5 Layout of the gyro-plasma probe experiment in the space simulation chamber. 86

3-6 Capacitance of an antenna in a plasma as a function of frequency; (a) $N_e = 1.22 \times 10^6$ cm^{-3}, and (b) $N_e = 9.29 \times 10^4$ cm^{-3} 86

3-7 Capacitance of antenna when the magnetic field is applied; (a) 0.42 gauss, (b) 2.1 gauss and (c) 3.1 gauss. f_{UHR} = 5.7 Hz, 7.9 MHz, and 10.3 MHz. f_{SHR} = 4.1 MHz, 5.9 MHz, and 8.7 MHz. 87

3-8 Capacitance of antenna in an inhomogeneous magnetic field. Uniform static field is 3.45 gauss. Small coil currents are 0, 1, 3, 6, 8, 12, 16, 22, and 25 A. 88

3-9 Self impedance measurement by gyro-plasma probe (a), and the received signal intensity (0 dB = 0.1 V_{rms}) obtained by mutual impedance probe (b). Left side; $N_e = 1.4 \times 10^5$ cm^{-3}, f_{UHR} = 3.70 MHz, and f_H = 1.55 MHz. Right side; $N_e = 1.5 \times 10^5$ cm^{-3}, f_{UHR} = 4.30 MHz, and f_H = 2.22 MHz. 89

3-10 Electrostatic wave forms measured by ASD and PSD methods. Argon plasma; gas pressure is 1.8×10^{-4} torr., $N_e = 3.0\sim3.1 \times 10^5$ cm^{-3}, T_e = 928°K, and B_0 = 0.7 gauss. $f = \omega/2\pi$ = 3.0 MHz. 90

3-11 (a) Received signal intensity as a function of function of frequency; f_H = 1.96 MHz, f_p = 4.92 ~ 5.03 MHz, f_{UHR} = 5.30 ~ 5.40 MHz, f_ν = 27 kHz, r_L = 1.43 cm and λ_D = 0.4 cm. (b) Received signal intensity as a function of distance. 91

3-12 Dispersion characteristics. Solid line is a dispersion curve of electrostatic Bernstein mode wave for f_p/f_H =

	2.24.	93
3-13	Dispersion relation of the Bernstein mode wave. (after F. W. Crawford et al.[283])	93
3-14	Frequency shift of capacitance probe versus applied bias potential.	94
3-15	Frequency shift of capacitance probe versus electron density.	95
3-16	Frequency shift of capacitance probe versus applied magnetic field Argon plasma; $N_e = 4.53 \times 10^5$ cm^{-3}, $f_p = 6.04$ MHz, $f_0 = 9.08$ MHz.	95
3-17	Langmuir curve for (a) Maxsellian and (b) non-Maxsellian distributions. Upper trace is the semi-logarithmic plots in arbitrary unit (after T. Dote).	97
3-18	Raw data obtained with the two-wire probe (after H. Mori) and the gyro-plasma probe.	98
3-19	Comparison of electron densities measured by the gyro-plasma probe and the Langmuir probe.	99
3-20	Comparison of electron densities measured by the two-wire probe and the Langmuir probe.	99
3-21	Comparison of electron densities measured by the two-wire probe and the gyro-plasma probe.	99
3-22	V_p dependence of wake structure behind the disk obstacle. Proton gas pressure = 1×10^{-6} torr.	101
3-23	Pressure dependence of wake structure. Argon plasma is used and z = 64 cm.	101
3-24	V_E dependence of wake structure. Proton gas pressure = 1×10^{-6} torr. and discharge r.f. high tension R_F = 1.5 kV.	102
3-25	Wake structure behind the obstacle. $V_E = 1$ kV, R_F = 1.5 kV, and P = 1×10^{-6} torr.	102
4-1	Geomagnetic field intensity along rocket flight path: Solid curve shows the theoretically computed values and dots indicate the observed ones (Digital numbers represent the time after rocket firing).	110

4-2	Output figures by computer-aided graphical display; (a) electron density, (b) geomagnetic field, and (c) rocket trajectory.	111
4-3	Trajectories of sounding rockets. (a) S 210-6, (b) Kappa 8-15, (c) Kappa 9M-41 and (d) Lambda 3H-6.	113
4-4	Geomagnetic field intensity along Lambda 3H-6 rocket flight path.	113
4-5	Electron density profile in the lower ionosphere. (a) S 210-6 (11:24, Jan. 1972). (b) S 210-8 (08:40, Jan. 1973).	115
4-6	Electron density profiles (Kappa 8-15).	116
4-7	Electron density distributions measured by Kappa 9M-35, 38 and 41.	117
4-8	Ionograms obtained by Yamagawa Radio Observatory. (a) 15:00, Feb. 22, 1972. (b) 18:00, Jan. 19, 1973. (c) 20:15, Jan. 23, 1971.	117
4-9	Diurnal variation of f_0F2 (Yamagawa, Jan. 23, 1971).	118
4-10	Geomagnetic latitude variation of N_m F2.	118
4-11	Daytime electron density profile in the topside ionosphere.	119
4-12	Night-time electron density profile in the topside ionosphere.	120
4-13	Electron density profiles in the topside ionosphere, measured by Lambda 3H-2 (after H. Oya[20]), 5, and 6.	120
4-14	Sheath capacitance at 300 kHz (Lambda 3H-5).	123
4-15	Electron temperature profile (Kappa 8-15).	123
4-16	Electron temperature profile (Lambda 3H-5).	124
4-17	Electron temperature profile measured by the retarding potential analyzer.	125
4-18	Ion composition ratio versus altitude.	126
4-19	Mean molecular weight versus altitude.	126
4-20	Altitude variation of amplitude of antenna capacitance versus frequency (Lambda 3H-6).	127
4-21	Records obtained by the mutual impedance probe; left,	

(a) received signal level, (b) equivalent capacitance of signal probe; right, altitude variation of f_{UHR} minimum. 128

4-22 The equivalent capacitance of cylindrical probe at different aspect angle θ (after H. Oya[291]). 129

4-23 Typical records of the probe capacitance versus frequency (Lambda 3H-2). 130

4-24 Observed values of $S(\theta) = (\omega_{UHR}-\omega_{MPR})/(\omega_{UHR}-\Pi_e)$, with respect to the geomagnetic aspect angle of the probe. The solid curve is the theoretically computed values using ionospheric plasma parameters at an altitude of 730 km. 130

4-25 Amplitude and phase changes of antenna admittance (Kappa 8-15). 131

4-26 Records of second harmonic cyclotron oscillation ($2f_H$) exhibited both in amplitude and phase of admittance (a = 172 km, b = 170 km, c = 168 km, d = 166 km, e = 165 km, f = 164 km, g = 163 km). 132

4-27 Records obtained by the Lambda 3H-5 (a) and 6 (b). 132

4-28 Change in received signal intensity at $2f_H$ (Lambda 3H-6). 133

4-29 Resonance frequencies; f_{UHR}, f_{SHR}, and nf_H. 134

4-30 Normalized admittance curve versus frequency. (a) plasma condition; f_p = 6.0 MHz, f_H = 1.18 MHz, f_ν = 0.1 MHz, T_e = 1000°K, and d = 0.1 m. sheath capacitance; A = 6.7 pF, B = 20 pF and C = 200 pF. (b) plasma conditions; f_H = 1.18 MHz, f_ν = 0.3 MHz, T_e = 1000°K, d = 0.1 m, $C_s = 3.3 \times f_p$ pF (f_p in MHz), f_p; A = 2 MHz, B = 4 MHz, C = 6 MHz and D = 10 MHz. The ordinate shows the logarithmic scale. 134

4-31 Electron density profiles obtained by the VLF Doppler method (after I. Kimura and T. Tomimoto) and by the gyro-plasma probe (Kappa 9M-35 and 38). 136

4-32 Comparison of electron densities obtained by Kappa

	9M-35 rocket experiment.	137
4-33	Deviation of electron density measured by the Kappa 9M-38 rocket experiment. "CPI ON" denotes the switch-on time of the electrical power of the ion mass spectrometer.	138
4-34	Comparison of the electron densities measured by Langmuir Probe (LP) (after H. Mori) and gyro-plasma probe (Kappa 9M-38).	140
4-35	Records obtained by two-wire probe (after H. Mori) and gyro-plasma probe (Kappa 9M-38).	140
4-36	Comparison of output wave forms obtained by gyro-plasma probe (GP) and two-wire probe (TWP). R denotes the received signals from GP and TWP.	140
5-1	Spacecraft REXS.	143
5-2	Block diagram of IPS instrument.	144
5-3	Schematic illustration of admittance-frequency characteristics. Frequency range 1 kHz ~ 15 MHz, equivalent capacitance = admittance/frequency.	147
5-4	Signal flow of science payloads.	147
5-5	Telemetry mode format; II_1 for IPH and II_2 for IPL.	148
5-6	Saw-tooth generator and voltage controlled oscillator.	149
5-7	Characteristics of the vari-cap diodes CR_1 and CR_2 (1S1619).	150
5-8	Oscillation frequency versus applied saw-tooth voltage (VCO 1).	150
5-9	Characteristics of swept frequency versus sweep time.	150
5-10	Block diagram of sweep signal generator. Frequency relations between f_S and $f_{1\sim6}$ are given in the parentheses.	151
5-11	Circuit diagram of sweep signal generator.	152
5-12	Frequency characteristics of low pass filter and video amplifier.	154
5-13	Output wave form; upper trace: 500 kHz sweep signal, lower trace: 600 kHz sweep local signal.	154

5-14	Mixer, IF amplifier, linear detector, logarithmic amplifier and d.c. amplifier.	155
5-15	Characteristics of input versus output of IF and logarithmic amplifiers. Dynamic range ≃ 60 dB.	156
5-16	Characteristics of input versus output of IF and linear d.c. amplifiers. Dynamic range ≃ 40 dB.	156
5-17	Frequency detector circuits (0.3 MHz and 13 MHz).	158
5-18	Output wave form from the tuned amplifier (upper trace) and frequency detect pulse with pulse width of 100 μsec from the monostable multivibrator (lower trace).	158
5-19	Functional block diagram of resonance detectors for Fh_1 and Fh_2 and sampling-hold circuit for $Lh_{1\sim3}$, including inhibit circuits.	160
5-20	Resonance detectors and sampling-hold circuit.	160
5-21	Pulse wave form (lower trace) from the comparator; dummy resonance circuit are used. The wave form of output signal from the logarithmic amplifier is superimposed (upper trace).	161
5-22	Output pulse of resonance detector; output from logarithmic amplifier is superimposed (upper trace).	161
5-23	Input versus output characteristics of the sampling-hold circuit.	162
5-24	Schematic time sequence of the sampling-hold circuit. Lh_1 whose detect pulse is fed to sampling-hold circuit at W_{25}, is transmitted to ENC at W_{26}, being reset at end of W_{26}.	162
5-25	Operational performance of inhibit circuit.	163
5-26	Output pulse (lower trace) of delayed monostable multivibrator of the inhibit circuit. First pulse is triggered by word synchronous pulse and second pulse is triggered by UHR detect pulse. Output from logarithmic amplifier is superimposed (upper trace).	163
5-27	Gate width control circuit.	164

5-28	Gate pulse (lower trace) and output pulse of the monostable multivibrator (upper trace). Gate width is 19.692 μsec and jitter of pulse appears because several traces are superimposed.	164
5-29	Frequency counter.	166
5-30	Functional block diagram of data selector, SN 54151.	166
5-31	Relative frequency error (E_0 and E_1) of frequency counter system.	166
5-32	System block diagram of swept frequency signal generator.	169
5-33	Circuit diagram of sweep frequency signal generator.	169
5-34	Saw-tooth wave form (0 to 4.5 volts) to voltage controlled oscillator (a), and frequency reference voltage (0 to 3 volts) for Fℓ and C$\ell_{1\sim4}$ (b).	170
5-35	Frequency characteristics of low-pass filter and high-pass filter; maximum attenuation frequency is 32 kHz.	172
5-36	Wave form of swept signal output applied to antenna. Saw-tooth wave form is superimposed (lower trace).	172
5-37	Swept frequency versus time curve.	172
5-38	IF amplifier and detector stage.	173
5-39	Frequency characteristics of band-pass filter with IF amplifier.	173
5-40	Input versus output characteristics of logarithmic amplifier and IF amplifier. Dynamic range ≃ 60 dB.	173
5-41	Frequency detector; center frequencies at 1.25 kHz, 3.80 kHz, 6.65 kHz and 10.1 kHz.	175
5-42	Frequency detect pulse sequence, $f_1 \sim f_4$; lower trace is resonance wave form to frequency detectors.	175
5-43	Circuit diagrams of lower hybrid resonance detector, sampling-hold circuit and data selector.	176
5-44	Performance of resonance detector; output wave form from logarithmic amplifier (upper trace) and resonance detect pulse (lower trace). (b) enlarged a	

	part of resonance of (a).	178
5-45	Input versus output characteristics of sampling-hold circuit (HOLd 2 for $L\ell_{1\sim3}$, and HOLD 3 for $F\ell$ and $C\ell_{1\sim4}$).	178
5-46	Circuit diagram of pre-amplifiers of both IPH and IPL.	179
5-47	Typical characteristics of wide band video-amplifier, SN5510L; (a) small-signal voltage gain versus frequency, and (b) common-mode rejection ratio versus frequency.	180
5-48	Antenna switching circuit.	182
5-49	Frequency calibration circuit.	184
5-50	Output wave form of frequency calibration of IPH (a) (fixed frequency of 357.5625 kHz) and IPL (b) (swept frequency of 321 kHz to 335 kHz).	184
5-51	Functional operation diagram of data processor; integrated circuits, HD203F and HD204F, are used.	186
5-52	Pulse sequences from TIM-ENC.	187
5-53	Pulse sequences from data processor.	187
5-54	Functional block diagram of ground-based data selector.	188
5-55	Gate control pulse sequences of ground-based data selector.	190
5-56	Electrical circuit of gate and buffer amplifier.	190
5-57	Structure of three monopole antennas and two loop antennas.	191
5-58	Main instrument of gyro-plasma probe and its pre-amplifier; (a) before and (b) after encapsulation.	192
5-59	Equivalent capacitance versus frequency characteristics of output from logarithmic amplifier (IPH).	195
5-60	Equivalent capacitance versus output decimal data (Lh_1 and Lh_3) through sampling-hold circuit and A/D converter of telemetry system.	195
5-61	Sampling-hold performance. Corresponding to 0.3 MHz, f_{UHR} and 13 MHz, frequencies are detected and potentials (Lh_1, Lh_2 and Lh_3) are sampled and stored.	

Output wave form of logarithmic amplifier is superimposed. Dummy antenna circuit C_0(L//C) (L = 100 μH, C = 30 pF, C_0 = 100 pF and damping resistor of 5.1 kΩ) are used. 197

5-62 Resonance frequency detection; (a) output of Fh_1 00101100 (binary) ≡ 44 (decimal) which is equal to 2.23 MHz, and (b) output of Fh_2 is 0011010 (binary) ≡ 26 (decimal) which is equal to 1.32 MHz. Output wave form of logarithmic amplifier is superimposed (Vertical: 0.5 V/div.). Dummy antenna circuit (L = 100 μH, C = 15 pF and C_0 = 100 pF) are used. 197

5-63 Equivalent capacitance versus frequency characteristics of output from logarithmic amplifier (IPL). 198

5-64 Equivalent capacitance versus output decimal data ($L\ell_1$, $L\ell_2$ and $L\ell_3$) through sampling-hold circuit and A/D converter. 198

5-65 An example of sampled and stored levels of $L\ell_1$, $L\ell_2$ and $L\ell_3$; frequency spectrum of admittance level is superimposed. 199

5-66 Resonance detect performance. Two resonances are detected and the last one is stored and transmitted as Fℓ. Output wave form of logarithmic amplifier is superimposed. The dummy antenna circuit with L of 1H, C of 1000 pF is used. 199

5-67 Frequency reference levels $C\ell_{1\sim4}$; saw-tooth wave form for this reference level is superimposed. Sampled potential is a little less than saw-tooth voltage due to input-output characteristics of the sampling-hold circuit (HOLD 3, see Fig. 5-45). 199

5-68 Results of thermal vacuum test; conditions, modes A~G, are listed in Table 5-3. 202

5-69 Monitor output of IPH (Horizontal; 125 ms/10 div, Vertical; 1 V/div.). (a) Mode C (temperature of 8.5°C). (b) Mode E (temperature of 30.0°C). Antenna is replaced

	by dummy electrical circuit, i.e., series circuit of (6.2 kΩ//100 pF) and (56 μH//4.7 kΩ//30 pF), and calibration level (100 pF) is superimposed.	202
5-70	Temperature dependence of gyro-plasma probe characteristics in vacuum.	203
5-71	A set of output data obtained in the space chamber experiment.	205
5-72	Equivalent capacitance characteristics obtained in the space chamber experiment. Dashed lines show the frequency characteristics of equivalent capacitance corresponding to indicated resistances.	207
5-73	Probe conductance versus electron density value. The values obtained simultaneously by Langmuir probe method are indicated.	208
5-74	Frequency change of upper hybrid resonance due to applied magnetic field; (a) 0.57 gauss, (b) 1.14 gauss.	209
5-75	(a) Orbit plane coordinate system (X_ω, Y_ω, Z_ω)and right ascension-declination coordinate system (X, Y, Z). (b) Geodetic coordinate system.	211
5-76	Flow chart of data analysis system	218
6-1	Attitude of the spacecraft in right ascension-declination coordinate system.	222
6-2	Orbit of REXS satellite.	223
6-3	Record of IPS quick-look (rev. #23, Aug. 21, 1972).	224
6-4	Records for IPL frequency calibration.	225
6-5	Temperature in IPS pre-amplifier obtained with house keeping equipment.	225
6-6	Upper hybrid resonance frequency (Fh_1); rev. #6.	227
6-7	Sheath resonance frequency (Fh_2); rev. #6.	227
6-8	Lower hybrid resonance frequency (Fℓ); rev. #8.	227
6-9	Equivalent capacitance at 300 kHz (Lh_1); rev. #6.	230
6-10	Equivalent capacitance at f_{UHR} (Lh_2); rev. #6.	230
6-11	Equivalent capacitance at 13 MHz (Lh_3); rev. #6.	230

6-12	Equivalent capacitance at 1.25 kHz; rev. #6.	233
6-13	Equivalent capacitance at 3.80 kHz; rev. #6.	233
6-14	Equivalent capacitance at 6.65 kHz; rev. #6.	233
6-15	Geomagnetic field intensity along the orbit of "REXS". The dots indicated on the curve are measured values with MGS.	236
6-16	Electron density profile deduced from measured values of f_{UHR} (see Fig. 6-6) during revolution #6.	236
6-17	Electron density profile versus altitude.	237
6-18	Electron density profiles versus altitude.	237
6-19	Average electron density profiles of three sets of observations along the same orbital phase.	239
6-20	Geomagnetic latitude dependence of F2 peak; (a) hight of F2 peak, (b) maximum electron density of F2 layer.	240
6-21	Electron density profile; constant height versus geomagnetic latitude.	241
6-22	Contour map of constant electron density in altitude-latitude domain.	241
6-23	Contour map of field aligned scale height.	242
E-1	Output decimal values vs. temperature in pre-amplifier of IPS.	255

LIST OF TABLES

4-1	List of sounding rocket experiments.	104
4-2	List of ionospheric conditions.	112
5-1	Observation items and abbreviations.	146
5-2	Electrical power consumption of IPS.	193
5-3	6 modes of the thermal vacuum test.	201
5-4	Experimental conditions of the plasma in the space chamber.	208

CONTENTS

ACKNOWLEDGEMENTS

PREFACE

LIST OF ILLUSTRATIONS

LIST OF TABLES

Chapter I REVIEW OF IONOSPHERIC MEASUREMENTS WITH R.F. PLASMA PROBES

§ 1. Observations of Ionospheric Plasma with In-situ Plasma Probes 1

§ 2. Electron Density Profile in the Ionosphere 3

2.1 Electron Density in the D and E Regions 6

2.2 Electron Density in the F1 and F2 Regions 11

2.3 Electron Density in the Topside Ionosphere 22

§ 3. Theory of R.F. Plasma Probes 27

3.1 Historical Survey of antenna Impedance Theory 28

3.2 Description of Plasma as a Dielectric Medium 33

3.3 Representation of Plasma by Equivalent Electrical Circuit 37

3.4 Impedance of Cylindrical Antenna in Plasma 42

Chapter II SYSTEM DESIGN OF R.F. PLASMA PROBES

§ 1. Introduction 45

§ 2. Gyro-plasma Probe System 47

2.1 Instrumentation 47

2.2 Calibration of Capacitance Bridge Unbalance 50

2.3 Collision Effect on Resonance Characteristics 53

2.4 Impedance of Antenna in Inhomogeneous Plasma 54

2.5 Impedance of Antenna in Warm Magnetoplasma 59

§ 3. Mutual Impedance Probe System 60

3.1 Instrumentation 60

3.2 Mutual Impedance in Magnetoplasma 62

§ 4. High Frequency Capacitance Probe System 65

4.1 Instrumentation 65
4.2 Design of Electrical Circuits 67
4.3 Collision Effect on Electron Density Measurement 70
§ 5. R.F. Response of Ion Sheath 71
5.1 Sheath Formation around a Body in Plasma 71
5.2 Sheath Capacitance of Plane Probe 73
5.3 Change in Floating Potential due to Applied High Tension R.F. Field 75

Chapter III R.F. PLASMA PROBE EXPERIMENTS IN LABORATORY PLASMA
§ 1. Introduction 80
§ 2. Generation of Plasma in the Space Simulation Chamber 81
2.1 System of Space Simulation Chamber 81
2.2 Plasma Source and its Characteristics 84
§ 3. Experimental Results 86
3.1 Gyro-plasma Probe Experiment 86
3.2 Mutual Impedance Probe Experiment 88
3.3 High Frequency Capacitance Probe Experiment 94
3.4 Comparison of Electron Density Measurement by R.F. and D.C. Probes in Laboratory Plasma 96
3.5 Wake Structure behind a Body in Plasma Stream ... 100

Chapter IV ROCKET OBSERVATIONS OF THE IONOSPHERE BY R.F. PLASMA PROBES
§ 1. Introduction ... 103
§ 2. Data Processing System ... 105
2.1 Determination of Rocket Trajectory ... 105
2.2 Computation of the Geomagnetic Field ... 108
§ 3. Electron Density and Temperature Measurements in the Ionosphere ... 111
3.1 Electron Density Profile in the Ionosphere ... 112
3.2 Electron Temperature in the Ionosphere ... 121
3.3 Ion Composition in the Topside Ionosphere ... 124

§ 4. Resonance Phenomena observed in the Ionospheric Plasma ... 126
4.1 Upper Hybrid and Sheath Resonances ... 126
4.2 Modified Plasma Resonance ... 128
4.3 Cyclotron Harmonic Resonance ... 131
§ 5. Comparison of Various Plasma Probe Methods ... 135
5.1 VLF Doppler Method and Gyro-plasma Probe ... 135
5.2 Langmuir Probe, Two-Wire Probe, Capacitance Probe and Gyro-plasma Probe ... 139

Chapter V GYRO-PLASMA PROBE ONBOARD THE SPACECRAFT REXS
§ 1. Introduction ... 142
§ 2. Instrumentation of the Gyro-plasma Probe ... 148
2.1 High Frequency Gyro-plasma Probe ... 148
2.2 Low Frequency Gyro-plasma Probe ... 167
2.3 Capacitance Bridge and Pre-amplifier ... 177
2.4 Frequency Calibration and Data Processor ... 183
2.5 Construction of Payload and Antenna ... 190
§ 3. Pre-flight Test of Instrument ... 194
3.1 Operational Characteristics ... 194
3.2 Thermal Test in Vacuum Environment ... 200
3.3 Simulation Experiment in Plasma ... 203
§ 4. Computer System for Data Analysis ... 210
4.1 Data Processing and Analysis System ... 210
4.2 Calibration Method ... 215
4.3 Computation of Electron Density ... 217

Chapter VI DISCUSSION OF RESULTS OBTAINED BY GYRO-PLASMA PROBE ONBOARD THE SPACECRAFT REXS
§ 1. Introduction ... 219
§ 2. Experiment and Results ... 220
2.1 Performance ... 220
2.2 Results and Data Analysis ... 222
2.3 Observation of Ionospheric Plasma Resonance ... 226
2.4 Observation of Antenna Admittance ... 229

§ 3. Electron Density Profile in the Ionosphere ... 235
3.1 Topside Ionosphere ... 235
3.2 Equatorial F Region ... 238

CONCLUDING REMARKS ... 244

APPENDICES

A. General Expression of Sheath Capacitance ... 247
B. Vehicle's Horizontal Distance from KSC ... 249
C. Standard Pre-flight Test Condition ... 252
D. Computation of Reliability of IPS ... 254
E. Calibration Coefficients for IPS ... 255

SYMBOLS AND CONSTANTS ... 257

REFERENCES ... 258

Chapter I REVIEW OF IONOSPHERIC MEASUREMENTS WITH R.F. PLASMA PROBES

Following World War II, it became clear that the use of in-situ probes carried on space vehicles played an important role in observing the properties of the upper atmosphere and provided significant scientific data which could not be obtained by ground-based observations. In this way, a new space age has been opened to the researchers in space physics especially in the exploration of the earth's upper atmosphere.

In this chapter, the history of observations of the ionosphere with in-situ plasma probes, expecially the progress of Japanese sounding rocket, are briefly reviewed. The electron density profiles and physical properties of the ionosphere are described, in order to understand the significance or explanation of the results that have been obtained by the rocket and satellite experiments described in this thesis. A survey of antenna impedance theory, and theoretical description of a plasma as a dielectric medium are given as the basis of r.f. plasma probe studies.

§ 1. Observations of Ionospheric Plasma with In-situ Plasma Probes

In order to investigate the ionospheric plasma, it is advantageous to measure the parameters of the ionosphere with in-situ plasma probes carried on rocket or satellite vehicles. Many measuring methods have been developed since the first radio propagation experiment by J. C. Seddon in 1947.[1] For the electron density measurements, r.f. impedance or capacitance probes and upper hybrid resonance probes have been established,[2~31] and also the Langmuir probe and its modifications have been used.[32~52] Excellent summaries of the survey of in-situ probes were given by J. Sayer[53] and others in Electromagnetic Probing of the Upper Atmosphere, edited by E. K. Smith.[54] Another important method for electron density measurement is the top-side sounder which have been successfully operated on Alouette I (launched September, 1962) and

Alouette II (launched November, 1965). Many papers have been published on experimental techniques, results of the electron density profiles and associated resonance phenomena in the ionospheric plasma.[55~84]

In Japan, the first attempt to measure the upper atmosphere with in-situ probes onboard a space vehicle was carried out during IGY (International Geophysical Year, 1957 ~ 1958). The various methods of measuring electron density in the ionosphere have been successfully performed since the Kappa 8 type rockets became available in 1960.

The resonance rectification probe was first used to investigate the resonance of a space plasma,[3,85] and the frequency corresponding to the probe current peak was taken as a measure of the plasma frequency. But, later, this resonance has been identified as a sheath resonance by many investigators.[86~95] It has been disclosed that, since the theory of sheath resonance is very complicated, it is virtually impossible to deduce electron density from this probe.

The fixed or swept voltage Langmuir probes were also used for measuring the electron density in the ionosphere.[96~97] The experiments in laboratory plasma as well as in space plasma made it clear that the contamination on the metal surface causes the hysteresis of current-voltage Langmuir curve.[98,99] The identification of the space potential with respect to the probe floating potential is very difficult because the phenomenon of electron current depletion near the space potential is still unsolved. There are additional problems such as the probe and the reference electrode (vehicle hull)dimensions, the contact potential of the metal surface, the photoelectric emission current, the magnetic field effect,[100] and the ram and wake effects. Nevertheless, this method has been extensively used, because of its simplicity.

The VLF Doppler method has been developed recently. The electron density is determined from the Doppler shift of a known continuous wave due to the vehicle motion.[101~103] The frequency shift of VLF signals (CW) transmitted from the ground-based station is measured by the instrument onboard the vehicle and telemetered to the ground. The Doppler shift can be detected with a precision of $\pm$ 2 % for most of the time of rocket flight except near the apex and in the lower part of the

ionosphere. Yet, it is felt that fine spatial structures or irregularities in the electron density fluctuation cannot be measured with this tequnique.

Since 1964, the gyro-plasma probe, a kind of frequency scanning impedance probe, has been developed to observe all kinds of plasma resonance phenomena related to the fundamental parameters of ionospheric plasma.[12,16,20] The probe system is designed to measure the probe impedance in a vector form, namely with amplitude and phase over the wide frequency range, including the electron gyro-frequency, the sheath resonance frequency and the upper hybrid resonance frequency. To eliminate contamination due to stray capacity, a capacitance bridge is employed in the sensor network. The electron density can be obtained within an accuracy of $\pm$ 1 % from the upper hybrid resonance frequency[27] which is independent of the probe shape, the probe aspect with respect to the geomagnetic field, and the ion-sheath formed around the probe.

Using various types of sounding rockets such as Kappa 8, Kappa 9M and Lambda 3H rockets, fine electron density and temperature profiles in the altitude range of 90 km to 2000 km have been measured by the gyro-plasma probe.[16,20,31,104~109]

The Mu 4S type satellite launching vehicle has been available since 1971, and the first scientific satellite SHINSEI was launched on September 28, 1971. This carried a fixed voltage Langmuir probe as Japan's first attempt to measure the electron density profile on a world-wide scale.[110] The spacecraft REXS was the second scientific satellite, and the gyro-plasma probe was installed to investigate the global electron density distributions of the topside ionosphere.

§ 2. Electron Density Profile in the Ionosphere

The earth is surrounded by electrons and charged atoms and molecules that make up the ionosphere. The discovery of the ionosphere was followed after Marconi's wireless transmission from England to the United States in 1909. The radio wave energy travelled much farther

than permitted by the inverse square law that had been well-known as the Austin-Cohen's equation. Earlier in 1902, A. E. Kennelly and O. Heaviside had suggested independently that an ionized layer around the earth could guide the energy to great distances. This ionized layer affecting radio waves has since been named the Kennely-Heaviside layer. E. V. Appleton and M. A. F. Barnett measured the refraction of the radio wave from the ionosphere. In 1925, G. Breit and M. A. Tuve succeeded in transmitting radio pulses vertically to the ionosphere and receiving the reflected echoes. These furnished much of our knowledge of the ionosphere until the experiments by rockets in the late 1940's and satellites in the late 1950's.

Theoretical treatments of the formation and the existence of ionized layers in the upper atmosphere had been first developed by S. Chapman[111] in 1931. He considered the absorption of monochromatic radiation from the sun in an isothermal atmosphere of which the density varies exponentially with height, and the energy of the radiation, or a definite fraction of it, is supposed to dissociate or ionize the air. The well-known Chapman's equation for the rate of production of ions, $I(\chi, h)$ at height h above the ground at the zenith distance χ gives us the fundamental concept of the formation of the ionosphere;

$$I(\chi, h) = I_0 \cdot \exp\{1 - Z - \sec \chi \cdot \exp(- Z)\}, \qquad (1.1)$$

and $$Z = (h - h_m(0))/H,$$

where H is the scale height, and $h_m(0)$ and I_0 are the values of the maximum ion production level $h_m(\chi)$ and $I(\chi)$ for $\chi = 0$. From eq. (1.1) height of the maximum ion production level $h_m(\chi)$ is deduced as

$$h_m(\chi) = h_m(0) + H \cdot \ell n \sec \chi \, . \qquad (1.2)$$

The Chapman layer is, thus, formed in the upper atmosphere, and the recombination of ions and electrons which are produced in this manner

proceeds slowly enough at the low gas densities involved so that high concentrations of electrons persist even throughout the night.

During the daytime, several distinct ionispheric "layers" or "regions" are recognized. In order of increasing altitude and

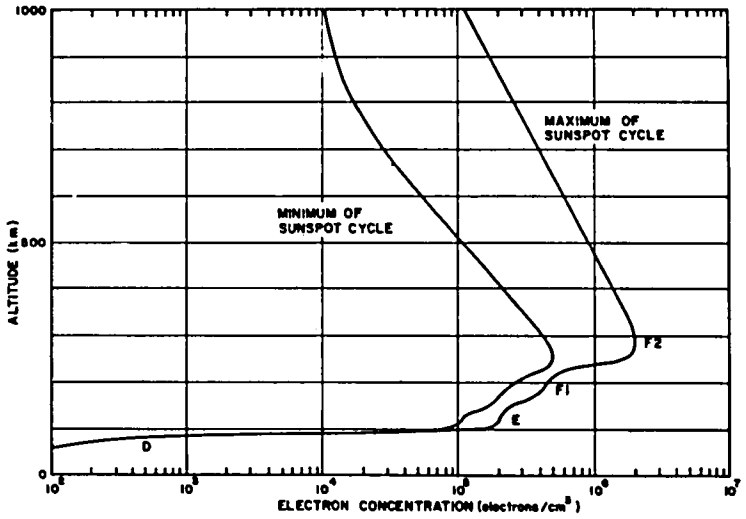

a. Daytime.

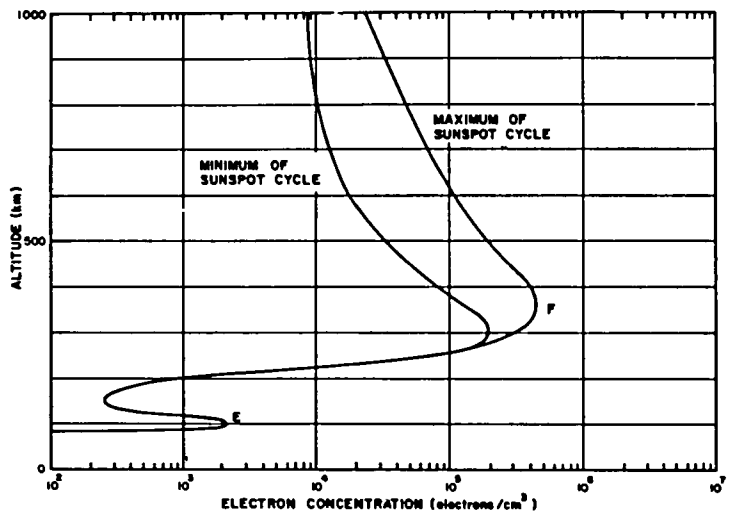

b. Nighttime.

Fig. 1-1 Normal electron distributions at the extremes of the sunspot cycle; (a) daytime and (b) night time (after W. B. Hanson[112]).

increasing ion concentration, they are called the D, E, F1, and F2 regions. Figure 1-1 shows typical daytime and nighttime electron density profiles in the mid-latitude ionosphere for the extremes of the sunspot cycle.[112] Above the maximum electron density in the F2 region, the electron density decreases monotonically out to several Earth radii. The F1 and F2 regions join at night, and a valley, or depression in electron density, appears between the E and F regions. A rather common perturbation of the electron density in the E region occurs near 100 km and consists of a thin layer (only a few kilometers thick) which is called sporadic E. The D region electron density also decreases drastically at night. The C region at the altitude of about 50 km is formed by the cosmic ray ionization. Since these ionized layers are mainly controlled by the sun, variations of electron densities are calssified into 3 main classes; the diurnal variation, the seasonal variation and the annual variation.

2.1 Electron Density in the D and E Regions

D Region The D region is the lowest ionospheric region close to the atmospheric mesosphere. The altitude usually ascribed to it is from 60 km to approximately 85 km. Its daytime electron density is estimated to be of the order of 10^3 cm^{-3} or less in normal conditions, but it may increase by as much as two order of magnitude when an intense solar flare is occuring. Cosmic rays (mostly protons at relativistic velocities) are the source of electrons below about 70 km in the D region, and X-rays and Lyman-α ultraviolet radiation are the sources at higher altitudes.[113] X-rays produce electrons by the photoelectric effect (2 to 8 Å with energies of 5 to 1.5 keV) and by Compton scattering (1 Å with energies larger than 10 keV). The X-ray reactions are X-ray + O_2 $\rightarrow$ $O_2^+ + e^-$ and X-ray + N_2 $\rightarrow$ $N_2^+ + e^-$ to form O_2^+ and N_2^+ ions and electrons. Lyman-α UV (1215.7 Å; 10 eV) reacts with nitric oxide to form NO^+ and an electron, i.e., Ly-α + NO $\rightarrow$ $NO^+ + e^-$.

The time variation of the electron density may be described by

$$\frac{dNe}{dt} = Q - \alpha_{eff} N_e^2 \qquad (1.3)$$

where Q is the electron production rate and α_{eff} is the effective recombination coefficient. It has been assumed that the number of electrons equals to the number of positive ions, i.e., the negative ions are neglected. In the D region, since the recombination time is short, ionization equilibrium can be determined by setting dN_e/dt equal to 0. Then, $N_e^2 = Q/\alpha_{eff}$. It is necessary to sum over the sources and recombination coefficients for varieties of atmospheric constituents involved. The dominating loss mechanism for electrons in the D region appears to be dissociative recombination of electrons on positive ions M^+. The neutral molecules or atoms are then left in exited state, viz., $e^- + M^+ \rightarrow M^*$.

From time to time the knowledge of electron density distributions in the D region increases considerably.[114] These phenomena are of great physical and practical interest; of practical interest because of their deleterious effect on radio propagation. The following four classes of perturbations are identified.

(1) The sudden ionospheric disturbance (SID).[115~117] A large simultaneous increase in electron density over the entire day hemisphere, which in turn gives rise to strong attenuation of radio signals, resulting in radio blackouts. SID's are caused by increase in solar X-ray flux during some large solar flares. They last a few minutes to several hours.

(2) The polar cap absorption event (PCA).[118,119] A large increase of ionization over the polar cap only. PCA's are caused by energetic protons emitted from the sun during large flares. They start to reach the earth an hour or so after the flare and last up to several days.

(3) The auroral absorption event (AZA).[120~123] A large increase associated with auroras and geomagnetic storms. These events are attributed to an influx of energetic electrons into the auroral zone and possibly also to their accompanying bremsstrahlung X-rays. They are common in the auroral zone, but they do occur equatorward of the auroral zone during geomagnetic storms.

Figure 1-2 shows the electron density versus altitude in the D

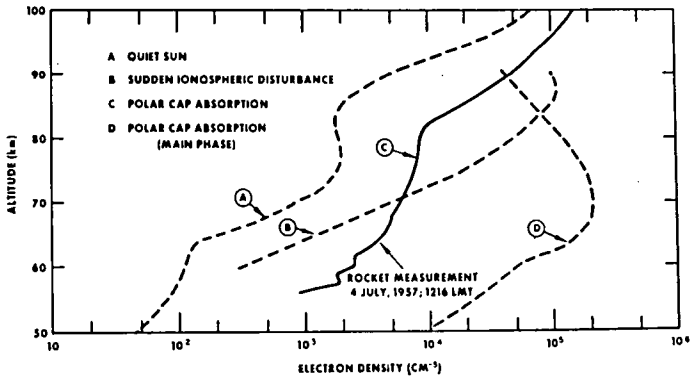

Fig. 1-2 The electron density versus altitude in the D region for typical normal conditions, sudden ionospheric disturbances, polar cap absorption, and auroral absorption (after R. E. Bourdeau[124]).

region for typical normal conditions, sudden ionospheric disturbance, polar cap absorption, and auroral absorption.[124]

(4) The winter anomaly event.[125~130] A moderate increase in D region electron densities associated with an enhanced mesospheric temperature occurs in the winter at middle latitude, lasting for several days.

E Region The altitude range from approximately 85 km to 140 km is designated the E region. The important solar radiations for the production of ionization in the E region are X-rays (10~100 Å), Lyman β (1025.7 Å), CIII line (977.0 Å) and Lyman continuum (865~911 Å).[131~132] The primary ions that are formed are N_2^+, O_2^+, and O^+. The main ionic species, however, are the diatomic ions O_2^+ and NO^+. The N_2^+ ions dissociatively recombine very rapidly, and they may react chemically with oxygen, resulting in the very small N_2^+ concentraction. It was first recognized by D. R. Bates[133] that ion-atom interchange reactions of the type $X^+ + YZ = XY^+ + Z$ should proceed rapidly in the ionosphere. Such chemical reactions of O^+ with O_2 and N_2 quickly remove the O^+ ions and produce either NO^+ or O_2^+ ions. The

rate of electron removal becomes to be of recombination type and the effective recombination coefficient α_{eff} in the E region is given by[132]

$$\alpha_{eff} = \frac{\alpha_1[NO^+] + \alpha_2[O_2^+] + \alpha_3[N_2^+]}{[NO^+] + [O_2^+] + [N_2^+]} \qquad (1.4)$$

where a pair of square brackets denotes the number density of atoms or molecules, and α_1, α_2, and α_3 are the dissociative recombination coefficients of NO^+, O_2^+, and N_2^+, respectively. The α_{eff} given by eq. (1.4) is nearly equal to α_1, because the greater part of ions in the E region are NO^+ ions. As α_{eff} does not change appreciably with altitude, the peak of electron density will appear at roughly the same level as that of peak of electron production (see eq. (1.3)). The height of peak level is about 110 km. In the lower part of E region, electrons are lost by dissociative recombination on O_2^+, i.e., $O_2^+ + e^- \rightarrow O + O$, and this controls the electron density at equilibrium in the lower E region.

The time variation of the E layer is relatively regular and its degree of variation with solar activity is less than that of F1 layer. The peak electron density is well represented by C. W. Allen's expression;[134]

$$N_m = 1.34 \times 10^5\{(1 + 0.0097\ R_z)\ \cos\chi\}^{0.5}\ [cm^{-3}] \qquad (1.5)$$

where R_z is the relative sunspot number. K. Maeda and S. Fukao[135] have studied the sunspot number (R_z) dependence of the E region maximum electron density (N_m) near noon, which is given by

$$N_m = N_{00}\sqrt{1 + \rho_e R_z}\ (\cos\chi)^{(1+\Gamma)/2}, \qquad (1.6)$$

where Γ is a positive scale height gradient, and N_{00} and ρ_e are constant values. K. Maeda[127,136,137] has investigated and summarized the electron density profiles in the lower ionosphere, based on data available from rocket experiments, and gave the standard electron density profile in the altitude range from about 60 km to 200 km.

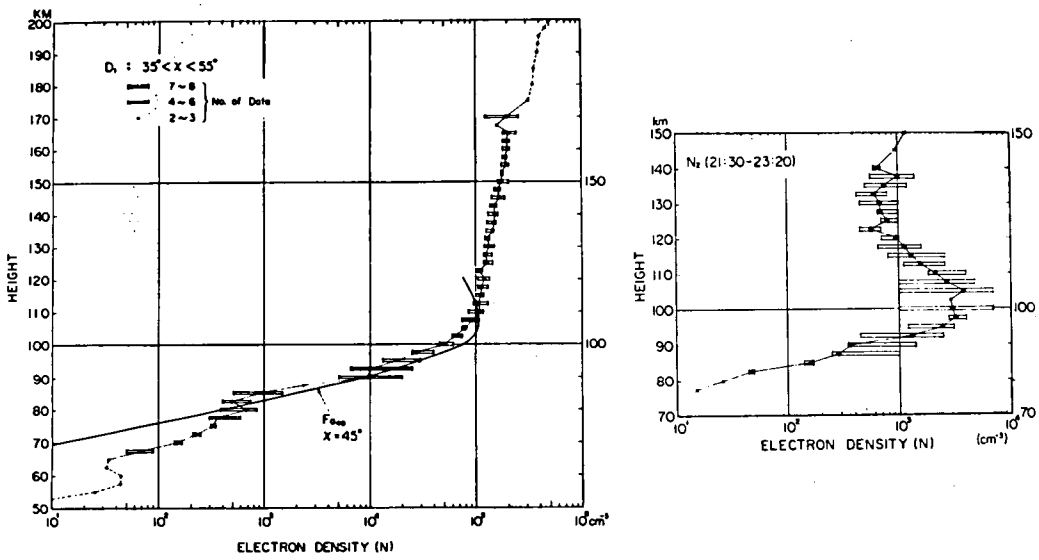

Fig. 1-3 The electron density profiles; (a) daytime and (b) nighttime (after K. Maeda[127,137]).

After sunset, N_mE decreases to its night time value, typically of the order of 5×10^3 cm^{-3}, which could probably be maintained by the extreme ultraviolet radiations from the night sky such as Lyman α, Lyman β, and the helium lines.[138~140] There exist deep valleys above the nighttime E layer, in which the electron concentration is much less than the electron density at E layer peak.[141] Representative electron density profiles in the daytime and in the night time are shown in Fig. 1-3.

Sporadic E(E_S) ionization is sometimes observed at about 110 km altitude in a thin layer of about a few kilometers thickness. In the equatorial E region, there appear strong non-blancketing reflections at 100 km height and also a slanted echo in the ionogram. The former is called as "equatorial sporadic E" or "q-type", and the latter as "equatorial slant sporadic E". These are closely related to the equatorial electrojet.[142,143] Theories of two-stream instability[144] and cross-field instability[145~148] are proposed to explain these types of irregularities. In the auroral zone and the polar cap, irregularities[149] seem to be roughly divided into two groups; one is closely related to

the precipitation of energetic auroral particles and the other is due to an intense current stream, i.e., the auroral electrojet. The mid-latitude Es layer is classified into the following two groups. One is the intense blanketing sporadic E layer, uniform over some tens of kilometer in horizontal dimension. The wind-shear process may be the main cause of this type of Es.[150~154] The other is diffuse nonblanketing, or scattering type sporadic E, in which the electron concentration is not large and irregular. The most probable formation mechanism is the cross-field instability.[145~147,155]

2.2 Electron Density in the F1 and F2 Regions

F1 Region The altitude demarcations between the E and F1 regions and the F1 and F2 regions are not clearly defined, and the altitude range from 140 km to 200 km is customaly called the F1 region. The layer is not present at night due to the depression in electron concentration above the E region. At times, even during the day, it may not be observed as a seperate layer. It is more liable to appear as a seperate layer in summer than in winter and near noon than near sunrise and sunset. The solar spectrum in the band from 200 Å to 900 Å is principally responsible for the photo-ionization in this region.[156] Because the photoelectrons are released with relatively high energy, which share principally with other electrons, the electron temperature is several hundred degrees higher than the atmospheric neutral temperature during the daytime.[157]

The predominant ions are NO^+ and O_2^+ near the low altitude boundary, and a gradual transition tekes place until, at the upper boundary, O^+ is the principal ion.

It is believed that the principal loss process is recombination for the E region and effectively attachment for the F2 region. The F1 layer is an intermediate region from recombination-type to attachment-type electron removal. T. Yonezawa[132] gave the effective recombination coefficient (α_{eff}) which involves the effects of the both types

of processes as,

$$\alpha_{eff} = \frac{\beta_1[N_2] + \beta_2[O_2]}{N_e + \frac{\beta_1}{\alpha_1}[N_2] + \frac{\beta_2}{\alpha_2}[O_2]} \qquad (1.7)$$

where β_1 and β_2 are rate coefficients of the ion-atom interchange reactions, i.e., $O^+ + N_2 \rightarrow N + NO^+$ and $O^+ + O_2 \rightarrow O + O_2^+$, respectively.

According to C. W. Allen[134] the peak electron density (N_m) in the daytime is expressed in the following form,

$$N_m = 2.40 \times 10^5 \sqrt{1 + 0.0124\, R_Z}\, (\cos\chi)^{1/2} \ [cm^{-3}] \qquad (1.8)$$

The height of the peak level is about 180 km. The electron concentration is typically of the order of 2.5×10^5 cm^{-3} at noon during sunspot minimum and 4×10^5 cm^{-3} at noon during sunspot maximum. K. Maeda[158] studied theoretically the electron density profile of the F1 region. Assuming $\alpha = \alpha_1 = \alpha_2$ in eq. (1.7), the following analytical expression of electron density is proposed

$$N_e = \frac{Q}{2B^*}\left\{1 + \left(1 + \frac{4B^{*2}}{\alpha Q}\right)^{1/2}\right\} \qquad (1.9)$$

where $B^* = \beta_1\left\{[N_2] + \frac{\beta_2}{\beta_1}[O_2]\right\}$.

The conclusions derived from K. Maeda's study are: In the F2 and upper F1 regions, $4B^{*2}/\alpha Q$ is very small and $N_e \simeq Q/B^*$; while in the E region, the above quantity is large and $N_e \simeq \sqrt{Q/\alpha}$. In the main part of the F1 region, N_e is proportional to neigher Q nor $\sqrt{Q}$. The complex relationship between Q_m (maximum Q) and N_m makes it meaningless to express N_m as a simple function of R_Z and χ, e.g., $N_m \propto \sqrt{1 + \rho_e R_Z}\,(\cos\chi)^k$ as customarily used. The example of electron density profile in the F1 region is shown in Fig. 1-4.

F2 Region The spatial and time variations of the F2 layer are strongly influenced by the geomagnetic field. The variation with the

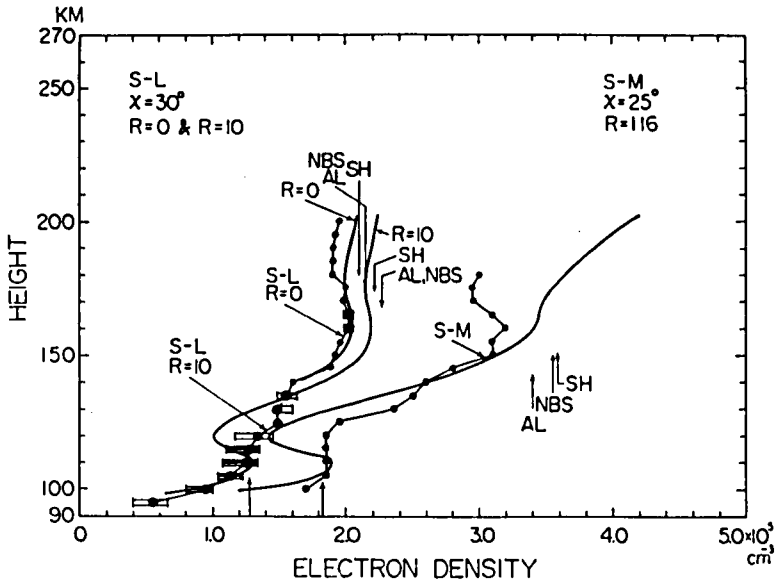

Fig. 1-4 The electron density profiles for summer in the F1 region (after K. Maeda[158]).

solar activity is also very pronounced. According to C. W. Allen,[134] the peak electron density is expressed in the following empirical form,

$$N_m = 5.9 \times 10^5 \ (1 + 0.0200 \ R_z) \cos \chi \quad [cm^{-3}] \qquad (1.10)$$

The level of the peak is normally situated at about 300 km by day and 350 km by night in middle latitude and at greater altitudes for higher solar activity and/or near the equator. The main ionized constituent is atomic oxgen (O^+) in the F2 region. The upper boundary of F2 layer is generally assigned to be up to the altitude where O^+ ceases to be the predominant ion. The electron density $N_e(h, t)$ at any height and time is given by the solution of the continuity equation for electrons in a general form of eq. (1.3),

$$\frac{\partial N_e}{\partial t} = Q - L(N_e) - \mathrm{div}(N_e \cdot \vec{v}) \qquad (1.11)$$

in which terms on the right-hand side are production, loss, and diver-

ging movement of ionization, respectively. The movement term can be written as the divergence of a transport flux of ionization,

$$\mathrm{div}(N_e \cdot \vec{v}) = \mathrm{div}[N_e \cdot (\vec{v}_{EM} + \vec{v}_T + \vec{v}_D)] \qquad (1.12)$$

Here three types of movement are recognized explicitly, namely, movement caused by electromagnetic forces, by atmospheric temperature changes and by ambipolar or plasma diffusion. The formation of the F2 layer can be well represented by the electron removal of the attachment-type loss and the vertical motion or the ambipolar diffusion in the following form of the continuity equation corresponding to quasi-equilibrium condition ($\partial N_e/\partial t \simeq 0$);

$$Q = \beta N_e + \frac{d}{dz}(N_e \cdot W_d) \qquad (1.14)$$

where z is the altitude and W_d serves to define changes in electron density by vertical motion. In the region up to the F2 peak, βN_e predominates over the diffusion term, and because it decreases more rapidly with altitude than the electron production rate (Q), N_e increases with altitude up to its maximum value. Near the F2 peak, the diffusion term becomes lager than βN_e and the electron density begins to decrease. At altitude well above the F2 peak where Q and βN_e can be considered negligible, the electron density distribution is given by the diffusive equilibrium equation;[153]

$$\frac{1}{N_e}\frac{d}{dz}[N_e \cdot \kappa(T_e + T_i)] + M \cdot g = 0 \qquad (1.15)$$

where g is the acceleration of gravity, κ is the Boltzmann constant, and T_e and T_i are the electron and ion temperatures. To take account of the temperature difference of electron and ion, especially by day in the F region, it is convenient to define the plasma temperature T_p and the plasma scale height H_p by the equation;

$$T_p = \frac{1}{2}(T_e + T_i), \quad \text{and} \quad H_p = 2\kappa T_p / M \cdot g. \qquad (1.16)$$

T. Yonezawa and H. Takahashi[160] showed that the extended Chapman's distributions with a constant scale height gradient (J. W. Wright[161]) cannot be representative of the actual electron density dstribution in the higher region above F2 peak. S. Chandra[162] developed a modified Chapman function with a variable scale height gradient, i.e.,

$$N_e(z) = N_m \cdot \exp \frac{1}{2} \left[1 - \int_{z_m}^{z} \frac{dz}{H} - \exp\left(- \int_{z_m}^{z} \frac{dz}{H}\right)\right] \qquad (1.17)$$

where $N_e(z)$ is the electron density at height z and z_m is the height of the maximum electron density, N_m. The scale height H, here, varies as a function of height; when the H value takes to be constant, eq. (1.17) is equivalent to the simple Chapman function. To give the analytical form for the variable scale height, a modified Chapman function has been found to be in good agreement with the electron distribution obtained experimentally within the height range from 100 km below the F2 peak to an altitude of about 700 km.

F Region Anomalies Early investigations of the F2 layer critical frequency revealed that it does not behave at all in the manner of a simple Chapman layer. Following H. Rishbeth and O. K. Garriott,[159] some of the outstanding problems of F2 layer morphology are:

(1) behavior of the F2 peak (maximum electron density N_mF2, and height of F2 peak h_mF2) and the diurnal behavior of electron concentration at fixed heights;
(2) the seasonal, annual, and semiannual anomalies;
(3) the maintenance of the F layer at night;
(4) the polar F layer;
(5) the equatorial anomaly;
(6) storm effects in the F region.

Some of these phenomena and the global electron density distributions in the mid- and low-latitudes are described below in brief.

As for the maximum electron density at F2 peak (N_mF2), J. O. Thomas et al.[163,164] made it clear that N_mF2 is peaked about noon in winter

during moderately high solar activity but is rather irregular in other seasons and also all seasons during low solar activity. The morning and evening maxima of N_mF2 appear in most summer months, and this mechanism has been attributed to the temperature change[165] and to vertical drift.[166,167] As regards the height of F2 peak (h_mF2), the heating and cooling of the atmosphere alters the height at which $D/H^2 \sim \beta$; D is diffusion constant in the F2 layer and H is the scale height. The detailed investigations about diurnal, seasonal, semiannual and annual anomalies have been made by L. V. Berkner,[168] T. Yonezawa and Y. Arima,[169] T. Yonezawa,[170] J. W. King and P. A. Smith[171] and many others.

At night the maximum electron density and its height in the F2 layer vary rather irregularly. In the hours proceeding F-layer sunrise, there may be noticeable increases or decreases. Some of these pre-sunrise phenomena may be attributable to an influx of photoelectrons along geomagnetic field lines, when the conjugate point is illuminated by the sun.[172,173] The maintenance of the night F2 layer has not been clearly explained. The F2 peak is higher at night than by day at mid-latitude,[163] and explained this by upward drift due to winds. Although this drift does tend to preserve the layer, by reducing the effective loss rate, it cannot halt the decay completely. The photoionization by extreme ultraviolet radiation in the night sky is also quite insufficient to maintain the night F2 layer,[138] but a possible alternative is considered to be corpuscular ionization, probably by soft electrons or protons of 10^2~10^3 eV energy,[174] and the penetration of electrons and ions slowly into the F2 region from the exosphere by ambipolar diffusion.[175]

The high-latitude F region behaves in more complexity; even at the geographic south pole where the diurnal variation of χ is negligible, there are diurnal changes of electron concentration which must be due to movement processes.[176] The variations of f_0F2 show appreciable dependence on universal time.[177,178] The possible mechanism considered by J. W. King et al.[179] is that the neutral air winds blow across

polar regions from the day hemisphere toward the night hemisphere, producing vertical drifts in the F region which depend on the orientation of the geomagnetic field. The maintenance of the F region ionization during the polar winter presents a problem which resembles that of the nighttime F2 layer.

In the equatorial region, geomagnetic line of force runs nearly horizontally so that diffusion of electrons and ions in the vertical direction across the geomagnetic field line is almost completely prohibited. In this case, however, two factors hitherto neglected must be taken into account. First, the radiative recombination of O^+ ions with electrons[126] (h, the Plank constant; ν, the frequency of the radiated wave),

$$O^+ + e^- \rightarrow O + h\nu \qquad (1.18)$$

will manifest its existance at sufficiently great heights, because the recombination coefficient of this process α_{rad}, though very small, does not change with height while the effective attachment coefficient β decreases rapidly with height. Another important, or perhaps most essential, process is the diffusion along the field line and the electrodynamical drift.[159,180~188] The observed electron density by day in the F2 layer as a function of latitude shows a pronounced "trough" centered on the magnetic dip equator, with "crests" 15° to 20° to the north and south.[43,63,79,189~191] The plots of the electron density at fixed height below (S. A. Croom et al.[192]) and above the F2 peak (J. W. King et al.[60]) are illustrated in Fig. 1-5 and Fig. 1-6. Figure 1-7 shows contours of the height of regions of constant scale height plotted against latitude.[60] Enhancement of electron density in the middle latitude towards the equatorial region are so-called the equatorial anomaly. As evident in Fig. 1-6, ledges of ionization occur aligned along a specific magnetic field line.

It was suggested by S. K. Mitra[193] that the anomaly might be due to the diffusion of ionization away from the equator, causing an

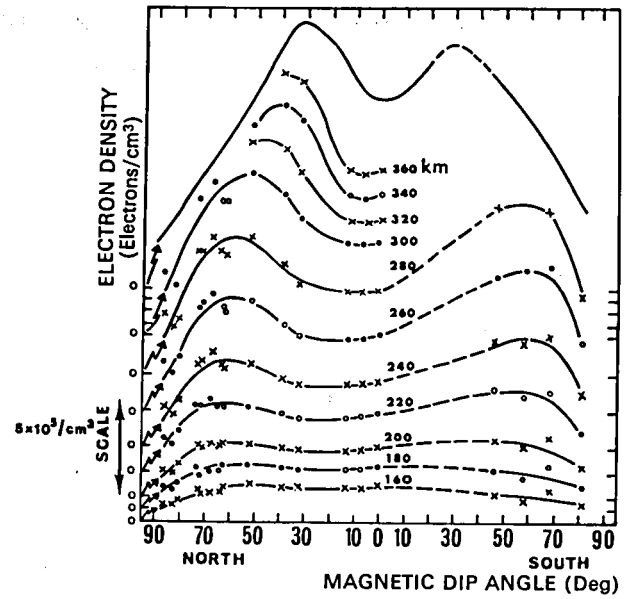

Fig. 1-5 The electron density versus the magnetic dip angle at various altitudes for the F region at local noon. The average peak electron density N_mF2 is given by the top curve (after S. A. Croom et al.[192]).

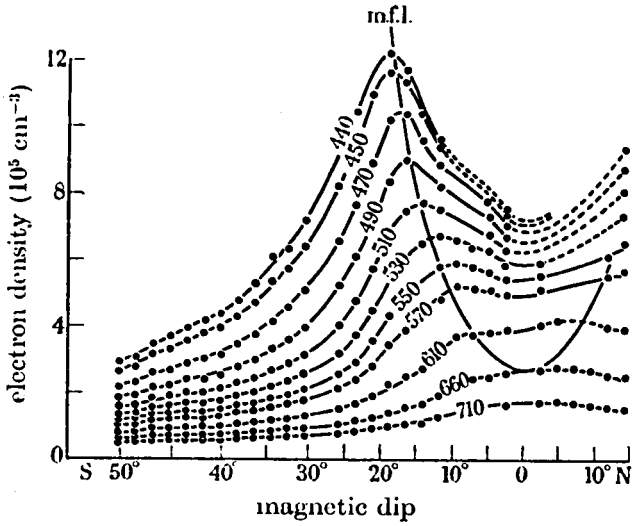

Fig. 1-6 Contours of electron density at constant real heights above ground for Singapore, 10:00 local time. The real heights above ground (km) are indicated on the curves and the field line calculated from magnetic dip is drawn in (after J. W. King et al.[60]).

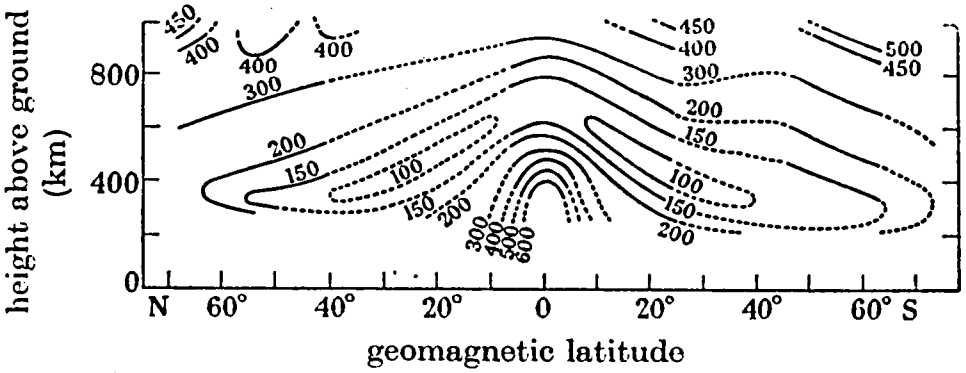

Fig. 1-7 Contours of constant electron density scale height. The values in km are indicated on the curves (after J. W. King et al.[60]).

accumulation of electrons to the north and south, but mechanism, however, can only produce a "trough" which is much "shallower" and "narrower" in latitude than the real equatorial trough.[194] Recently E. N. Bramley and M. Peart[186] calculated numerically the continuity equation including the diffusion along geomagnetic field line and electromagnetic drift,[181] together with electron production and loss, and showed that an upward electromagnetic drift of a few m/sec, when combined with field-aligned plasma diffusion, is sufficient to produce equilibrium ionospheric distribution closely resembling those observed in the equatorial region. Figure 1-8 shows an example of contours of electron density as a function of latitude (in degree) and height (in unit of scale hight of ionizable gas); the dashed line represents the gemagnetic field line and the dotted line is the locus of points of maximum density at fixed heights. W. B. Hanson and R. J. Moffett[187] obtained the similar results and also explained the asymmetrical distribution about the equator by horizontal winds blowing across the trough, of the order of 50 m/sec. The vector plots of electron flux in the meridian plane, the so-called equatorial fountain, are shown in Fig. 1-9, calculated by W. B. Hanson and R. J. Moffett.[187] The motion is due to the combined action of

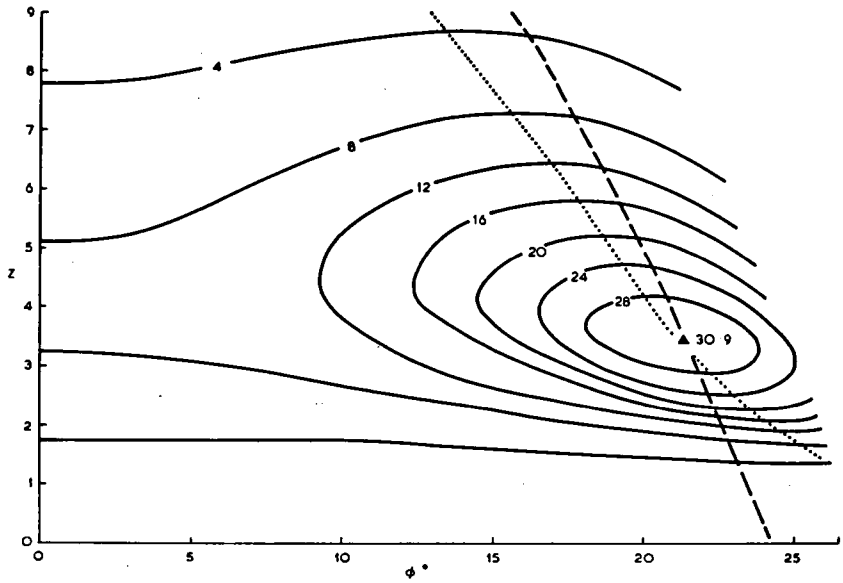

Fig. 1-8 Contours of electron density as a function of latitude (in degree) and height (in unit of scale height). The electron density values (in unit of 10^5 cm^{-3}) are indicated on the curves. The dashed line represents the geomagnetic field line and the dotted line is the locus of points of maximum density at fixed height (after E. N. Bramley and M. Peart[186]).

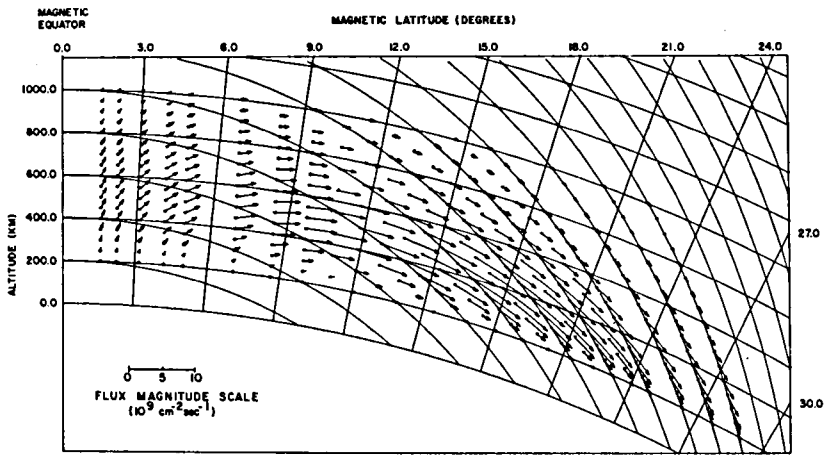

Fig. 1-9 A vector plot of electron fluxes (the equatorial fountain). Magnetic field lines are shown every 200 km (after W. B. Hanson and R. J. Moffett[187]).

plasma diffusion along magnetic field lines and electromagnetic drift across field lines, produced by an assumed distribution of eastward electric field. The incoherent scatter technique has now developed to measure the actual vertical ionization drifts over a height range of about 200 km to 700 km[195] and obtained the values of 10 to 30 m/sec which is upward during most of the day and downward at night.[196]

Some small perturbations of the low-latitude F2 layer can be related to local lunar time, and are probably caused by electromagnetic drifts associated with lunar tides.[197]

Ionospheric F region disturbances are characterized by changes in global electron density profile over the period of a few days accompanied by geomagnetic storms. Extensive studies on morphology of ionospheric storms, especially, on the behavior of N_mF2 were made by T. Obayashi,[198~200] and the global electron density changes in the topside ionosphere have been investigated by E. S. Warren,[201] and K.L.Chan and L. Colin[202] and others. The electron density in the F region is generally enhanced in low latitudes, while it is depressed in middle and high latitudes, but its variations manifest complicated features depending on stage of storm development, location (altitude, latitude) and longitude), season, local time and so on. T. Obayashi and M. Matuura[203] have shown that the abundance ratio of atomic oxygen to molecular oxygen or nitrogen is a dominant parameter to control the electron density change, and proposed the theoretical model of F region storm.

Sometimes the F region shows a diffuse character which is attributed to clouds of electrons having concentrations different from the ambient surroundings. This condition is called spread F, and it occurs mainly at night.[204] The name "spread F" has been adopted for the phenomena because of the visual appearance of ionograms, which show rather diffuse F region traces. There are two main classes of spread F, frequency spreading and range spreading. The phenomena of spread F occur more often at high latitudes during periods of high sunspot activity,

show a minimum at all times near 35-deg geomagnetic latitude, and occur more often at low latitude during periods of low sunspot activity. There also exist traveling ionospheric disturbances (TID) and the irregularities principally responsible for radio star scintillations. The F region irregularities responsible for spread F and its effects upon radio wavepropagation as well as the movement of irregularities have been investigated and summaried in Spread F and its Effects upon Radio Wave Propagation and Communication edited by P. Newman.[205]

2.3 Electron Density in the Upper Ionosphere

The topside ionosphere, above the F2 peak, has been explored by satellites carrying topside sounders, such as Alouette, and direct measuring instruments of various kinds of plasma probes. From these a broad picture of the spatial distributions of electron concentration and temperature, and of ion composition have been obtained. Information about the topside at particular sites is also obtained by ground-based techniques, such as incoherent scatter and rocket experiments.

Because of the relatively small scale height of oxygen ions, their abundance quickly diminishes with increasing altitude above the F2 peak, at a rate that depends very sensitively on temperature. This upper region of the ionosphere, in which protons are the dominant ions, is often referred to as the protonosphere. The source of ions in the protonosphere is due only in a minor degree to direct photo-ionization of atomic hydrogen; most of the ionization arises through charge exchange in the upper portion of the F region according to the reaction[206]

$$O^+ + H \rightleftarrows H^+ + O . \qquad (1.19)$$

The geomagnetic-latitude and local-time behaviors of electron density (N_e) and temperature (T_e) at a fixed height (1000 km) are illustrated in Fig. 1-10, which is taken from the results obtained by L. H.

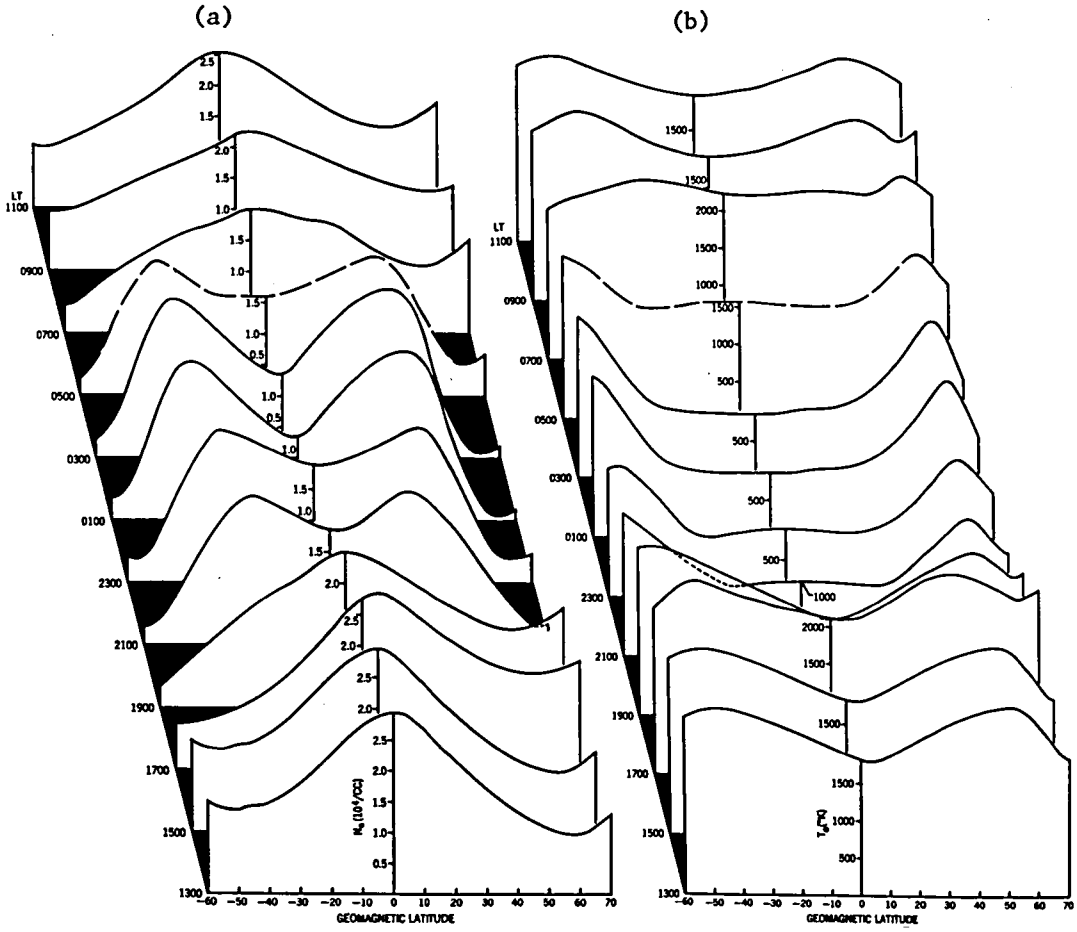

Fig. 1-10 Averaged latitudinal and local-time behaviour of the electron density N_e (a) and temperature T_e (b), at 1000 km near 1965 vernal equinox (after L. H. Brace et al.[66]).

Brace et al.[66] using the cylindrical electrostatic probe. The continuous evolution of N_e from a peak during the day to a valley during the night is clearly shown. Likewise, the temperature trough at the equator, which varies through the day, and the maxima at 60° geomagnetic latitude are evident. The important processes controlling the 1000 km ionosphere are the photoelectron heat source and the electron cooling by the local electrons and protons. The equatorial maximum of N_e is explained[207] as the diffusion upward of electrons and ions along magnetic field lines in response to the daytime heating by photoelectrons. The equatorial

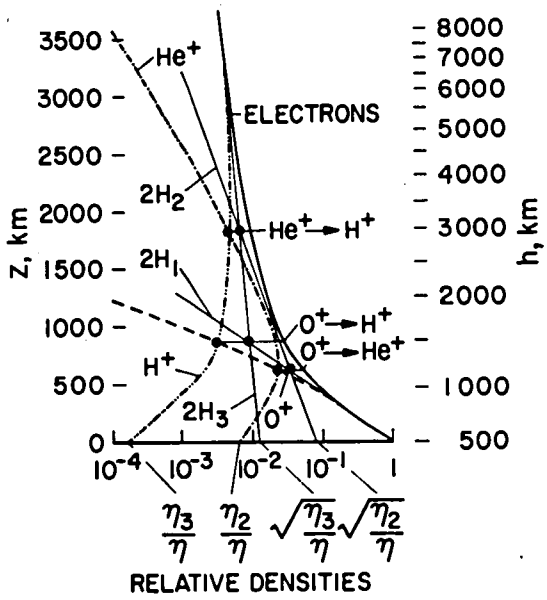

Fig. 1-11 Relative electron and ion densities along line of force as a function of the temperature-modified geopotential height z and the vertical altitude scale h. η, η_2, and η_3 are the density ratios of the electrons, the He^+, and the H^+ ions with respect to the O^+ ions (after J. J. Angerami and J. O. Thomas[208]).

minimum of N_e at night is caused by the downward diffusion of electrons and protons because of nighttime cooling.

As for the distribution of electrons and ions along the geomagnetic field line, J. J. Angerami and J. O. Thomas[208] gave the theoretical consideration about its diffusive equilibrium, taking into account the effects of the electric field that arises from charge seperation, the centrifugal force arising from the rotation of the earth, and the effect of the gravitational field. Figure 1-11 illustrates the relative electron and ion densities along a line of force as a function of the temperature-modified geopotential height z and the vertical altitude scale h for a constant temperature of 1500°K. The electrons and ions are assumed to be at the same temperature, and the ionic composition at the base level is given by $\eta_2 = 6.3 \times 10^{-3}$, and $\eta_3 = 1.6 \times 10^{-4}$ where η_2 and η_3 are the density ratios of He^+ and H^+ ions with respect to O^+ ion. This theory can be applicable to the electron density distribution in the protonosphere and the helium ion layer; the helium ion layer is not well established, but some direct measurements of the helium ions have been reported.[209,211]

S. J. Bauer[212] and A. Eviatar et al.[213] also calculated and discus-

sed about the electron density profile of a collisionless or ion-exosphere model distribution, and gave the theoretical distribution function as

$$N(R) = N_M \exp(-\frac{R'}{H}) \cdot \{1 - (1 - \frac{B}{B_M})^{1/2} \exp[1 - \frac{R'B}{H(B_M - B)}]\} \quad (1.20)$$

where B is the field strength of the geomagnetic field at the appropriate level, H the scale height, R the radius vector along a geomagnetic field line, R' a geopotential length parameter, and the subscript M refers to a reference level below which a Maxwellian distribution is valid. This type of distribution is one which corresponds to a diffusive equilibrium (first term),[208] weighted by a function dependent on the intensity of the geomagnetic field (in curly brackets). Experimental data from knee whistlers[214,215] are in good agreement with the empirical model R^{-4} plasma density distribution from the high altitude towards the boundary of the plasmasphere; R^{-3} power law approximates eq. (1.20) at great distances. Figure 1-12 shows the four types of the plasma density distribution along a magnetic field line.

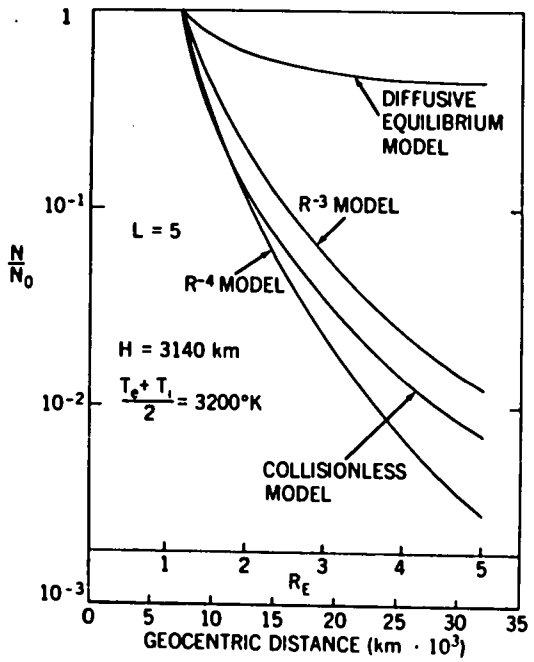

Fig. 1-12 Plasma density distributions along magnetic field line, whose apex in the equatorial plane is at L = 5 R_e, are shown for a diffusive equilibrium, and collisionless or ion-exosphere model, as well as for R^{-3} and R^{-4} power law models (after S. J. Bauer[212]).

The transition region between the upper portion of the F region, where the predominant ion is O^+, and the protonosphere can be described in terms of the aforementioned diffusive equilibrium ion distributions. However, such a description is an over simplification and not a very good approximation to the actual situation, because the hypothesis of diffusive equilibrium requires that there be no significant diffusive flow of ions. Especially in high latitude the structure of the ionosphere is closely affected by dynamical plasma flow mechanism.[216~218] In the polar ionosphere which appears to be sharply divided from the mid-latitude F region by a "trough", the escape of ionization from the ionosphere occurs with sufficient rapidity to suppress the H^+ and He^+ densities, leaving O^+ as the dominant ion to 3000 to 7000 km. Since the O^+ scale height is small relative to that for H^+, the overall electron densities are greatly reduced below plasmaspheric values.[219,220]

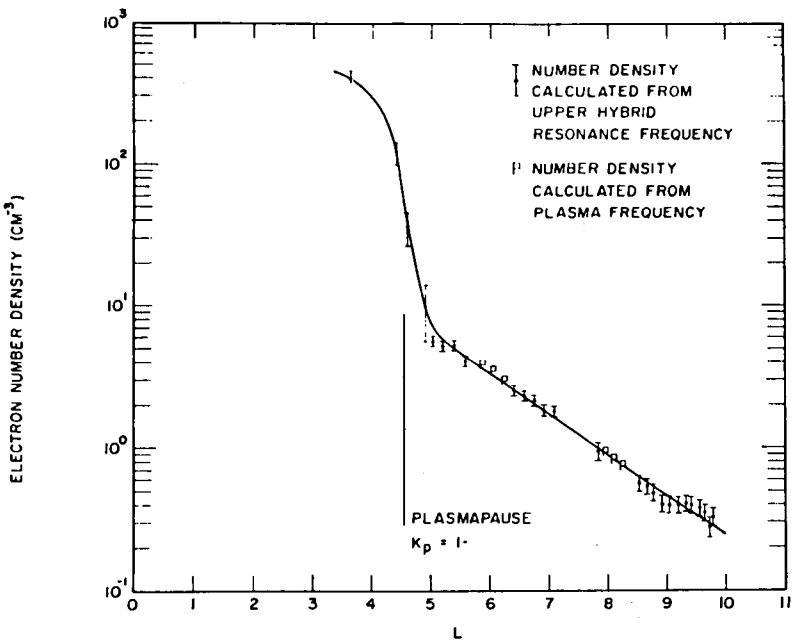

Fig. 1-13 Electron number density profile deduced from the upper hybrid resonance noise observed by IMP-6 (after R. R. Shaw and D. A. Gurnett[221]).

It is very difficult to measure the electron density precisely in the outer region of magnetosphere with plasma probes. There have been so poor data about the electron density distribution in this region. Recently R. R. Shaw and D. A. Gurnett[221] measured the electron number densities as low as 0.1 cm^{-3} in the region beyond the plasmapause, from the observed noises of the upper hybrid resonance and also of the plasma resonance. The electron density values deduced from these resonance frequencies are shown in Fig. 1-13, which clearly shows the sharp plasmapause boundary between $L = 4$ and $L = 5$ (L: McIlwain's L-value[222]), and the decreasing electron number density to the several earth radii beyond the plasmapause.

The accumulation of data for electron density distributions together with the values of electron temperature in the upper ionosphere has been required to understand the physical and dynamical properties of the ionosphere, and also to investigate the coupling between the ionospheric plasma and the outer space beyond the magnetosphere, and interplanetary space.

§ 3. Theory of R.F. Plasma Probes

The r.f. plasma probes such as the gyro-plasma probe, the mutual impedance probe, and the capacitance probe, measure the self and/or mutual antenna impedance as a function of frequency. The frequency response of impedance of an antenna in a magneto-ionic environment is of interest from both the theoretical and experimental viewpoints. For theoretical plasma physicists, it poses important problems in electromagnetic theory and boundary value problem, while for experimental researchers it is of practical use to measure ionospheric parameters as well as parameters of a low density plasma in the laboratory.

The permittivity, ε, of an isotropic homogeneous cold plasma is given by the well known relation of[223]

$$\varepsilon = \varepsilon_0 \left(1 - \frac{\Pi_e^2}{\omega^2}\right) , \qquad (1.21)$$

where collisions and the effect of heavy positive ions have been neglected; ε_0 is the permittivity of free space, ω the angular frequency and Π_e the electron plasma angular frequency proportional to the square root of the electron density. Consequently, the ambient electron density may be deduced from the impedance value of an antenna in such an idealized plasma if the capacitance of an antenna system is assumed to be proportional to the dielectric constant of the medium. However, antenna impedance is generally a function of electron and ion densities, collision frequencies, temperature or velocity distribution functions, magnetic field intensity and direction, and antenna configuration. The theory is so complicated that appropriate approximations should be introduced for the calculation of an antenna impedance.

Considering a sensor network including a surrounding plasma as a part of the electrical circuit, it is convenient to represent a plasma as an equivalent electrical circuit, which has the equivalent properties of a linear frequency response of a plasma when r.f. electric potential is applied to the antenna. This representation being an oversimplified model of a plasma, is, however, extremely useful, provided that there is no serious consequences of the antenna impedance due to the electromagnetic and electrostatic wave excitations and other dissipative mechanisms of nonlinearity.

In this section, historical survey of r.f. antenna impedance theory is briefly described, and a permittivity of a plasma and its equivalent electrical circuit are introduced by solving the Maxwell's equation with the hydrodynamic equation of motion. The theoretical expression of the impedance of a short cylindrical antenna in a cold magnetoplasma is, also, presented, following T. R. Kaiser[224] and K. G. Balmain.[225]

3.1 Historical Survey of Antenna Impedance Theory

R.F. probes were developed from the electro-static probe which was investigated by I. Langmuir and H. Mott-Smith[226] in 1924. In the case of the electro-static probe method, the d.c. electric current collected

by the d.c. potential of the metalic probe in a plasma is used to deduce the electron density and temperature, while in the case of r.f. probes the radio-frequency impedance of a probe is measured as the high frequency response of a plasma when a small r.f. potential is applied to the probe. Therefore, the r.f. probe study poses interesting problems not only on the fundamental plasma theory but also on the electromagnetic boundary value problem.

As for the theoretical treatment of antenna impedance, the plasma can be classified into cold and warm plasmas. The theory of cold plasma with an external static magnetic field has been developed to yield the fundamental formula of antenna impedance and some kinds of resonances. However, in recent years, the existence of various plasma waves excited by probes has been revealed by experiments with space and laboratory plasmas. The thermal motion of electrons and ions are important in these phenomena, and, therefore, theoretical analysis of warm plasma is required.

Another classification of calculations is introduced by following M. L. Schiff and J. A. Fejer.[223] In the first category (refered as I), the antenna is assumed to have a three-dimensional closely spaced mesh-like structure inside which the electric field vanishes. The calculation of antenna impedance is greatly simplified because the undisturbed plasma can be taken to be uniform over all space and δ-function of the current source can be assumed. In the second category (refered as II), it is assumed that the parallel component of the electric field and the normal component of the fluid velocity vanish on the surface of the antenna conductor. The uniform plasma occupies only the space outside the antenna. This second category implies the boundary value problem of the interaction of the conductor surface and the plasma because the ion sheath around the antenna is realistically taken into account.

Theory of Antenna Impedance in Cold Plasma Assuming the plasma as a dielectric medium with dielectric tensor as introduced by T.H.Stix[223] and others, the potential and electric fields around an antenna in cold magneto-active plasma are calculated by solving the boundary value

problem of the modified Laplace's equation or the source problem of the modified Poisson's equation with the quasi-static approximation. The admittance of the bi-conical dipole in a magneto-ionic medium was calculated by T. R. Kaiser.[224] K. G. Balmain[225] obtained the analytical expression of the impedance of a short cylindrical antenna in a magneto-active plasma, assuming a filamentary triangular current distribution. The effects of the upper hybrid resonance, plasma resonance, and gyro-resonance were clearly revealed. J. P. Lafon and H. Weil[228] discussed about the current distribution on the antenna surface more strictly. H. Oya[229] calculated the high frequency field around the quasi-points dipole using the Fourier transformation method. K. E. Miller[230] computed the Maxwell's equation numerically and obtained the frequency spectrum of antenna surface current and admittance of an infinite cylindrical antenna parallel to the external magnetic field.

Hydrodynamic Approach of Warm Plasma Theory The theory of antenna impedance in a warm plasma usually employs either the linearized Boltzmann-Vlasov equation (the Kinetic approach) or the hydrodynamic equations together with either Poisson's equation in a quasi-static approach or Maxwell's equations. Taking a stress tensor or a scalar pressure as a representative value for the effect due to the electron thermal motion instead of its distribution function, the linearized equations of motion (or momentum transfer) and continuity (or mass transfer) in terms of the macroscopic particle density and velocity are used in the hydrodynamic approach.

In category I, the Fourier transformation method can be applied and the theoretical calculations have been made by J. K. E. Tunaley and R. J. L. Grard[231] for the mesh sphere and plane grid probes, M.L.Schiff and J. A. Fejer[227]for the mesh sphere probe and K. G. Balmain[232] for the short dipole. H. Oya[233] computed the effect due to the electron acoustic wave in the case of the cylindrical dipole parallel to a magnetic field, and J. R. Wait[234] also calculated the radiation resistance. R. L. Monroe[235] derived the analytical formulae of the current distribution and the admittance of an infinite cylindrical antenna in a lossy,

compressible plasma, using the integro-differential equation. M. L. Schiff[236] also obtained the self-consistent current distribution on a grid type dipole antenna. The electroacoustic wave excitation and the resistive component of an antenna impedance near the resonance frequency are derived from these calculations, results on the fixed frequency impedance measurements in the ionosphere by H. A. Whale[237] being verified. On the other hand, R. J. L. Grard[238], and B. Rooy et al.[239] calculated the mutual impedance and showed quantitatively that as the parameter δ (dimension of the antenna / Debye length) decreases, the radiation of electro-acoustic wave from the antenna increases and the resonance peak of the impedance is gradually damped.

In category II, the Fourier transformation method cannot be applied because the ambient plasma is bounded by the antenna surface. M. H. Cohen[240] argued that the equivalent mechanical force should be considered on the boundary, and K. G. Balmain[241] defined the absorption coefficient A as $(v_1/v_0) = A(n_1/n_0)$, where v_1 and v_0 are the perturbed and mean thermal velocity of electrons, and n_1 and n_0 are the perturbed and equilibrium electron densities. Setting the quantity A equal to zero and $\sqrt{2/\pi}$, which are equivalent to assume rigid or reflecting boundary and a perfect absorptive boundary, respectively. J. A. Fejer[242] ($A = 0$) and K. G. Balmain[241] ($A = \sqrt{2/\pi}$) solved the problem for the spherical probe. O. Holt and J. Trøim[243] also obtained the impedance of parallel plates. A. D. Wunsh,[244] and K. R. Cook and B. C. Edger[245] showed that the current distribution valid only for an antenna in a cold environment can be incorrect when applied to an antenna in a warm plasma. S-H. Lin and K. K. Mei[246,247] also investigated the cylindrical antenna when A is not equal to zero, and both current distribution and impedance were numerically computed. Similar calculations were made by G. L. Maxam and K. M. Chen.[248] D. H. Preis[249] discussed more strictly the boundary conditions and the integral equations for a cylindrical antenna in a warm plasma. J. Tarstrup and W. J. Heikkila[250] computed the impedance of a spherical probe with a smooth sheath model and obtained good agreement with the experimental results.

Thus the hydrodynamic approach can be used to explain the effect on

the impedance due to electron thermal motion which is impossible to derive from a cold plasma approximation, but the Landau damping and resonance effects of the Bernstein mode wave[251] can not be accounted by this theory.

Kinetic Approach of Warm Plasma Theory The linearized Bolzmann-Vlasov equation, together with Maxwell's equations, are used in the kinetic approach. In category I, H. H. Kuehl[252] formulated the longitudinal and transverse components of electric field as the integral of the product of the Fourier transform of the dyadic Green's function and the source current density. And also H. H. Kuehl[253,254] calculated the input resistance of a short filamental antenna and compared it with the results of the hydrodynamic equations. The comparison shows that the hydrodynamic result is incorrect below the plasma frequency but is a good approximation above the plasma frequency if the antenna is longer than the Debye length. For antenna lengths comparable with the Debye length, however, hydrodynamic results are valid only at frequencies far above the plasma frequency. The resistance for frequencies below plasma frequency is due to Landau damping and has no counterpart in hydrodynamic theory. Similar calculations were made by M. L. Shiff and J. A. Fejer for sphere[227] and M. L. Shiff for cylinder.[255] The standing wave above the plasma frequency predicted in the hydrodynamic theory is affected by Landau damping. G. Baenzinger and H. H. Kuehl[256] made comparison between cold plasma model, hydrodynamic theory, the kinetic theory. When the external magnetic field is applied, theories in general become very complex. F. W. Crawford et al.[257] took into account the equivalent plasma permittivity component perpendicular to the magnetic field and calculated the impedance of the plane parallel plates and that of the coaxial cylinder. The impedance change due to the resonances associated with cyclotron harmonics of the Bernstein mode wave has been revealed. R. Buckley[258] obtained the admittance of a plane grid capacitor and discussed the electric field distribution with respect to the distance from the grid.

In category II, J. Pavkovich and G. S. Kino[259] solved the linearized

Vlasov equation assuming a zero order parabollic potential distribution in the sheath of an infinite plane probe. Similarly, R. Buckley[260] calculated the electric field and the impedance of a spherical probe, taking the steady potential in the sheath from the work of I. B. Bernstein and I. N. Rabinowitz.[261] The resonance rectification of the resonance probe was studied quantitatively. F. C. Shure[262] obtained the impedance of a plasma-filled parallel plate condensor as a function of the effective dielectric coefficient. These theories treated a warm plasma with no external static magnetic field, and the impedance calculation of an antenna in a warm magneto-active plasma is required to explain experimental results in space and laboratory plasmas.

3.2 Description of Plasma as a Dielectric Medium

The r.f. probe methods are principally to detect a linear frequency response of a plasma when a small r.f. potential is applied to an antenna in a plasma. The plasma is represented by dielectric tensor, and also by specific admittance of an unit circuit which has the same electrical properties.

Following L. Spitzer, Jr.,[263] macroscopic quantities of plasma current $\vec{J}$ and velocity $\vec{v}$ are determined by the macroscopic equation of motion, viz., the transfer (or transport) equations of kinetic theory. For a single particle of type k in a region where an electric field $\vec{E}$ and a magnetic field $\vec{B}$ are present, the equation of motion is given by

$$n_k m_k \left(\frac{\partial v_k}{\partial t} + \vec{v}_k \cdot \nabla \vec{v}_k\right) = n_k q_k \vec{F}_k - \nabla \cdot \vec{\Psi}_k - n_k m_k \nabla \Phi_g + \vec{P}_k, \qquad (1.22)$$

$$\vec{F}_k = \vec{E} + \vec{v}_k \times \vec{B}, \qquad (1.23)$$

and

$$\vec{P}_k = - n_k m_k \nu_k \vec{v}_k, \qquad (1.24)$$

where n_k is macroscopic particle density, m_k mass, $\vec{v}_k$ mean velocity,

q_k charge, $\vec{\Psi}$ stress tensor, Φ_g gravitational potential, and ν_k collision frequency of the particle k, respectively. The plasma current density $\vec{j}$ and charge ρ satisfy the continuity equation as tion as

$$\frac{\partial \rho}{\partial t} + \nabla \cdot \vec{j} = 0 \tag{1.25}$$

where $\vec{j} = \sum_k q_k n_k \vec{v}_k$, and $\rho = \sum_k q_k n_k$. (1.26)

Finally, completing the list of basic relations, the Maxwell's equations for the electromagnetic field are introduced as follows;

$$\nabla \times \vec{E} = - \frac{\partial \vec{B}}{\partial t} , \tag{1.27}$$

$$\nabla \times \vec{H} = \frac{\partial \vec{D}}{\partial t} + \vec{j}, \tag{1.28}$$

$$\nabla \cdot \vec{D} = \rho , \tag{1.29}$$

$$\nabla \cdot B = 0 \tag{1.30}$$

and $\vec{B} = \mu_0 \vec{H}$, $\vec{D} = \varepsilon_0 \vec{E}$, and not ations are used in the usual meaning (in M.K.S. unit system). Equation (1.25) above may also be derived from eqs. (1.28) and (1.29).

Here, it is assumed in eq. (1.22) that;

(1) the gradient of the gravitational potential is negligible, i.e., $\nabla \Phi_g \simeq 0$;

(2) the stress tensor can be expressed by the pressure, and the temperature T_k is homogeneous, i.e., $\nabla \cdot \vec{\Psi} = \nabla n_k \kappa T_k = m_k a_k{}^2 \nabla n_k$ where $a_k{}^2 = \kappa T_k / m_k$;

(3) the time dependence of all the variables is proportional to $\exp(j\omega t)$;

(4) the static magnetic field $\vec{B}_0$ is applied parallel to the z-axis in the Cartesian coordinates (x, y, z).

Equation (1.22) is rewritten in terms of plasma current $\vec{j}_k$ and

displacement $\vec{D}$ as

$$\frac{\partial \vec{j}_k}{\partial t} + \vec{v}_k(\nabla\cdot\vec{j}_k) + \vec{j}_k\cdot\nabla\vec{v}_k + \nu_k\vec{j}_k + \vec{\Omega}_k\times\vec{j}_k = \Pi_k^2\vec{D} - a_k^2\nabla_k\rho_k \qquad (1.31)$$

where $\Pi_k = \left(\frac{q_k^2 n_k}{m_k\varepsilon_0}\right)^{1/2}$; angular plasma frequency,

and $\vec{\Omega}_k = \frac{q_k\vec{B}_0}{m_k}$; angular gyro-frequency.

The sign of Ω_k is defined to be same sign with q_k, i.e., $\Omega_k > 0$ for a positive charged particle and $\Omega_k < 0$ for electron or negative charged particle. Since the total current density $\vec{J}$ which flows through the antenna surface to a plasma is equal to the sum of the plasma convection current $\vec{j}$ and the displacement current $\partial D/\partial t$, i.e., $\vec{J} = \partial D/\partial t + \vec{j}$, the relation between $\vec{J}$ and $\vec{D}$ is deduced from eq. (1.31) by linearized, as

$$\vec{J} = j\omega\left(1 + \frac{1}{j\omega}\sum_k \Delta_k^{-1}\cdot\Pi_k^2\right)\vec{D} - \sum_k \Delta_k^{-1}a_k^2\nabla\rho_k \qquad (1.32)$$

where $$\Delta_k = \begin{bmatrix} j\omega + \nu_k & -\Omega_k & 0 \\ \Omega_k & j\omega + \nu_k & 0 \\ 0 & 0 & j\omega + \nu_k \end{bmatrix}$$

The second term in the right hand side of eq. (1.32) is attributed to the electrostatic wave excited by an antenna,[107] while the value in the round brackets of the first term shows the well-known dielectric tensor (K) of a plasma,[273]

$$(K) = \begin{bmatrix} \varepsilon_{xx} & \varepsilon_{xx} & 0 \\ -\varepsilon_{yx} & \varepsilon_{yy} & 0 \\ 0 & 0 & \varepsilon_{zz} \end{bmatrix} \qquad (1.33)$$

and $$\varepsilon_{xx} = \varepsilon_{yy} = 1 + \sum_k \frac{\Pi_k^2}{j\omega}\cdot\frac{j\omega + \nu_k}{(j\omega + \nu_k)^2 + \Omega_k^2}, \qquad (1.34)$$

$$\varepsilon_{xy} = \varepsilon_{yx} = \sum_k \frac{\Pi_k^2}{j\omega}\cdot\frac{j\omega + \nu_k}{(j\omega + \nu_k)^2 + \Omega_k^2}, \qquad (1.35)$$

$$\varepsilon_{zz} = 1 + \sum_{k} \frac{\Pi_k^2}{j\omega} \cdot \frac{1}{j\omega + \nu} \cdot \tag{1.36}$$

The specific admittance is defined as the admittance of an unit volume (an unit length with an unit area) and calculated from eq. (1.32).

$$\begin{aligned}
[\dot{y}] &= \frac{\vec{J}}{\vec{E}} = \varepsilon_0 \frac{\vec{J}\cdot\vec{D}}{D^2} \\
&= j\omega\varepsilon_0\{\varepsilon_{xx} \sin^2\theta + \varepsilon_{zz} \cos^2\theta\} \\
&= y_\perp \sin^2\theta + y_\parallel \cos^2\theta
\end{aligned} \tag{1.37}$$

where θ is the angle of a vector $\vec{E}$ with respect to the z-axis. $y_\perp$ and $y_\parallel$ are the components of a specific admittance perpendicular and parallel to the externally applied magnetic field $\vec{B}_0$.

In warm magnetoplasma, the specific admittance $y_\perp$ plays a very important role. Under the condition of the electrostatic approximation, when the wave number vector $k_\perp$ is perpendicular to the magnetic field, the dielectric constant $K_\perp$ for an electron longitudinal wave is written as

$$K_\perp = 1 + \sum_{n=1}^{\infty} \frac{\Pi_e^2}{j\omega} \cdot \frac{\exp(-\lambda) I_n(\lambda) n^2 (j\omega + \nu)}{(\frac{\lambda}{2})\{(j\omega + \nu)^2 + n^2\Omega_e^2\}} \tag{1.38}$$

and the corresponding specific admittance $y_\perp{}^W$ is,

$$y_\perp{}^W = j\omega\varepsilon_0 K \tag{1.39}$$

where $\lambda = (k_\perp r_\perp)^2$; $r_\perp = (\kappa T_e/m)^{1/2}/\Omega_e$ is the gyro-radius of an electron with thermal energy κT_e and $k_\perp$ is the wave number perpendicular to the magnetic field, $I_n(\lambda)$ is modified Bessel function of order n, and the suffix e denotes the quantities for electron. This mode of wave propagation has been designated as a Bernstein mode by I. B. Bernstein[251] and T. H. Stix[223] who derived this dispersion relation for a collisionless plasma. F. W. Crawford et al.,[257] taking collisions into accout approximately, gave the same expression of eq.

(1.38). In this model of electrostatic wave for propagation at $\theta = \pi/2$, Landau damping is rigorously neglected.

In the above treatment of the behavior of the particle k described in eq. (1.31), the equation of mortion is linearized by neglecting the cross terms of $\vec{v}_k(\nabla \cdot j_k)$ and $\vec{j}_k \cdot \nabla \vec{v}_k$. These terms, however, play a very important role in the highly inhomogeneous plasma region such as near the antenna boundary. Since the gradient of the particle velocity is considered to act upon the impedance of a plasma as a resistive loss, the effect of these terms may be estimated by the following rough approximation, assuming one dimensional inhomogeneity of particle velocity in the x-direction; $\vec{v}_k = (v_{0x} + v_x)\hat{i} + v_y\hat{j} + v_z\hat{k}$, where $\hat{i}$, $\hat{j}$, $\hat{k}$ are respectively unit vectors in x, y, z directions.

$$\vec{v}_k(\nabla \cdot \vec{v}_k) + \vec{v}_k \cdot \nabla \vec{v}_k \simeq 2 \frac{\partial v_{0x}}{\partial x} \cdot \vec{v}_k \tag{1.40}$$

Therefore, this effect can be involved implicity in the collision frequency by introducing the effective collision frequency;

$$\nu_{eff} = \nu + 2 \nabla_x v \tag{1.41}$$

It should be noted, however, that the linear approximation is, principally, unable to apply the equation of motion of the particle in the sheath region where the neutrality or the quasi-neutrality of a plasma does not hold.

3.3 Representation of Plasma by Equivalent Electrical Circuit

It is possible to represent specific physical phenomena in terms of an equivalent electrical circuit, provided that there be the same differential equations which describe each physical and electrical properties of them. The admittance (or impedance) of a plasma means that the equivalent electrical circuit with its admittance has the same response of the resultant current cuased by the externally applied

potential or electric field, or vice versa. It is, therefore, unable to represent exactly an equivalent response for the excited electromagnetic or electrostatic waves. Y. Itatani[264] first introduced this concept of plasma impedance. T. Dote and T. Ichimiya[265] tried to explain the resonance frequency obtained with the resonance rectification probe, using the equivalent electrical circuit.

Here, the plasma is assumed to consist of electrons and one kind of positive ions denoted by suffix e and suffix i, respectively. From eq. (1.33), (1.34) and (1.36), the specific admittances $y_\perp$ and $y_\parallel$ can be rewritten in the following forms;

$$y_\perp = j\omega\varepsilon_0 + \sum_{n=i,e} \frac{1}{\frac{\nu_k}{\varepsilon_0 \Pi_k^2} + j\omega\frac{1}{\varepsilon_0 \Pi_k^2} + \frac{1}{\frac{\varepsilon_0 \Pi_k^2 \nu}{\Omega_k^2} + j\omega\frac{\varepsilon_0 \Pi_k^2}{\Omega_k^2}}}$$

$$= j\omega C_0 + \sum_{k=i,e} \frac{1}{R_k + j\omega L_k + \frac{1}{G_k + j\omega C_k}} \qquad (1.42)$$

$$y_\parallel = j\omega\varepsilon_0 + \sum_{k=i,e} \frac{1}{\frac{\nu_k}{\varepsilon_0 \Pi_k} + j\omega\frac{1}{\varepsilon_0 \Pi_k^2}}$$

$$= j\omega C_0 + \sum_{k=i,e} \frac{1}{R_k + j\omega L_k}\ , \qquad (1.43)$$

where $R_k = \frac{\nu_k}{\varepsilon_0 \Pi_k^2}$; equivalent specific resistance,

$\omega L_k = \frac{\omega}{\varepsilon_0 \Pi_k^2}$; equivalent specific reactance,

$G_k = \frac{\varepsilon_0 \Pi_k^2 \nu_k}{\Omega_k^2}$; equivalent specific conductance,

$\omega C_k = \frac{\varepsilon_0 \omega \Pi_k^2}{\Omega_k^2}$; equivalent specific susceptance,

$C_0 = \varepsilon_0$; specific capacitance in free space.

In accordance with these formulae, the equivalent electrical circuits for $y_\perp$ and $y_\parallel$ are illustrated in Fig. 1-14.

Total equivalent specific admittance of the probe system in a plasma is defined as a ratio of the probe admittance in a plasma to that in free space. Assuming the spherical symmetry for a sphere probe and the axial symmetry for a cylindrical probe, the total equivalent specific admittance y_T is deduced from eq. (1.33) as

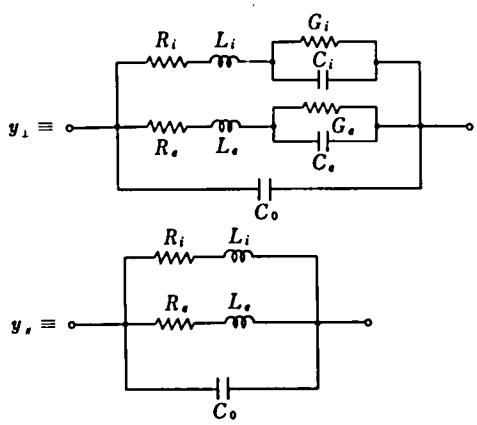

Fig. 1-14 Equivalent electrical circuits of the specific admittance $y_\perp$ and $y_{||}$ of cold plasma.

$$y_T = j\omega\{1 - p^2)y_\perp + p^2 y_{||}\} \tag{1.44}$$

where p is geometrical factor; $p = \cos\theta$ for plane probe, $p = 1/\sqrt{3}$ for sphere probe, and $p = (1/\sqrt{2})\sin\alpha$ for cylindrical probe, where θ and α are the angles of the symmetrical axis of plane probe and cylindrical probe relative to the static magnetic field line. Taking account of simple sheath model, namely, the electron plasma frequency and $\nabla_x v$ in eq. (1.41) are constant in the sheath region, the total equivalent specific admittance y_T is calculated and the equivalent electrical circuit is shown in Fig. 1-15. The suffix s denotes the quantities in the sheath region. From Fig. 1-15, the low frequency response of the current J collected by the plane probes is deduced when the voltage V is applied to the sheath,

$$J = \frac{\varepsilon_0 \Pi_{es}^2}{2\nabla_x v} \cdot \frac{V}{L_s} \tag{1.45}$$

where L_s is the thickness of sheath. This is equivalent to so-called Langmuir current-voltage characteristics; since $\nabla_x v$, Π_{es} and L_s largely depend upon the applied voltage, J is generally a nonlinear function of V. This resistance can be replaced by the diode; its inverse current including a dark current, and the forward saturation

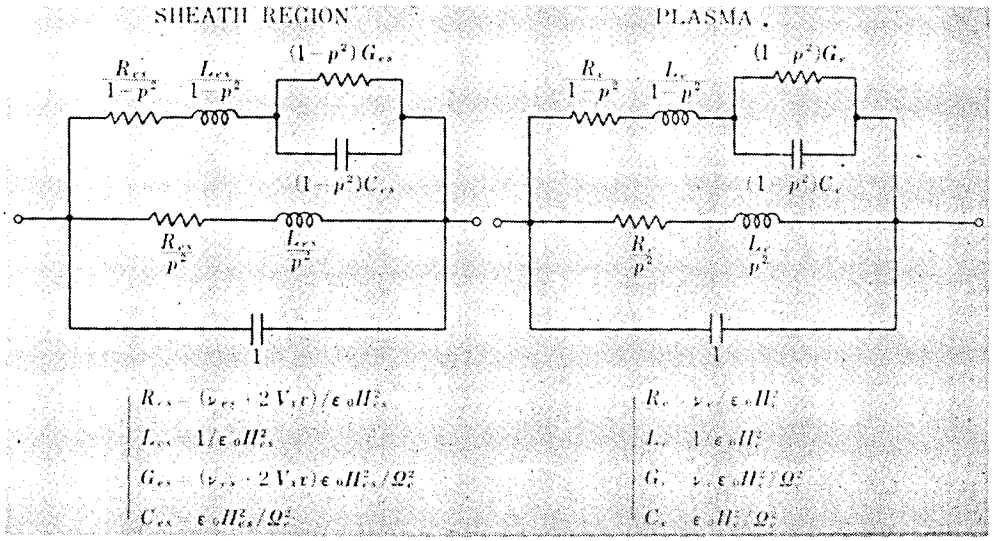

Fig. 1-15 Equivalent electrical circuits of the total specific admittance y of sheath region (denoted by a suffix s) and plasma, ions being neglected.

current are corresponding to the ion and electron saturation current in the Langmuir characteristics, and the current-voltage characteristics of both the diode and the sheath show an exponential type current response for an applied voltage.

For the warm plasma, the specific admittance $y_\perp{}^W$ in eq. (1.39) can be, also, rewritten in the following form;

$$y_\perp{}^W = j\omega\varepsilon_0 + \sum_{n=1}^{\infty} A_n(\lambda) \cdot \frac{1}{\dfrac{\nu_e}{n^2\varepsilon_0\Pi_e{}^2} + j\,\dfrac{1}{n^2\varepsilon_0\Pi_e{}^2} + \dfrac{1}{\dfrac{\varepsilon_0\Pi_e{}^2\nu_e}{\Omega_e{}^2} + j\omega\dfrac{\varepsilon_0\Pi_e{}^2}{\Omega_e{}^2}}}$$

$$= j\omega C_0 + \sum_{n=1}^{\infty} \frac{1}{R_{en} + j\omega L_{en} + \dfrac{1}{G_{en} + j\omega C_{en}}} \qquad (1.46)$$

where $R_{en} = \frac{1}{A_n(\lambda)} \cdot \frac{\nu_e}{n^2 \varepsilon_0 \Pi_e^2}$; equivalent specific resistance,

$\omega L_{en} = \frac{\omega}{A_n(\lambda)} \cdot \frac{1}{n^2 \varepsilon_0 \Pi_e^2}$; equivalent specific reactance,

$G_{en} = A_n(\lambda) \cdot \frac{\varepsilon_0 \Pi_e^2 \nu_e}{\Omega_e^2}$; equivalent specific conductance,

$\omega C_{en} = \omega A_n(\lambda) \cdot \frac{\varepsilon_0 \Pi_e^2}{\Omega_e^2}$; equivalent specific susceptance,

and $A_n(\lambda) = \frac{2}{\lambda} \exp(-\lambda) I_n(\lambda) \sim \frac{1}{n!}(\frac{\lambda}{2})^{n-1}$ + terms of higher order in λ for small λ.

The equivalent electrical circuit for $y_\perp^W$ is shown in Fig. 1-16. As is obvious from this figure, series resonances occur at the frequencies $\omega_n = 1/\sqrt{L_{en}C_{en}} = n\Omega_e$ (n = 1, 2, 3 .....), i.e., higher harmonics of the cyclotron resonance frequency, if the collision frequency ν_e is negligible. In the case of actual condition of a probe system, the series resonance frequency is affected by a capacitance of the sheath around the sensor. The series resonance of an antenna admittance is called the sheath resonance (SHR). The upper hybrid resonance frequency, which is given as $(\Pi_e^2 + \Omega_e^2)^{1/2}$ in eq. (1.42) when $\nu_e = 0$, is also modified by higher harmonic gyro-resonances in a warm magnetoplasma. The resonance frequencies are given as roots of the following equation,

$$1 - \sum_{n=1}^{\infty} A_n(\lambda) \cdot \frac{n^2 \Pi_e^2}{\omega^2 - n^2 \Omega_e^2} = 0. \qquad (1.47)$$

For example, if the parameters are chosen such that $\Pi_e/\Omega_e = 1.0$, $\lambda \simeq 0.4$, the ratio of the fundamental root to the upper hybrid resonance frequency in cold plasma approximation is 0.98.

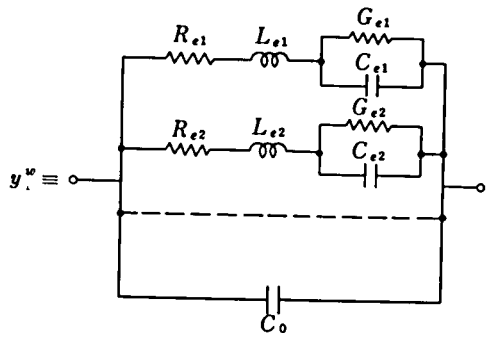

Fig. 1-16 Equivalent electrical circuit of the specific admittance $y_\perp^W$ of warm plasma.

3.4 Impedance of Cylindrical Antenna in Plasma

The data on the frequency response of a cylindrical antenna impedance have been obtained in the ionospheric plasma using many rockets and in the laboratory plasma using the space simulation chamber. An example of the record obtained by the gyro-plasma probe onboard the Kappa 8-15 sounding rocket[27] is shown in Fig. 1-17. The probe system is designed to measure the antenna admittance Y in vector form, namely with amplitude C (equivalent capacitance) and phase Ψ,

$$Y/\omega = C \exp(-j\Psi) \tag{1.44}$$

where ω is applied angular frequency and $j = \sqrt{-1}$. When the antenna impedance is capacitive or inductive, the phase angle Ψ is equal to $-\pi/2$ or $+\pi/2$, respectively. The upper hybrid resonance frequency

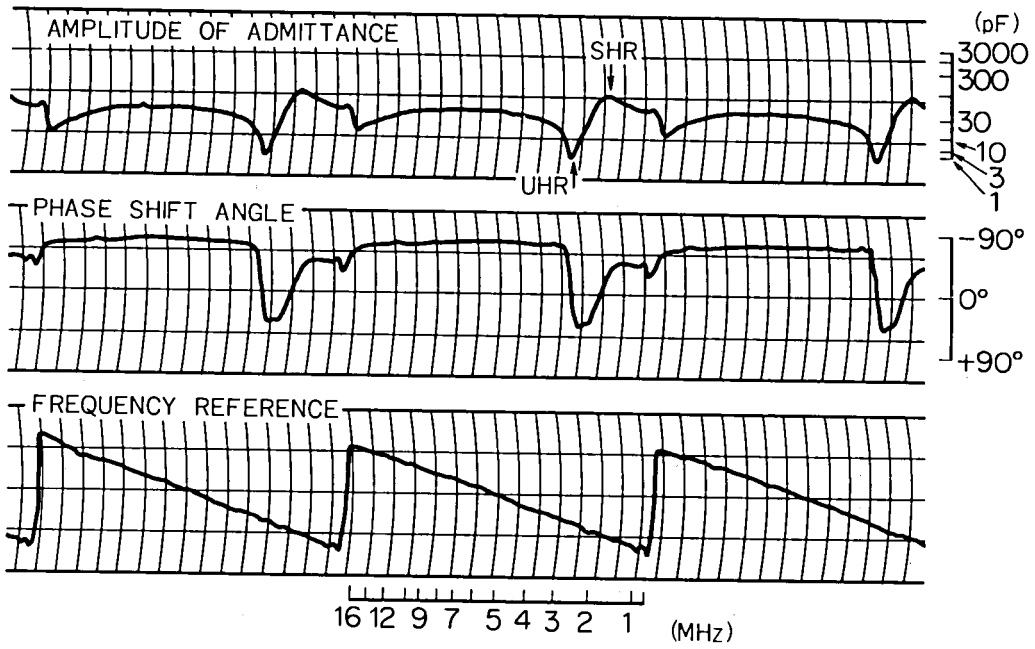

Fig. 1-17 Typical record of antenna admittance versus frequency (Kappa 8-15 rocket on Jan. 9, 1969).

is given as $C(\omega) = 0$, under collisionless cold plasma approximation, and the electron density value N_e (electrons/cm^3) can be deduced from the measured upper hybrid resonance frequency f_{UHR} (MHz) as

$$N_e = 1.24052 \times 10^4 \ (f_{UHR}^2 - f_H^2) \tag{1.45}$$

where f_H is the gyro-resonance frequency in MHz.

Theoretical treatments of a short cylindrical antenna (length L and radius r_a) in cold magnetoplasma have been performed by many workers. Following Balmain,[225] the impedance is expressed as

$$Zp = \frac{a'}{j\omega 2\pi\varepsilon_0 K' L F^{1/2}} \left[\ln \frac{L}{r_a} - 1 - \ln \frac{a' + F^{1/2}}{2F} \right] \tag{1.46}$$

where
$$F = \sin^2\alpha + a'^2 \cos^2\alpha$$
$$a' = (K'/K_0)^{1/2}$$
$$K_0 = 1 - X_e/U$$
$$K' = 1 - X_e U/(U^2 - Y_e^2)$$
$$X_e = \Pi_e^2/\omega^2$$
$$Y_e = \Omega_e/\omega$$
$$U = 1 - j(\nu_e/\omega)$$
α = angle of the antenna axis with respect to d.c. magnetic field

In the above formulation, $r_a \ll L$ and the filamentary triangular current distribution on the antenna surface is assumed. In computing $a' = (K'/K_0)^{1/2}$ and $F^{1/2}$, the square root having a positive real part should be used.

The antenna immersed in a plasma rapidly acquires negative charges because random electron currents are greater than random ion currents. The accumulation of charge is limited by the negative potential which develops between the body and the medium, and equilibrium is established when electron and ion currents become to be equal. Consequently, the antenna is surrounded by an ion sheath, whose admittance is capacitive in the high frequency region.

The antenna impedance is largely affected by the sheath impedance, and if the sharp boundary model of the sheath is considered, the total impedance of an antenna Z is written as

$$Z(\omega) = \frac{1}{j\omega C_s} + Z_p(\omega) \tag{1.47}$$

where C_s is the effective capacitance of ion sheath. The series and parallel resonance frequencies are determined as $Z(\omega)$ equal to minimum and maximum values. The maximum value of $Z(\omega)$ is equivalent to $Z_p(\omega) = \infty$, and $C = 0$ in eq. (1.44) with collisionless cold plasma approximation. From eq. (1.46), the upper hybrid resonance frequency, $\omega_{UHR} = (\Pi_e^2 + \Omega_e^2)^{1/2}$, satisfies the condition of parallel resonance. This frequency is independent of the angle α and is not affected by the impedance of the ion sheath. This result is very important in measuring the electron density of a plasma with r.f. probe methods. The series resonance frequency is largely affected by the sheath impedance, as is expected in eq. (1.47). This resonance is called the sheath resonance (SHR). Both UHR and SHR are indicated in Fig. 1-17.

Chapter II SYSTEM DESIGN OF RF PLASMA PROBES

§ 1. Introduction

Various kinds of r.f. plasma probes for measuring an electron density in the upper atmosphere have been investigated with the development of space vehicles since 1940's. As noted in the preceding chapter, the resonance rectification probe was investigated originally by Japanese scientists[8,34] and applied to the observation of the ionospheric plasma density. It has been, however, cleared that this resonance frequency is not identical with a plasma resonance frequency.

The gyro-plasma probe was initiated by H. Oya,[229] which has been used as the most useful probe to measure the electron density in space as well as in laboratory plasmas. Section 2 is devoted to the description of the gyro-plasma probe system and theoretical considerations of the probe impedance. This probe is designed to measure the antenna impedance as a function of frequency which is scanning in a wide range including various kinds of resonance frequencies. The parallel resonance of antenna impedance is identified as the upper hybrid resonance of the ambient plasma. A capacitance bridge is employed in its sensor network in order to eliminate a small unbalance due to stray capacity. It should be noted that the upper hybrid resonance frequency may be affected by electron-neutral collisions, especially in a weakly ionized plasma, besides the collisional damping of the resonance. In an inhomogeneous plasma where the electron density or the magnetic field intensity gradient exists around an antenna, the question arises how to define the upper hybrid resonance frequency relevant to such a medium. The experimental results which are described in the next chapter, show that there can be observed one parallel resonance of an antenna impedance despite of the inhomogeneity of the medium. The resonance frequency is identified as one obtained by integrating a specific admittance of the plasma over the whole space. Frequency characteristics of an antenna impedance in a warm magnetoplasma are examined by calculating the specific admittance given in eq. (1.39).

The mutual impedance probe consists of two whip antennas, which are made up a transmitter-receiver antenna system. Since the received signal intensity is a function of plasma impedance between two antennas, this probe is to measure the frequency response of mutual impedance of two separated antennas. S. Miyazaki[266] calculated analytically the potential field and the impedance of a two-wire probe, using a dielectric tensor of a cold plasma. Resonance effects on the received signal due to the upper hybrid resonance and the harmonics of the gyro-resonance were verified by the Lambda 3H-6 sounding rocket experiment[31] (see section 4, Chapter IV). It has been also revealed that the electrostatic Bernstein mode wave propagating perpendicular to the magnetic field produces considerable effects on the received signal intensity (see section 3, Chapter III). Section 3 explains the instrumentation of this probe system and the mutual impedance in cold plasma as well as in warm plasma, using the specific admittance of a plasma.

Two types of the capacitance probe have been used in the rocket experiments[9,18,19,30]; one is a fixed frequency impedance probe which measures the capacitance value of antenna, and the other is a high frequency capacitance probe measuring the frequency shift of the LC oscillator in which the capacitance C of an antenna changes its value with change of plasma parameters. This probe method is used to detect the fine structure of low electron density in the upper atmosphere, namely, in the ionospheric D region and the magnetosphere. section 4 describes the instrumentation of this probe system, and the collision effect on the electron density measurement in the D region.

In section 5, the capacitance of the ion sheath surrounding a body in a plasma is investigated. When r.f. potential is applied to the body, the charge accumulation is modulated by the nonlinear response of the sheath. The equilibrium d.c. potential of the body with respect to the plasma decreases until electron and ion currents become to be equal. Some experimental and theoretical investigations of r.f. response of the sheath have been reported.[267] The deformation of ion sheath due to this should be taken into consideration in the experiments of r.f. plasma probes, and also in satellite experiments when the high tension r.f.

field is used in the onboard instrument. The floating potential of a body affected by such r.f. potential is calculated analytically and the effect on the measurement of electron density is discussed.

§ 2. Gyro-plasma Probe System

2.1 Instrumentation

As noted before, the gyro-plasma probe is designed to measure the antenna admittance in vector form, namely with amplitude and phase over a wide frequency range, and a capacitance bridge is employed in its antenna network in order to eliminate contamination due to stray capacity. Figure 2-1 shows the block diagram of the gyro-plasma probe system which is designed for sounding rocket experiments. (The probe system onboard the spacecraft REXS will be described in Chapter V.) The swept frequency range is usually from 0.2 MHz to 15 MHz, which include the gyro-resonance frequency determined by the geomagnetic field (about from 1.3 MHz to 0.9 MHz in the altitude range up to 2000 km) and the electron plasma resonance frequency (about 0.9 MHz to 13 MHz in the altitude range from 90 km to 2000 km) in the ionosphere. The scale-values of the gyro-plasma probe are calibrated in the pre-launching test.

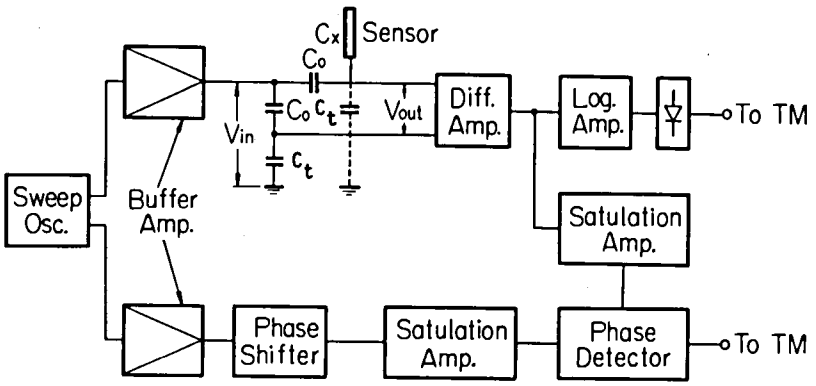

Fig. 2-1 Block diagram of rocket borne gyro-plasma probe system.

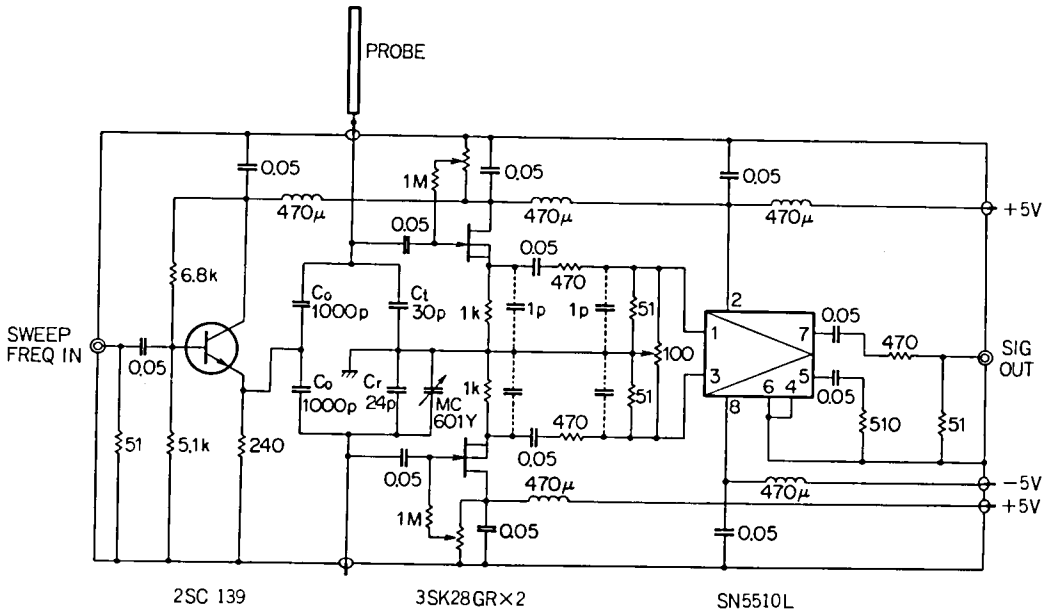

Fig. 2-2 Typical example of antenna network circuit. The capacitance bridge with an antenna comprises the four capacitor arms; C_0, C_0, C_t, C_r and the variable capacitor MC601Y.

The detailed circuits of the antenna network is shown in Fig. 2-2, in which the capacitance bridge with the antenna comprises the four capacitor arms of C_0, C_0, C_t and C_r and the variable capacitor MC601Y. The differential amplifier consists of two field effect transistors with high input impedance and the integral circuit of a differential operational amplifier.

Taking the equivalent capacitance of the antenna to be C, the amplitude of the output potential ΔV of the differential amplifier is calculated as

$$\Delta V = \frac{C_0 |C^* + C|}{(C_0 + C_t + C)(C_0 + C_r)} G_2 V_{IN} \qquad (2.1)$$

where $C^* = (1 - \beta')C_0 + C_t - \beta' C_r$, and $C = C(\omega)$,

$\beta' = G_1/G_2$.

G_1 and G_2 are the voltage gains of the input FET amplifiers, and V_{IN} is the amplitude of input potential to the capacitance bridge. The capacitance bridge should be balanced by adjusting the variable capacitor MC601Y, the gains of the input FET amplifiers to be $G_1 = G_2$, and the input impedance of the differential amplifier. When $C^* = 0$ and $C_0 >> C$, the output signal ΔV is simply proportional to the equivalent antenna capacitance C, namely

$$\Delta V \propto C(\omega) . \qquad (2.2)$$

This probe system is capable of detecting the changes of ΔV over about 80 dB of the absolute amplitude V_{OUT}. The phase difference between V_{IN} and V_{OUT} is measured in the range of π radian using the phase comparator with saturation amplifiers. Figure 2-3 (a) and (b) shows the amplitude and phase characteristics of the gyro-plasma probe, and their response to dummy antenna elements are illustrated in Fig. 2-4 (a), (b), and (c). As the equivalent capacitance of an antenna in a plasma can be shown in eq. (1.47) together with eq. (1.46), the output voltage ΔV has its minimum value at the upper hybrid resonance frequency and its maximum value at the sheath resonance frequency provided that the collision frequency is negligible and that the capacitance bridge is just balanced.

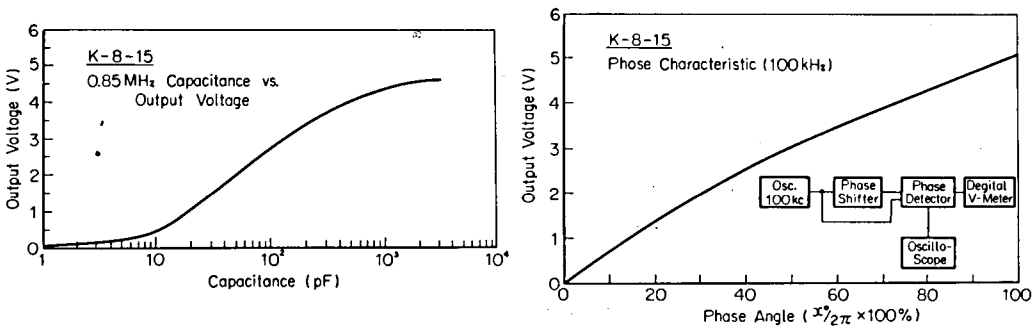

(a) (b)

Fig. 2-3 (a) Amplitude measuring circuit conversion-scale at 0.85 MHz. (b) Phase measuring circuit characteristic at IF frequency, 100 kHz.

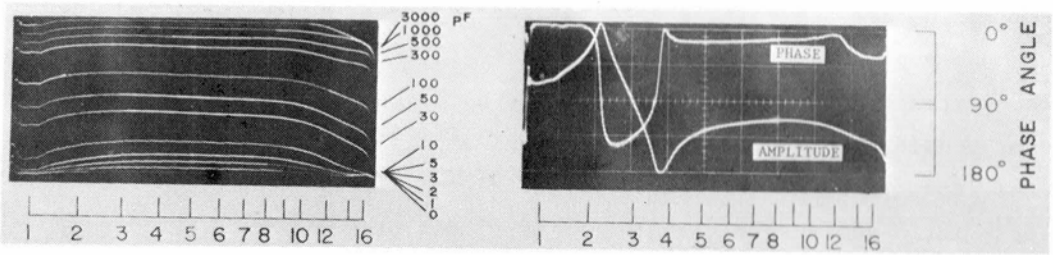

(a) (b)

Fig. 2-4 (a) Simulation of amplitude by pure capacitance (1 - 3000 pF). (b) Simulation of amplitude and phase variation by L-C-R resonance circuit (L=50 μH, C=37 pF, R=10 kΩ). (c) Simulation of amplitude variation resonance damping due to R (L=25 μH, C=35 pF, R=∞, 10 K, 7.5 K, 5.1 K, 3.0 K, 1.0 kΩ), and lower trace shows the reference frequency marker.

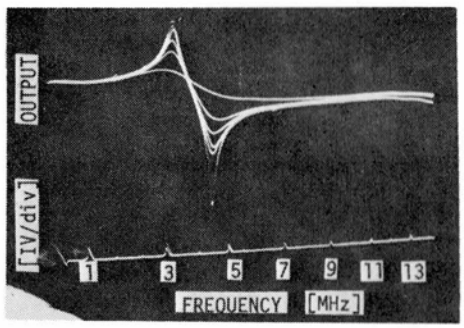

(c)

2.2 Calibration of Capacitance Bridge Unbalance

The balancing of the capacitance bridge should be carefully adjusted so that C^* in eq. (2.1) becomes to be zero. But, if an unbalanced quantity still remains, the resonance frequency will shift and the calculated electron density must be corrected. For cold and homogeneous plasma, neglecting the edge effect of antenna, the equivalent capacitance of the cylindrical antenna is deduced from eqs. (1.47) and (1.46) as

$$C = \frac{C_s C_p}{C_s + C_p} \tag{2.3}$$

and

$$C_p = \frac{2\pi\varepsilon_0 L a'^{-1} \cdot K' F^{1/2}}{\ell n(L/r_a) - 1 - \ell n\{(a'+F^{1/2})/2F\}} . \tag{2.4}$$

Here, the deviation of the measured electron density is defined as

$$\alpha' = \frac{\Delta N_e}{N_e} = \frac{\omega^{*2} - \omega_{UHR}^2}{\Pi_e^2} \tag{2.5}$$

where ω^* is the angular frequency at the minimum point of the antenna capacitance and $\omega_{UHR} = (\Pi_e^2 + \Omega_e^2)^{1/2}$. In the collisionless approximation, the correction factor α^* for the deviation of the measured electron density N_e^* from N_e, is obtained from eqs. (2.1), (2.3), and (2.4) as $(\alpha^* = -\alpha'(1 + \alpha')^{-1})$

$$N_e = (1 + \alpha^*)N_e^*, \tag{2.6}$$

and

$$\alpha^* = \frac{C_s}{C_{p0}} \cdot \frac{\Delta_c + \beta^*(C_0 + C_r)}{\Delta_c + \beta^*(C_0 + C_r) + C_s}, \tag{2.7}$$

where $\Delta_c = C_t - C_r$; stray capacity,

$\beta^* = 1 - \beta'$; gain difference of two FET amplifiers,

C_{p0} ; antenna capacitance in free space,

$C_s = 2\pi\varepsilon_0 L/\ell n(r_s/r_a - r_a/r_s)$, r_s : sheath radius.

N_e^* is the estimated electron density assuming ω^* to be ω_{UHR}. Figure 2-5 (a) and (b) show the correction term α^* which is computed as a function of normalized stray capacitance, Δ/C_{p0}, and the gain difference of two FET differential amplifiers, β^*, when the cylindrical antenna is parallel to the static magnetic field. The parameters are chosen as $C_0/C_{p0} = 50$, $C_r/C_{p0} = 30$ and $C_s/C_{p0} = 2.5$. The normalized stray capacitance must be reduced less than 10^{-2} (- 40 dB) and the gain difference of two input FET differential amplifiers must balance at about 2×10^{-4} (- 74 dB), in order to hold the correction term α^* within about $\pm$ 1 %.

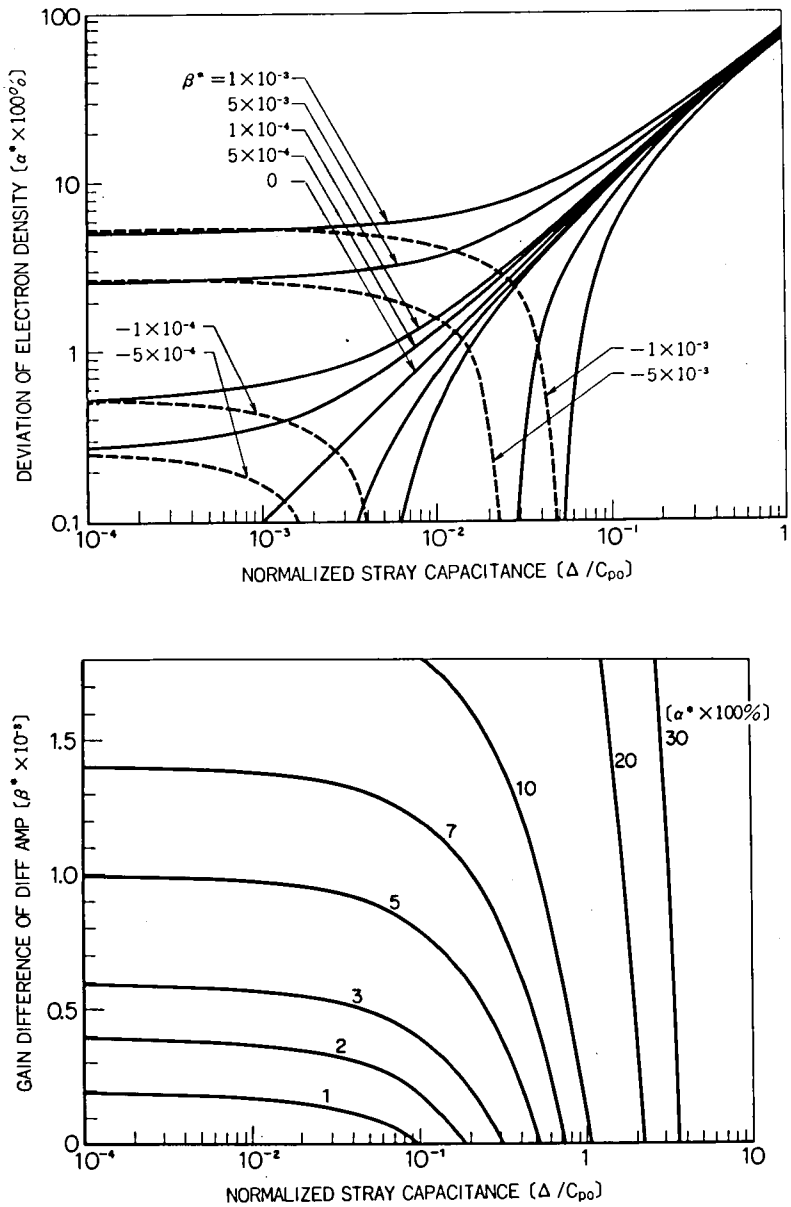

Fig. 2-5 Deviation of electron density (α^*) due to the gain difference of two FET amplifiers (β^*) and the normalized stray capacitance (Δ/C_{p0}).

2.3 Collision Effect on Resonance Characteristics

When the electron-neutral collision frequency is not negligible compared with the electron gyro-frequency and electron plasma frequency, the parallel resonance frequency is deviated from the upper hybrid resonance frequency, together with the effect of collisional broadening of the resonance. Consequently, the electron density value deduced from the parallel resonance frequency should be corrected. Figure 2-6 shows the probe capacitance in eq. (2.3) normalized by the capacitance in free space. As the collision frequency increases, the frequency to give minimum value of the probe capacitance, indicated by dots, increases and the resonance is gradually flattened out. The correction factor α defined in eq. (2.5) versus the collision is shown in Fig. 2-7. If the gyro-frequency is less than the plasma frequency or the collision

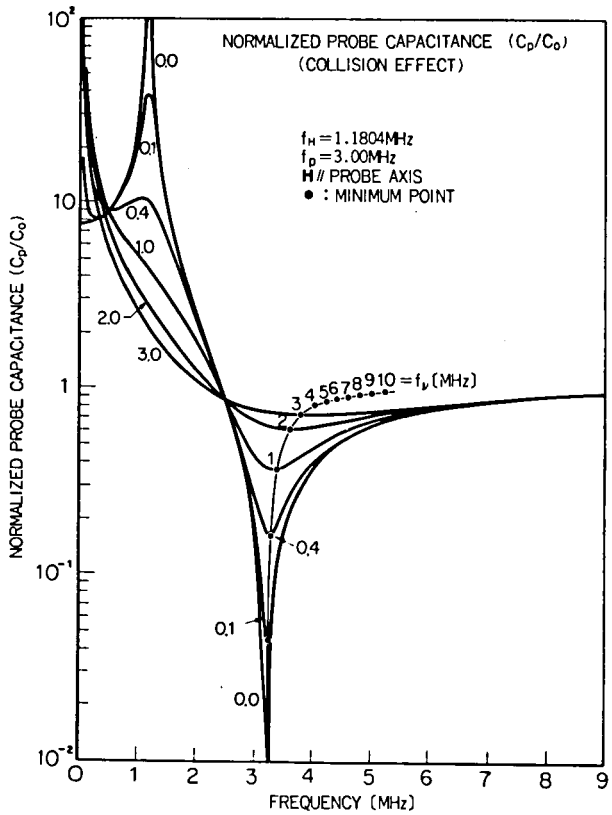

Fig. 2-6 Collisional damping of resonance and resonance frequency shift. Dots indicate minimum points of normalized probe capacitance.

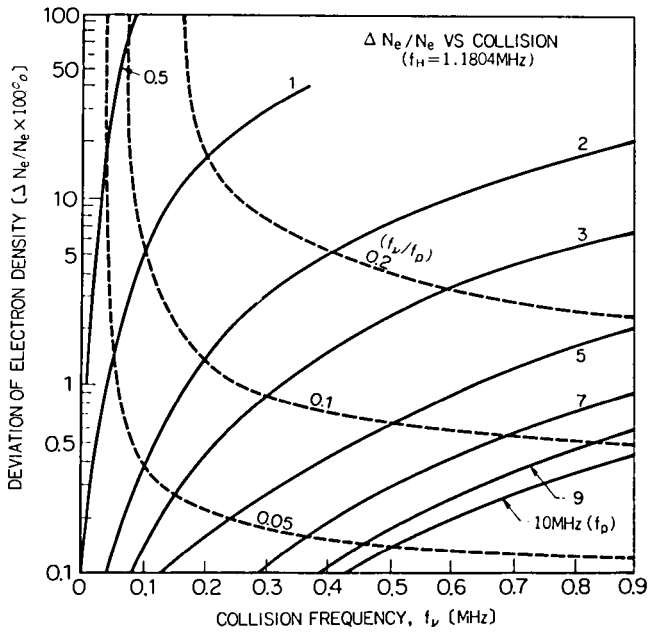

Fig. 2-7 Deviation of electron density due to electron-neutral collision; solid lines for constant f_p and dashed lines for constant f_ν/f_p.

frequency, the asymptotic solution of this value is given by

$$\alpha' = \frac{\sqrt{1 + 2\xi^2} - 1}{2} \qquad (2.8)$$

where $\xi = \nu/\Pi_e$. The electron density N_e is equal to $(1 + \alpha')^{-1}N_e^*$. This correction factor is very small except in the lower ionosphere below about 100 km.

2.4 Impedance of Antenna in Inhomogeneous Plasma

The plasma in space around the antenna is considered to be homogeneous on a scale of the antenna dimension. It is necessary, however, to examine the behavior of the antenna impedance in an inhomogeneous plasma because the ion sheath is formed around the vehicle when the vehicle's body acquires a negative charge. The error in the electron density measurement with r.f. probes due to the density gradient is also appreciable in the laboratory plasma experiments.

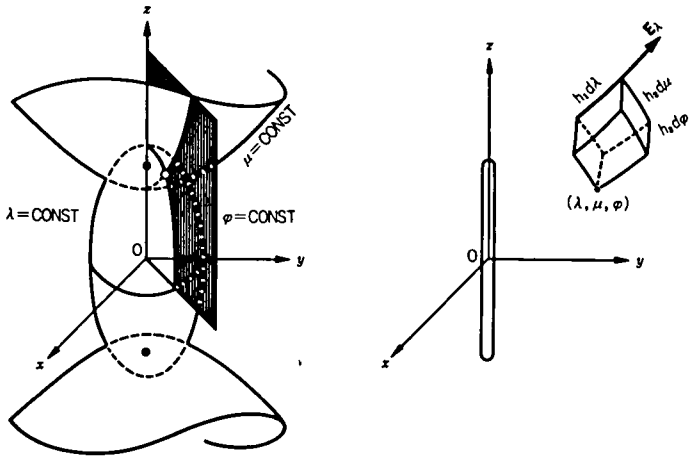

Fig. 2-8 Prolate spherical coordinate system.

It is considered here that the local plasma frequency is a function of position, the sheath electrostatic field being expressed in the prolate spherical coordinate system (λ, μ, Ψ) as shown in Fig. 2-8. The cylindrical antenna (length L and radius r_a) is approximately represented in this coordinate system as

$$\lambda_0 = (L/2)/c \qquad (2.9)$$

where $c = \sqrt{(L/2)^2 - r_a^2}$.

The metric coefficients h_1, h_2, and h_3 are given as follows,

$$\begin{aligned} h_1 &= c\sqrt{(\lambda^2 - \mu^2)/(\lambda^2 - 1)}\ , \\ h_2 &= c\sqrt{(\lambda^2 - \mu^2)/(1 - \mu^2)}\ , \\ h_3 &= c\sqrt{(\lambda^2 - 1)(1 - \mu^2)}\ . \end{aligned} \qquad (2.10)$$

If the equipotential surface is assumed to be λ = constant and the static magnetic field is perpendicular to the electrostatic field, the specific admittance of a volume $d\tau(h_1h_2h_3d\mu d\lambda d\Psi)$ is

$$\frac{j\omega\varepsilon(\lambda,\ \mu,\ \Psi)h_2h_3d\mu d\Psi}{h_1d\lambda} \tag{2.11}$$

where $\varepsilon(\lambda, \mu, \Psi)$ is a dielectric constant. The total admittance of an antenna is obtained by integrating the specific admittance over all space outside the antenna, then,

$$Y = \left[\frac{1}{j\omega 2c}\int_{\lambda_0}^{\infty}\frac{d\lambda}{\int_0^{2\pi}\int_0^1 \varepsilon(\lambda,\ \mu,\ \Psi)(\lambda^2 - 1)d\mu d\Psi}\right]^{-1} \tag{2.12}$$

For example, when a dielectric constant is that of free space, ε_0, the admittance of an antenna in free space is easily calculated as

$$Y = \frac{j\omega 2\pi\varepsilon_0 L}{\cosh^{-1}(L/2r_a)} \tag{2.13}$$

When inhomogeneity of plasma such as density gradient or gradient of the static magnetic field exists in μ and Ψ directions, the above

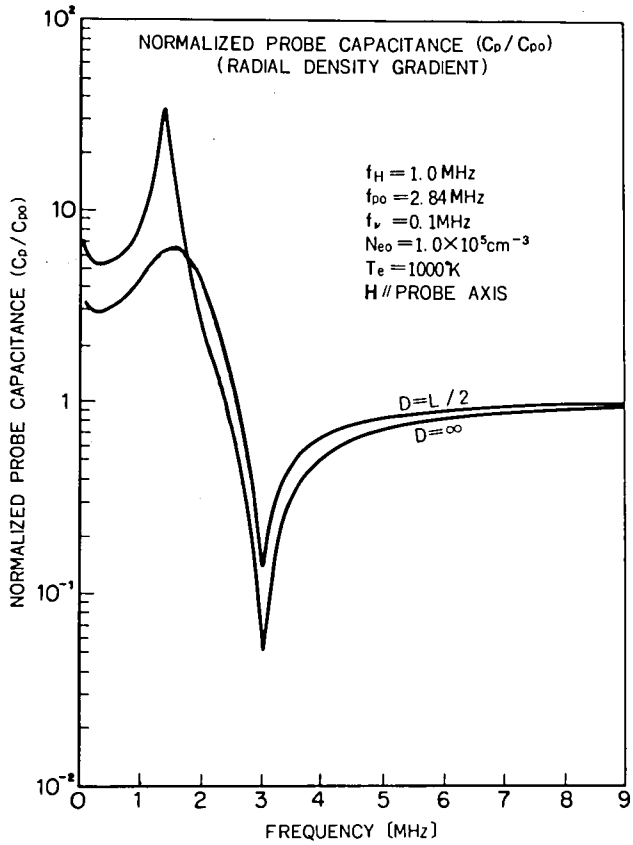

Fig. 2-9 Normalized probe capacitance. D indicates the e-hold distance of electron density gradient, and L is the length of cylindrical probe.

formulation is not an exact solution. To estimate the effect of density gradient in measuring an electron density from the parallel resonance frequency of antenna impedance, it is useful to compute the frequency response of the admittance given in eq. (2.12). Figure 2-9 shows the admittance of a cylindrical antenna (L = 2000 mm and r_a = 5 mm) in plasma, in which the radial gradient of the electron density distribution function is assumed as

$$N_e = \begin{cases} 0, & \lambda_0 < \lambda < \lambda_s \\ N_{e0} \exp\{(\lambda_s - \lambda)/D\}, & \lambda_s < \lambda \end{cases} \qquad (2.14)$$

where the sharp boundary sheath model is employed, λ_s is the distance of the sheath boundary from the antenna surface, and D is the e-fold distance of electron density gradient. The parallel resonance just coincides with the upper hybrid resonance corresponding to the maximum electron density. When the density gradient in μ direction is assumed, the electron density deduced from the parallel resonance is not the value of maximum electron density but an average value of the distribution function. In this case, deviations of measured electron density from the maximum value N_{e0} can be calculated. The results are shown in Fig. 2-10,

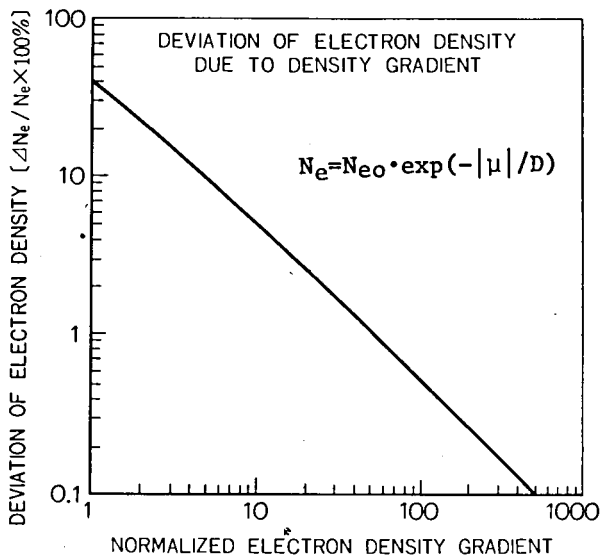

Fig. 2-10 Deviation of electron density due to density gradient in the μ direction.

assuming an $\exp(-|\mu|/D)$ type of the electron density gradient, where D is the e-hold distance of the electron density gradient normalized by L/2. As evident from this figure, when the normalized e-hold electron density gradient D is unity, the electron density deduced from the parallel resonance frequency is lower than the local maximum density about - 40 %.

In the sounding rocket experiments, the density gradient is mainly caused by the sheath region around the antenna. In this case, since the density inhomogeneity is considered to be radial gradient and the ambient plasma is homogeneous, the measured electron density shows the value of ambient plasma density. Considering the case of an antenna in a rocket wake region which is produced by the vehicle motion or the case that a part of an antenna is covered by the ion sheath around the vehicle's body, the density gradient along the antenna axis or the azimuthal density gradient should be considered. In the laboratory experiments, as it is generally difficult to generate homogeneous plasmas in a scale larger than the antenna dimension, the above-mentioned calculations must be introduced.

When the gradient of the static mangetic field in the probe axis direction expressed by the form $B(z) = B_0/(z + z_0) + B_{00}$ where B_0, B_{00} and z_0 are constant, the admittance of an cylindrical antenna is computed from eq. (2.12). This is the integrated form of the specific admittance given in eq. (1.44) along the z-axis, when the angle α of the static magnetic field with respect to the z-axis is $\pi/2$ and the electron gyro-frequency is a function of z. The specific capacitance in eq. (1.42), i.e., $\varepsilon_0 \Pi_e^2/\Omega_e^2$, decreases with increase of magnetic field intensity. The contribution of sheath capacitance to the total admittance becomes to be negligible when $\Pi_e^2 << \Omega_e^2$, because the specific capacitance of a plasma becomes to be much smaller than the specific capacitance of the ion sheath. Consequently, the sheath effect on the admittance of an antenna is neglected in the following calculations. Figure 2-11 shows the antenna capacitance normalized by that in free space for the inhomogeneous magnetic fields. The frequency shift and the broadening of resonance are caused by the inhomogeneity of the applied magnetic field. Experimental results (described in Chapter III)

agree well with this calculations.

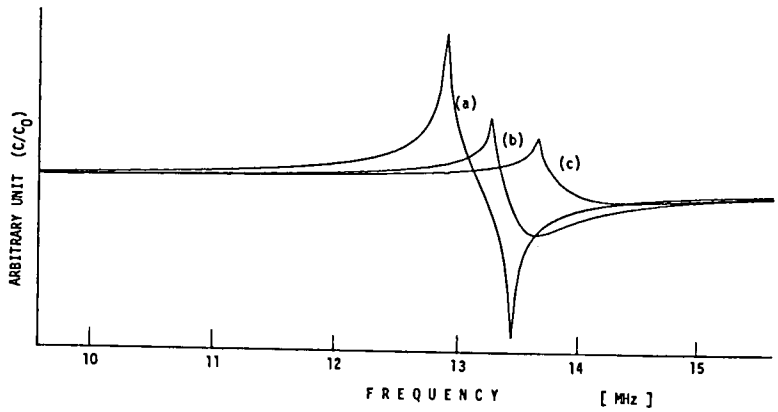

Fig. 2-11 Damping of resonance and resonance frequency shift due to the inhomogeneity of applied magnetic field. The cylindrical probe length 62 cm, z_0 = 1 cm, and B_{00} = 4.6 gauss. Three curves are corresponding to the magnetic field gradient; the parameters of B_0 [gauss·m] are (a) 1×10^{-4} (b) 4.5×10^{-2}, and (c) 9×10^{-2}.

2.5 Impedance of Antenna in Warm Magnetoplasma

There have been known some evidences that the admittance of an antenna changes its values at the harmonics of the electron gyro-resonance frequency. This admittance change cannot be predicted by the cold plasma theory. The second harmonic of gyro-resonance was first discovered by the Kappa 8-15 sounding rocket experiment (M. Ejiri and T. Obayashi[27]). V. F. Meltzer and H. H. Rabben[29] also detected this second harmonic resonance. The third and higher harmonics effects on the antenna admittance has been revealed in our laboratory experiments. In the most simple configuration of the parallel plates along the static magnetic field, the admittance of the probe is well represented by $y_{\perp}^{W}$ given in eq. (1.39). Figure 2-12 shows the capacitance of the probe as a function of frequency. Two cases are considered; plate distances are d = 0.1 m and 1.0 m but their capacitances in free space are the

same, the collision frequencies f_ν = 0.01 MHz and 0.50 MHz. The plasma frequency, the gyro-frequency, and the electron temperature are 5.00 MHz, 1.18 MHz and 1000°K, respectively. For simplicity, the wave number k is selected to be constant value of $2\pi/d$. For the case d = 0.1 m and f_ν = 0.01 MHz, a sharp resonance effect appears at the harmonics of gyro-resonance. This indicates that, as the parameters δ' (dimension of the probe system / Larmor radius) decreases, the cold plasma theory cannot be applicable. The warm plasma theory is essential for such computation of the antenna impedance.

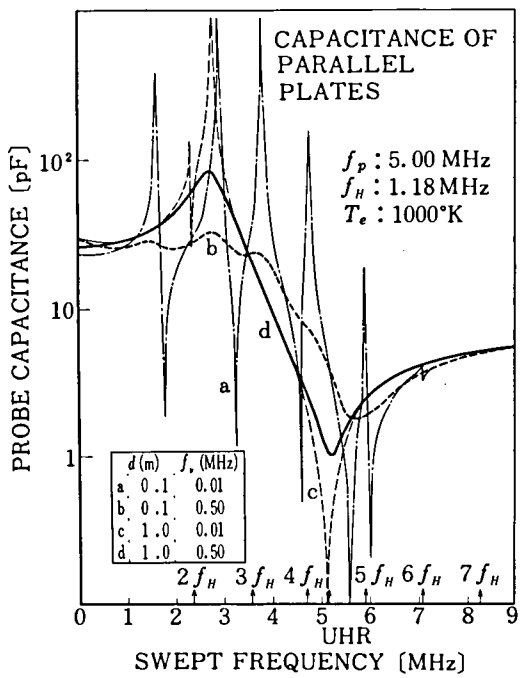

Fig. 2-12 Capacitance of parallel plates in warm plasma.

§ 3. Mutual Impedance Probe System

3.1 Instrumentation

The mutual impedance probe consists of two whip antennas, which are made up a transmitter-receiver antenna system. The swept frequency signal of constant voltage or constant current is fed to the transmitting antenna and the signal intensity of the resultant near field is detected by the receiving antenna with the pre-amplifier of the high input or low input impedance. Figure 2-13 shows the block diagram of measuring circuits for self and mutual impedance in Lambda 3H-5 sounding rocket experiment. The swept frequency range is from 0.2 MHz to

Measuring Circuit for Self & Mutual Impedance

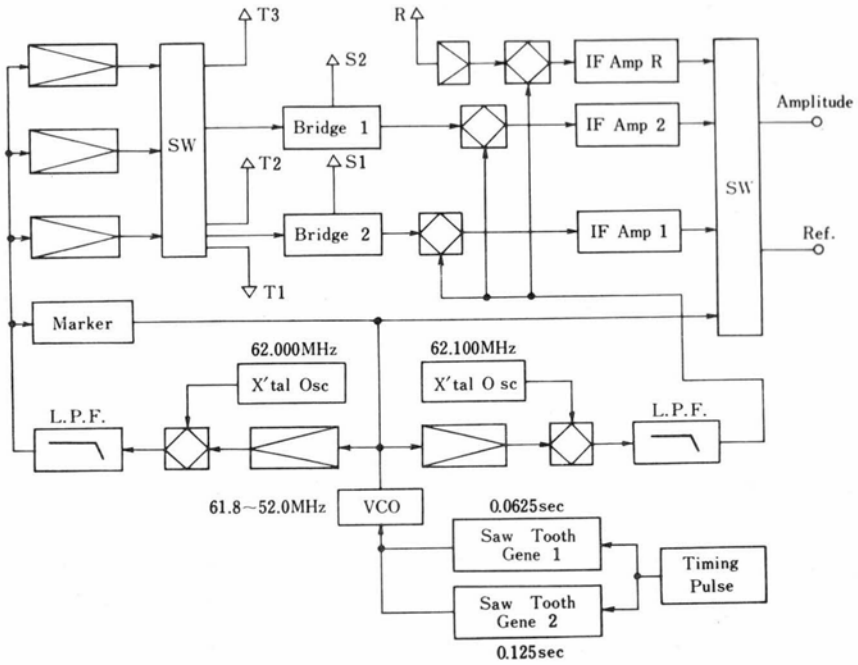

Fig. 2-13 Block diagram of self and mutual impedance measurement system. T1, T2, T3 are transmitting antennas and R receiving antenna.

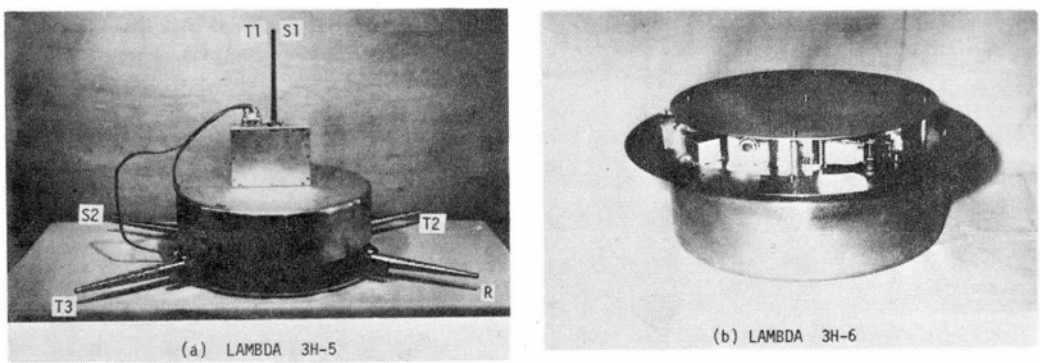

Fig. 2-14 Rocket borne instruments. (a) Lambda 3H-5 (four whip antennas with 130 cm in length and one vertical antenna with 60 cm in length); (b) Lambda 3H-6 (two whip antennas with 160 cm in length).

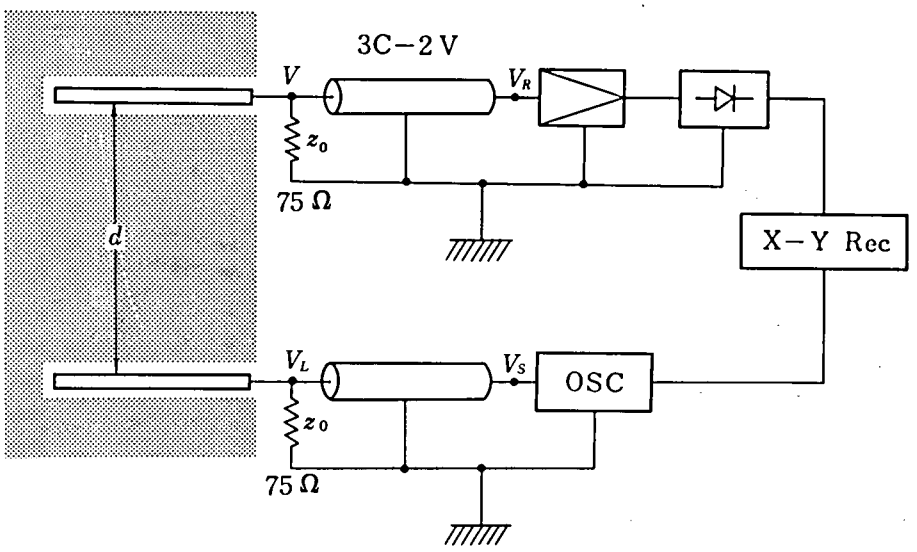

Fig. 2-15 Block diagram of mutual impedance probe system.

10.0 MHz and the applied constant voltage to transmitting antennas (T1, T2 and T3) is 0.1 V_{rms}. The r.f. electric field is detected by the receiving antenna (R) with its input resistance of 200 kΩ and capacitance of 7.8 pF. Similar experiment was also carried out by Lambda 3H-6 sounding rocket. The rocket borne instruments are shown in Fig. 2-14. Electrical circuits of this probe system except the antenna network circuit are much the same as that of the gyro-plasma probe.

In the laboratory experiment, the receiver with low input impedance of 75 Ω and the coaxial feeder of 3C-2V are used to match the output and input impedances of the oscillator and the receiver. The block diagram is shown in Fig. 2-15. The parallel cylindrical antennas set in a close distance is designated "Two Wire Probe". In general, the cylindrical antennas perpendicular to each other and the parallel mesh discs with a movable distance are used for mutual impedance probe.

3.2 Mutual Impedance in Magnetoplasma

To obtain the characteristics of the received signal intensity as

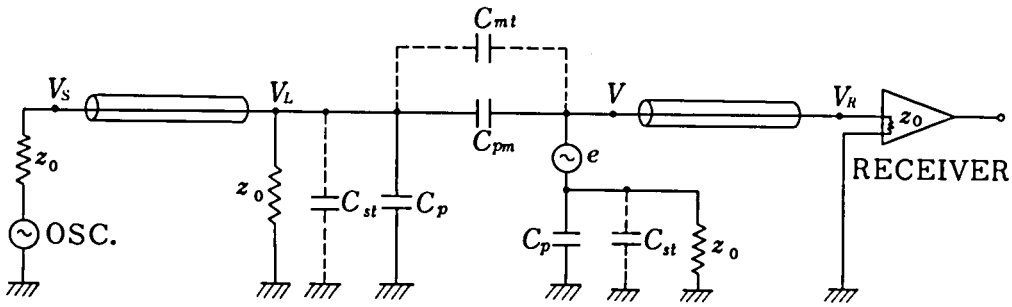

Fig. 2-16 Equivalent circuit for mutual impedance probe system.

a function of frequency, a simplified model of the probe system is considered as follows. The transmitting signal is fed to the antenna through the coaxial cable which is terminated by the characteristic impedance Z_0. The receiving antenna is also terminated by Z_0. The equivalent circuit for this probe system is illustrated in Fig. 2-16. C_p and C_{pm} are the capacitance of a antenna and the capacitance between two antennas in a plasma which are the functions of frequency. e is the induced voltage, i.e., $e = -j\,(M'/Z_p)V_L$ where M' and Z_p are the mutual inductance between two antennas and the self impedance of a antenna. C_{st} and C_{mt} are the stray capacitances. V_S, V_L, V and V_R are voltages at the points indicated in the figure.

The input voltage V_R to the detector of the receiver is expressed as

$$V_R = V \exp(-\gamma\ell) \simeq V \tag{2.14}$$

and

$$V \simeq \frac{C_{pm} + C_{mt} - C_m^{-1}(C_{st}+C_p)(C_0+C_p+C_{pm}+C_{st}+C_{mt})}{C_0 + C_p + 2C_{pm} + C_{st} + 2C_{mt}} \cdot V_0 \tag{2.15}$$

where $C_0 = (j\omega Z_0)^{-1}$, $C_m = (-\omega^2 M')^{-1}$, V_0 is an output voltage of the end of coaxial cable when an antenna is removed;

$$V_0 = V_S/(\cosh \gamma\ell + \sinh \gamma\ell) \simeq V_S. \tag{2.16}$$

γ and ℓ are the propagation constant and the length of a coaxial

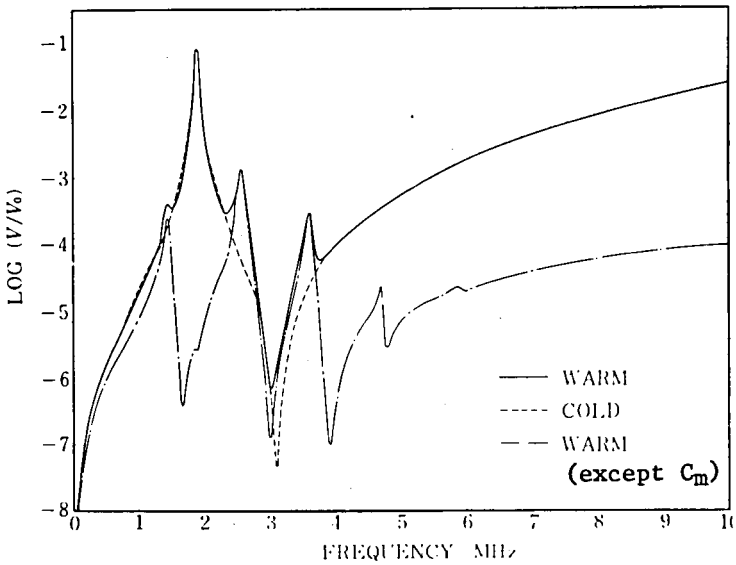

Fig. 2-17 Received signal intensity as a function of frequency. f_p = 3 MHz, f_H = 1.18 MHz, f_ν = 0.05MHz, and T_e = 1000°K. Probe distance is 0.1 m, and C_{p_0} = 5 pF, C_{st} = 1 pF, C_{mt} = 0.5 pF, and M' = 0.25 μH. Sheath capacitance is assumed to be 30 pF.

cable; the condition, $\gamma\ell << 1$, is assumed in eqs. (2.14), (2.15) and (2.16). Figure 2-17 shows the calculated received signal intensity versus frequency under the condition; f_p = 3.0 MHz, f_H = 1.18 MHz, f_ν = 0.05 MHz, T_e = 1000°K, and the distance between two antennas 0.1 m. The abrupt sheath model is employed and the sheath capacitance is assumed to be 30 pF. The capacitance of an antenna and the capacitance between two antennas in free space are 10 pF and 5 pF. The mutual inductance M' is selected to be 0.25 μH. The plasma is considered as the dielectric medium which has a dielectric constant given in eq. (1.34) for cold plasma or eq. (1.38) for warm plasma. In Fig. 2-17, the solid curve shows the ratio of the received signal intensity to the input voltage in warm plasma, and the dashed curve shows that in cold plasma approximation. If the mutual inductance is neglected, the intensity ratio is given by the chained curve. The effect of higher harmonics of the gyroresonance upon the received signal intensity can be clearly demonstrated

in the figure. The frequency of the parallel resonance is shifted from $f_{UHR} = (f_p^2 + f_H^2)^{1/2}$. The comparison with the experimental results is described in the next chapter.

§ 4. High Frequency Capacitance Probe System

4.1 Instrumentation

The probe in a plasma being used as a capacitance in the LC tank circuit of the Hartley-type oscillator, the change in oscillator frequency is related to the electron density of a plasma. The choice of oscillator frequency in free space well above the upper hybrid resonance frequency and the collision frequency, permits simplification in both the theory and the instrumentation. The typical Hartley-type oscillator circuit diagram is illustrated in Fig. 2-18. C_p is a probe capacitance and C_0 is a fixed capacitance which controlls the range of frequency change. This type of oscillator has such advantages that it is possible to oscillate in low voltage ($\sim 0.2\,V_{pp}$) and that a negative potential can be applied to both electrodes of the capacitor C_p. To suppress the thermal drift of frequency, the oscillator is covered by the thermal insulator and controlled by the electrical heater, the observational temperature being kept a constant.

The change in oscillator frequency Δf is obtained as

$$\Delta f \simeq \frac{f_p^2}{2f_0} \cdot \frac{C_{p0}}{C_0 + C_{p0}} \qquad (2.17)$$

where f_0 and C_{p0} are the oscillator frequency and the probe capacitance in free space, and the condition, $f_0^2 \gg f_{UHR}^2$ and f_ν^2, is assumed. Consequently, Δf is linearly proportional to

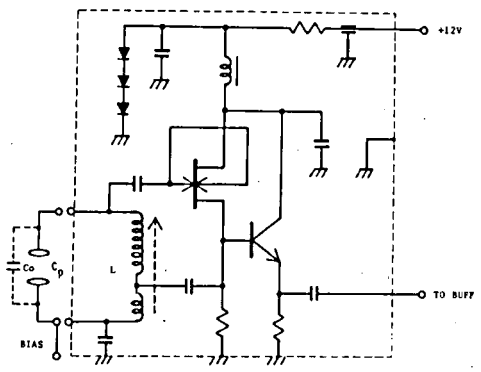

Fig. 2-18 Circuit diagram of the Hartley-type oscillator.

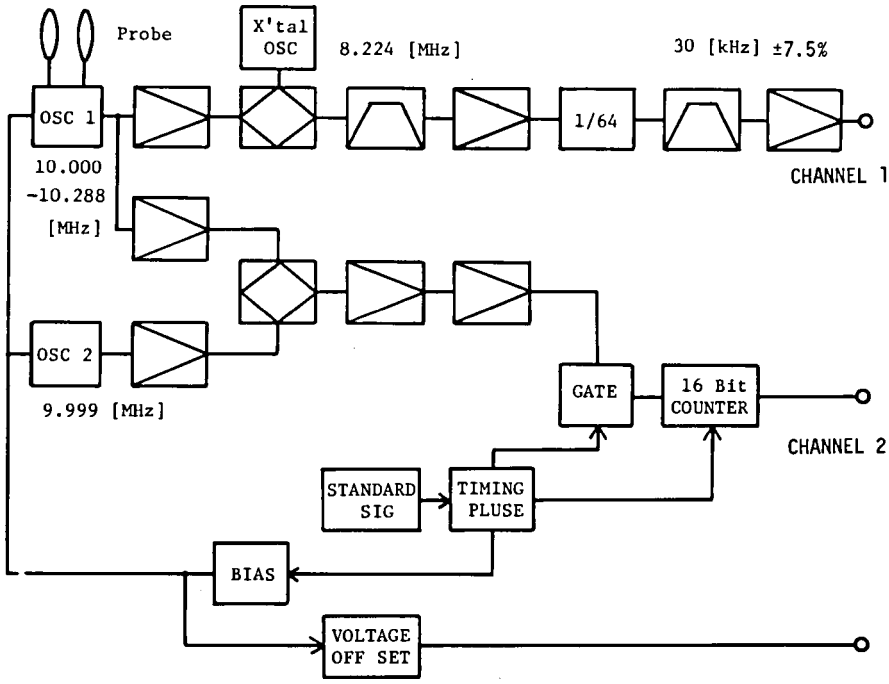

Fig. 2-19 System block diagram of the capacitance probe onboard S 210-6 sounding rocket.

the electron density value. The compromised choice of the oscillator frequency is also required, because the sensitivity of the frequency shift is inversely proportional to the oscillator frequency, while a more complicated theoretical calculation is needed for a low operating frequency.

In the present experiments, the technique for counting the frequency shift has been employed as shown in Fig. 2-19. This system has two channels. In the channel 1, the frequency difference, subtracting a constant frequency of the crystal controlled oscillator from the oscillator frequency, is demultiplied by the binary chain and transmitted through the FM-FM telemetry as a subcarrier frequency. The frequency of the crystal controlled oscillator and the number of the binaries are determined such that the allowable change in frequency is within the given frequency bandwith. In the channel 2, the same type oscillator (OSC 2) is provided. The frequency difference between OSC 1 and 2 is measured precisely by using a gated counter and directly transmitted as

binary bits using the VCO channel of FM-FM telemetry system. The several kinds of d.c. potential are applied to the sensors. The use of a deep negative potential to the probe provides the inflight calibration, giving the frequency of oscillator in free space, so that any systematic drift in the oscillator frequency due to environmental changes could be adequately corrected. Langmuir characteristics of probe current versus applied voltage are obtained simultaneously when the saw-tooth voltage is applied to the probe. The change in frequency response to the applied potential give the information about the sheath.

4.2 Design of Electrical Circuits

The Hartley circuit consists essentially of a grounded-base amplifier having a tuned collector load. Conditions to be fulfilled for the amplifier of this type are; (i) the amplitude of current fed back to the input be the correct value to obtain the corresponding output, and (ii) the phase of the fed-back current be in phase with the output, hence giving positive feedback.

In the capacitance probe, the silicon N-channel unjunction field effect transistor (3SK28G) are used. This type of the transistor feedbackoscillator is very similar to a vacuum tube oscillator. The basic Hartley circuit, without the biasing network, is shown in Fig. 2-20 (a); part (b) is the diagram as a four terminal network. The condition of oscillator can be expressed in terms of the admittance matrix as

$$\begin{vmatrix} Y_{11} & Y_{12} \\ Y_{21} & Y_{22} \end{vmatrix} \leq 0 \qquad (2.18)$$

where Y_{11}, Y_{12}, Y_{21}, and Y_{22} are the input admittance, reverse transadmittance, forward transadmittance, and output admittance, respectively. Considering the conductance g of the condencer C in a plasma and the complex admittance matrix of the transister, i.e., $y_i = g_i + j\omega c_i$, $y_r = g_r + j\omega c_r$, $y_f = g_f + j\omega c_f$, and $y_o = g_o + j\omega c_o$,

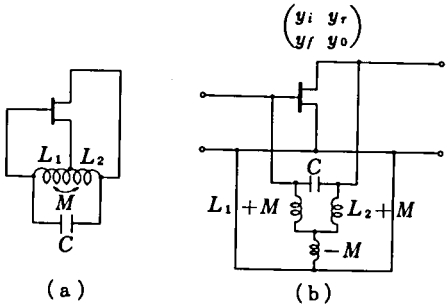

Fig. 2-20 Hartley oscillator; (a) a.c. equivalent of Hartley oscillator and (b) representation as the four terminal network.

the oscillator frequency is deduced from eq. (2.18).

$$\omega^2 = \frac{1 + A/B^2}{C(L_1+L_2+2M)+\Delta g(L_1L_2-M^2)+(L_2c_0+L_1c_i-Mc_r-Mc_f)} \tag{2.19}$$

where $\Delta g = (g_ig_0 - g_rg_f) + g(g_i + g_r + g_f + g_0)$,

$$\frac{A}{B^2} = \frac{(L_1L_2-M^2)\{c_ic_0-c_rc_f+C(c_i+c_r+c_f+c_0)\}}{\{C(L_1+L_2+2M)+\Delta g(L_1L_2-M^2)+(L_2c_0+L_1c_i-Mc_r-Mc_f)\}^2}$$

When $g << 10^{-1}$ mho, the frequency is approximated by

$$\omega^2 \simeq \frac{1}{C(L_1 + L_2 + 2M)} . \tag{2.20}$$

The condition of oscillation is also found to be

$$\frac{g_f+g_f-2g}{g_i+(\frac{L_2+M}{L_1+M})^2 g_0+\{1+(\frac{L_2+M}{L_1+M})^2\}g} \geq \frac{L_1+M}{L_2+M} - \frac{L_1+L_2+2M}{C} \cdot \frac{L_1L_2+M^2}{(L_1+M)(L_2+M)} \cdot \sum g_c , \tag{2.21}$$

where $\sum g_c \equiv (g_i+g)c_0+(g_0+g)c_i-(g_f-g)c_f-(g_f-g)c_r$

Since the term $\sum g_c$ is negligible compared with the other terms, and $g_r << g_f$ and $g_0 << g_i$ in the low frequency approximation, the condition given in eq. (2.21) becomes to be

$$\frac{g_f}{g_i} - \frac{(L_1+L_2+2M)}{(L_1+M)(L_2+M)} \cdot \frac{g}{g_i} \geq \frac{L_1+M}{L_2+M} \tag{2.22}$$

If $g = 0$, eq. (2.22) is reduced to the well-known formula;

$$\frac{g_f}{g_1} (\equiv h_f) \geq \frac{L_1 + M}{L_2 + M} \tag{2.23}$$

where h_f is a forward current amplification ratio of the transistor. This value should be large enough to satisfy the inequality of eq. (2.23).

The index of stability of the oscillation is defined as a ratio of the left hand side to the right hand side of eq. (2.22). The index of stability decreases with the increase of the conductance of the probe in a plasma. Using the parameters of 3SK28G, Fig. 2-21 shows the relation of the index of stability with respect to the conductance. The index of stability is usually chosen to be greater than 25 for the stable oscillation. The conductivity is deduced from the imaginary part of permittivity in eq. (1.34). The oscillator of the capacitance probe is

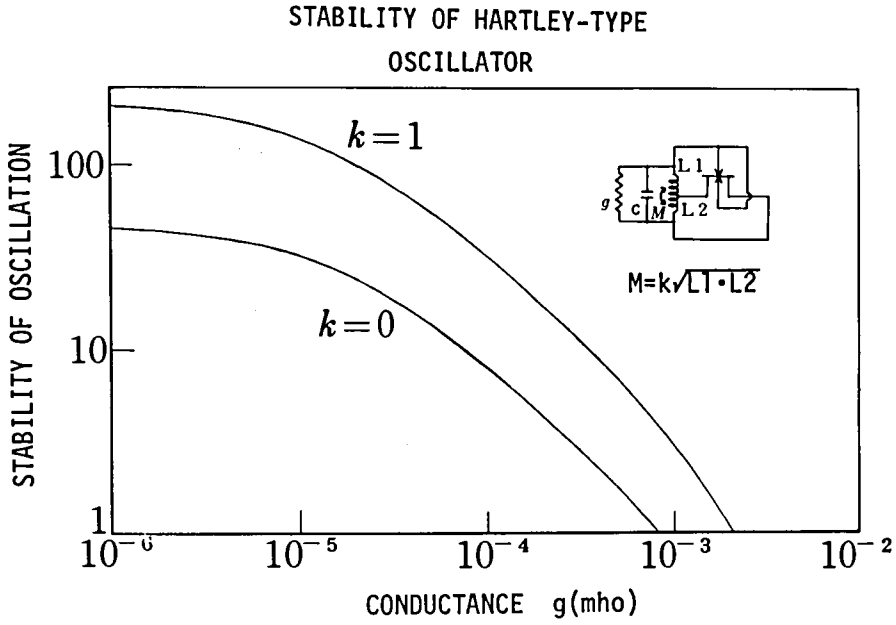

Fig. 2-21 Index of stability of Hartley-type oscillator versus conductance of the capacitor. ($C = 30$ pF, $L_1 = 3$ μH, $L_2 = 0.33$ μH, $g_1 = 20$ μmho, $g_f = 9.2$ mmho (3SK28G)). k is a coupling factor of L_1 and L_2.

found to be always stable in the ionosphere, while unstable in the laboratory plasma when the electron density becomes greater than 10^7 cm^{-3} at the collision frequency about 1 MHz.

To design the electrical circuit, some stabilizations of the oscillator frequency have been considered; (i) to increase the Q value of LC tank circuit, (ii) to increase the ratio of C to L, (iii) the reactance stabilization to compensate the changes of y parameter of the transistor, (iv) to stabilize the quiescent point of the load line of the transistor by the stabilized d.c. power supply.

4.3 Collision Effect on Electron Density Measurement

Since the electron-neutral collision frequency is greater than the plasma frequency below the altitude of about 85 km in the lower ionosphere and the oscillator frequency is usually chosen to be 10 MHz to 15 MHz in the S 210 sounding rocket experiments, the linear relation of the change in oscillator frequency given in eq. (2.17) should be corrected in the lower ionosphere where the condition, $f_0^2 >> f_\nu^2$, is not satisfied. As mentioned above, the imaginary part of the permittivity of a dielectric constant does not contribute to the change in oscillator frequency because the conductance is much less than 10^{-1}mho, the usual probe dimension being assumed. Using the real part of permittivity deduced from eq. (1.34) and the condition, $f_0^2 >> f_{UHR}^2$, eq. (2.17) is rewritten as

$$\Delta f \approx \frac{f_p^2}{2f_0} \cdot \frac{C_{p0}}{C_0 + C_{p0}} \left(1 - \frac{f_\nu^2}{f_0^2 + f_\nu^2}\right) \qquad (2.24)$$

To evaluate the correction factor due to collision, the model collision profile in the lower ionosphere is adopted from the values given by J. S. Belrose and I. A. Bourne.[268] If the oscillator frequency in free space is taken to be 14 MHz, the condition that the correction factor is equal to or less than about 10 % is satisfied in the region above 70 km.

As for the effect due to ion sheath formed around a probe, the capacitance probe has such disadvantage as to measure the very low electron density where the Debye shielding length becomes much longer than the probe dimensions. The oscillator frequency is, also, shifted due to stray capacitance of a sensor and temperature drift of the electrical elements. Consequently, it may not be appropriate to measure the absolute value of electron density otherwise to measure the fine structure of electron density variations.

§ 5. R.F. Response of Ion Sheath

In this section the ion sheath formation around a probe in a plasma is investigated. It is assumed that neutrals, ions and electrons are in thermal equiliblium and isotropic, and that the earth's magnetic field will be neglected. Furthermore, the variation of the equilibrium potential low enough to let electrons adjust their density instantaneously to the ambient potential, but high enough to let the ion density remain the same. In the following analysis, the plane probe without an edge effect is considered.

5.1 Sheath Formation around a Body in Plasma

A body immersed in plasma rapidly acquires a negative charge because random electron currents are greater than random ion currents. The accumulation of charge is limited by the negative potential which develops between the body and the medium, and equiliblium with the medium is established when electron and ion currents become to be equal. This equilibrium potential is called "floating potential". The difference of the densities between electrons and ions, in turn, results in the equilibrium of the potential in the sheath region which is well represented by the Poisson's equation.

For the quasi-static condition where the mean free path is larger than the probe and the sheath dimension, the Boltzmann's law is applied to the electron density. Assuming a Maxwellian velocity distribution of electrons, the electron current density, J_e, to a surface at potential V with respect to the plasma is given as ($V < 0$, $q > 0$)

$$J_e = - N_0 q \left(\frac{\kappa T_e}{2\pi m}\right)^{1/2} \exp(qV/\kappa T_e), \tag{2.25}$$

where N_0 is ambient plasma density and $-q$ is electron charge ($q > 0$). The electron density, N_e, at potential V can be expressed as

$$N_e = N_0 \exp(qV/\kappa T_e). \tag{2.26}$$

As for the ion distribution, ions accelerated through the pre-sheath region have the drift-Maxwellian velocity distribution function as

$$f(u,v,w) = \left(\frac{M}{2\pi\kappa T_i}\right)^{3/2} \exp\left[-\frac{M}{2\kappa T_i}\{u^2+(v-v_0)^2+w^2\}\right] \tag{2.27}$$

where v is the component of the velocity vector perpendicular to the probe surface, and $v_0 (= \sqrt{\kappa T_e/M})$ is the ion velocity acquired through the pre-sheath region where the quasi-neutrality holds. Then, the ion current density J_i is calculated as

$$J_i = N_0' q \int v f(u,v,w)\,du\,dv\,dw$$

$$= N_0 q \cdot \exp\left(-\frac{1}{2}\right)\left\{\left(\frac{\kappa T_i}{2M}\right)^{1/2} + v_0\right\}, \tag{2.27}$$

where $N_0' (= N_0 \exp(-\frac{1}{2}))$ is the density at the boundary edge of the pre-sheath region. The ion density N_i is determined by the equation of continuity;

$$N_i v_i = N_0' v_0 \tag{2.28}$$

and the ion velocity v_i is calculated by the conservation of energy,

$$\frac{1}{2} Mv_i^2 + qV = \frac{1}{2} M(v_{th}^2 + v_0^2) + qV_t \qquad (2.29)$$

where $V_t (= -\kappa T_e/2q)$ is the potential at a point of the pre-sheath boundary.[269] If the ion thermal velocity v_{th} is negligible compared with v_0, the ion density, N_i, at potential V is calculated from eq. (2.28) and eq. (2.27) as

$$N_i = N_0 \exp(-\frac{1}{2}) \cdot (\kappa T_e/2qV)^{1/2}. \qquad (2.30)$$

The Poisson's equation can be expressed as

$$\nabla^2 V = -\frac{q}{\varepsilon_0} (N_i - N_e). \qquad (2.31)$$

5.2 Sheath Capacitance of Plane Probe

Once the potential distribution in the sheath region is obtained by solving the Poisson's equation, the capacitance of a probe is easily deduced as the 2nd derivative of the potential with respect to the distance, r, and the potential at the probe surface (see Appendix A);

$$\Lambda = \frac{C}{S} \frac{\lambda_D}{\varepsilon_0} = -\frac{\partial}{\partial y} \left(\frac{\partial y}{\partial x}\right)\Big|_0 \qquad (2.32)$$

where C is the capacitance, S the probe area, $\lambda_D = (\varepsilon_0 \kappa T_e/N_e q^2)^{1/2}$; the Debye length of medium, $x = r/\lambda_D$, and $y = qV/\kappa T_e$. Suffix 0 indicates the quantity at the boundary of the probe surface. Using eq. (2.26) and eq. (2.30), the Poisson's equation given in eq. (2.31) is rewritten as

$$\frac{d^2y}{dx^2} = \exp y - \frac{1}{\sqrt{-2ey}}, \quad (y < -\frac{1}{2}). \qquad (2.33)$$

where $e = 2.71828.....$ (Napier's number). Since the quasi-neutrality holds in the pre-sheath region where $y \geq 1/2$, boundary conditions at the surface of sheath are given, approximately

$$d^2y/dx^2 = dy/dx = 0 \qquad \text{where} \quad y = -1/2 \tag{2.34}$$

Then, the normalized capacitance Λ is expressed in the following form,

$$\Lambda(y) = \frac{(-2qy)^{-1/2} - \exp y}{\{2(\exp y + (-2y/e)^{1/2} - 2\exp(-1/2))\}^{1/2}}. \tag{2.35}$$

If the ion density in the sheath is assumed to be constant and same as the ion density in the ambient plasma, eq. (2.35) is given as

$$\Lambda(y) = \frac{1 - \exp y}{\{2(\exp y - y - 1)\}^{1/2}}. \tag{2.36}$$

Figure 2-22 shows the normalized capacitance Λ_1 given in eq. (2.35) and Λ_2 given in eq. (2.36) versus the potential on the probe surface. The normalized capacitance decreases with decrease of the potential because of the increase of the sheath distance or radius, as is evident in the figure. The equivalent sheath radius is given by λ_D/Λ.

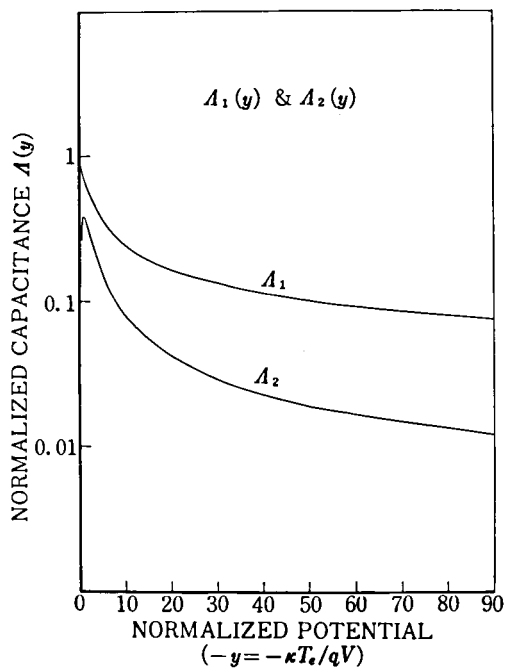

Fig. 2-22 Normalized capacitance Λ versus probe potential.

5.3 Change in Floating Potential due to Applied High Tension R.F. Field

When the high tension r.f. field is applied to a body the equilibrium potential of the body is affected and changes its potential to satisfy the quasi-floating condition of electron and ion currents; that is,

$$\frac{1}{2\pi}\int_0^{2\pi}\{J_e(V_f+V_a \sin \omega t) + J_i(V_f)\}d\omega = 0 \qquad (2.37)$$

where V_f and $V_a \sin \omega t$ are the floating potential and the applied r.f. potential with angular frequency ω. The electron current density is given as (see eq. (2.25))

$$J_e = - N_0 q(\frac{KT_e}{2\pi m})^{1/2}\exp\{\frac{q}{KT_e}(V_f + V_a \sin \omega t)\}$$

$$\equiv J_{e0} \exp\{\frac{q}{KT_e}(V_f + V_a \sin \omega t)\}, \qquad (2.38)$$

while the ion current density, assuming $v_{th} \ll v_0$, is deduced from eq. (2.27)

$$J_i = N_0 q(\frac{KT_e}{M})^{1/2}\exp(-\frac{1}{2}) \equiv J_{i0}. \qquad (2.39)$$

From eqs. (2.37), (2.38) and (2.39), the change in floating potential ΔV_f is

$$\Delta V_f \equiv V_{f0} - V_f = \frac{KT_e}{q} \ln I_0(\frac{qV_a}{T_e}) \qquad (2.40)$$

where V_{f0} is the floating potential without an impressed r.f. field and I_0 is a modified Bessel function of order zero. Figure 2-23 shows the variation of ΔV_f versus r.f. potential V_a, for various electron temperatures. This temperature dependence of the change in ΔV_f as a function of applied r.f. potential, has been utilized to the r.f. electron temperature probe.[270,271]

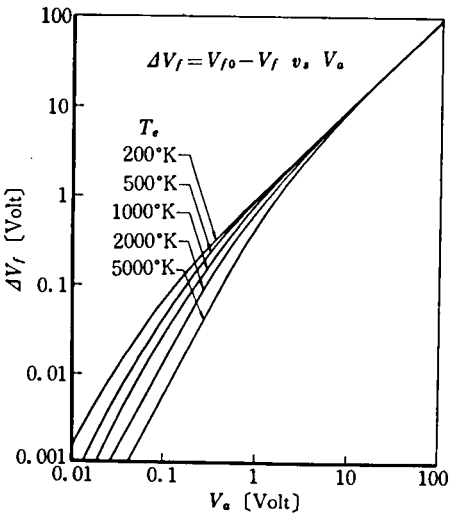

Fig. 2-23 Change in floating potential due to applied r.f. potential.

Here, the transient response of floating potential is formulated for the case that r.f. potential, $V_a \sin \omega t$, is applied. Denoting that potential with respect to the plasma, capacitance, charges, electron and ion current densities, and surface areas are V_k, C_k, Q_k, J_{ek} and J_{ik}, and S_k (k = 1 and 2), the derivative of Q_k gives the total current,

$$\frac{d}{dt} \sum_{k=1,2} Q_k = \frac{d}{dt} \sum_{k=1,2} C_k V_k = \sum_{k=1,2} (J_{ek}+J_{ik}) S_k . \qquad (2.41)$$

The following dimensionless quantities are introduced;

$$y = \frac{qV_1}{\kappa T_e} , \qquad a = \frac{qV_a}{\kappa T_e} , \qquad (2.42)$$

and the parameters,

$$A_e = \frac{q\lambda_D}{\varepsilon_0 \kappa T_e} J_{e0}, \quad A_{i0} = \frac{q\lambda_D}{\varepsilon_0 \kappa T_e} J_{i0}, \quad \Lambda_k = \frac{\lambda_D C_k}{S_k}, \quad \delta = \frac{S_2}{S_1+S_2}, \qquad (2.43)$$

and it is assumed that ion current density is equal to the ion

saturation current density, i.e., $J_{i1} = J_{i2} = J_{i0}$. Using the relation that $V_2 = V_1 + V_a \sin \omega t$, eq. (2.41) is written as

$$\frac{d}{dt}\{((1-\delta)\Lambda_1+\delta\Lambda_2)y+\delta\Lambda_2 a\cdot\sin\omega t\}=A_{e0}\exp y\cdot\{(1-\delta)+\delta\exp(a\cdot\sin\omega t)\}+A_{i0} \tag{2.43}$$

where $\Lambda_1 = \Lambda_1(y)$ and $\Lambda_2 = \Lambda_2(y + a\cdot\sin \omega t)$. For simplicity, Λ_1 and Λ_2 are assumed to be equal to Λ, which means that the capacity of each body is determined by its surface area and unperturbed sheath thickness. Then, eq. (2.43) is reduced to

$$\frac{d}{dt}(y+\delta a\cdot\sin\omega t) = A_1\exp(y)+A_2\exp(y+a\cdot\sin\omega t)+A_3 \tag{2.44}$$

where $A_1 = (1-\delta)A_{e0}/\Lambda$, $A_2 = \delta A_{e0}/\Lambda$ and $A_3 = A_{i0}/\Lambda$. This differential equation can be solved analytically under the initial condition that $y = y_0$ at $t = 0$.

$$\begin{aligned} y = {} & A_3 t-\delta a\cdot\sin\omega t-\ell_n\Big[e^{-y_0}+\frac{A_2}{A_3}\cdot\frac{1-e^{A_3 t}}{\delta}\cdot(\delta' I_0(\delta a)+\delta I_0(\delta' a)) \\ & + 2\sum_{n=1}^{\infty}(-1)^n\Big\{\Big(\frac{\sin^2\alpha_{2n}}{A_3}-\frac{A_2 e^{A_3 t}\sin(2n\omega t+\alpha_{2n})}{\delta\sqrt{A_3^2+4n^2\omega^2}}\Big)(\delta' I_{2n}(\delta a)+ I_{2n}(\delta' a) \\ & - \Big(\frac{\cos^2\alpha_{2n-1}}{(2n-1)\omega}-\frac{A_2 e^{A_3 t}\cos((2n-1)\omega t+\alpha_{2n-1})}{\delta\sqrt{A_3^2+(2n-1)^2\omega^2}}(\delta' I_{2n-1}(\delta_a)-\delta I_{2n-1}(\delta' a))\Big\}\Big] \end{aligned} \tag{2.45}$$

where $\sin\alpha_n = \dfrac{A_3}{\sqrt{A_3^2+n^2\omega^2}}$, $\cos\alpha_n = \dfrac{n\omega}{\sqrt{A_3^2+n^2\omega^2}}$,

and $\delta' = 1 - \delta$.

In the rocket experiment, the body 1 and 2 are considered to be the vehicle and the probe, and then $\delta \ll 1$. The above equation becomes

$$y \simeq A_3 t - \ell_n\Big[e^{-y_0}+\frac{A_1}{A_3}(1-e^{A_3 t})\Big(1+\frac{\delta}{1-\delta} I_0(a)\Big)\Big] \tag{2.46}$$

The equilibrium potential is obtained as $(t \to \infty)$,

$$y \simeq y_0 - \delta I_0(a) \tag{2.47}$$

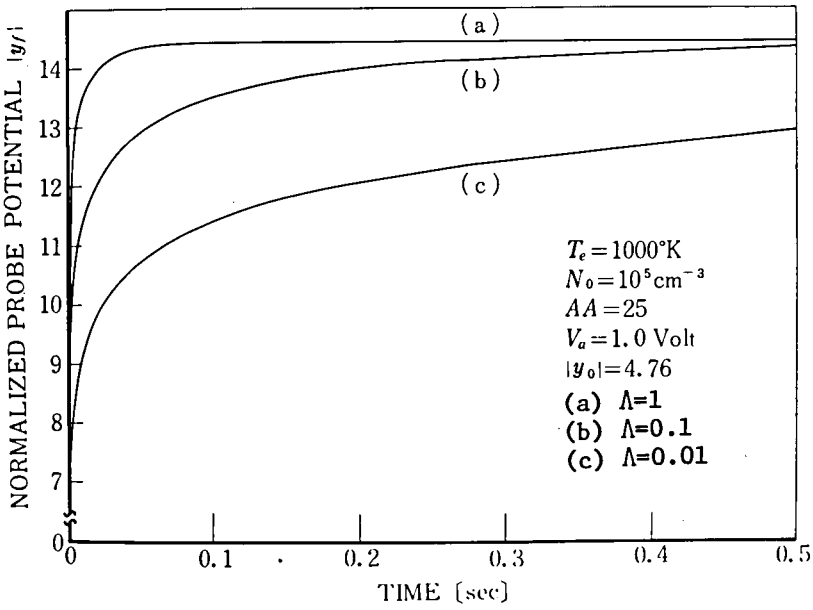

Fig. 2-24 Change in quasi-equilibrium floating potential due to applied r.f. potential. (T_e = 1000°K, N_0 = 1 × 10^5 cm^{-3}, ion molecular weight AA = 25, and V_a = 1.0 volt).

where y_0 is the floating potential at t = 0. The second term of the right hand side of eq. (2.47) is the effect of applied potential. From eq. (2.45), the time constant of potential y, i.e., e-hold time, is given approximately as,

$$\tau \simeq \frac{1}{A_3} \equiv \frac{1}{\Lambda} \cdot \frac{q\lambda_D}{\varepsilon_0 K T_e} J_{i0}. \qquad (2.48)$$

When the equilibrium potential y decreases, Λ also decreases (see Fig. 2-22) and the time constant increases. Figure 2-24 shows the change of the quasi-equilibrium potential y_f, defined by eq. (2.37), when the r.f. potential with the amplitude of 1.0 volt is applied between a body and a plasma. The curves (a), (b) and (c) are for different time constants corresponding to the different normalized capacitances, Λ = 1, 0.1, and 0.01. Figure 2-25 shows the time response of potential y in the same condition of Fig. 2-24 for the operating frequency 1 MHz. The quasi-equilibrium potential y_f is indicated by the dashed

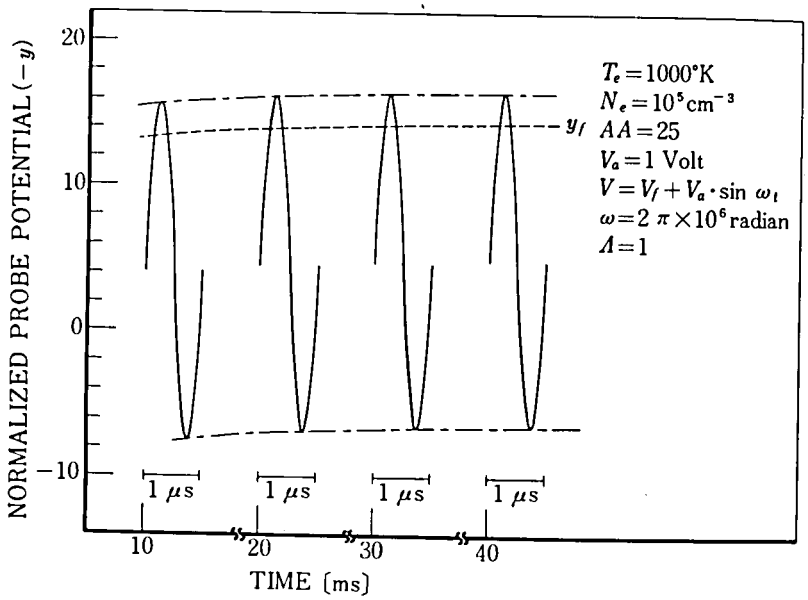

Fig. 2-25 Change in body's potential; frequency 1.0 MHz.

line.

This potential change causes the deformation of the ion sheath. This modulation effect is essential not only to the r.f. probe, but also to any static analyser in the rocket and satellite experiments, when a high tension r.f. field is applied to the sensor immersed in a plasma. The above calculation is not self-consistent, because it is assumed that Λ is a constant value to solve the differential equation and then Λ is varied as a function of the potential y. The analytical expression given in eq. (2.45), however, reveals the changes in potential y and quasi-equilibrium potential y_f, which is obtained by integrating eq. (2.45).

Chapter III R.F. PLASMA PROBE EXPERIMENTS IN LABORATORY PLASMA

§ 1. Introduction

Various experiments of r.f. plasma probes have been carried out in laboratory plasma which has the electron density of 10^3 to 10^6 cm^{-3} and electron temperature less than about 4×10^3 °K. This tenuous plasma with low electron temperature has been made possible by the development of high vacuum techniques and a particular plasma source. The back diffusion type plasma gun is employed as the plasma source to simulate the condition in the upper atmosphere. A large plasma chamber at the Institute of Space and Aeronautical Science, University of Tokyo[272] has also been used for the present experiments.

Measurements of antenna impedance in a plasma have been made by using the gyro-plasma probe and the mutual impedance probe. The electron density is deduced from the measured upper hybrid resonance frequency. The effect of higher harmonics of the gyro-resonance on the antenna impedance is revealed. The excitation of electrostatic wave from an antenna and its propagation characteristics have been investigated. The Bernstein mode wave is identified from the observed dispersion characteristics of the wave, propagating perpendicular to the magnetic field.[251] The antenna impedance in a plasma with an inhomogeneous magnetic field is measured with the gyro-plasma probe and compared with the aforementioned theory given in section 2.4, Chapter II.

The electron density is also measured by the high frequency capacitance probe. The frequency change characteristics versus the bias potential applied to the probe show the maximum at the space potential. The dependences of frequency shift on the electron density and the applied magnetic field are presented.

The comparison of the gyro-plasma probe, the mutual impedance probe and the Langmuir probe has been carried out. Values of electron density deduced from the gyro-plasma probe are in good agreement with the results obtained by the Langmuir probe, its space potential being determined by the r.f. method developed by T. Dote.[273] The methods of correction for

electron-neutral collision and density gradient, discussed in the gyro-plasma probe system in section 2, Chapter II, have been confirmed.

A body moving in a plsma with a velocity higher than the ion thermal velocity produces a wake region behind the body itself. The wake of this kind produced by the spacecraft in an ionospheric plasma has been studied both theoretically and experimentally by many scientists[274~282,109] since 1960. The model experiment in the laboratory plasma for simulating the moving body is made by employing an ion beam with supersonic velocities. The back diffusion type plasma gun and the solar wind simulator are used for this purpose. Several implications of this wake effect to measurements by r.f. plasma probes as well as electrostatic probes are described.

§ 2. Generation of Plasma in the Space Simulation Chamber

2.1 System of Space Simulation Chamber

To simulate the space plasma, it requires rather large volume and homogeneous plasma; its dimension should be, at least, comparable with some tens or hundreds of Debye shielding length and of the characteristic wave length. The vacuum vessel with 600 mm in diameter and 1000 mm in length has been utilized as a space plasma simulation chamber. The system block diagram is illustrated in Fig. 3-1. The 6-inch oil diffusion UHV (ultra-high vacuum) pump (PUL-06) with the chevron type buffle cooled by water is used as a main vacuum pump, followed by the 2-inch oil diffusion pump (PUL-02) and the rotary-vane pump (PVD-150). The liquid nitrogen trap is equipped at the top of the main pump. The titanium getter pump (PGT-12) is equipped as a final sublimation pump. Boiled water flows through the copper pipe surrounding the vacuum vessel, and the mantle-heater and the ribbon heater shield the manifold and the vacuum gauge, for baking the equipment. These arrangements are essential to attain ultra-high vacuum. The ultimate pressure of this system is designed to be less than 3×10^{-9} torr. Figure 3-2 shows

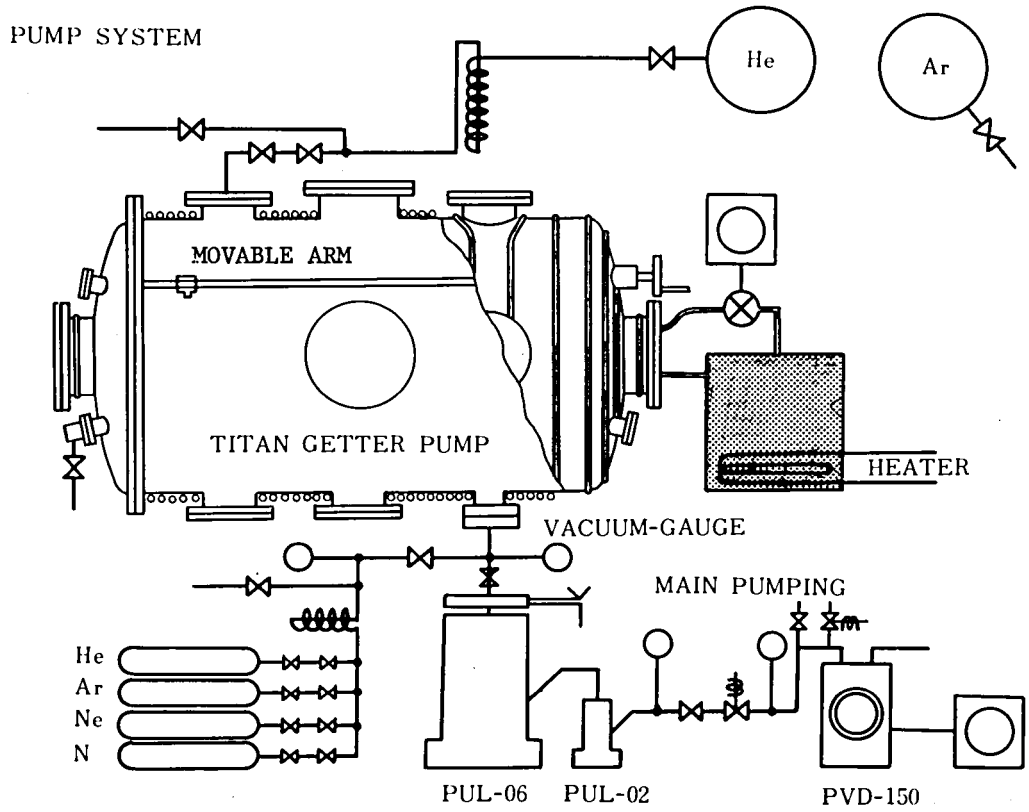

Fig. 3-1 System of space plasma simulation chamber.

the pumping sequence and the characteristic curve of pressure in the vessel.

The copper wire coil is wound round the wall of the vessel (stein-less steel) to produce a homogeneous magnetic field. The magnetic field intensity changes its value from 0.3 gauss to 9.5 gauss, linearly proportional to the applied current from 0 A to 1.0 A. The scanning arm controlled externally, is installed to fix or sweep the antenna, at any position in the vessel.

Selected pure gasses such as helium, neon, argon and nitrogen can be injected into the high vacuum vessel through the liquid nitrogen trap, except for, A_r and N, eliminating the mixture of inpurities. The

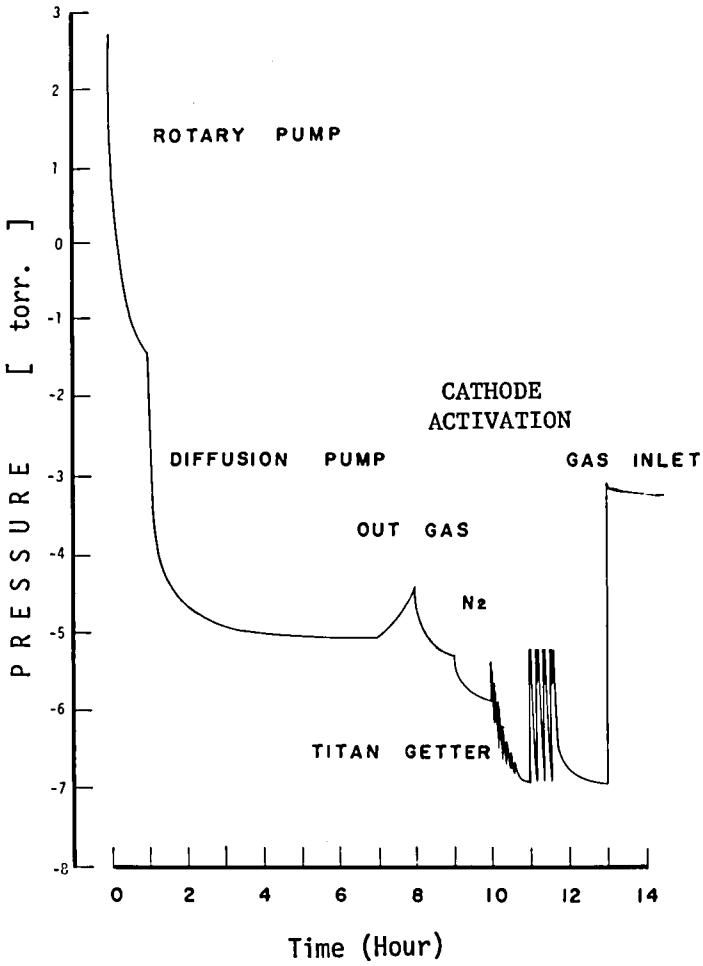

Fig. 3-2 Pressure versus vacuum pumping sequence.

gas pressure in a range from 10^{-3} torr. to 10^{-6} torr. is controlled by two ways,; (i) the pressure balance of differential pumping between pumping speed and gas flow speed which can be adjustable by the variable needle valve or the variable leakage valve, (ii) some amount of gas is to be introduced after closing the main exhaust valve. To obtain a stable plasma, the gas pressure should be maintained constant during the experiment.

The large-scale space chamber is available at the ISAS. The size of its main cylindrical vessel is 2000 mm in diameter and 3000 mm in length. A set of Helmholz-coil is equipped to apply homogeneous static magnetic field (about 0.4 gauss to 100 gauss) in the direction

parallel to the axis of the vessel. The vessel is made of non-magnetic material (stainless steel). A residual gas back pressure of 10^{-9} torr. is attained, using two 36-inch oil diffusion pumps, a titanium sublimation pump and a small sputter ion pump. The antenna can be moved by the scanning arm which can mechanically move to any desired position in the vessel.

2.2 Plasma Source and its Characteristics

Many types of plasma source are available to simulate the space plasma condition in the laboratory. Most of them are concerned to generate high density and high temperature plasmas, which are relevant to the study of controlled nuclear fusion. The space plasma in the present study is, however, concerned with rather tenuous and low electron temperature gas. The so-called back diffusion type plasma gun has been developed to simulate the plasma of the earth's ionosphere.

Figure 3-3 shows the back diffusion type plasma gun used in the space simulation plasma chamber. Hot cathodes coated BaO or tantalum metal are used as electron emitter filaments. Emitted

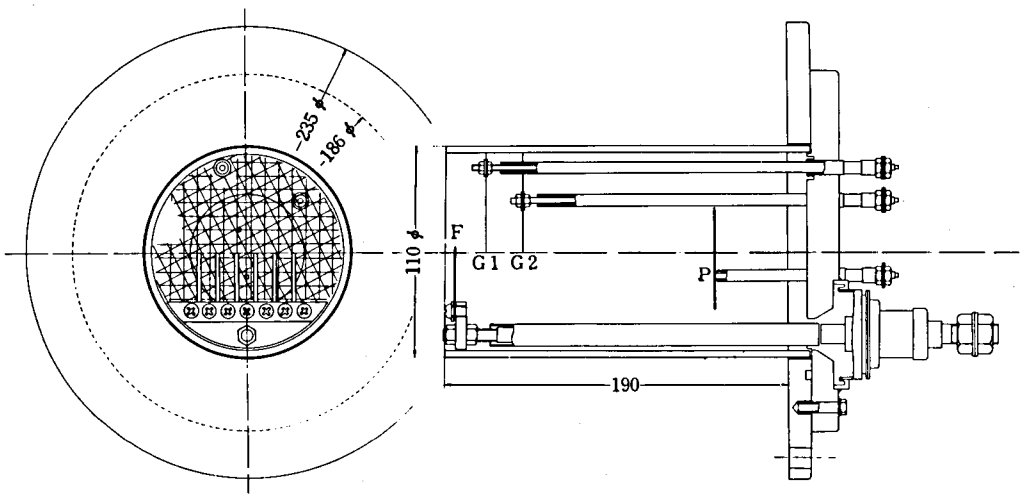

Fig. 3-3 Back diffusion type plasma gun.

electrons are accelerated by the potential difference between the grid G1 and G2, and they act to induce the gas discharge. The produced ions diffuse backward with electrons emitted from filaments, the ambipolar diffusion. The electron density can be controlled by the electron current flow to the filament, grid G1, grid G2 and plate P, and the gas pressure. The characteristic curves of electron density versus plate current with various other parameters are shown in Fig. 3-4 (a) and (b). The electron density increases monotonously with increasing plate and grid currents, until the pressure reaches a certain level. The stability and reproducibility of electron density values are excellent.

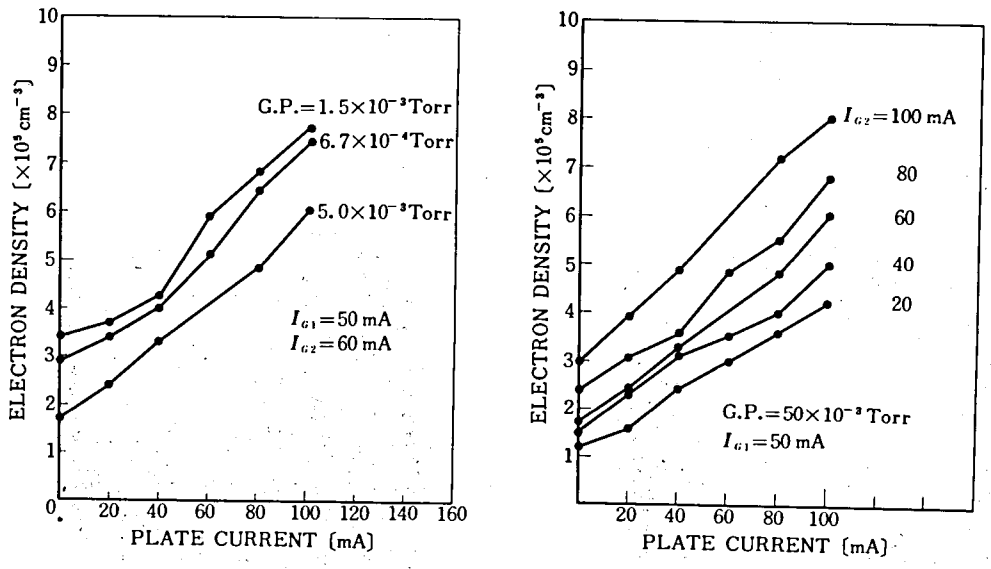

Fig. 3-4 Electron density versus plate current. Argon plasma is produced by the back diffusion type plasma gun with tantalum metal cathodes (filament current 170 A and grid G1 current 50 mA); (a) grid G2 current 60 mA and G.P. the gas pressure, and (b) gas pressure 5.0×10^{-3} torr. and I_{G2} the grid G2 current.

§ 3. Experimental Results

3.1 Gyro-plasma Probe Experiment

Layout of the present experiment, including a cylindrical antenna with 600 mm in length and 10 mm in diameter, is shown in Fig. 3-5. As noted in section 2.1, Chapter II, an antenna impedance is measured in a form of $C \cdot \exp(-j\psi)$ given in eq. (1.44). Typical examples of antenna capacitance C as a function of frequency are given in Fig. 3-6 (a) and (b). Argon plasma with gas pressure of 1.6×10^{-3} torr. is produced by the barium oxide cathode plasma gun. In the case of (a), the measured upper hybrid resonance frequency is 9.99 MHz from which electron density is deduced to be 1.22×10^{6} cm^{-3}; the gyro-resonance frequency is 1.18 MHz (the geomagnetic field intensity of 0.42 gauss). Simultaneously, electron density and temperature are measured by the

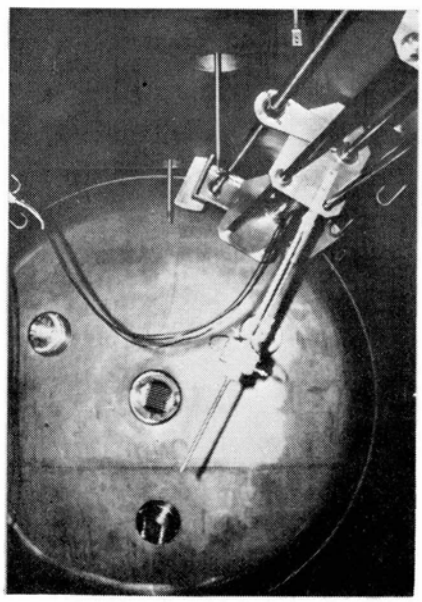

Fig. 3-5 Layout of the gyro-plasma probe experiment in the space simulation chamber.

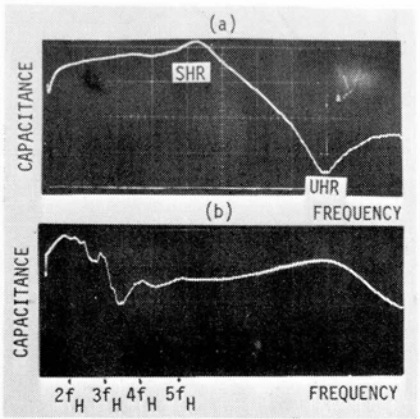

Fig. 3-6 Capacitance of an antenna in a plasma as a function of frequency; (a) $N_e = 1.22 \times 10^{6}$ cm^{-3}, and (b) $N_e = 9.29 \times 10^{4}$ cm^{-3}.

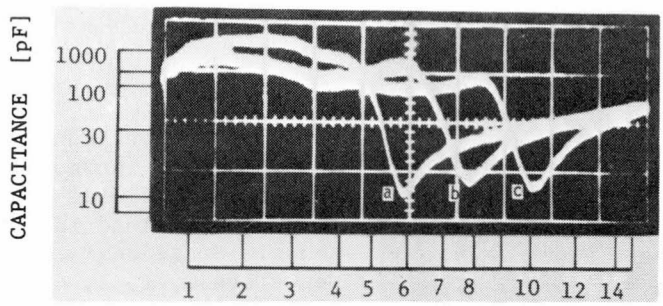

Fig. 3-7 Capacitance of antenna when the magnetic field is applied; (a) 0.42 gauss, (b) 2.1 gauss and (c) 3.1 gauss. f_{UHR} = 5.7 Hz, 7.9 MHz, and 10.3 MHz. f_{SHR} = 4.1 MHz, 5.9 MHz, and 8.7 MHz.

Langmuir probe, which yields the values of 1.18×10^6 cm^{-3} and 2400 °K. The relative error of electron density values measured by two probe methodes is $\pm$ 3.2 %. In the experiment (b), f_{UHR} = 2.98 MHz and then $N_e = 9.29 \times 10^4$ cm^{-3}. As is evident in this figure, characteristic peaks are found near 2nd, 3rd, and 4th harmonics of the gyro-resonance frequency. These resonance peaks are well-understood by the theory of a warm magnetoplasma discussed in section 2.5, Chapter III.

When a homogeneous magnetic field is added, both upper hybrid resonance and gyro-resonance frequencies increase. Figure 3-7 shows the changes of resonance frequencies for three different applied magnetic field intensities. The upper hybrid resonance frequency changes according to the relation as $f_{UHR} = \sqrt{f_H^2 + f_p^2}$. The calculated f_p for three cases, 5.58 MHz, 5.26 MHz, and 5.53 MHz, agree with each other within $\pm$ 5 %. When the magnetic field intensity is large, 3.1 gauss in the case (c), the sheath resonance frequency is found to be very close to the gyro-resonance frequency. This fact indicates that the contribution of sheath capacitance to the total admittance of an antenna becomes negligible when the strong magnetic field is applied, i.e., $\Pi_e^2 << \Omega_e^2$, as discussed in section 2.4, Chapter II.

Inhomogeneous magnetic field can be superposed by a small rectangular coil (250 mm × 300 mm) set near the antenna tip. The intensity changes inversely proportional to the distance along the antenna axis. The homogeneous static magnetic field (3.45 gauss; f_H = 9.67 MHz) is applied by the helmholtz coil in the nitrogen plasma ($N_e = 8.65 \times 10^5 cm^{-3}$),

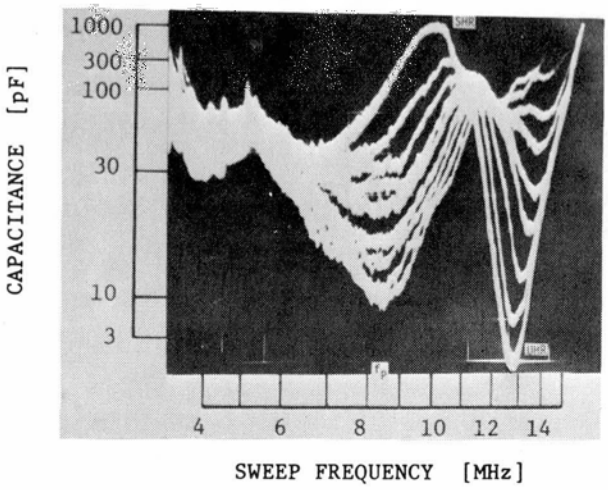

Fig. 3-8 Capacitance of antenna in an inhomogeneous magnetic field. Uniform static field is 3.45 gauss. Small coil currents are 0, 1, 3, 6, 8, 12, 16, 22, and 25 A.

and the small coil current is varied from 0 A to 25 A. The results are shown in Fig. 3-8. As the coil current increases, the capacitance gradually increases near f_{UHR} and decreases near f_{SHR}. Both f_{SHR} and f_{UHR} are shifted to higher frequency when the applied magnetic field increases. The capacitance in lower frequency part shows dents and the minimum appears near the plasma resonance frequency. The results accord with the theory of an antenna in an inhomogeneous plasma given in section 2.4, Chapter II.

3.2 Mutual Impedance Probe Experiment

A rocket-borne mutual impedance probe with two whip antennas was tested in the laboratory plasma. The distance between two antennas is kept constant in the first experiment. To study the effect of electrostatic wave excitation upon the measurement of the mutual impedance, the movable receiving antenna is used to measure the dispersion characteristics of wave.

The instrument is set in the center portion of the chamber filled with argon plasma with electron density of about 1.5×10^5 cm^{-3}, and gas pressure 2.7×10^{-5} torr. The received signal intensity as a

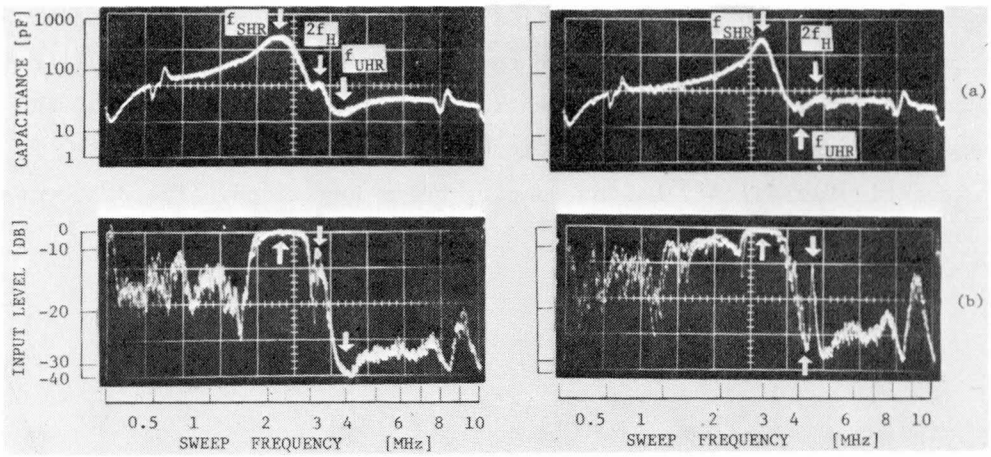

Fig. 3-9 Self impedance measurement by gyro-plasma probe (a), and the received signal intensity (0 dB = 0.1 V_{rms}) obtained by mutual impedance probe (b). Left side; $N_e = 1.4 \times 10^5$ cm^{-3}, $f_{UHR} = 3.70$ MHz, and $f_H = 1.55$ MHz. Right side; $N_e = 1.5 \times 10^5$ cm^{-3}, $f_{UHR} = 4.30$ MHz, and $f_H = 2.22$ MHz.

function of frequency is compared with the capacitance of antenna measured by the gyro-plasma probe, as shown in Fig. 3-9. The resonances corresponding to f_{SHR}, f_{UHR} and $2f_H$ are identified in the received signal intensity, especially a marked change at the 2nd harmonic gyro-resonance frequency.

In the second experiment, a disk mesh sensor with 195 mm in diameter is used as a transmitter, the swept frequency signal being applied through a coaxial cable terminated to the ground by the low impedance of 50 Ω. The disk plate with 100 mm in diameter is used as a receiving antenna, which is movable approximately perpendicular to the applied magnetic field. Two methods are used to detect the electrostatic mode wave propagating in a plasma; one is square-law or linear amplitude detection system (ASD). The input potential to the receiver is considered to take the form as

$$e_{IN} = A_a(r)\sin(\omega t+\phi_1)+B_a\cdot\exp(-k_i r)\sin(\omega t+k_r\cdot r+\phi_2) \qquad (3.1)$$

where $k = k_r + jk_i$ is a wave number vector, r the distance from the

transmitter, ϕ_1 and ϕ_2 the initial phase shifts, and $A_a(r)$ and B_a the amplitudes. The first term of the right hand side of eq. (3.1) represents a directly coupled potential between two antennas and the second term stands for electrostatic wave propagating perpendicular to the magnetic field line, Landau damping being neglected. The d.c. output of square-law detector is ($B_a^* = B_a \cdot \exp(-k_i \cdot r)$)

$$e_{OUT} \propto \frac{1}{2\pi} \int_0^{2\pi} e_{IN}^2 \, d\omega$$

$$= \frac{1}{2}(A_a^2(r)+B_a^{*2})+A_a(r)B_a^* \cos(k_r \cdot r+\phi_2-\phi_1). \qquad (3.2)$$

The PSD system has a ring modulator to multiply the input signal by the same frequency signal with a selected phase of $\phi_3 = \phi_1 + \pi/2$ and a constant amplitude C_a,

$$e_{OUT} \propto \frac{1}{2\pi} \int_0^{2\pi} e_{IN} \cdot C_a \cdot \sin(\omega t+\phi_3) d\omega$$

$$= \frac{1}{2} B_a^* C_a \cos(k_r \cdot r+\phi_2-\phi_3). \qquad (3.3)$$

Figure 3-10 shows the outputs of the electrostatic mode wave obtained by ASD and PSD methods. From this record, the wave length is deduced to be approximately the same values of 13.67 cm (ASD) and 13.92 cm (PSD), and $k_i \simeq 0$.

When the antenna position is fixed and the frequency is swept, the output of received signal intensity shows the plasma resonance phenomena.

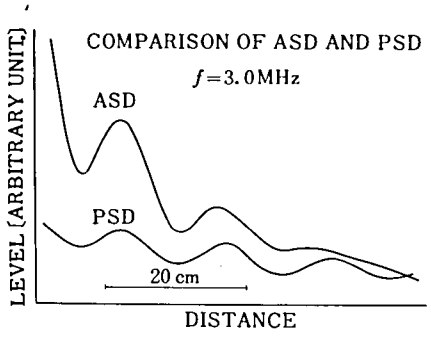

Fig. 3-10 Electrostatic wave forms measured by ASD and PSD methods. Argon plasma; gas pressure is 1.8×10^{-4} torr., $N_e = 3.0\sim3.1 \times 10^5$ cm^{-3}, $T_e = 928$ °K, and $B_0 = 0.7$ gauss. $f = \omega/2\pi = 3.0$ MHz.

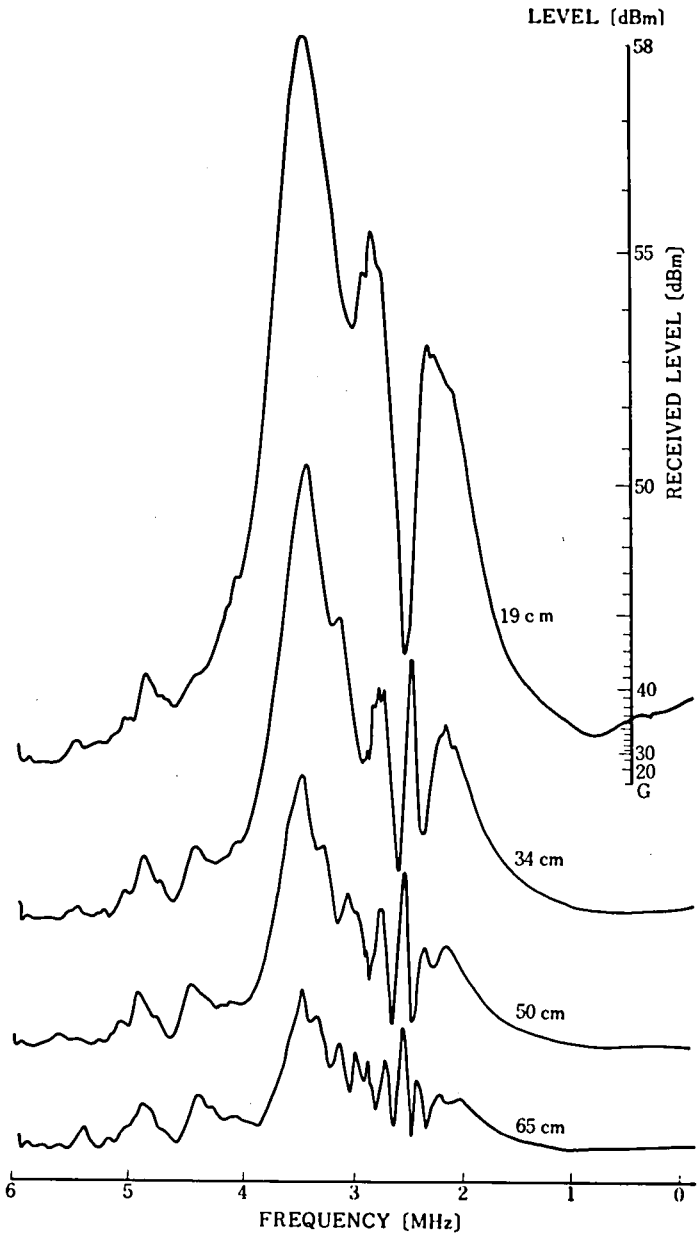

Fig. 3-11 (a) Received signal intensity as a function of frequency: f_H = 1.96 MHz, f_p = 4.92 ~ 5.03 MHz, f_{UHR} = 5.30 ~ 5.40 MHz, f_ν = 27 kHz, r = 1.43 cm and λ_D = 0.4 cm.

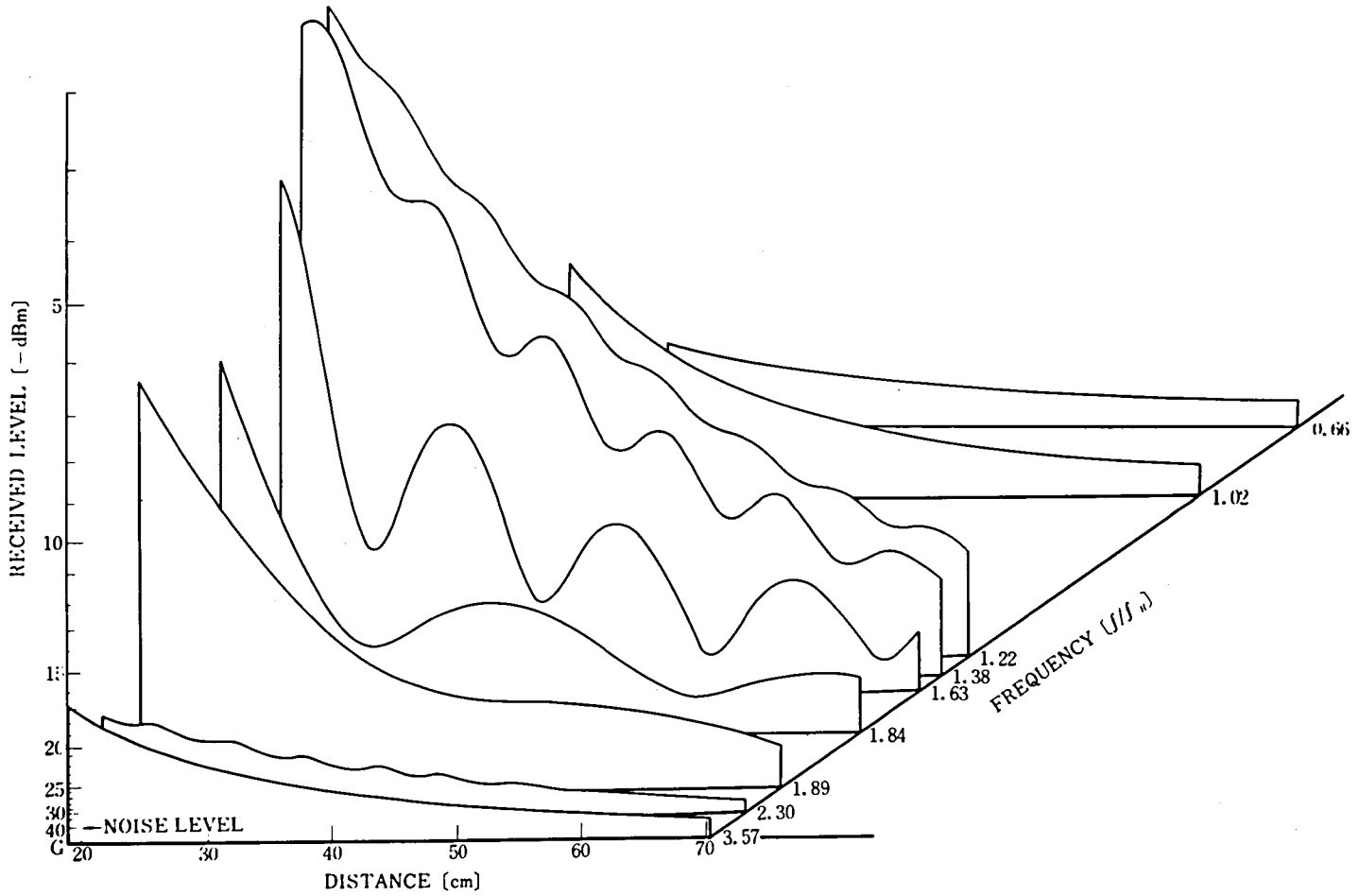

Fig. 3-11 (b) Received signal intensity as a function of distance.

Figure 3-11 (a) shows some examples of data obtained by ASD method, the distance between two antennas being fixed to be 19 cm, 34 cm, 50 cm, and 65 cm. Besides the decrease of the received signal intensity, a complex interference pattern appears, which changes with the distance. The results of received signal intensity measured as a function of distance are summarized in Fig. 3-11 (b). The effect of an electrostatic wave propagation is recognized above the electron gyro-resonance frequency, with large amplitude oscillations in the frequency region, $1 < f/f_H < 2$. The intersect spectrum of this figure (b) at a fixed position gives the same spectrum as figure (a). That is, the received signal intensity, measured by the mutual impedance probe, is affected by the phase mixing of the electrostatic mode wave. The dispersion relation (frequency versus wave number) is illustrated in Fig. 3-12. This $\omega - k$ diagram indicates that the electrostatic wave excited by a transmitter is the Bernstein mode wave propergating perpendicular to the magnetic field. The dispersion relation of the Bernstein mode wave for various

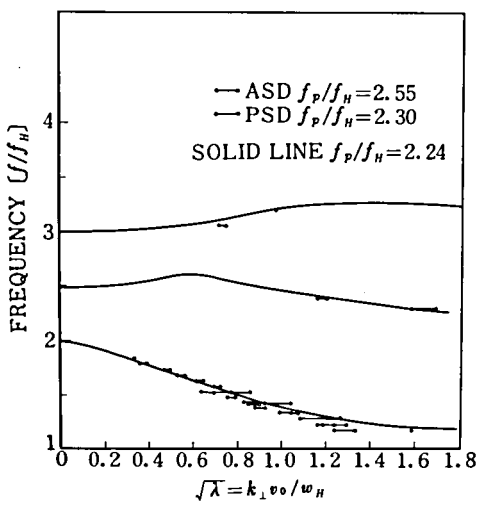

Fig. 3-12 Dispersion characteristics. Solid line is a dispertion curve of electrostatic Bernstein mode wave for $f_p/f_H = 2.24$.

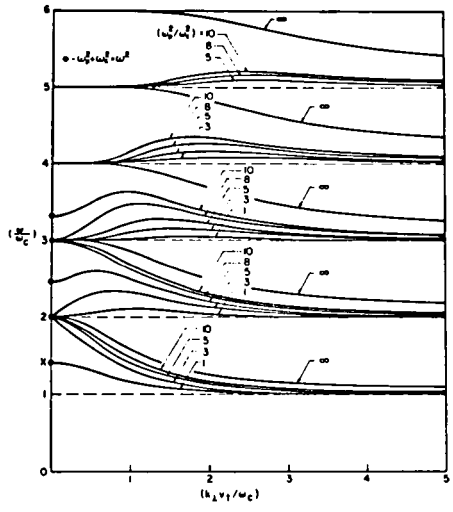

Fig. 3-13 Dispersion relation of the Bernstein mode wave. (after F. W. Crawford et al.[283])

parameters $(\Pi_e/\Omega_e)^2$ is illustrated in Fig. 3-13 (after F. W. Crawford, et al.[283]). This gives an experimental evidence for the theory of mutual impedance of an antennas in a warm magnetoplasma, discussed in section 3.2, Chapter II (see Fig. 2-17).

3. 3 High Frequency Capacitance Probe Experiment

Basic experimental study of a high frequency capacitance probe has been made to develop the rocket-borne instrument. As noted in section 4, Chapter II, the frequency shift of oscillation is a function of permittivity of a plasma between two electrodes, which includes the effect of an ion sheath surrounding the probe. The thickness of an ion sheath can be controlled by d.c. potential applied to electrodes. The parallel mesh plates with 80 mm in diameter and spacing of 34 mm was used as a sensor. Figure 3-14 shows the bias potential dependence of the oscillation frequency for different electron densities as a parameter. The potential at the maximum frequency shift is found to be the space potential, above which the frequency decreases again due to the electron sheath. The oscillator ceases to oscillate for very high electron density. As the conductance g increases, the condition of oscillation stability given in eq. (2.22) becomes to be unstable. The change in oscillation frequency at the floating potential with respect to electron density

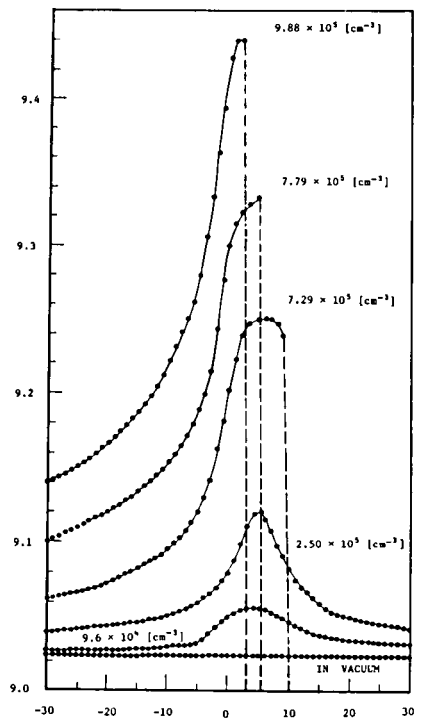

Fig. 3-14 Frequency shift of capacitance probe versus applied bias potential.

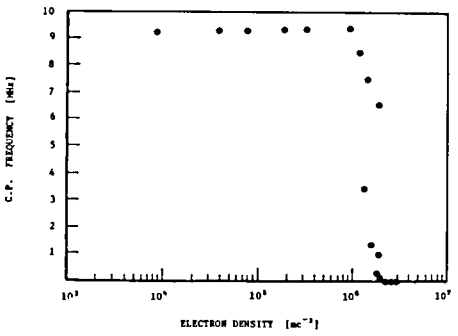

Fig. 3-15 Frequency shift of capacitance probe versus electron density.

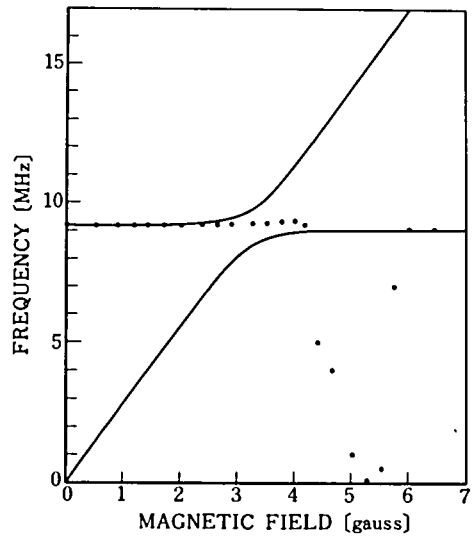

Fig. 3-16 Frequency shift of capacitance probe versus applied magnetic field. Argon plasma; $N_e=4.53\times10^5 cm^{-3}$, $f_p=6.04$ MHz, $f_0=9.08$ MHz.

is shown in Fig. 3-15. The gyro-resonance frequency (f_H = 1.29 MHz) is negligible compared with the oscillator frequency in free space (f_0 = 9.08 MHz in this experiment).

The permittivity of a plasma approaches unity when a strong magnetic field is applied parallel to the plate surface i.e., $\Omega_e >> \Pi_e$ and ω. If a collision frequency is neglected, the oscillator frequency of LC tank circuit is given as

$$\omega^2 = \frac{1}{2}\{(\omega_0^2 + \Pi_e^2 + \Omega_e^2) \pm \sqrt{(\omega_0^2 + \Pi_e^2 + \Omega_e^2)^2 - 4\Omega_e^2}\} \qquad (3.4)$$

where $\omega_0^2 = 1/LC_0$ and $C = C_0\varepsilon_0\varepsilon_{xx}$. Figure 3-16 shows the oscillation frequency as a function of magnetic field intensity. The electron density of an argon plasma is 4.53×10^5 cm^{-3} (f_p = 6.04 MHz). Solid line indicates the theoretically calculated frequency, and the values obtained by the experiment are given by dots. The measured values deviate from the upper branch of solid lines near the crossing

point of $\omega_0 = \Omega_e$ and the oscillation becomes unstable. In the region where $\Omega_e >> \omega$ and Π_e, the oscillation is, again, stable and the frequency coincides with the lower branch of solid lines. The mechanism of this transition has not been clearly understood, but if the frequency ω deviates far from that of free space ω_0, the quality factor of LC tank circuit is very low and the oscillation becomes to be unstable.

The most essential problem concerning the high frequency capacitance probe is how to eliminate the effect of the ion or electron sheath. Stability of the oscillating frequency is also important for the accuracy of electron density measurement.

3.4 Comparison of Electron Density Measurement with R.F. and D.C. Probes in Laboratory Plasma

Measurements of electron density with three different kinds of probes, i.e., Langmuir probe, gyro-plasma probe, and two-wire probe, were made to compare with each other. The argon and helium gases are used, which are generated by back diffusion type plasma guns with BaO cathodes. The gas pressure is controlled in the range from 1.3×10^{-5} to 4.7×10^{-2} torr., electron density from 2×10^{4} cm^{-3} to 1.7×10^{6} cm^{-3} and temperature from 500 °K to 1500 °K.

The Langmuir probe measures electron and ion currents collected by the spherical probe with 50 mm in diameter, the applied potential being supplied from a triangular voltage generator. The space potential of plasma can be determined by the electron saturation current at intersecting point of two Langmuir curves representing the electron saturation region and the retarding potential region. Another method to determine the space potential is the r.f. method which measures r.f. current response of the probe. The detected signal indicates a maximum intensity at the space potential. The electron saturation current I_{e0} at the space potential can be, thus, determined. Unless the particle distribution function in a plasma is Maxwellian, there are some differences in values of space potential determined by two methods. The r.f.

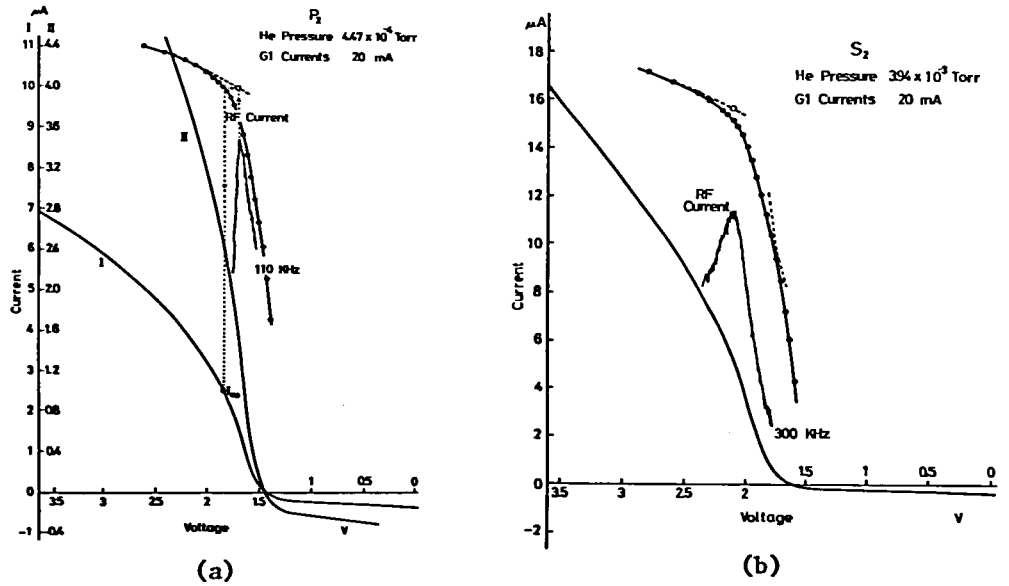

Fig. 3-17 Langmuir curve for (a) Maxwellian and (b) non Maxwellian distributions. Upper trace is the semi-logarithmic plots in arbitrary unit (after T. Dote).

method is more reliable technique than the other, because of the deformation of the Langmuir curve due to non-Maxwellian distribution. Figure 3-17 shows typical examples of the Langmuir curve corresponding to the case of Maxwellian distribution (a) and non-Maxwellian distribution (b), together with the r.f. current response intensities. The measured electron density, when the gas pressure is rather high, must be corrected, taking the shielding effect into account, i.e., multiplying the measured values by the factor $\{1 + R_p(1 + \lambda_e/R_p)/\lambda_e)\}$, where R_p is a probe radius and λ_e the mean free path of electrons.

The gyro-plasma probe with a cylindrical antenna (L = 300 mm, r_a = 10 mm) was used to measure the electron density; a swept frequency range is from 0.8 MHz to 10 MHz, a period 0.3 sec, and an amplitude of r.f. potential applied to the antenna 0.1 V_{rms}. The collisional effect must be taken into account for the resonance frequency shift in a plasma when the electron neutral collision frequency is high. The collision frequency is calculated as a ratio of thermal mean velocity to the mean

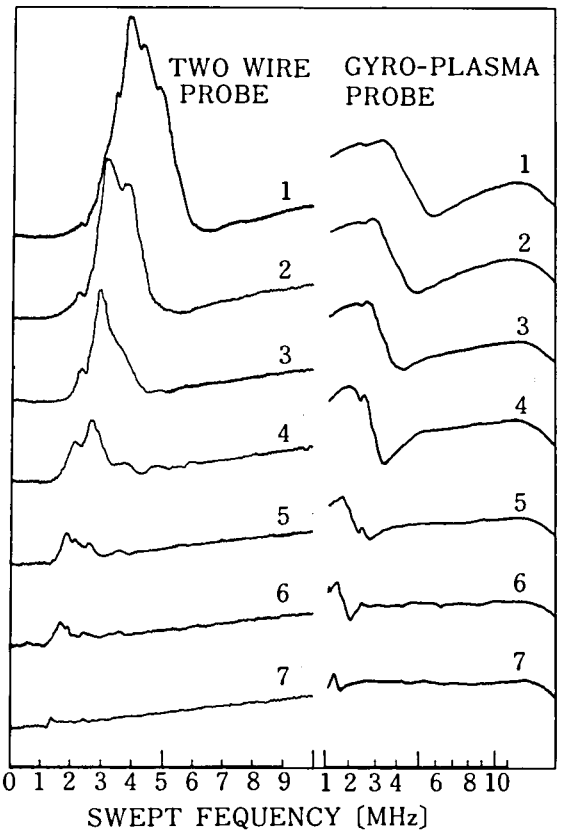

Fig. 3-18 Raw data obtained with the two-wire probe (after H. Mori) and the gyro-plasma probe.

free path which is deduced from the collisional cross section of the particle.[284]

The two-wire probe consists of two parallel wires with 300 mm in length and 2 mm in diameter, and the spacing of two wires is 70 mm. The frequency is swept from 0 to 10 MHz and the signal supplied to the transmitting wire through a coaxial cable with a characteristic impedance of 75 Ω. The electron density is deduced from the frequency at main dip (minimum) of the received signal intensity, assuming that this is the upper hybrid resonance.

Figure 3-18 shows the data obtained by the gyro-plasma probe and the two wire probe. The electron density decreases in numerical order indicated on the curves. The data of the two-wire probe show rather complex intensity spectrum, which are corresponding to the large wave number k discussed in section 3.2, Chapter II (see Fig. 2-17).

The results of electron densities obtained by three probe methods are summarized in Fig. 3-19, 20, and 21. The letters indicated on the data points represent the different plasma conditions; B, C, D, J, K, L, N, and O for argon plasmas, and F, H, P, Q, R, S, T, and U for helium plasmas. The comparison of the gyro-plasma probe and the Langmuir

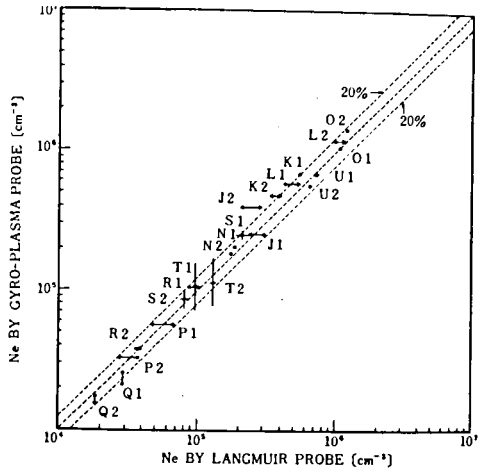

Fig. 3-19 Comparison of electron densities measured by the gyro-plasma probe and the Langmuir probe.

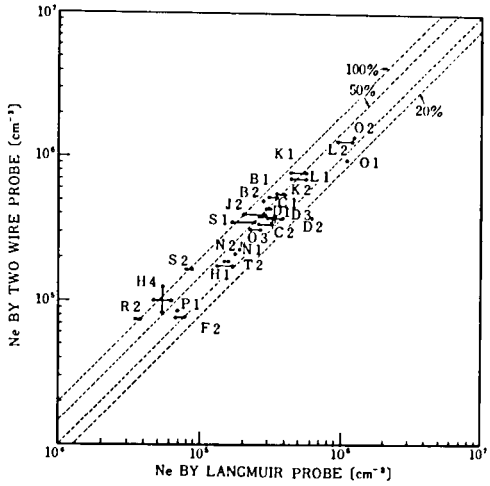

Fig. 3-20 Comparison of electron densities measured by the two-wire probe and the Langmuir probe.

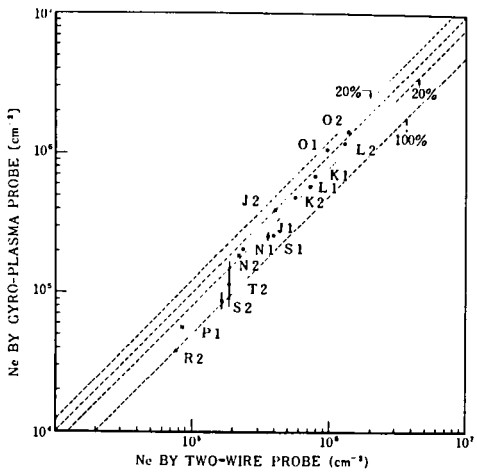

Fig. 3-21 Comparison of electron densities measured by the two-wire probe and the gyro-plasma probe.

probe is shown in Fig. 3-19. A good agreements within a relative error of ± 20 % is obtained in the electron density range from 10^4 cm^{-3} to 10^6 cm^{-3}. Though the physical principles of these two methods are different, i.e., r.f. response of a plasma and collection of charged particle in a plasma, the coincidence between these two methods is remarkable. The comparisons of the two-wire probe and other two probe methods are shown in Fig. 3-20 and 21. The systematic deviation of the measured values is found; the two wire probe gives the higher electron density value than the other methods, especially in low electron density plasmas. This is caused either by the mis-identification of resonances and/or frequency shifts from the principal resonance frequencies, f_{UHR} and nf_H.

3.5 Wake Structure behind a Body in Plasma Stream

A back diffusion type plasma gun (BaO cathode; filament current of 66 A and voltage of 4V) which produces proton or argon plasma with high speed ion streams[285] was used to simulate a moving body with super sonic velocity in a plasma. The solar wind simulator[286] produces a proton stream by r.f. discharge and subsequent select of H^+ ions through the Benett-type mass spectrometer. This apparatus was also employed for the purpose of this experiment. A disk plate obstacle with 190 mm in diameter was set in front of the plasma source to obstruct the ion stream. The ion beam flux intensity ($N_i v_i$ particles/cm^2·sec) behind the obstacle was measured with a Faraday cage collector with 40 mm in diameter which excludes electrons by negative potentials applied to four grids. Only the ion current collected by the plate is amplified by 10^8 (160 dB) with an operational amplifier. In the present experiment, the output potential of 0.2 volts corresponds to the flux of 1×10^9 particles/cm^2·sec.

Experiment with Back Diffusion Type Plasma Gun Figure 3-22 shows the distributions of ion flux intensity at different particle velocities. V_p is an accelerating voltage applied between the filament and the grid. z shows the distance of a measuring point from the obstacle. As the ion

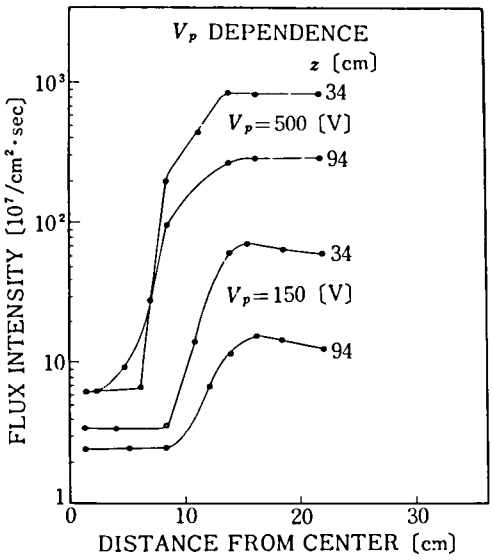

Fig. 3-22 V_p dependence of wake structure behind the disk obstacle. Proton gas pressure = 1×10^{-6} torr.

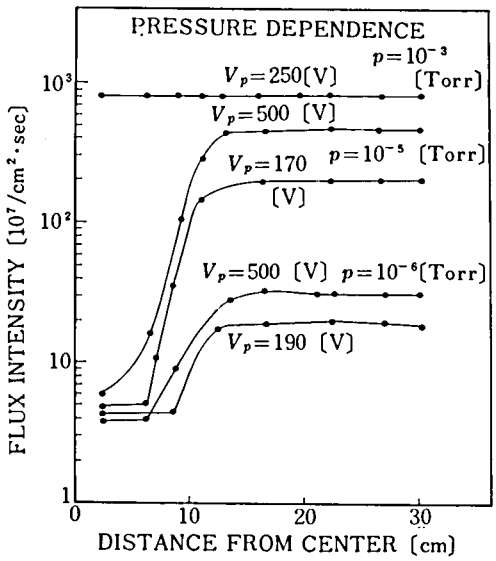

Fig. 3-23 Pressure dependence of wake structure. Argon plasma is used and z = 64 cm.

beam velocity increases with increasing V_p, the ion flux increases and the wake region becomes narrow. The pressure dependence of the distribution is shown in Fig. 3-23. The distance of the measuring point behind the obstacle is 64 cm. The plasma condition changes as the gas pressure varies. In the case of $P = 10^{-3}$ torr., the flat distribution is observed and the wake region behind the obstacle disappears. As the argon plasma is used in this experiment, the ion flux intensity corresponding to the same accelerating voltage is much less than the case of a proton plasma (see Fig. 3-22).

Experiment with Solar Wind Simulator The velocity of proton streams can be determined by the amplitude of applied acceleration voltage V_E. Figure 3-24 shows V_E dependence of wake structure behind the obstacle. The wake boundary can clearly be identified by the enhancement of ion flux intensity from which the angle of Mach cone are calculated to be 7.6°, 5.7°, and 3.8° corresponding to the acceleration voltage of 1 kV, 3 kV, and 6 kV, respectively. The ion density produced by this plasma

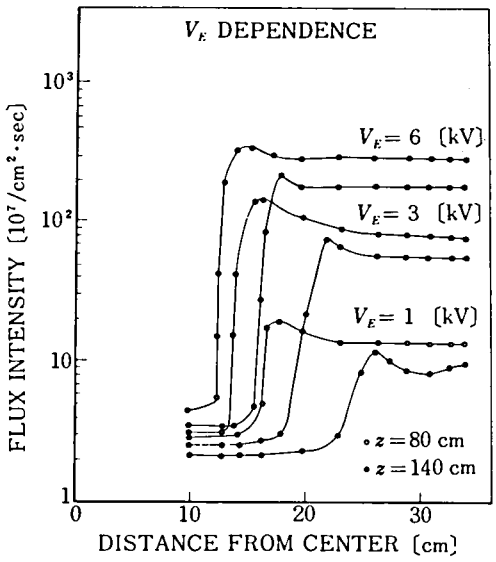

Fig. 3-24 V_E dependence of wake structure. Proton gas pressure = 1×10^{-6} torr. and discharge r.f. high tension R_F = 1.5 kV.

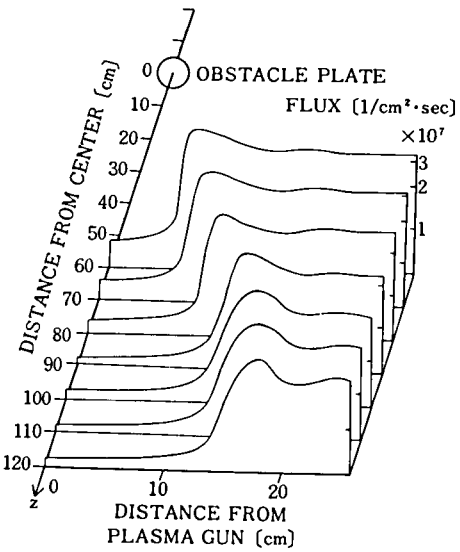

Fig. 3-25 Wake structure behind the obstacle. V_E = 1 kV, R_F = 1.5 kV, and P = 1 × 10^{-6} torr.

source depends on the acceleration voltage, because the flux intensity ratio of V_{E1} and V_{E2} is not proportional to V_{E1}/V_{E2}. The wake boundary obtained in this experiment shows more distinct edge effect than in Fig. 3-22. The reason may be that the electron temperature produced by r.f. discharge is much higher than that produced by back diffusion type plasma guns. Figure 3-25 shows the fine wake structure under the condition; V_E = 1 kV, R_F (discharge r.f. high tension) = 1.5 kV, and P (pressure) = 1 × 10^{-6} torr. The wake boundary shows the Mach cone angle of about 5.7° which suggests the electron temperature of the order of 5 × 10^4 °K, assuming the Mach number is simply defined as a ratio of ion bulk velocity, $\sqrt{2qV_E/M}$, to the ion sound velocity, $\sqrt{\kappa T_e/M}$. In the outside region of wake, the flux intensity shows wavy structure, propagating to the z direction. Although physical mechanism of this effect has not been explain theoretically, it is very likely that some wave excitation may occur near the boundary of the wake region.

Chapter IV ROCKET OBSERVATIONS OF THE IONOSPHERE WITH R.F. PLASMA PROBES

§ 1. Introduction

A number of experiments of r.f. plasma probes have been carried out since 1966, using Japanese sounding rockets such as S 210, Kappa 8, Kappa 9M and Lambda 3H. The r.f. plasma probes such as gyro-plasma probe, mutual impedance probe, high frequency capacitance probe have been used to study the various plasma resonances in the ionosphere in order to obtain the electron density and temperature profiles in the altitude range from about 70 to 2000 km and also the ion composition in the topside ionosphere.[27,31,106,287~289] The rocket launching station is the Kagoshima Space Center (KSC), Institute of Space and Aeronautical Science, University of Tokyo. The location of launching site is the geographical coordinates of 131°04'45" east and 31°15'00" north, the geomagnetic coordinates of 198.4° east and 20.0° north, and the height above the sea level is 276 m. Series of experiments which were performed up to now, are listed in Table 4-1, in which the instruments denoted by asterisks were taken in charge of other experimenters.

The observed data transmitted from the rocket to the ground station through the FM/FM telemetry system are analysed with the precise rocket trajectory to fix the time-space of each datum point. The position of the rocket is measured by the radar-transponder equipment installed onboard the vehicle and the ground-based radar equipment. In section 2, the method to determine the rocket trajectory is explained. The geomagnetic field is computed using the geomagnetic reference field.[290]

Using the gyro-frequency determined by the calculated geomagnetic field intensity, the ionospheric electron density is deduced from the upper hybrid resonance frequency within an accuracy of ± 1 %. The high frequency capacitance probe and the Langmuir probe also give the electron density values. The results of all the measured electron density profiles in the ionosphere are presented in section 3. The electron temperature is also deduced from the probe admittance level at lower

Table 4-1 List of sounding rocket experiments.

No.	Rockets	Date	Launching Time (JST)	Altitude Range(km)	Remarks
1.	L-3H-2	July 23, 1966	15:35	220-1800	GP***
2.	K-8-15	Jan 9, 1969	16:40	90-190	GP
3.	L-3H-6	Jan 21, 1970	11:10	350-1850	GP,MIP
4.	L-3H-5	Sept 19, 1970	20:30	300-2050	GP,MIP
5.	K-9M-32	Sept 27, 1970	15:42	—	GP (Failure)
6.	S-210-5	Sept 28, 1970	10:20	—	CP (Failure)
7.	K-9M-35	Jan 23, 1971	20:20	180-340	GP,VLF**
8.	S-210-6	Jan 21, 1972	11:24	70-110	GP, LP, CP
9.	K-9M-38	Jan 22, 1972	15:00	95-360	GP,TWP*,VLF**,LP*
10.	S-210-8	Jan 16, 1973	08:40	70-120	CP, LP
11.	K-9M-41	Jan 19, 1973	18:00	95-330	GP

Abbreviation: GP = Gyro-plasma Probe, MIP = Mutual Impedance Probe, CP = Capacitance Probe, LP = Langmuir Probe, TWP = Two-Wire Probe, and VLF = VLF doppler method. Experimenters: *H. Mori, **I. Kimura, and ***H. Oya. JST is the 135°E meridian time.

frequency.[108] Assuming a diffusive equilibrium distribution of electrons in the topside ionosphere,[208] the ion composition is calculated using the measured electron density and temperature profiles.[287] All these profiles are also given in section 3.

In section 4, various plasma resonances observed by the gyro-plasma probe and the mutual impedance probe are described. The upper hybrid resonance is detected unambiguously by the antenna impedance measurement, and this procedure is well-understood theoretically. The sheath resonance is rather complex, coupled with the gyro-resonance and its harmonics. An effort is made to explain its nature by the theory of a warm magnetoplasma, as discussed in section 3.3, Chapter I and section 2.5, Chapter II. Using Balmain's formula[225] for a short cylindrical antenna given in eq. (1.46), H. Oya[291] predicted a new kind of plasma resonance, viz., a modified plasma resonance, near the upper hybrid resonance. The experimental data obtained by Lambda 3H-2 sounding rocket demonstrate distinctly two parallel resonances, that is, the upper hybrid resonance and the modified plasma resonance. It is shown that the angle θ (θ; the angle of antenna axis relative to the geomagnetic field) dependence of this

resonance frequency can be predicted theoretically. The modified plasma resonance was discovered by this analysis.[106] Both amplitude and phase of the antenna admittance changes its values appreciably near the harmonics of electron gyro-frequency. This admittance change was recognized by Kappa 8-15 sounding rocket experiment,[27] and confirmed by successive rocket experiments and also by laboratory plasma experiments as described in section 3.1, Chapter III.

The comparisons of electron density measurements with gyro-plasma probe, VLF doppler method, two-wire probe, and Langmuir probe have been made using Kappa 9M-35 and 38 sounding rockets. In the experiment of Kappa 9M-35, the electron densities obtained by the gyro-plasma probe and the VLF doppler method are in good agreement with each other. But, some systematic discrepancies in measured electron densities were found between the VLF doppler method and other probe methods in the experiment of Kappa 9M-38. These experiments brought some problems on the sheath formation around a rocket and its potential change due to an applied r.f. high tension (see section 5.3, Chapter II). It also gives attention to the behavior of the antenna impedance in an inhomogeneous plasma, viz., the case that a part of an antenna is immersed in a sheath region surrounding a rocket body, as described in section 2.4, Chapter II. The high frequency capacitance probe, the Langmuir probe, and the gyro-plasma probe have been, also, compared with each other using S 210-6 and 8 sounding rockets. The results of these comparisons of various plasma probes are presented in section 5.

§ 2. Data Processing System

2.1 Determination of Rocket Trajectory

The position of the rocket $\vec{x}_i$ (x_i, y_i, z_i) corresponding to the time t_i is measured by the tracking radar equipment. Provided that this measured data are exactly equal to the true positions of the rocket, there are two methods commonly used to determine the position $\vec{x}$ at

time t ($t_i \leq t \leq t_{i+1}$); (i) linear interpolation or extrapolation method using two vector points $\vec{x}_i$ and $\vec{x}_{i+1}$, and (ii) parobolic approximation using three vector points $\vec{x}_i$, $\vec{x}_{i+2}$ and $\vec{x}_{i+2}$. The former is equivalent to assume the constant vehicle's velocity between t_i and t_{i+1}, and the latter is equivalent to assuming the constant gravitational acceleration of the earth between t_i and t_{i+2}.

The motion of rocket after burn-out in the very tenuous atmosphere is well represented by the Kepler's law. The equation of motion in the polar coordinate system in the vehicle's orbital plane (r, Φ), is

$$\frac{d^2r}{dt^2} - r\left(\frac{d\Phi}{dt}\right)^2 = -\frac{\mu_E}{r^2} \tag{4.1}$$

and

$$\frac{d}{dt}\left(r^2\frac{d\Phi}{dt}\right) = 0 \tag{4.2}$$

where $\mu_E = 398{,}603 \times 10^9\ m^3/sec^2$ is a gravitational constant of the earth. By integrating eq. (4.1) and (4.2), dr/dt is obtained as

$$\frac{dr}{dt} = \pm\frac{1}{r}[-2E_T\{(r - a_v(1-e_v))(a_v(1+e_v) - r)\}]^{1/2} \tag{4.3}$$

where

$$a_v = -\mu_E/2E_T,$$
$$e_v = (1 + 2h_E^2E_T/\mu_E^2)^{1/2},$$

and E_T and h_E are integral constants for eqs. (4.1) and (4.2), respectively. Equation (4.3) represents the elliptic trajectory of the vehicle with the semimajor axis a_v and eccentricity e_v. Using an eccentric anomaly E as a parameter by solving eq. (4.3), the distance from the center of the earth r and the time T ($T = 0$ at $E = 0$) are given by the following well-known formulas,

$$r = a_v\ (1 - e_v \cdot \cos E), \tag{4.4}$$

and

$$T = \frac{a_v}{\sqrt{-2E_T}}\ (E - e_v \cdot \sin E). \tag{4.5}$$

Since the measured positions are given in the geodetic coordinates,

the transformation of coordinate system from geodetic to geocentric coordinates and vice versa must be introduced. This procedure is also necessary for the analysis of the satellite orbit, and they are described in section 4, Chapter V.

After transformation to the geocentric coordinate systems, the angle, i_i, of the vehicle's orbital plane relative to the meridian plane at KSC is deduced using the spherical trigonometry as

$$i_i = \sin^{-1} (\sin \Delta\Lambda^* / \sin \Delta\Phi), \tag{4.6}$$

and

$$\Delta\Phi = \cos^{-1}\{\sin\psi_0 \cdot \sin(\psi_0+\Delta\psi) \cdot \cos\Delta\lambda + \cos\psi_0 \cdot \cos(\psi_0+\Delta\psi_0)\}, \tag{4.7}$$

$$\Delta\Lambda^* = \cos^{-1}\{1 + \sin^2(\psi_0+\Delta\psi) \cdot (\cos\Delta\lambda - 1)\}, \tag{4.8}$$

where ψ_0 is the geocentric colatitude of KSC from the north pole, $\Delta\psi$ the angle difference of colatitude between the measured position and KSC, and $\Delta\lambda$ that of east longitudes, taking account of the earth's rotation speed (4.3752695×10^{-3} radians/min). The angle i_0 is determined by averaging all the calculated values i_i corresponding to the measured positions. The inverse transformation from (i_0, $\Delta\Phi$) to ($\Delta\psi$, $\Delta\lambda$) is given as

$$\Delta\psi = \tan^{-1} (\tan \Delta\Phi \cdot \cos i_0), \tag{4.9}$$

and

$$\Delta\lambda = \cos^{-1}\left[1 + \frac{\cos\{\sin^{-1}(\sin \Delta\Phi \cdot \sin i_0)\} - 1}{\sin^2(\psi_0 + \Delta\psi)}\right]. \tag{4.10}$$

Similar calculations are performed about the integral constants h_E and E_T, that is,

$$h_E = \frac{1}{N} \sum_{i=1}^{N} \left(\frac{r_i + r_{i-1}}{2}\right)^2 \cdot \frac{\Delta\Phi_i - \Delta\Phi_{i-1}}{t_i - t_{i-1}} \tag{4.11}$$

and

$$E_T = \frac{1}{N} \sum_{i=1}^{N} \frac{1}{2}\left(\frac{r_i - r_{i-1}}{t_i - t_{i-1}}\right)^2 - \frac{2\mu_E}{r_i + r_{i-1}} + \frac{2h_E^2}{(r_i + r_{i-1})^2} \tag{4.12}$$

where the suffix i denotes the value measured at time t_i. From eqs.

(4.3), (4.4), and (4.5), the elliptic curve of the vehicle's trajectory is determined in the orbital plane. Finally, the initial condition $r_0 = r\ (t = 0)$ is determined by the least square method, that is,

$$f(r_0) \equiv \sum_{i=1}^{N} \{r_i - r(t_i)\}^2 \Big|_{\text{minimum}} \tag{4.13}$$

where $r(t_i)$ is the calculated position at time t_i using the initial condition $r_0 = r\ (t = 0)$.

The rocket trajectory is computed in terms of the time and the position where the measurement was carried out at the time t. This method, however, is not applicable to the lower altitude range where the friction force due to the atmosphere decelerates the vehicle's velocity. As it is simply assumed that the earth can be represented to be an oblate spheroid, any anomalies of the earth's gravitational field are neglected. The distance from the launch pad to the vehicle's position projected on the earth's surface is calculated as a length of an intersecting arc between a quadric (the earth's surface) and a plane (the orbital plane) as given in Appendix B.

2.2 Computation of Geomagnetic Field

As noted in section 3, Chapter I, the gyro-frequency can be deduced from the geomagnetic field intensity. The geomagnetic reference field is expressed by a series of spherical harmonics in geocentric spherical coordinates (r, ψ, λ_E) with the geomagnetic potential V and intensity components given by

$$V = a_0 \sum_{n=1}^{10} \sum_{m=0}^{n} \left(\frac{a_0}{r}\right)^{n+1} \cdot F_{nm}(\lambda_E) \cdot P_n^m(x), \tag{4.14}$$

$$X = \frac{1}{r}\frac{\partial V}{\partial \psi} = -\sin\psi \sum_{n=1}^{10} \left(\frac{a_0}{r}\right)^{n+2} \sum_{m=0}^{n} F_{nm}(\lambda_E) D \cdot P_n^m(x),$$

$$Y = \frac{-1}{r \cdot \sin\psi}\frac{\partial V}{\partial \lambda_E} = \frac{1}{\sin\psi} \sum_{n=1}^{10} \left(\frac{a_0}{r}\right)^{n+2} \sum_{m=0}^{n} m \cdot G_{nm}(\lambda_E) P_n^m(x),$$

$$F_{nm}(\lambda_E) = g_n^m \cdot \cos m\lambda_E + h_n^m \cdot \sin m\lambda_E \ ,$$

$$G_{nm}(\lambda_E) = g_n^m \cdot \sin m\lambda_E - h_n^m \cdot \cos m\lambda_E \ ,$$

$$DP_n^m(x) = dD_n^m(x)/dx.$$

In the above expressions, $P_n^m(x)$ is the associated Legendre function of the Schmidt quasi-normalized type defined by

$$P_n^m(x) = \frac{1}{2^n n!} \left[\frac{\varepsilon_m (n-m)!\,(1-x^2)^m}{(n+m)!}\right]^{1/2} \frac{d^{m+n}(x^2-1)^n}{dx^{m+n}} \ , \qquad (4.15)$$

with $$\varepsilon_m = \begin{cases} 1 & \text{for } m = 0 \\ 2 & \text{for } m \geq 1 \end{cases}$$

and $x = \cos\psi$ where ψ is a geocentric colatitude measured from the north pole. a_0 is the radius of the reference sphere (6371.2 km), r the radial distance from the center of the reference sphere, and λ_E the geocentric longitude measured eastward from Greenwich. X, Y, and Z are the northward, the eastward and the downward components of the magnetic field vector. g_n^m and h_n^m are the spherical harmonic Gaussian coefficients, and the values proposed by J. C. Cain and R. E. Sweeney[290] are employed in this calculation. The total scalar intensity F and the gyro-frequency f_H are obtained as

$$F = \sqrt{X^2 + Y^2 + Z^2} \qquad (4.16)$$

and $$f_H = 2.7992048 \times F \quad [\text{MHz};\ F \text{ in gauss}] .$$

In computing $P_n^m(x)$ and $dP_n^m(x)/dx$, the following recurrence formulas are introduced from eq. (4.15), as,

$$P_n^m(x) = \begin{cases} \dfrac{1}{\sqrt{n^2-m^2}}\left[(2n-1)x \cdot P_{n-1}^m(x) - \sqrt{(n-1)^2-m^2} \cdot P_{n-2}^m(x)\right] & \text{for } 0 \leq m \leq n-2, \\ \dfrac{1}{\sqrt{(n+m)(n-m+1)}} \cdot \left[2(m-1) \cdot \dfrac{x}{y} \cdot P_n^{m-1}(x) - \sqrt{(n+m-1)(n-m+2)} \cdot P_n^{m-2}(x)\right] & \text{for } 2 \leq m \leq n, \end{cases} \qquad (4.17)$$

and $$\frac{dP_n^m(x)}{dx} = -\frac{\sqrt{(n+1)^2-m^2}}{y^2} P_{n+1}^m(x) + \frac{(n+1)x}{y^2} P_n^m(x). \qquad (4.18)$$

The measurement of the geomagnetic field using the sounding rocket was made by the flux-gate magnetometer onboard the Kappa 8-15. The comparison between the measured geomagnetic field intensity[292] and the theoretically calculated ones has been performed, and the result is illustrated in Fig. 4-1. The error between computed values (solid curve) and observed ones (dots) is less than 200 gamma, which, in turn, contributes the error of the electron density value, deduced from f_{UHR}, less than about ± 0.5 %. From the measured upper hybrid resonance frequency f_{UHR} and the data for the vehicle's trajectory obtained by the radar, the electron density together with the observed position is calculated. The computer-aided graphical displays have been performed. An example of the output display from the X-Y plotter is shown in Fig. 4-2, using the data obtained by Kappa 9M-35 sounding rocket. In this case, the eccentricity of the trajectory is 0.98 and the semimajor axis is 3388.2205 km. The electron density profile shows a remarkable wake effect, and the envelope of local peak values is considered to be the profile representing the true ambient electron density.

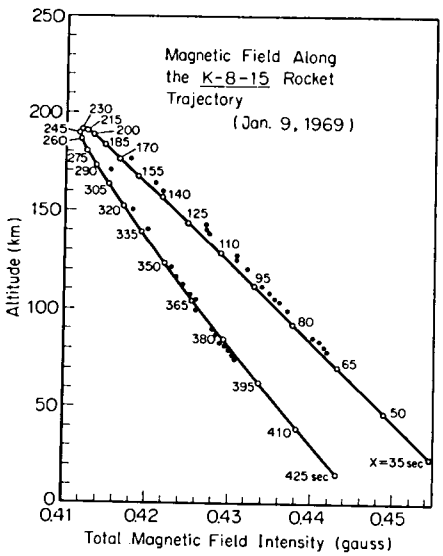

Fig. 4-1 Geomagnetic field intensity along rocket flight path: Solid curve shows the theoretically computed values and dots indicate the observed ones (Digital numbers represent the time after rocket firing).

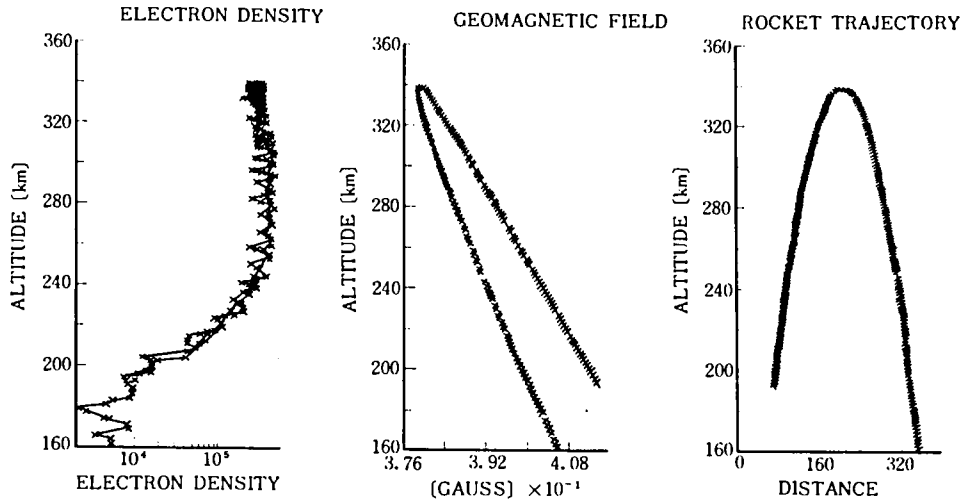

Fig. 4-2 Output figures by computer-aided graphical display; (a) electron density, (b) geomagnetic field, and (c) rocket trajectory.

§ 3. Electron Density and Temperature Measurements in the Ionosphere

Using four kinds of sounding rockets, the electron density distributions in the ionosphere have been investigated. S 210 rocket is used for measurement of the lower ionosphere in the altitude range from 70 km to 120 km. The gyro-plasma probe, the high frequency capacitance probe, and the Langmuir probe are usually installed. The gyro-plasma probe can be used to measure the electron density above about 90 km, because the electron-neutral collision prevents the resonance detection in the region where the plasma frequency is less than the collision frequency. The high frequency capacitance probe can measure the weakly ionized plasma, giving the electron density in the lower ionosphere (70 km to 120 km). The Langmuir probe is to monitor the current density to the sensor. In the latter two methods, the absolute electron density is inferred only when it is compared with the electron density deduced from the gyro-plasma probe or the f_0E of the ionogram. Kappa 8 and 9M rockets are designed to measure the E, F1 and F2 regions in the altitude range from 90 km to 340 km. Lambda 3H rocket has the capability of lifting the payloads up to

Table 4-2 List of ionospheric conditions.

Rocket	Date and Time (JST)	Solar Zenith Angle χ[deg]	K_p Index	Daily Solar Flux S_a	Wolf Number R_z	$\bar{R}_z$
S-210-6	11:24, Jan.	52.1°	6^-	127.9	78	79
S-210-8	08:40, Jan.	70.9°	2^-	93.8	11	43
K-8-15	16:40, Jan.	85.7°	1^-	183.3	152	112
K-9M-35	20:20, Jan.	129.6°	2	182.9	107	79
K-9M-38	15:00, Feb.	60.1°	2_+	180.4	167	80
K-9M-41	18:00, Jan.	100.4°	3^+	94.8	47	43
L-3H-5	20:30, Sept.	120.6°	3^+	134.7	98	93
L-3H-6	11:10, Jan.	52.7°	2	182.9	118	112

Note: χ[degree] is the solar zenith angle, K_p the geomagnetic index, $S_a[10^{-22}\ Wm^{-2}\ Hz^{-1}]$ the daily solar flux at 2800 MHz, R_z the relative sunspot number, and $\bar{R}_z$ the three month average of R_z.

the altitude of about 2000 km. The electron density profile and the electron temperature of the topside ionosphere above F2 peak are revealed by this rocket.

The parameters of ionospheric conditions such as solar zenith angle χ [degree], geomagnetic index K_p, daily solar flux at 2800 MHz $S_a[Wm^{-2}\ Hz^{-1}]$, and relative sunspot number R_z for individual rocket experiments are summarized in Table 4-2.

Typical rocket trajectories obtained by the radar are illustrated in Fig. 4-3 (a) S 210-6, (b) Kappa 8-15, (c) Kappa 9M-41, and (d) Lambda 3H-6. The variation of the geomagnetic field along the trajectory is given in Figs. 4-1 and 2 for Kappa 8-15 and Kappa 9M-35. For 3H-6 experiment shown in Fig. 4-4, the geomagnetic field intensity varies in the range from about 0.46 gauss to less than 0.2 gauss.

3.1 Electron Density Profile in the Ionosphere

Lower Ionosphere Using S 210-6 and 8, the electron density distributions in the lower ionosphere were obtained. The results are

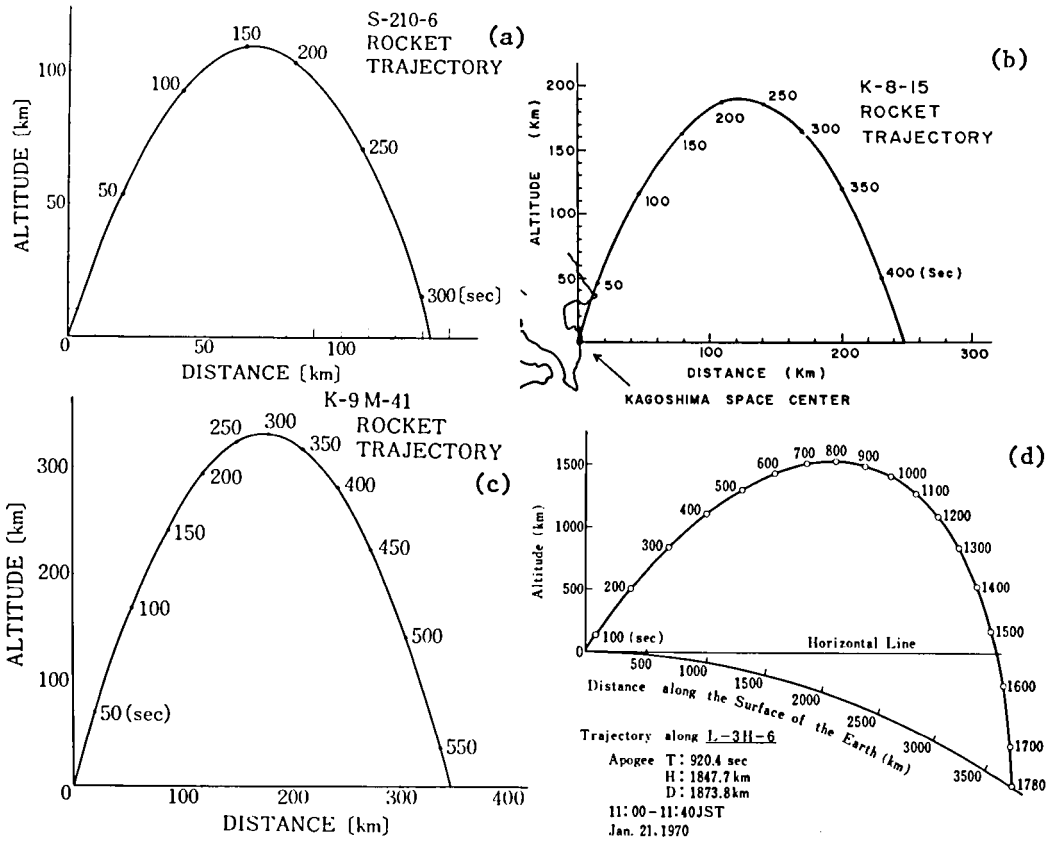

Fig. 4-3 Trajectories of sounding rockets.

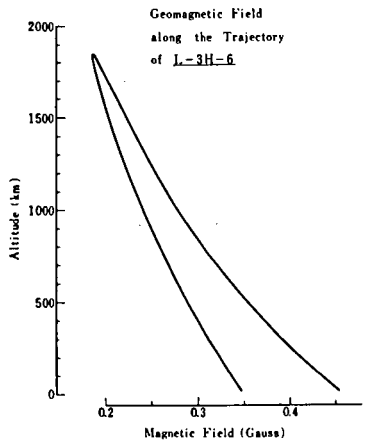

Fig. 4-4 Geomagnetic field intensity along Lambda 3H-6 rocket flight path.

illustrated in Fig. 4-5. The arrows in the figure indicate the corresponding electron densities deduced from the critical frequencies f_0E and f_0E_s of the ionogram obtained simultaneously at KSC.

In the S 210-6 rocket experiment, the antenna of gyro-plasma probe was located in such a position that the wake effect of electron density is clearly seen in both ascending and descending cases. The maximum electron density of E layer was 1.5×10^5 cm^{-3} which agrees well with the value deduced from f_0E_s, and its height about 107 km. Below the altitude of 88 km, the upper hybrid resonance could hardly detected. Two high frequency capacitance probes (CP #1 and #2) with different spacing of parallel plates were used. Their sensors were mounted at the tip of arm which was diployed at the top of the rocket. The electron density distribution obtained by the capacitance probe was not affected by the wake effect in the ascending path, while the large electron density depletion was observed in the descending path. The dotted circle denotes the estimated electron density value deduced from the antenna admittance. The fix-biased Langmuir probes (LP #1 and #2) were also equipped. The electron densities measured by three probe methods are in good agreement with each other.

In the S 210-8 rocket experiment, the capacitance probe and the Langmuir probe were installed. The coaxial mesh cylinder located on the top of the rocket was used as a sensor. To modify the ion sheath, the swept voltage was applied to the sensor. From the maximum frequency shift, the absolute values of electron density are calculated and shown in Fig. 4-5 (b) by the dots. The dashed line shows the value deduced from the frequency shift at the floating potential.

As for the maximum electron density of E layer in the middle-latitude, K. Maeda and S. Fukao[135] give the empirical expression as,

$$\text{for summer,} \quad N_m = 1.32 \times 10^5 \sqrt{1+0.01\,\overline{R}_Z}\,(\cos\chi)^{0.6}, \quad (4.1)$$

$$\text{for winter,} \quad N_m = 1.34 \times 10^5 \sqrt{1+0.01\,\overline{R}_Z}\,(\cos\chi)^{0.52}. \quad (4.2)$$

Using ionospheric conditions listed in Table 4-2, the corresponding N_m

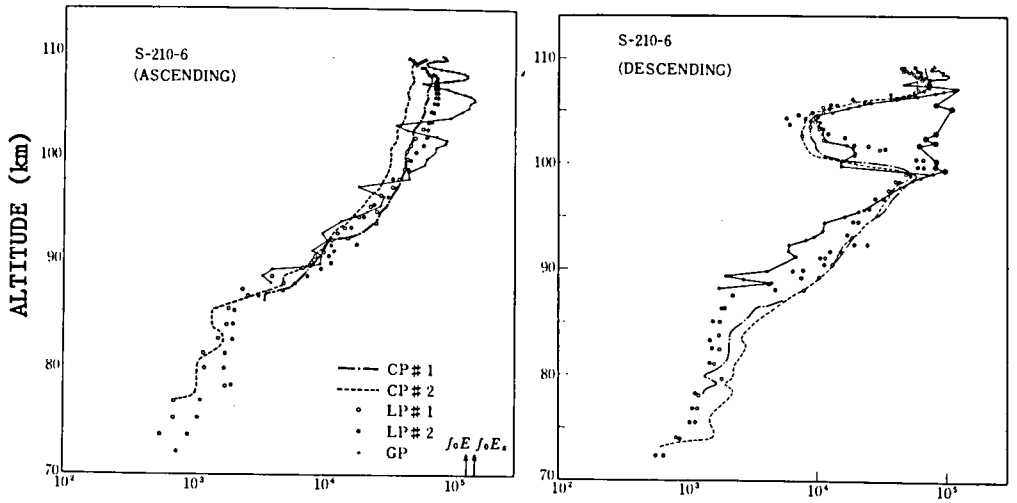

(a) S 210-6 (11:24, Jan. 1972).

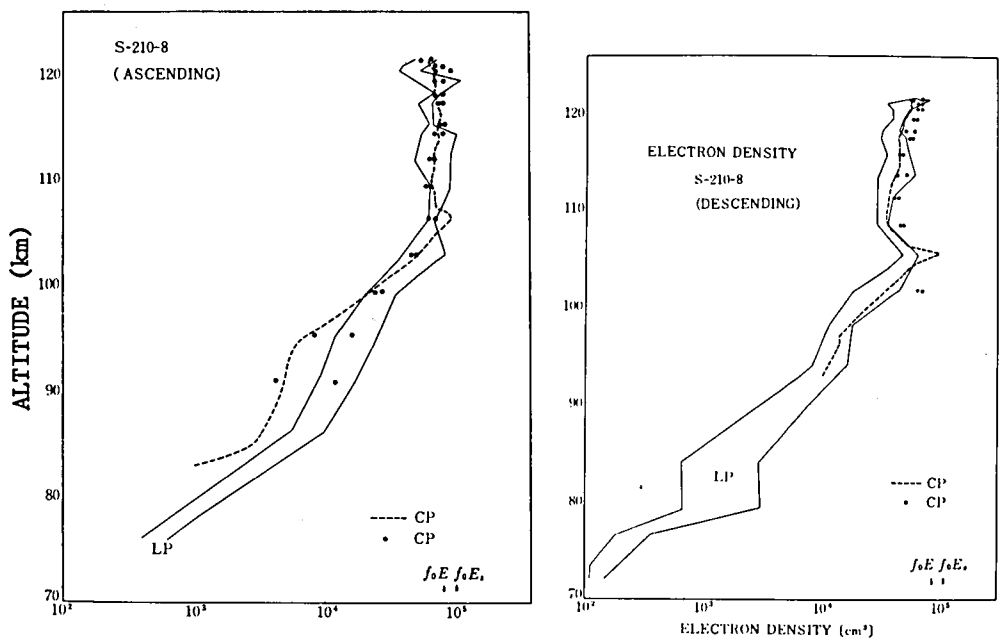

(b) S 210-8 (08:40, Jan. 1973).

Fig. 4-5 Electron density profile in the lower ionosphere.

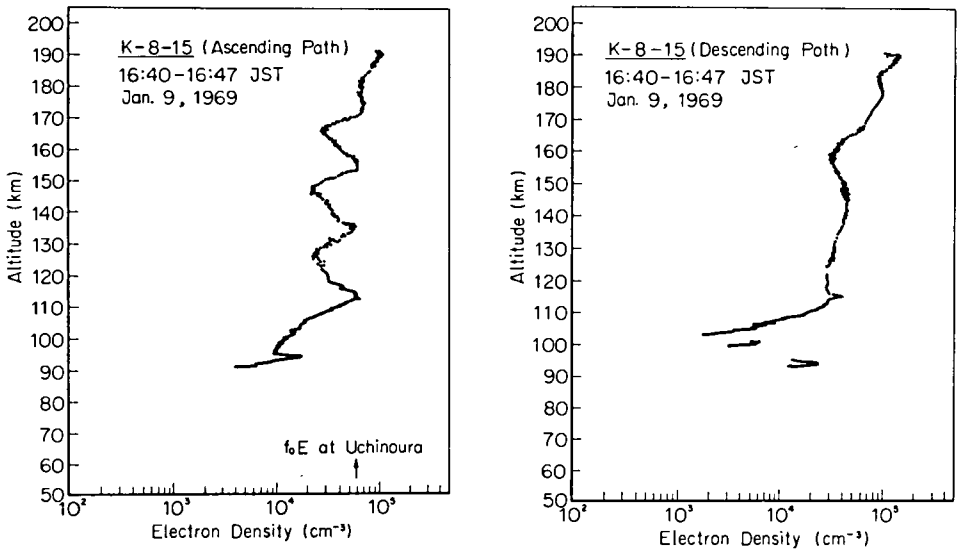

Fig. 4-6 Electron density profiles (Kappa 8-15).

are calculated to be 1.4×10^5 cm^{-3} (S 210-6) and 1.0×10^5 cm^{-3} (S 210-8). These calculated values are in good agreement with the observed ones.

E to F Region Ionosphere Electron density profiles obtained by the gyro-plasma probe onboard the Kappa 8-15 sounding rocket are illustrated in Fig. 4-6. The value N_m (5.9×10^4 cm^{-3}) deduced from the verical incident ionogram is indicated by the arrow. The calculated N_m from eq. (4.2) is 5.1×10^4 cm^{-3}. A large electron density ($N_e = 2 \times 10^4$cm^{-3}) at the altitude of 94 km persisted during the rocket flight, in spite of an obvious expectation of the reduction in electron density below E layer according to the transition of local time in the evening ionosphere (about a quarter of an hour interval). There exists a small trough between D and E layer both in the ascending and descending cases.

The structure of winter ionosphere and its diurnal variation were measured with the series of rocket flights; Kappa 9M-35, 38, and 41. An example of the raw data displayed by the computer-aided X-Y plotter is illustrated in Fig. 4-2 (a). The results of three rocket observations are summarized in Fig. 4-7. Along with these rocket experiments,

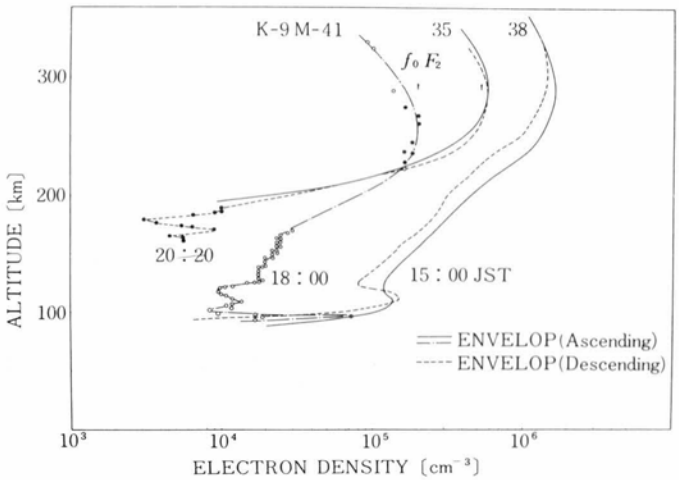

Fig. 4-7 Electron density distributions measured by Kappa 9M-35, 38 and 41.

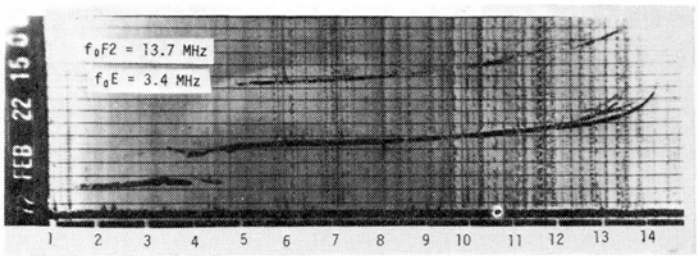

(a) 15:00, Feb, 22, 1972.

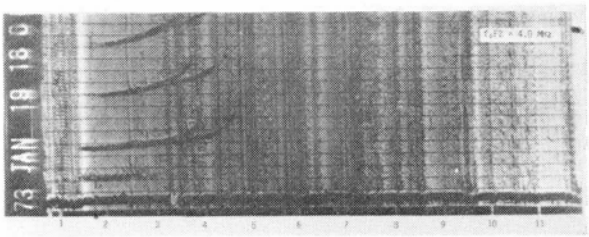

(b) 18:00, Jan. 19, 1973.

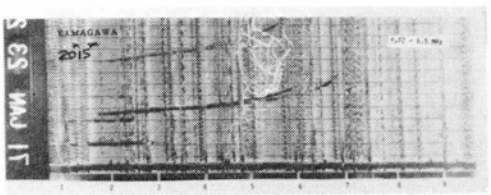

(c) 20:15, Jan. 23, 1971.

Fig. 4-8 Ionograms obtained by Yamagawa Radio Observatory.

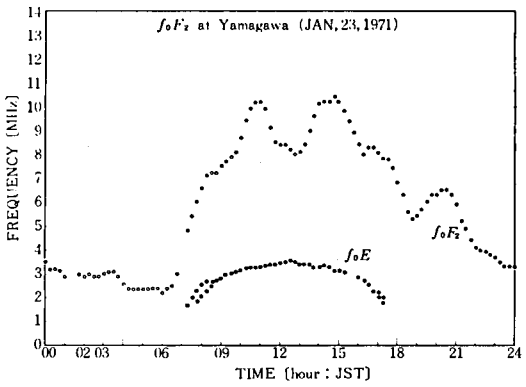

Fig. 4-9 Diurnal variation of f_0F2 (Yamagawa, Jan. 23, 1971).

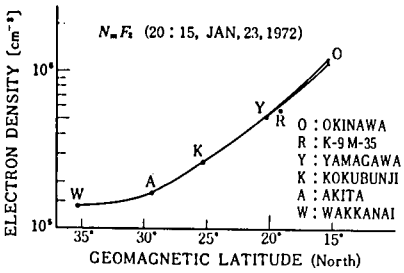

Fig. 4-10 Geomagnetic latitude variation of N_mF2.

vertical incidence ionograms shown in Fig. 4-8 were simultaneously taken at the Yamagawa Radio Observatory. In the case of Kappa 9M-41, the shadow line is calculated to be an altitude of 106 km (χ = 100.4°). The daily solar flux S_a and the Wolf number R_z at that time were about half of the values in other cases. The maximum electron density N_mF2 obtained by Kappa 9M-41 was much smaller than the others. The typical diurnal variation of f_0F2 observed on Jan. 23, 1971, at Yamagawa is shown in Fig. 4-9. Before and after the noon, the peak electron densities were observed, and also after the sunset there was an enhancement of f_0F2. The N_mF2 deduced from ionograms is indicated by the arrow in Fig. 4-7. It does not necessarily follow that the measured value of N_mF2 by the rocket-borne instrument coincides the value deduced from f_0F2, because of the latitude difference of observations. The geomagnetic latitude dependence of N_mF2, obtained at the same time of Kappa 9M-35 rocket launching, is illustrated in Fig. 4-10. The electron density at F2 peak is noticeably increasing towards the equator. The latitudinal variation of daytime electron distribution in the F2 layer is discussed in Chapter VI using the data obtained by the spacecraft REXS.

Topside Ionosphere The day and night-time electron density distributions in the topside ionosphere were measured by the gyro-plasma probe onboard Lambda 3H-5 and 6 sounding rockets. Figure 4-11 shows the day-

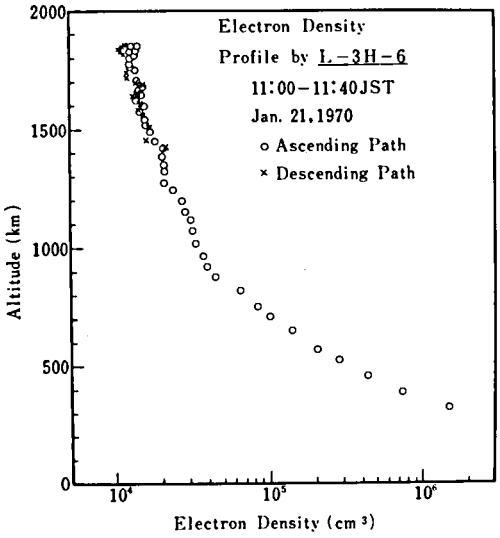

Fig. 4-11 Daytime electron density profile in the topside ionosphere.

time ionospheric electron density profile (11:00 JST, Jan.). The slope of the logarithmic electron density, which is proportional to the scale height, changes with altitude. The scale height below 800 km level is approximately 200 km, while above the 1200 km level it is 950 km. This indicates that the predominant ionospheric constituent is hydrogen above the 1000 km level (theoretically predicted scale height is about 1500 km for hydrogen atmosphere with temperature of 1000 °K). The night-time ionospheric electron density profile (20:30 JST, Sept.) is shown in Fig. 4-12, in which the arrow indicates the maximum electron density of F2 layer ($N_e = 5.2 \times 10^5$ cm^{-3}) deduced from ionograms. The solid curve is the envelope of the measured data. Up to now, the observations of topside ionosphere with gyro-plasma probe were carried out three times (Lambda 3H-2, 5 and 6). Figure 4-13 illustrates three observations with different local times. The electron density distribution of F2 layer changes remarkably; the maximum electron density of night-time F2 layer is much less than that of day-time F2 layer. The systematic difference between day and night-time electron density distributions far above 500 km level is not recognized from these experiments. These electron density profiles can be well represented by the diffusive equillibrium distribution[208] as described in section 2.3, Chapter I (see Fig. 1-11).

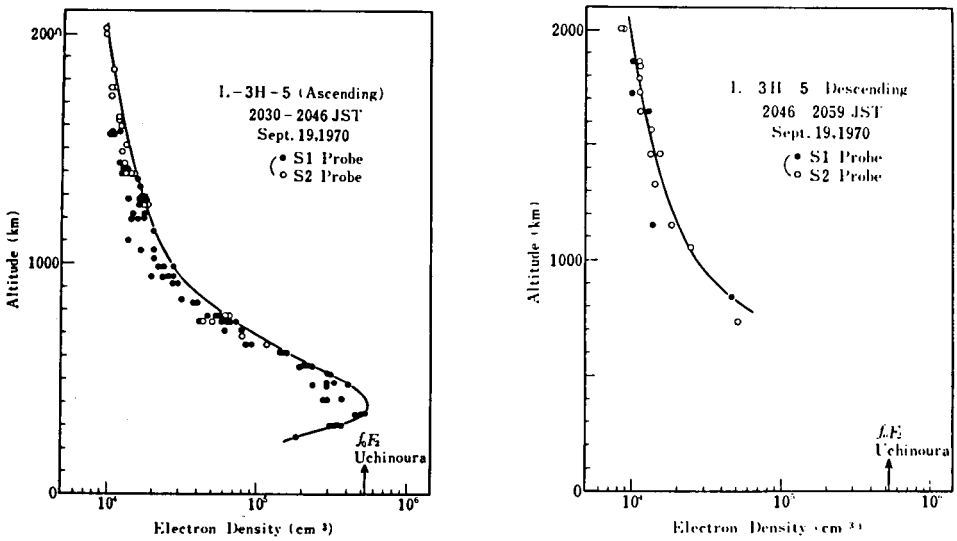

Fig. 4-12 Night-time electron density profile in the topside ionosphere.

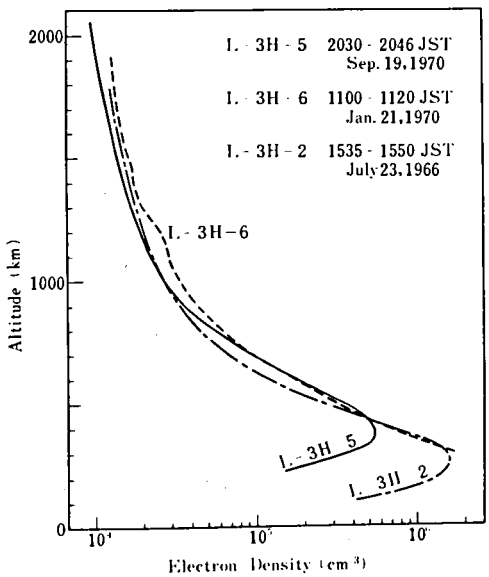

Fig. 4-13 Electron density profiles in the topside ionosphere, measured by Lambda 3H-2 (after H. Oya[20]), 5, and 6.

3.2 Electron Temperature in the Ionosphere

Taking account the effect of the ion-sheath formation around a probe at the floating potential, the electron temperature is deduced from the admittance of the probe. At frequency much lower than the sheath resonance the admittance is pure capacitive, and an amplitude of admittance represents an ion sheath capacitance. For the cylindrical sensor,

$$C_{sheath} = 2\pi\epsilon_0 L/\ell n\ (r_s/r_a), \tag{4.3}$$

where L and r_a are the length and the radius of the sensor. The radius of the sheath boundary r_s can be deduced from this capacitance. To determine the floating potential, Poisson's equation around the sensor must be solved. Assuming one dimensional azimuthal symmetry in cylindrical coordinates, Poisson's equation reduces to (see eq. (A.8) in Appendix A)

$$\frac{1}{x}\frac{d}{dx}\left(x\frac{dy}{dx}\right) = \exp y - 1, \tag{4.4}$$

where $y = qV/\kappa T_e$ and $x = r/\lambda_D$. Here, it is assumed that the ion sheath region is free from electrons, and that the ion concentration is constant. The above equation is readily integrated under the initial conditions; $V(r_s) = 0$ and $dV(r_s)/dr = 0$. And, V_f is given as $V(0)$.

The electron current I_e to the probe at floating potential is calculated as a function of electron temperature, using Maxwellian distribution function.

$$I_e = 2\pi r_s L \cdot J_e, \tag{4.5}$$

where J_e is given in eq. (2.25).

Considering the rocket motion relative to the environmental plasma, the ion current collected by the vehicle's body is predominated by the vehicle's velocity W. It is assumed that the ion particle velocity

measured in the reference frame fixed to the moving vehicle is approximately W, because the ion thermal velocity is sufficiently small compared with the vehicle's velocity. Following H. Oya and T. Aso,[108] the ion current collected to the probe is calculated as follows. The energy and the angular conservation of a particle are hold as

$$\frac{1}{2} M(u_s^2 + v_s^2) = \frac{1}{2} M(u_0^2 + v_0^2) + qV_f, \tag{4.6}$$

$$r_s v_s = r_a v_0 \tag{4.7}$$

where u, v are the radial and the perpendicular velocity components, and suffix s and 0 denote the values of the sheath and the probe surfaces, respectively. As an ion which reaches the probe surface has the positive velocity component u_0, the following relation should be satisfied,

$$v_s^2/b^2 - u_s^2/a^2 < 1 \tag{4.8}$$

where $a^2 = -2qV_f/M$,

$$b = -\frac{r_a^2}{r_s^2 - r_a^2} \cdot \frac{2qV_f}{M} .$$

The critical velocity $v = b$ is the maximum limit of the tangential velocity component of particle arriving at the body surface having zero radial velocity component at the edge of the ion sheath, and $u = a$ is the velocity acquired by the potential V_f. Therefore, the ion current is calculated as

$$I_i = N_i qL \cdot 2 \int_0^{\alpha_0} r_s u' \cdot \cos\alpha \, d\alpha \tag{4.9}$$

where $u' = W \sin\theta$ and θ is an angle between the cylindrical probe axis and the direction of the vehicle's velocity. The angle α_0 is determined so as to satisfy the equation (4.8) with $u_s = u' \cdot \cos\alpha$ and $v_s = u' \cdot \sin\alpha$.

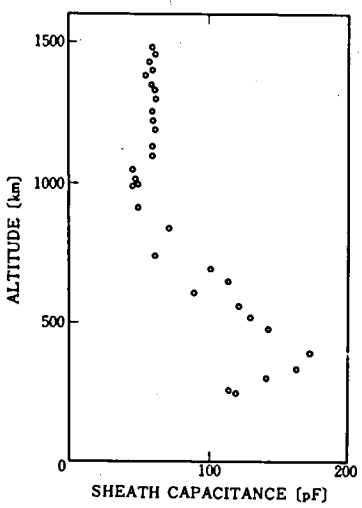

Fig. 4-14 Sheath capacitance at 300 kHz (Lambda 3H-5).

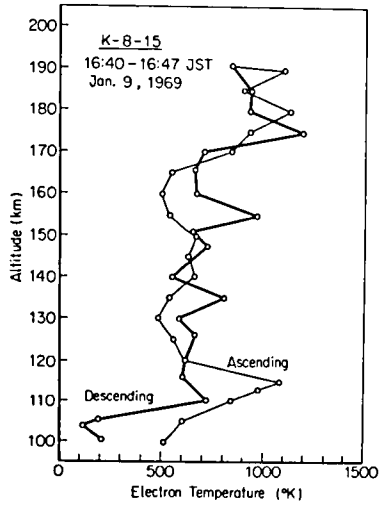

Fig. 4-15 Electron temperature profile (Kappa 8-15).

$$\alpha_0 = \begin{cases} \dfrac{\pi}{2} & ; \text{ for } W\cdot\sin\theta < b, \\ \sin^{-1}\{\dfrac{r_a}{r_s}(1 - \dfrac{2qV_f}{MW^2\cdot\sin^2\theta})^{1/2}\} & ; \text{ for } W\cdot\sin\theta > b. \end{cases} \quad (4.10)$$

Then,

$$I_i = \begin{cases} 2r_s LN_i qW\cdot\sin\theta & ; \text{ for } W\cdot\sin\theta < b, \\ 2r_a LN_i qW\cdot\sin\theta(1 - \dfrac{2qV_f}{MW^2\cdot\sin^2\theta})^{1/2} & ; \text{ for } W\cdot\sin\theta > b. \end{cases} \quad (4.11)$$

The floating condition is expressed as

$$I_e + I_i = 0. \quad (4.12)$$

From the above equation, the electron temperature in the ionosphere was computed. The altitude variation of the sheath capacitance C_{sheath} in eq. (4.3) obtained by the gyro-plasma probe onboard Lambda 3H-5 rocket, is illustrated in Fig. 4-14. The results of electron temperature profile obtained by Kappa 8-15 rocket are shown in Fig. 4-15. The electron temperature in E to F1 region is about 500 °K to 1000 °K. It shows large spatial irregularities in the same way as the electron density profile due to the wake effect. The electron temperature in the E region is rather high,

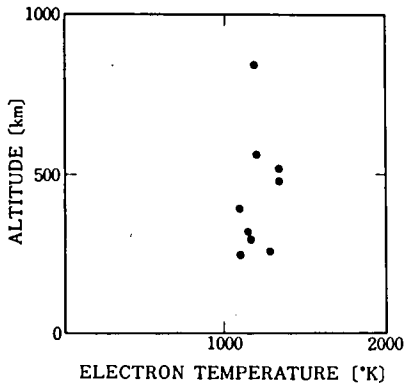

Fig. 4-16 Electron temperature profile (Lambda 3H-5).

ranging from 500 °K to 1100 °K. This fact, as well as high electron concentration of the D layer, may be important clue to interpreting the radio absorption anormaly. It is noted that the present theory is only applicable to the region where the plasma frequency is much higher than neutral-electron collision frequency, i.e., the region above approximately 100 km. In the topside region, the night-time electron temperature profile obtained by Lambda 3H-5 is illustrated in Fig. 4-16. The electron temperature in the altitude range from 250 km to 850 km is about 1100 °K to 1400 °K. This value agrees with the electron temperature deduced by the retarding potential analyzer.[293] Above mentioned theory is rather simple for the ion sheath, and it is necessary to establish the sheath model taking consideration of the wake effect formed around the probe itself.

3.3 Ion Composition in the Topside Ionosphere

As discussed in section 2.3, Chapter I, the topside ionosphere is well represented by the electrons and ions in diffusive equilibrium (see Fig. 1-11). Assuming that each ion is in diffusive equilibtium above 500 km, the ion density is given by[208]

$$N_i(z) = N_{i0}\left(\frac{T_{e0}}{T_e(z)}\right)^2 \exp\left(-\int \frac{dz}{H_i(z)}\right)\left(\frac{N_e}{N_e(z)}\right) \qquad (4.13)$$

where z is the altitude measured from the reference level at 500 km, and suffix 0 denotes the value at the base. The scale height H_i of the i-th ion species is given as a function of altitude

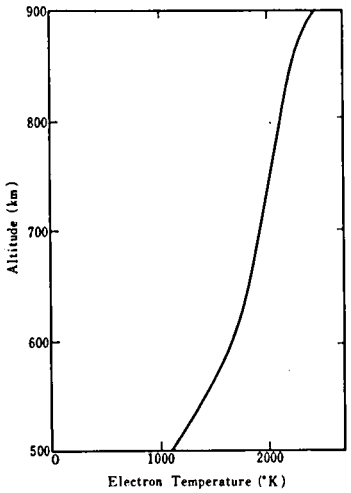

Fig. 4-17 Electron temperature profile measured by the retarding potential analyzer.

$$H_i(z) = \kappa T_e(z)/M_i \cdot g. \qquad (4.14)$$

Ions are considered to be consisted of O^+ (i = 1), H_e^+ (i = 2) and H^+ (i = 3), and their composition ratio at the base is taken from the data given by S. J. Bauer,[294] that is,

$$N_{20}/N_{10} = 2.48 \times 10^{-2} \quad \text{and} \quad N_{30}/N_{10} = 1.01 \times 10^{-1}.$$

Introducing the density ratio of the i-th ion with respect to the electron density as,

$$\eta_i(z) = N_i(z)/N_e(z) = \gamma_i \eta_{i0} / \sum_{i=0}^{3} \gamma_i \eta_{i0}$$

where $$\gamma_i = N_i(z) / \sum_{i=0}^{3} N_{i0} . \qquad (4.15)$$

Hence, η_{i0} is calculated as follows; $\eta_{10} = 0.88826$, $\eta_{20} = 0.02203$, and $\eta_{30} = 0.08971$.

The calculation was carried out in the case of Lambda 3H-5 rocket experiment, using the electron density distribution given in Fig. 4-12 and the electron temperature distribution given in Fig. 4-17 which was measured by the retarding potential analyser onboard Lambda 3H-5.[293]

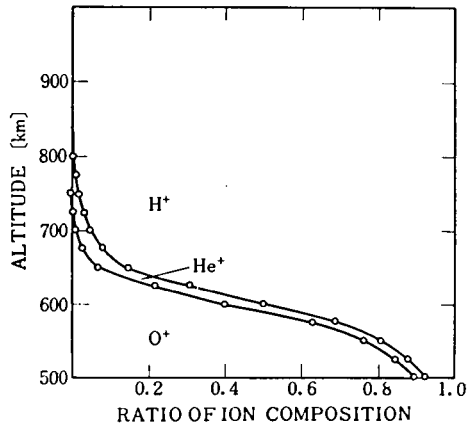

Fig. 4-18 Ion composition ratio versus altitude.

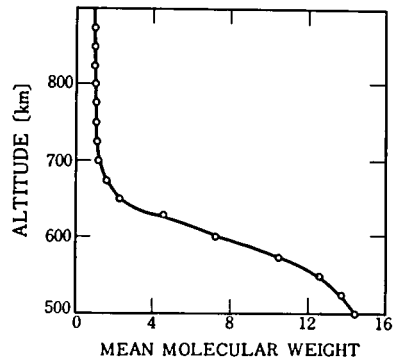

Fig. 4-19 Mean molecular weight versus altitude.

The ion composition ratios η_1, η_2 and η_3 are obtained from eq. (4.15), integrating eq. (4.13) numerically along the altitude. The result is shown in Fig. 4-18. Below and above about 600 km, the main constituent ion species changed from O^+ to H^+, while H_e^+ ion was the minor constituent. From Fig. 4-18, the mean molecular weight is calculated and shown in Fig. 4-19.

§ 4. Resonance Phenomena observed in the Ionospheric Plasma

Various kinds of resonance effects on the impedance of an antenna in a plasma have been investigated in laboratory plasma as described in the previous chapter. In the rocket experiments, these resonance phenomena have been observed by the gyro-plasma probe and the mutual impedance probe. The modified plasma resonance was also identified, which has not been observed in laboratory plasma.

4.1 Upper Hybrid and Sheath Resonance

The frequency characteristics of antenna admittance exhibit the

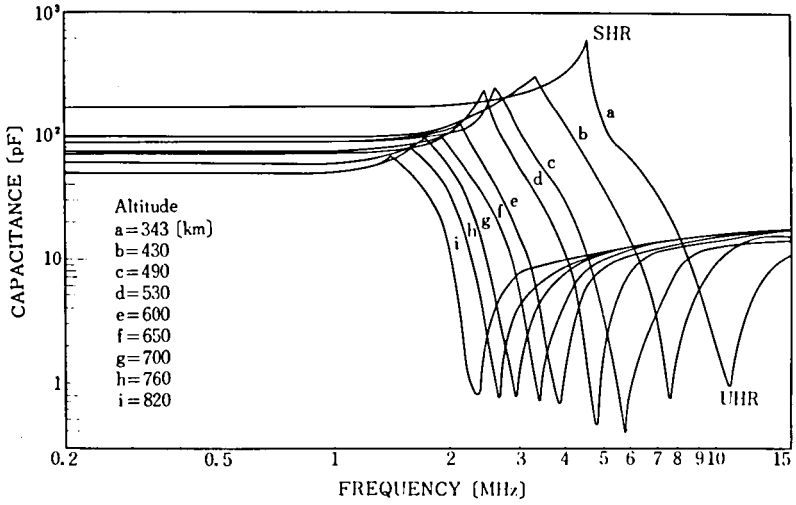

Fig. 4-20 Altitude variation of amplitude of antenna capacitance versus frequency (Lambda 3H-6).

parallel and series resonances which are identified with the upper hybrid resonance (UHR) and the sheath resonance (SHR), respectively. Figure 4-20 illustrates the output signal of the amplitude of antenna admittance which was obtained by the Lambda 3H-6 rocket experiment. The UHR and SHR frequencies decrease with increasing altitude corresponding to the decreasing electron density and the geomagnetic field intensity in the topside ionosphere. The admittance value at UHR frequency represents a Q value of resonance. The admittance value is inversely proportional to the Q value. The maximum of Q value is observed at the altitude of about 500 km in three Lambda 3H rocket experiments, and at the higher altitude Q value decreases. This fact indicates that there may be some dissipative mechanisms even in a collision-free plasma. H. Oya[233] has pointed out that the electrostatic wave excitation from the antenna reduces the Q value of plasma resonance. An example of the amplitude and phase variations as a function of frequency obtained by the Kappa 8-15 rocket is shown in Fig. 1-17, in section 3.4, Chapter I.

The mutual impedance probe onboard the Lambda 3H-6 gave the transmitted signal intensity as a function of frequency which represents the mutual admittance of the transmitter-receiver antennas. Curves of

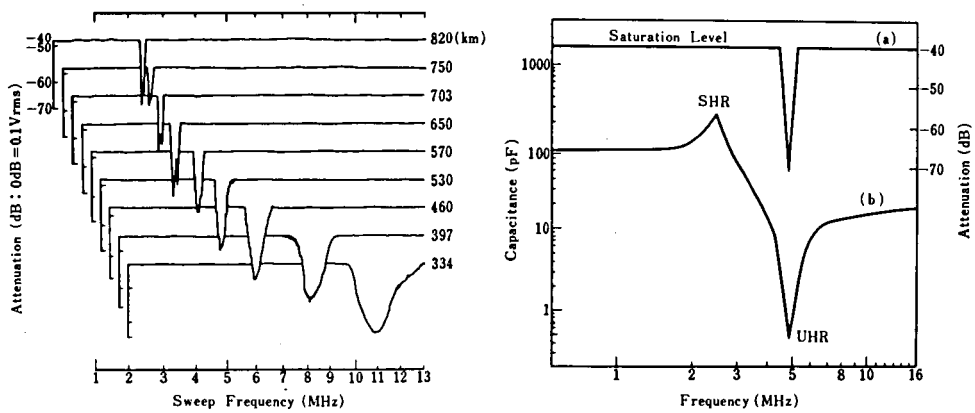

Fig. 4-21 Records obtained by the mutual impedance probe; left, (a) received signal level; (b) equivalent capacitance of single probe; right, altitude variation of f_{UHR} minimum.

signal level (0 dB = 0.1 Vrms) plotted against frequency are shown in Fig. 4-21. A sharp minimum in the signal level is found near the upper hybrid resonance frequency. The frequency at which the minimum occurs changes with altitude, coincident with f_{UHR} identified by the gyro-plasma probe. In this experiment the change in received signal intensity at the sheath resonance frequency was not detected, because of level saturation of the receiver's amplifier near SHR frequency.

4.2 Modified Plasma Resonance

The total impedance $Z(\omega)$ of an antenna in a plasma is expressed approximately as a sum of two impedances, as given in eq. (1.47), viz., $Z(\omega) = 1/j\omega C_s + Z_p(\omega)$, where Z_p is the impedance of the ambient plasma and C_s is the effective capacitance of ion sheath. Under collisionless conditions, resonances occur in the following cases; (i) $1 + j\omega C_s Z_p = 0$ and (ii) Z_p = infinity. Condition (i) results in the sheath resonance, while condition (ii) gives two resonances; one is the upper hybrid resonance, $\omega_{UHR} = \sqrt{\Pi_e^2 + \Omega_e^2}$, and the other the modified plasma resonance, ω_{MPR}. Using Balmain's formula[225] for a short cylindrical probe immersed in a homogeneous magnetoactive plasma, H. Oya[291]

predicted this modified plasma resonance, which occurs near the upper hybrid resonance. From eqs. (1.46) and (1.47), the modified plasma resonance frequency is expressed as

$$\omega_{MPR} = \frac{1}{\sqrt{2}}\{(\Pi_e^2+\Omega_e^2) + \sqrt{\Pi_e^4+2\Omega_e^2\Pi_e^2\cos 2\theta+\Omega_e^4}\}^{1/2} \qquad (4.16)$$

where θ is the angle between the probe axis and the geomagnetic field.

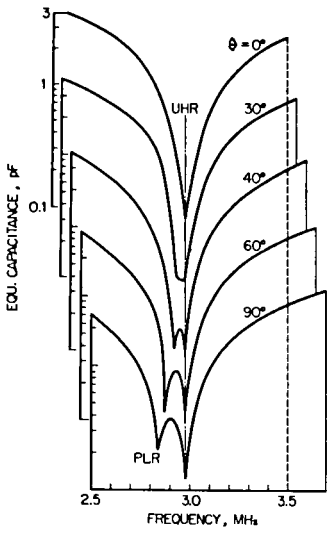

Fig. 4-22 The equivalent capacitance of cylindrical probe at different aspect angle θ (after H. Oya[291]).

Theoretically computed curves of the probe capacitance at different aspect angles θ are shown in Fig. 4-22, in which the upper hybrid and modified plasma resonances are indicated. The variations in the modified plasma resonance frequency is represented by the parameter $S(\theta)$, which is defined

$$S(\theta) = \frac{\omega_{UHR}-\omega_{MPR}}{\omega_{UHR}-\Pi_e} = \frac{1}{1-\alpha}[1 - \frac{1}{\sqrt{2}}\{1+(1-4\alpha^2\beta^2\sin^2\theta)^{1/2}\}^{1/2}] \qquad (4.17)$$

where $\alpha = \Pi_e/\omega_{UHR}$ and $\beta = \Omega_e/\omega_{UHR}$. The frequency of the modified plasma resonance coincides with the upper hybrid resonance frequency ($S = 0$) when $\theta = 0°$, and with the plasma resonance frequency ($S = 1$) when $\theta = 90°$.

Typical records of the probe admittance (equivalent capacitance) versus frequency are reproduced in Fig. 4-23, which were obtained by the gyro-plasma probe with a cylindrical sensor ($L = 1600$ mm, $r_a = 20$ mm) onboard Lambda 3H-2 sounding rocket. They demonstrate distinctly two parallel resonances, that is, the upper hybrid resonance (UHR) and the

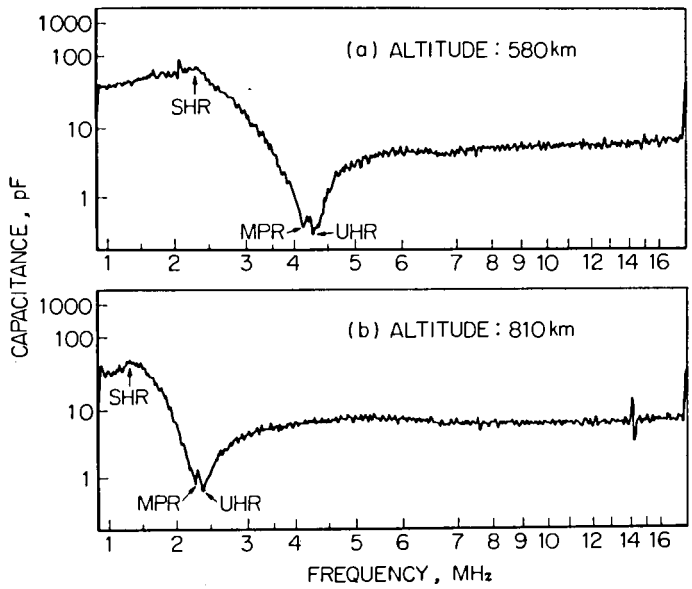

Fig. 4-23 Typical records of the probe capacitance versus frequency (Lambda 3H-2).

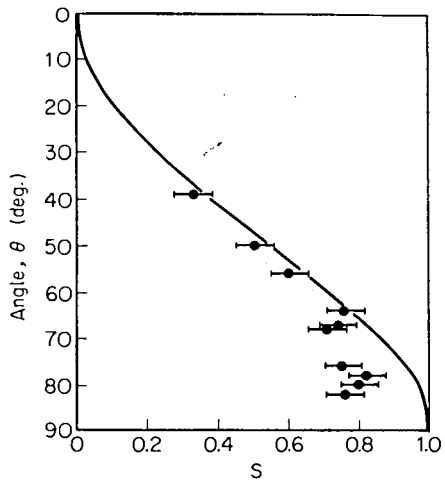

Fig. 4-24 Observed values of $S(\theta)=(\omega_{UHR}-\omega_{MPR})/(\omega_{UHR}-\Pi_e)$, with respect to the geomagnetic aspect angle of the probe. The solid curve is the theoretically computed values using ionospheric plasma parameters at the altitude of 730 km.

modified plasma resonance (MPR). The sheath resonance (SHR) appears as a series resonance. The effect of parallel resonances are very pronounced when the sensor is located outside the rocket wake.

The angle of the probe axis with respect to the geomagnetic field

line was deduced using a magnetic aspectometer onboard. The observed values of $S(\theta)$ are shown in Fig. 4-24. The solid curve shows the value computed theoretically from eq. (4.17) for the case that $\Pi_e/2\pi = 2.54$ MHz and $\Omega_e/2\pi = 0.91$ MHz, which are representative values at the altitude of 730 km. It is evident that the observed resonance characteristics are in good agreement with the theoretical predictions and that the existance of a modified plasma resonance has been confirmed experimentally.

4.3 Cyclotron Harmonic Resonance

In warm magnetoplasma, the specific admittance $y_\perp^W$ appeared in eq. (1.46) plays a very important role; especiallywhen the parameter δ' (dimension of the probe system/Larmor radius) decreases, the cold plasma theory cannot be applicable. Theoretical considerations of the cyclotron harmonic resonance effects on antenna impedance are given in section 3, Chapter I, and section 2.5, Chapter II.

The second harmonic of gyro-resonance was first discovered by the Kappa 8-15 sounding rocket experiment. Figure 4-25 shows the record in which second harmonic gyro-resonance effect is exhibited both in amplitude and phase of admittance. Series of the antenna admittance curve versus frequency at different electron densities (different altitudes)

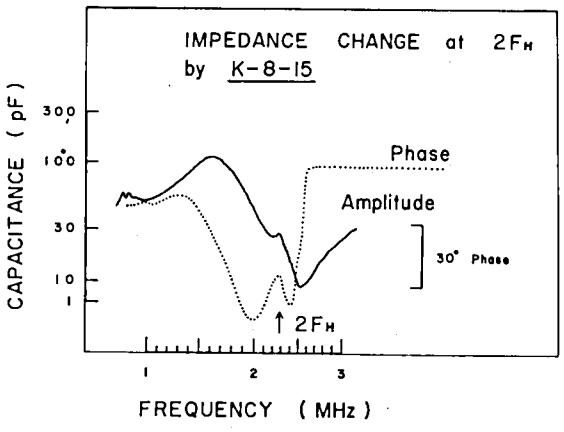

Fig. 4-25 Amplitude and phase changes of antenna admittance (Kappa 8-15).

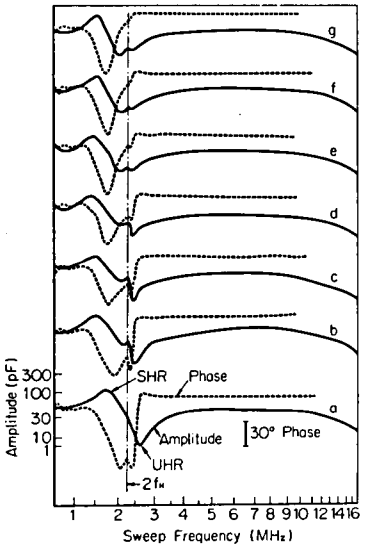

Fig. 4-26 Records of second harmonic cyclotron oscillation ($2f_H$) exhibited both in amplitude and phase of admittance (a = 172 km, b = 170 km, c = 168 km, d = 166 km, e = 165 km, f = 164 km, g = 163 km).

are demonstrated in Fig. 4-26. It is evident from the figures that the amplitude and phase of admittance show appreciable changes at the second cyclotron harmonic, $2f_H$ when the admittance is sufficiently low, i.e., near the upper hybrid resonance. This observed resonance characteristics agree well with the aforementioned warm plasma theory and also with the results obtained by the laboratory plasma experiments (see Fig. 3-6 (b) in section 3.1, Chapter III). The 3rd and higher order cyclotron harmonics

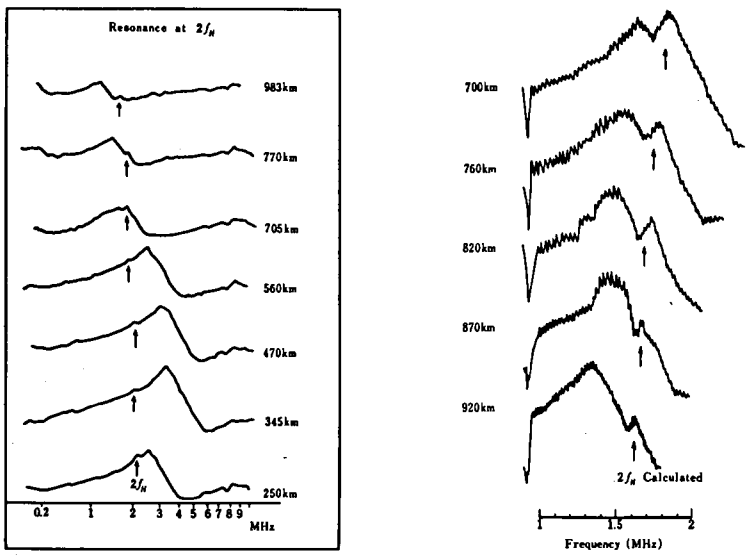

Fig. 4-27 Records obtained by the Lambda 3H-5 (a) and 6 (b).

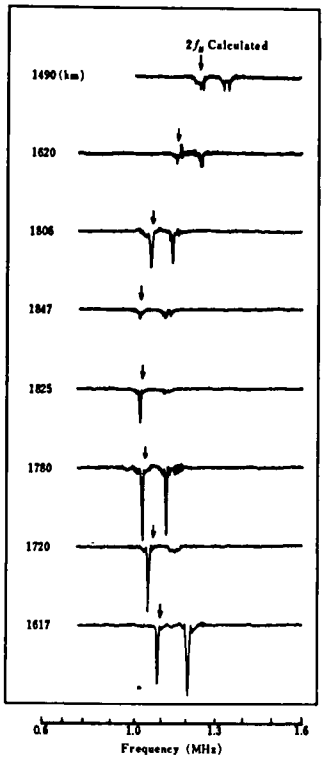

Fig. 4-28 Change in received signal intensity at $2f_H$ (Lambda 3H-6).

are not detected because of the low frequency response of the telemetry channels due to the narrow band width of FM-FM telemetry systems adopted in the present experiment. Examples of the second harmonic of gyro-resonance obtained by the experiments of Lambda 3H-5 and 6 are shown in Fig. 4-27, in which the arrow indicates $2f_H$ calculated from the geomagnetic field intensity. The admittance change at $2f_H$ is not appeared in the records illustrated in Fig. 4-20, because the admittance change at $2f_H$ is very small under the condition that $2f_H \ll f_{UHR}$ or $f_{UHR} \ll 2f_H$, as is expected from eq. (1.46)and Fig. 4-26. In the experiment of the mutual impedance probe, two sharp minima of the received signal intensity appear in the altitude range above 1500 km; one is located at f_{UHR} and the other at $2f_H$, as given in Fig. 4-28. The agreement between the spike frequency and the theoretically computed $2f_H$ is excellent. There has no well-established theoretical interpretation of this spike phenomena at $2f_H$.

In the experiment of Kappa 9M-38, the relation between the higher harmonics of gyro-resonance, the sheath resonance and the upper hybrid resonance was investigated. Figure 4-29 shows the variations of these resonance frequencies versus the rocket flight time. The change in admittance appears at the frequency between f_{SHR} and f_{UHR}. The frequency does not coincident with the theoretically calculated nf_H. Figure 4-30 (a) and (b) show the variation of the resonance characteristics of antenna admittance versus frequency at various sheath capacitances (a),

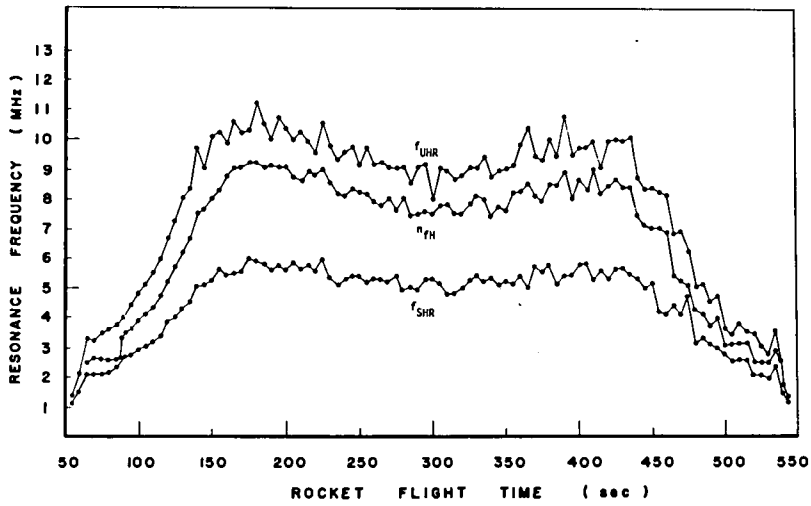

Fig. 4-29 Resonance frequencies; f_{UHR}, f_{SHR}, and nf_H.

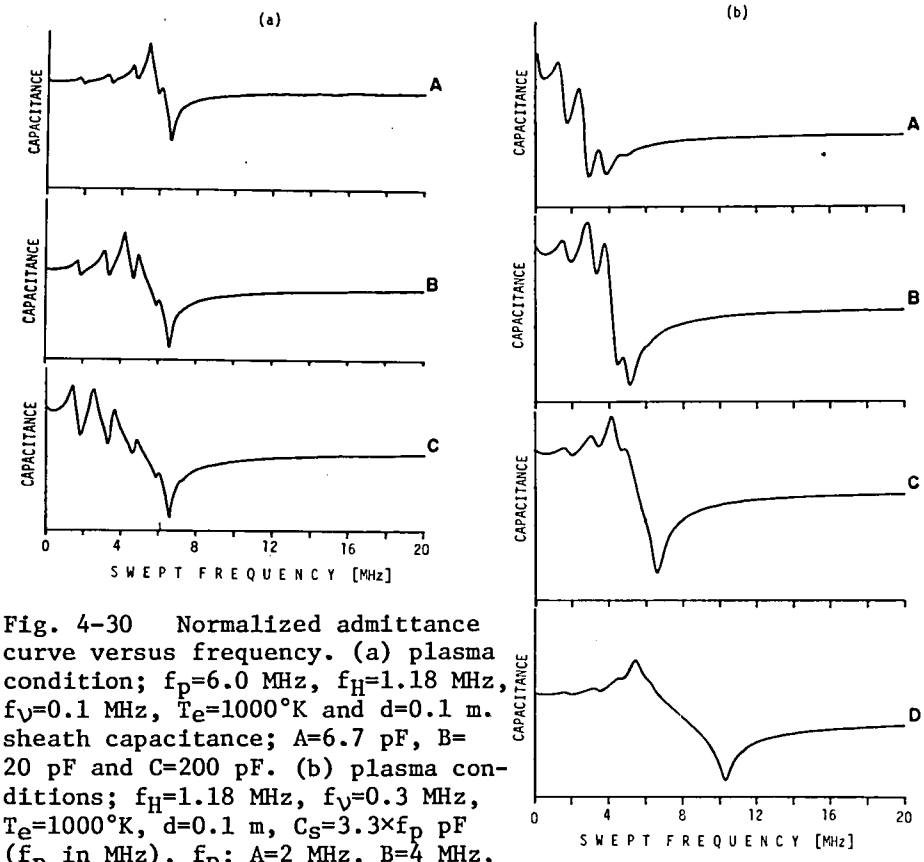

Fig. 4-30 Normalized admittance curve versus frequency. (a) plasma condition; f_p=6.0 MHz, f_H=1.18 MHz, f_ν=0.1 MHz, T_e=1000°K and d=0.1 m. sheath capacitance; A=6.7 pF, B= 20 pF and C=200 pF. (b) plasma conditions; f_H=1.18 MHz, f_ν=0.3 MHz, T_e=1000°K, d=0.1 m, C_s=3.3×f_p pF (f_p in MHz), f_p; A=2 MHz, B=4 MHz, C=6 MHz and D=10 MHz. The ordinate shows the logarithmic scale.

and electron densities (b). The transition of the gyro-resonance is clearly understood. This fact indicates that the higher harmonics of gyro-resonance of the antenna admittance are largely affected by the sheath capacitance and the electron density as is predicted from the theoretical calculation given in section 2.5, Chapter II (see Fig. 2-12).

§ 5. Comparison of Various Plasma Probe Methods

The measurements of electron density with three different kinds of probes, i.e., Langmuir probe, gyro-plasma probe, and two-wire probe, were carried out in the laboratory plasma experiment as described in section 3.4, Chapter III. The values obtained by the Langmuir probe and the gyro-plasma probe show a good agreement with each other, in spite of the physical principles of the two plasma probe methods being based on the different physical properties. In the rocket experiment, comparisons of electron density measurement with gyro-plasma probe, VLF doppler method, two-wire probe, Langmuir probe, and the high frequency capacitance probe, were performed by the Kappa 9M-35 and 38, and the S 210-6 and 8 sounding rockets, to evaluate the reliability of each method.

5.1 VLF Doppler Method and Gyro-plasma Probe

The VLF Doppler method[101~103] is to determine the electron density from the Doppler shift of a known continuous wave due to the vehicle's motion, viz., the frequency shift of VLF signals from the ground-based station is measured by the instrument onboard the vehicle and telemetered to the ground. In the experiment of the Kappa 9M-35, a 40 kHz ground signal (JG2AS) transmitted from Kemigawa Station (35°38'north, 140°04' east) near Tokyo and a 22.3 kHz signal from North West Cape (21°49' south 114°10' east) in Australia were received by a loop antenna (0.091 m^2, 20 turns).[295] In the experiment of the Kappa 9M-38, a 17.4 kHz signal from

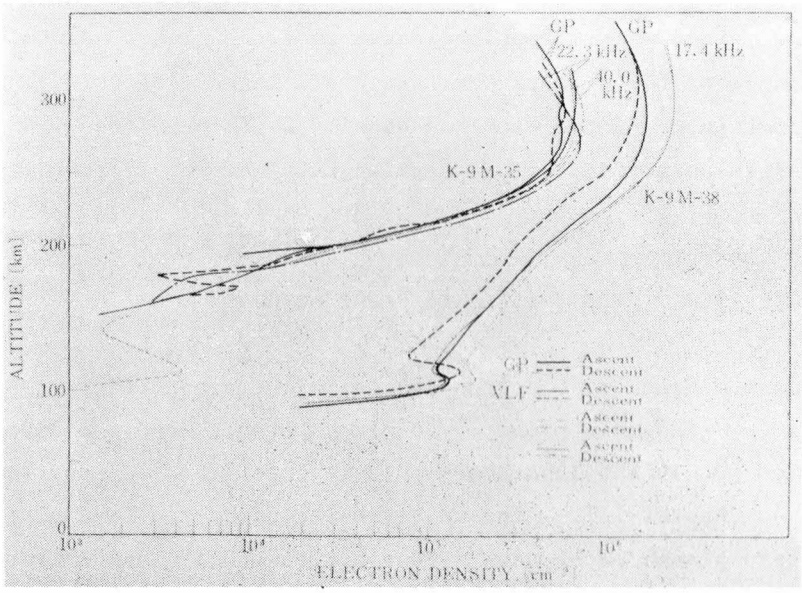

Fig. 4-31 Electron density profiles obtained by the VLF Doppler method (after I. Kimura and T. Tomimoto) and by the gyro-plasma probe (Kappa 9M-35 and 38).

Yosami Station (34°36' north, 137°01' east) was received by the dipole antenna (3 m in length from tip to tip). From the 22.3 kHz source in southern hemisphere, two signals were received by the rocket; a down-coming signal which propagated to the rocket along the magnetic field line and an upgoing signal which propagated through the earth-ionosphere wave guide and then upward through the ionosphere to the rocket. The Doppler shift can be detected with a precision of ± 2 % for most of the time of rocket flight except near the apex and in the lower part of the ionosphere.

The cylindrical antennas (600 mm and 1150 mm in length and 15 mm in diameter) was used as a sensor of the gyro-plasma probe which was standarized to measure the amplitude of antenna admittance. The electron density is deduced from the measured upper hybrid resonance frequency and the results are shown in Fig. 4-7, in section 3.1.

The measured electron density distributions versus altitude are summarized in Fig. 4-31. In the experiment of Kappa 9M-35, the electron

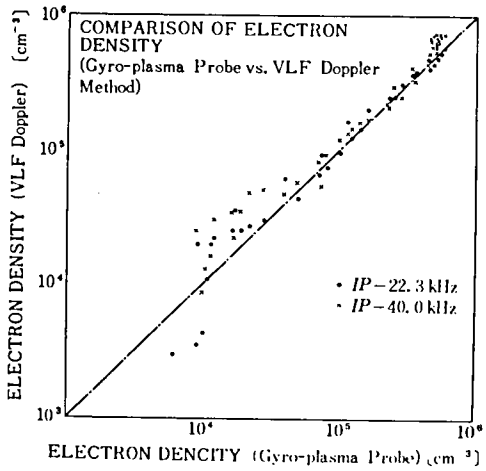

Fig. 4-32 Comparison of electron densities obtained by Kappa 9M-35 rocket experiment.

density values in the range from 10^4 cm^{-3} to 5×10^5 cm^{-3} show a good agreement with each other. In the region around the apex of the rocket there exist some difference between two methods, and also between the values obtained by the VLF Doppler method along the ascending path and is the descending path. The latter discrepancy is due to the ionosphere model which is assumed a perfectly concentric ionospheric layer with no horizontal gradient in the electron density. This error is corrected in the Kappa 9M-38 rocket experiment, introducing the inclination of the ionospheric layer as shown in Fig. 4-31. The correlation diagram of the electron densities measured with two probe methods in the Kappa 9M-35 rocket experiment is shown in Fig. 4-32. The relative error is somewhat increasing towards the low electron density value. In the experiment of Kappa 9M-38, a large systematic difference in electron density between two methods are observed. The deviation of electron density is defined by the difference in electron density normalized by the value of the VLF Doppler method, and shown in Fig. 4-33. Two methods give approximately the same values till the altitude of 180 km along the ascending path, and then the deviation gradually increases up to about 50 %. The maximum electron density at F2 peak deduced from f_0F2 of the ionogram (see Fig. 4-8) is 2.32×10^6 cm^{-3} which is coincides with the value obtained by the VLF Doppler method. It is considered that the electron density around the vehicle's body decreases for some reason. The wake effects which is the cause of the depletion of electron density behind a moving vehicle, are eliminated from the data of the gyro-plasma probe. The most probable reason to be considered is that an accumulation of negative charge on a vehicle's surface causes the vehicle's potential

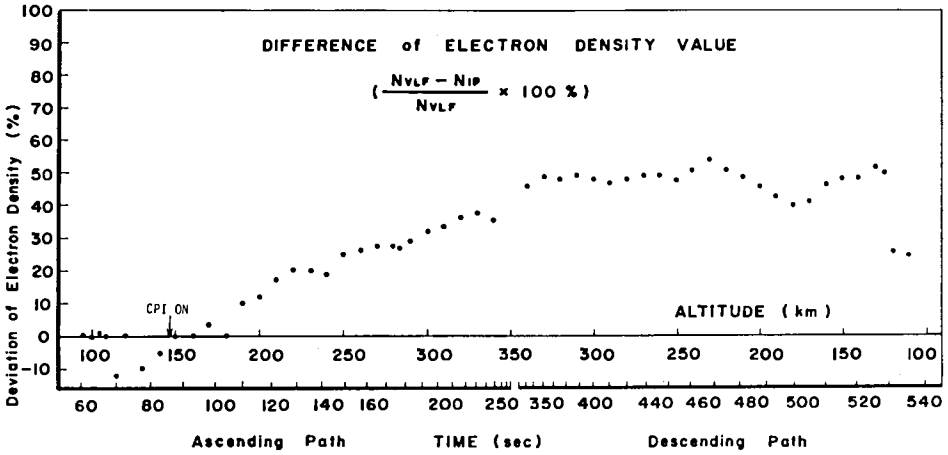

Fig. 4-33 Deviation of electron density measured by the Kappa 9M-38 rocket experiment. "CPI ON" denotes the switch-on time of the electrical power of the ion mass spectrometer.

to decrease and the radius of sheath surrounding the vehicle to increase. To measure the ion composition, the instrument of a mini-Q type ion mass spectrometer was installed and an r.f. high tension with a swept voltage of 100 volts to 600 volts and its oscillating frequency of 650 kHz were applied to the grid of sensor. As described in section 5, Chapter II, the quasi-floating potential decreases when the r.f. high tension field applied to the body in a plasma. Assuming that $N_e = 10^5$ cm^{-3}, T_e = 1000 °K, ion molecular weight = 25, V_a = 1 volt and the dimension of the Kappa 9M-type rocket is taken into account, the floating potential y given in eq. (2.47) becomes to be about 13, which, in turn, gives the value of the normalized capacitance $\Lambda = 0.06$. Since the Debye shielding length λ_D calculated to be of the order of a few mm throughout the rocket flight above 100 km, the ion sheath radius, λ_D/Λ, is estimated to be about 10 cm. When a part of an antenna is immersed in a sheath region surrounding a rocket body, the electron density deduced from the gyro-plasma probe is lower than the value in the ambient plasma, as discussed in section 2.4 Chapter II. The electron density deduced by the VLF Doppler method may be regarded as the mean value of the region much larger than that of the gyro-plasma probe, and it may be free from the effect of an ion sheath.

5.2 Langmuir Probe, Two-Wire Probe, Capacitance Probe, and Gyro-plasma Probe

As is well known, electron density and temperature can be deduced from the current-voltage characteristics of electrons collected by a metalic probe, viz., a swept voltage Langmuir probe. Conveniently, it may be assumed that the electron temperature is constant and, then, the electron current is directly proportional to the electron density. The method is called a fixed voltage Langmuir probe. While the Langmuir probe is very simple technique to measure the electron density in a plasma, an uncertainty remains in absolute electron density value unless taking a surface contamination away and determining a space potential precisely and so on. Problem on the electron current depletion near the space potential is still unsolved. In the rocket experiment, there are particular problems such as the probe reference electrode (vehicle hull) dimensions, the photoelectric emission current, the geomagnetic field effect, and wake effects. The comparison of electron density measurements with the swept voltage Langmuir probe (LP) and the gyro-plasma probe (GP) was carried out in the experiment of Kappa 9M-38 rocket. The cylindrical probe with 200 mm in length and 2 mm in diameter was used for the Langmuir probe. The measured electron density profile versus altitude is shown in Fig. 4-34, in which the region with the shadow lines are the reliable range of electron density values and the dotted lines indicate the error region. A fair agreement of electron densities measured by two probe methods is found in this experiment. The arrow of f_0F2 denotes the electron density deduced from the vertical incidence ionogram, and it does not agree with the maximum electron density at F2 peak measured by probe methods. The cause may be due to the local positional difference.

In the same rocket experiment, the comparison of the two-wire probe (TWP) and the gyro-plasma probe (GP) was also performed. The two-wire probe consists of two parallel cylindrical antennas with 638 mm in length, 2 mm in diameter and the spacing of 50 mm. The records obtained by two methods at different altitude are illustrated in Fig. 4-35, in which the

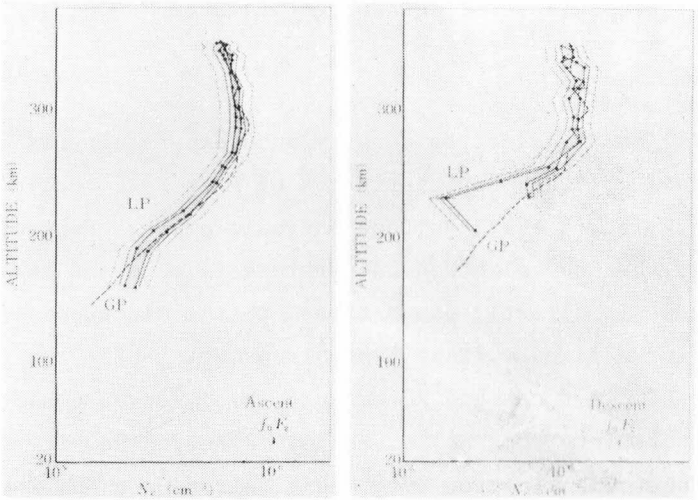

Fig. 4-34 Comparison of the electron densities measured by Langmuir Probe (LP) (after H. Mori) and gyro-plasma probe (Kappa 9M-38).

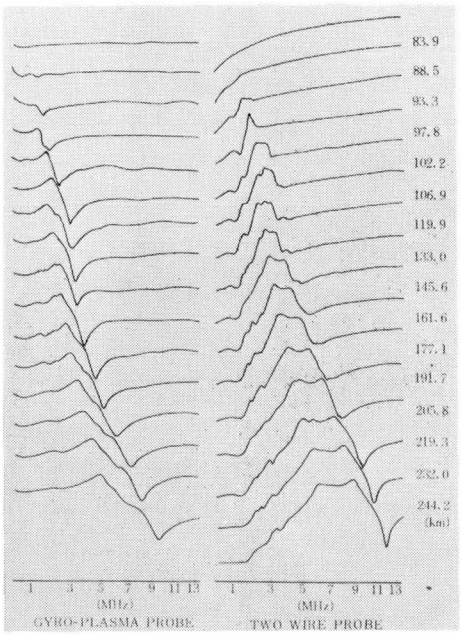

Fig. 4-35 Records obtained by two-wire probe (after H. Mori) and gyro-plasma probe (Kappa 9M-38).

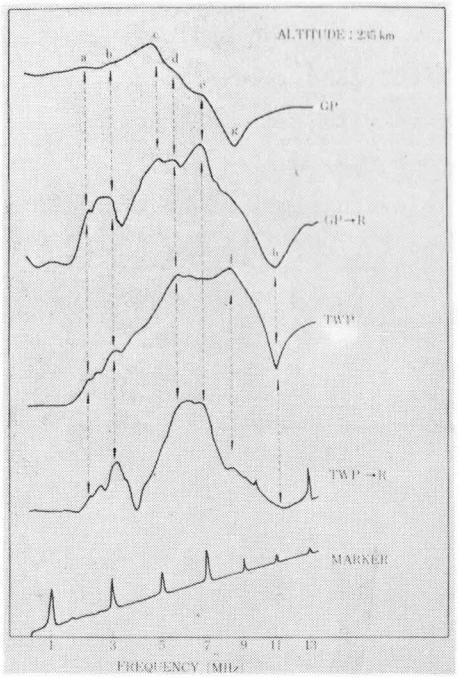

Fig. 4-36 Comparison of output wave forms obtained by gyro-plasma probe (GP) and two-wire probe (TWP). R denotes the received signals from GP and TWP.

ordinate denotes the received signal intensity in arbitrary unit for TWP and the antenna capacitance for GP. Their altitude variations are very similar with each other, but the resonance frequencies are somewhat different. For example, Fig. 4-36 illustrates the comparison of the each output wave form obtained at the altitude of 235 km. In this experiment the receiver (R) with monopole antenna of 620 mm in length was also equipped to receive the r.f. electric fields excited by GP and TWP. The resonance identifications are indicated by alphabets, a to h. The gyro-frequency f_H is 1.13 MHz. The resonances at d, e, and f are corresponding to nf_H where $n = 5$, 6, and 7, respectively. These characteristics are well explained by the theoretically computed self admittance of the gyro-plasma probe (see Fig. 2-12) and received signal intensity of the mutual impedance probe (see Fig. 2-17). The higher harmonic gyro-resonance nf_H as is indicated in Fig. 4-29 is the resonance "e" in Fig. 4-35.

CHAPTER V GYRO-PLASMA PROBE ONBOARD THE SPACECRAFT REXS

§ 1. Introduction

On August 19, 1972, REXS (designated as DENPA after injection into the orbit) was launched to observe space plasma parameters, VLF plasma waves and geomagnetic field in the orbit with the perigee of 240 km the apogee of 6570 km, and inclination of 31°. In the spacecraft (77 cm diagonal length and 68 cm tall, with three 2m antennas, see Fig. 5-1), the "Impedance Probe for Satellite Observation (IPS)" has been installed together with other payloads that were planned to make an integrated observation for plasma structure and wave-particle interaction phenomena in the ionosphere and the low part of the magnetosphere. These equipments include the electron temperature probe (TEL), the electromagnetic and plasma wave receiver (PWP), the flux-gate magnetometer (MGS), the cyclotron instability experiment (CIE) and the electron beam analyser (EBA).

The swept frequency impedance probe IPS, which is designed to measure ionospheric plasma parameters, consists of an impedance measuring equipment, automatic sample-detection sub-systems and a 2m antenna as a sensor immersed in space plasma. The impedance measuring equipment is known as a gyro-plasma probe. Various plasma resonance frequencies are detected and antenna impedance values at several frequencies are measured. Those digitalized data are fed to PCM telemetry through a data sampling system.

The pre-flight operation and plasma-simulation tests were found to be satisfactory; they provided, also, the calibration data on equipment characteristics at different temperature values that can be realized in the flight condition.

In this chapter, all of the technical information to construct the IPS system for the REXS satellite are given in detail in section 2. Operational Characteristics of pre-launching tests and the data handling method are given in sections 3 and 4.

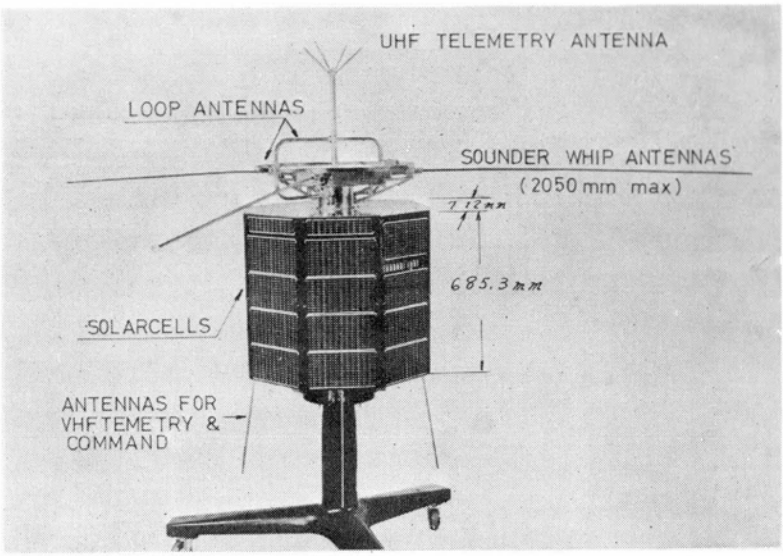

Fig. 5-1 Spacecraft REXS.

Design Concept of Gyro-plasma Probe The gyro-plasma probe for the REXS satellite (IPS) is designed to measure the antenna impedance characteristics as a function of frequency over a wide range which includes various plasma resonances. Since the observed data are transmitted through a time-sharing PCM telemetry, the onboard data processing system are required to provide all digital information of measured plasma resonances and antenna impedance values.

A block diagram of the general concept of IPS is shown in Fig. 5-2. The system consists of the high frequency gyro-plasma probe (IPH), the low frequency gyro-plasma probe (IPL), the frequency calibration circuits (IPS CAL), the timing control signal generator including the antenna switching circuit, and the data processing system.

The swept frequency ranges are 0.2-15 MHz for IPH channel and 0.3-15 kHz for IPL channel. The upper hybrid resonance frequency (f_{UHR}) and the sheath resonance frequency (f_{SHR}), and antenna admittance values are detected and stored in the IPH channel. The lower hybrid resonance frequency (f_{LHR}) is detected and the antenna admittance values

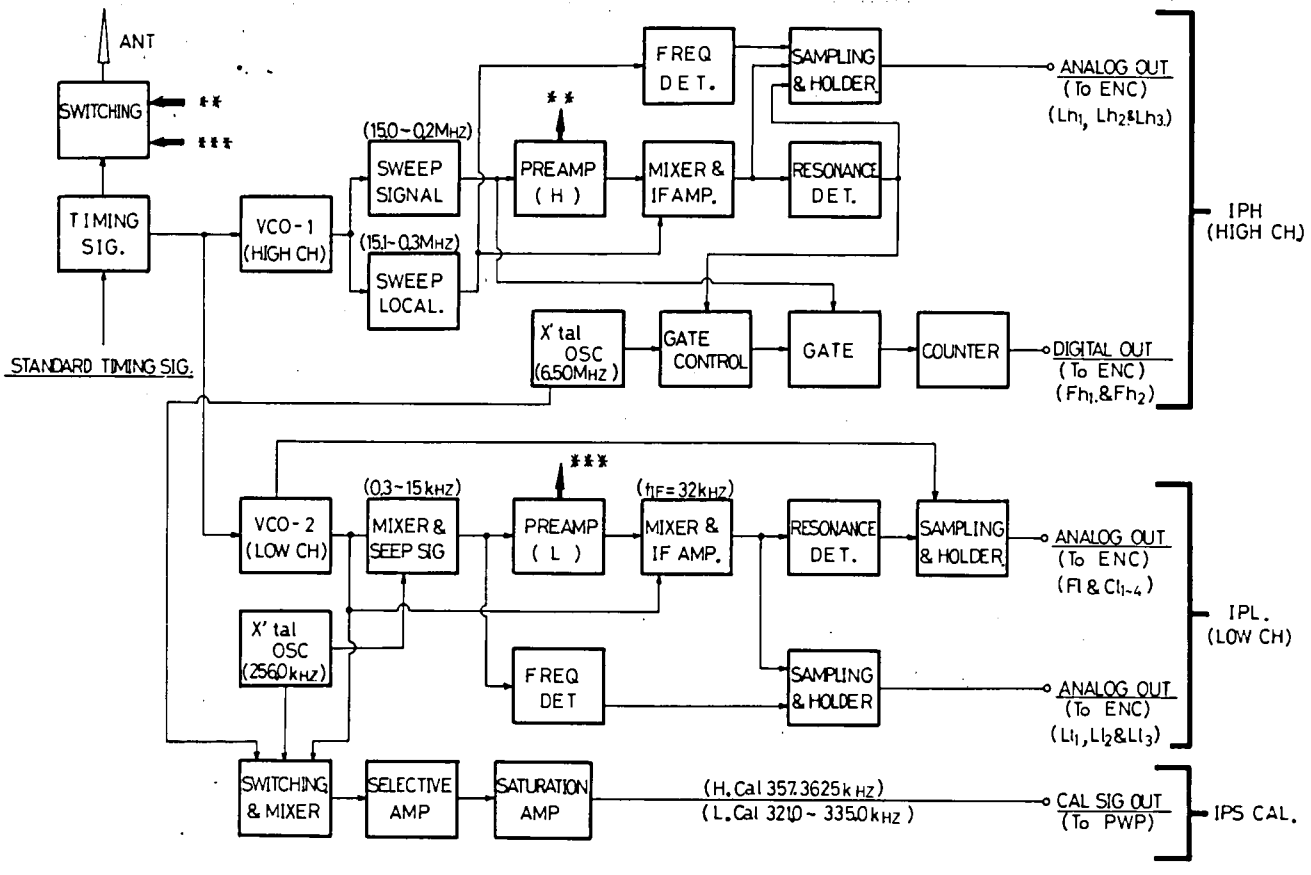

Fig. 5-2 Block diagram of IPS instrument.

are sampled and stored in the IPL channel. The measuring items are summarized in Table 5-1. For the reference, an analog form of the admittance-frequency curve of an antenna in a plasma is shown in Fig. 5-3.

Both the IPH and IPL systems consist of r.f. swept signal generator, and data processing circuits. Utilizing the frequency spectrum analyser technique, the output signal from the capacitance bridge is amplified and mixed with local sweep signal to be IF amplitude modulated signal, and it is compressed by the logarithmic operational amplifier. As for the resonance frequency detection of IPH, the triggering signal to the gate control circuit is fed by the monostable multi-vibrator after resonance identification through the differentiator and level comparator.

To check the standard frequency, the IPS CAL section is provided. The IPS CAL section consists of the switching circuit, mixer, selective amplifier and saturation amplifier.

The timing signal generator produces the various time-sequence control pulses for the data processor and switching circuits using the standard timing pulse out of the timing encoder instrument of this spacecraft.

To check the standard frequency, the IPS CAL section is provided. The IPS CAL section consists of the switching circuit, mixer, selective amplifier and saturation amplifier.

The timing signal generator produces the various time-sequence control pulses for the data processor and switching circuits using the standard timing pulse out of the timing encode instrument of this spacecraft.

To design IPS circuits, as a satellite-borne instrument, following constraints should be observed.

i) To reduce hard-wave components and their weight.

ii) To minimize the power consumption; circuits are operated in time-sequencially by switching the power source, except for the common parts where the high stability is required.

iii) To secure the reliability of operations in a thermal vacuum environment and in the radiation hazard ; individual instru-

Table 5-1 Observation items and abbreviations.

Abbreviation		Items
IPH	Fh_1	Upper Hybrid Resonance Frequency
	Fh_2	Sheath Resonance Frequency
	Lh_1	Equivalent Capacity at 300 KHz
	Lh_2	Equivalent Capacity at UHR
	Lh_3	Equivalent Capacity at 13 MHz
IPL	$F\ell$	Lower Hybrid Resonance Frequency
	$C\ell_{1\sim4}$	Frequency Calibration
	$L\ell_1$	Equivalent Capacity at 1.25 KHz
	$L\ell_2$	Equivalent Capacity at 3.80 KHz
	$L\ell_3$	Equivalent Capacity at 6.65 KHz

The equivalent capacitance is the absolute value of the representative antenna admittance devided by the operating angular frequency.

ment parts are tested under simulated space conditions before the integration of circuits.

PCM Telemetry System The data transmission has been made through two telemetry channels at 136.695 MHz (VHF TM) and 400.500 MHz (UHF TM) with PCM/DPSK/AM (Pulse Code Modulation/Differential Phase Shift Keyed/Amplitude Modulation). FM/AM mode (IRIG BAND #10) is also used in UHF telemetry channel, the operation of this channel being selected by the command item "SIG. CHANGE-2". The observed data has been stored in the onboard data recorder which is capable to store the data (recording time of 133 min and playback time of 7 min). The outline of the signal flow is shown in Fig. 5-4. The telemetry signal is 768 Hz square wave phase shift-keyed by a 64 bps split-phase-mark code stream in a real-time mode, and 3648 Hz square wave phase-shift-keyed by a 1216 bps split-phase-mark code stream in a playback mode.

In the present PCM coding, one sampling datum is quantized by 8 bits pulses which correspond to decimal counts of 255, and the bit rate of this data transmission system in a normal sampling mode is 64 bits. One frame of the telemetry unit consists of 32 words, that

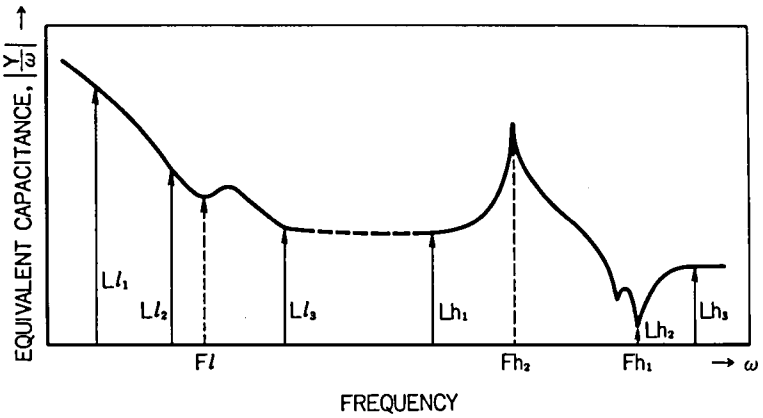

Fig. 5-3 Schematic illustration of admittance-frequency characteristics. Frequency range 1 KHz-15 MHz, equivalent capacitance = admittance/frequency.

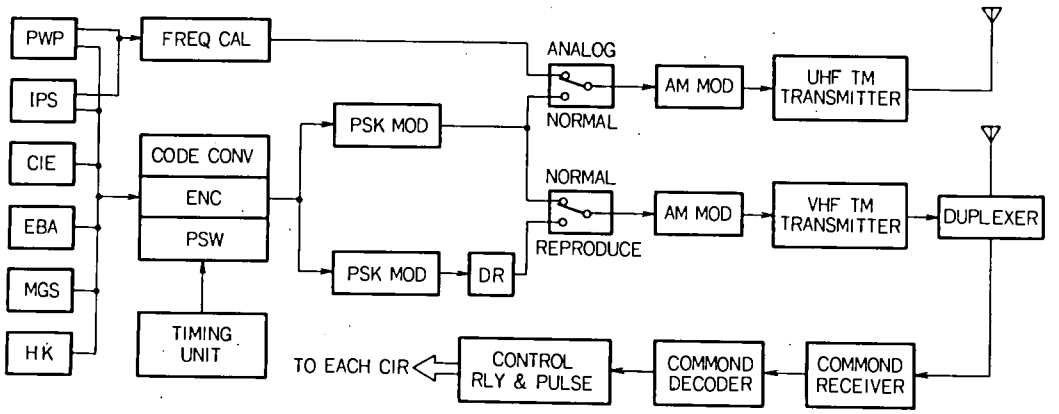

Fig. 5-4 Signal flow of science payloads.

is transmitted in 4 sec; that is defined as one mode. In the REXS satellite system the mode changes in cyclic form; a period of one rotation of these modes is 32 sec that contains 8 frames.

The telemetry mode format of the time-sequential words is shown in Fig. 5-5, in which the data obtained with the gyro-plasma probe are allocated in mode II_1 (IPH) and Mode II_2 (IPL). SY is a frame

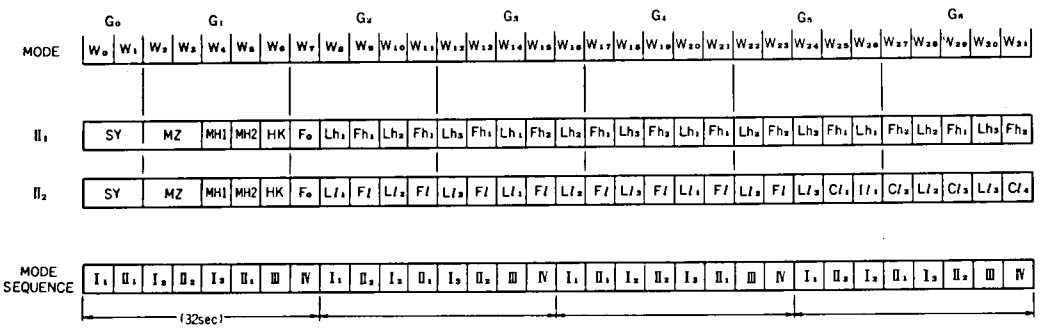

Fig. 5-5 Telemetry mode format; II_1 for IPH and II_2 for IPL.

synchronous pattern and MZ, $MH_{1\sim2}$, and HK are the axial component, two horizontal components of geomagnetic field, and the house keeping data, respectively. F_0 is used as a frame counter to identify the frame mode from I to IV.

§ 2. Instrumentation of the Gyro-plasma Probe

2.1 High Frequency Gyro-plasma Probe

The detailed circuit designs and construction for the high frequency gyro-plasma probe (IPH) are given. The swept frequency signal is generated by the voltage controlled oscillator, buffer amplifiers, crystal oscillators, mixers, and video-amplifiers with low pass filters. The antenna impedance is measured by the capacitance bridge with pre-amplifier, the output signal from which is converted to IF signal (100 KHz) and detected through the IF amplifier and the linear detector. The frequency and resonance detectors for identification of the time at 300 KHz, 13 MHz, f_{UHR}, and f_{SHR} associated with logarithmic and linear amplifiers, sampling-hold circuit and data processing circuits are presented. The gate width control circuit with a crystal oscillator and 8-bit binary counter for Fh_1 and Fh_2 are also explained.

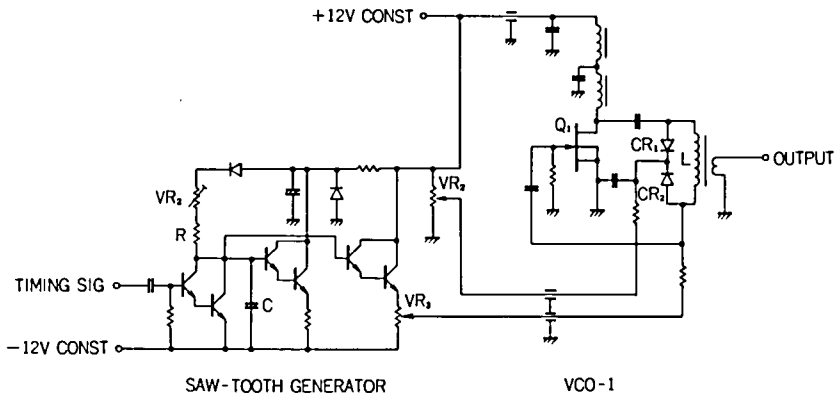

Fig. 5-6 Saw-tooth generator and voltage controlled oscillator.

Saw-tooth Generator and Voltage Controled Oscillator (VCO1) The saw-tooth generator used in this instrument is a kind of boot-strap circuit as shown in Fig. 5-6. The output swept voltage to VOC1 is a potential difference between two points of trimmer resistor VR_2 and VR_3. The period of the time-base is given by the timing and encoder instrument (TIM-ENC) of the spacecraft and coincides with the time interval of a word rate of ENC, that is, 125 ms.

The voltage controlled oscillator (VCO1) is a Colpitts Type. Q_1 is the sillicon N-channel junction-type field effect transistor (FET), and CR_1 and CR_2 are the epitaxial diffused junction Mesa type silicon diodes (vari-cap diodes), characteristics of which are shown in Fig. 5-7. The frequency of this oscillator is expressed as

$$f = \frac{1}{2\pi}\sqrt{\frac{1}{LC} + \frac{\Delta y}{C_1 \cdot C_2}} \qquad (5.1)$$

where $C_0 = (C_1 \cdot C_2)/(C_1 + C_2)$ and $\Delta y = y_i y_0 - y_r y_f$. C_1 and C_2 are the capacities of the vari-cap diodes CR_1 and CR_2 which change its values depending upon the applied voltage from the saw-tooth generator. y_i, y_0, y_r, and y_f are the input admittance, output admittance, reverse transadmittance, and forward transadmittance of the transistor Q_1,

respectively. Therefore, this type of oscillator is influenced by an active element in general.

The swept frequency range of this oscillator is 77.1 MHz to 62.3 MHz and its output voltage amplitude is 50 mV $\pm$ 1 dB. The relation of the swept frequency to the saw-tooth voltage applied to the VCO 1 is illustrated in Fig. 5-8. The time versus swept frequency is shown in Fig. 5-9.

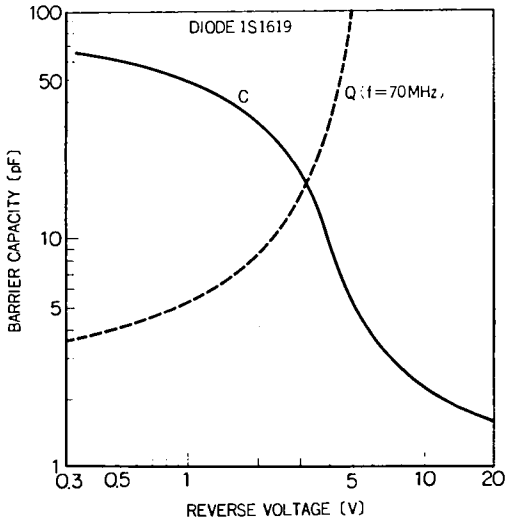

Fig. 5-7 Characteristics of the vari-cap diodes CR_1 and CR_2 (1S1619).

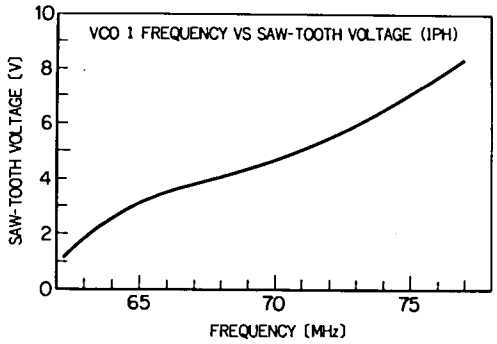

Fig. 5-8 Oscillation frequency versus applied saw-tooth voltage (VCO 1).

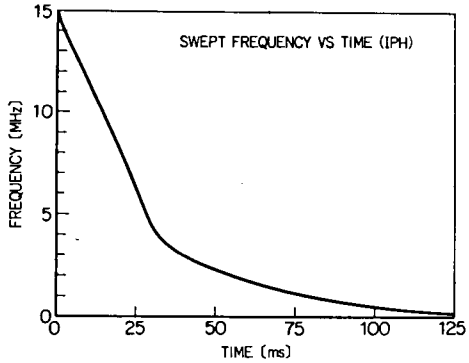

Fig. 5-9 Characteristics of swept frequency versus sweep time.

Swept Frequency Signal and Local Signal Generators The swept frequency signal (77.1 MHz to 62.3 MHz) of VCO 1 is converted into two values by two mixers with two different crystal oscillators. These systems are illustrated in Fig. 5-10. The frequency relation between f_S and $f_{1\sim6}$ is as follows. Mixer 1 and mixer 2 are double balanced modulators, then, $f_3 = f_S \pm f_1$ and $f_4 = f_S \pm f_2$. The high

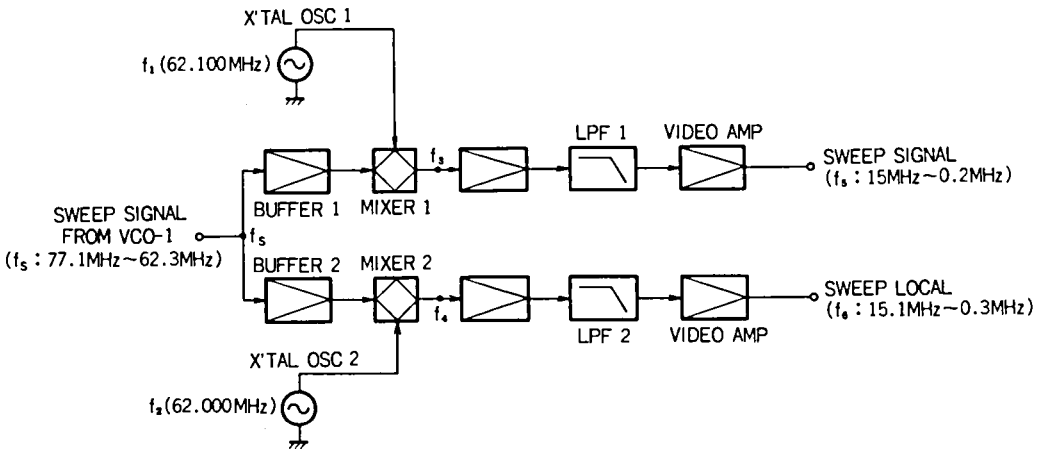

Fig. 5-10 Block diagram of sweep signal generator. Frequency relations between f_s and $f_{1\sim6}$ are given in the parentheses.

frequency components of them are eliminated through the low path filters (LPF 1 and 2), after which $f_5 = f_s - f_1$ and $f_6 = f_s - f_2$.

The frequency difference between f_5 (SWEEP SIGNAL) and f_6 (SWEEP LOCAL) is always 100 KHz, being used for the intermediate frequency of the IF amplifier. As the frequency difference between two crystal oscillators is just 100 KHz, the signal to noise ratio (S/N) is made extremely low by mixing the two signals if the buffer amplifiers are removed. Buffer amplifier 1 and 2 act as isolaters to prevent the crystal oscillator signal on the other channel from mixing with the signal. The electrical circuits diagram of this section is given in Fig. 5-11.

1) X'tal Oscillator: The crystal controlled oscillator used here is a Pierce-type of overtone oscillator with the crystal (HC-18/U) and the frequency stability is 3×10^{-5} /°C (- 30°C ~ + 60°C). Frequencies of LOCAL 1 and 2 are 62.100 MHz and 62.000 MHz, respectively. These signals are used for local signals to the balanced modulators through buffer amplifiers which suppress the interference from signals from VCO 1.

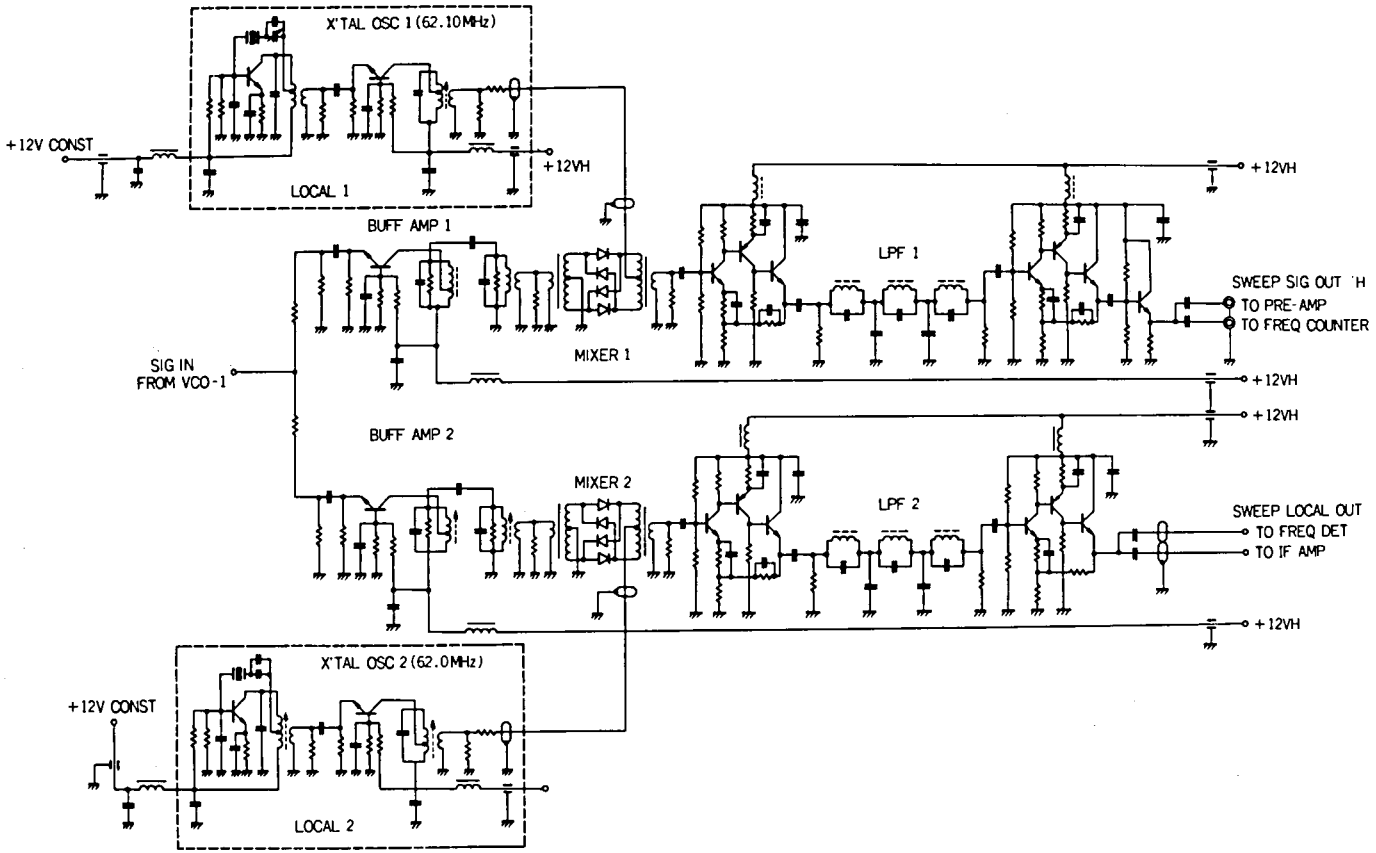

Fig. 5-11 Circuit diagram of sweep signal generator.

2) Buffer 1 and 2: These amplifiers are double-tuned amplifiers which have broad band width and 6 dB gain. The center frequency is 69.5 MHz and the bandwidth is $\pm$ 8 MHz at - 3 dB. As mentioned above, these amplifiers also act as isolaters, and their isolation is - 46 dB.

3) Mixer 1 and 2: The use of double balanced modulators, which possess an appearance somewhat like the push-pull amplifier, automatically elliminates both the carrier (f_S) and the modulating frequency (f_1 or f_2), as well as many of the intermodulation frequencies. The carrier f_S is balanced by the transformer and controls the values of resistance of the diodes against the modulating signal. Namely, the output signal contains frequency components of $f_S \pm f_1$ and $f_S \pm f_2$ without the carrier term f_S.

4) LPF and Video Amplifier: To eliminate a high frequency component of the output signal from the mixer, a low-pass filter (inductive M-drived wave filter) is designed to have an image impedance of 50 Ω, a cut-off frequency of 25 MHz, and a frequency of maximum attenuation of 40 MHz. The video amplifier is a current feedback amplifier which possesses 3 direct-coupled transistors. The cut-off frequency (- 3 dB) is 18 MHz and its gain is 20 dB. Frequency characteristics of this system are shown in Fig. 5-12, and outputs of the swept frequency signals are 2.1 V_{p-p} for the supplied voltage to the pre-amplifier and 4.2 V_{p-p} for the local sweep signal. The sinusoidal wave forms are illustrated in Fig. 5-13.

Signal Detection System The output swept frequency signal from the pre-amplifier associated with a capacitance bridge and a sensor is converted into an intermediate frequency signal by the mixer and IF amplifier. The use of double balanced mixer makes intermediate frequency and upper side band frequency signals, that is, $f_{IF} = f_L \pm f_S$ where F_L is the swept local signal frequency and f_S the swept frequency that is adjusted to make difference 100 kHz from f_L. The upper side band frequency is eliminated by the selective amplifier (IF AMP) and only the intermediate frequency signal is amplified and rectified by

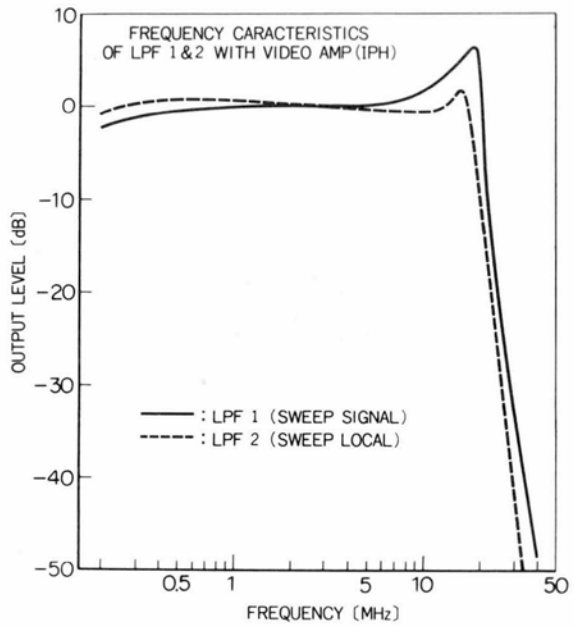

Fig. 5-12 Frequency characteristics of low pass filter and video amplifier.

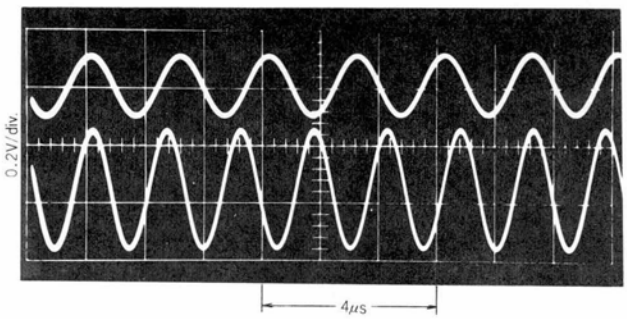

Fig. 5-13 Output wave form; upper trace: 500 kHz sweep signal, lower trace: 600 kHz sweep local signal.

the linear detector. This d.c. signal from the rectifying circuit is supplied to the logarithmic amplifier; the output signal from the logarithmic amplifier is fed to the resonance detector circuit for the upper hybrid resonance frequency (Fh_1) and to the level hold circuit for $Lh_{1\sim3}$. In the other channel, the d.c. signal is fed to the linear amplifier for detection of the sheath resonance frequency (Fh_2). The electrical circuit diagram are described in Fig. 5-14.

1) Mixer: As illustrated in the figure, the mixer is a diode bridge-type double balanced modulator whose input and output impedances

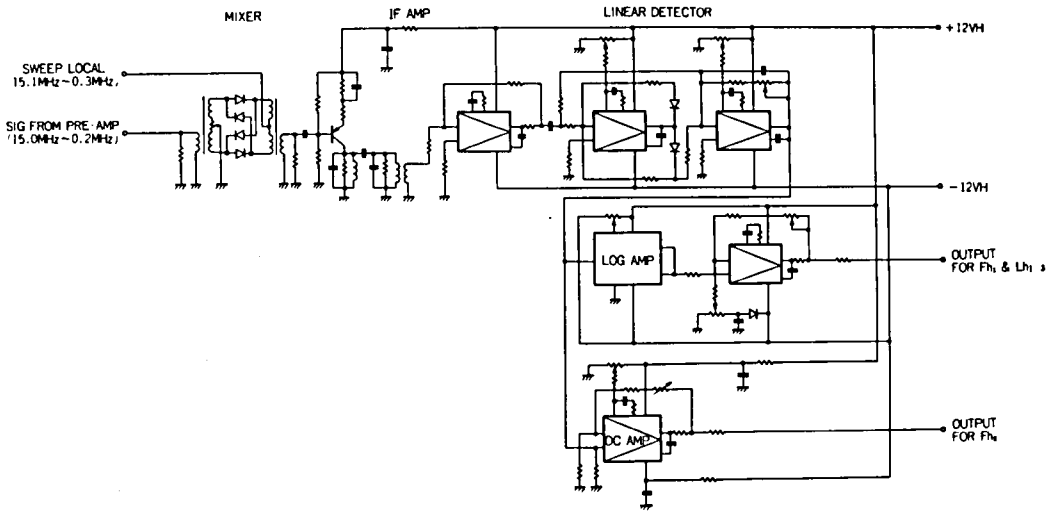

Fig. 5-14 Mixer, IF amplifier, linear detector, logarithmic amplifier and d.c. amplifier.

are 50 Ω and 600 Ω respectively. The unbalance characteristics of the diodes are corrected by the variable resistor VR located at the middle point of the secondary winding of the input transformer. The output swept signal frequency f_L (15 MHz to 0.2 MHz) from the pre-amplifier is converted to 100 kHz by mixing the local swept signal frequency f_S (15.1 MHz to 0.3 MHz).

2) IF Amplifier: A selective amplification of the 100 kHz signal is made by the IF amplifier that is double tuned at the frequency 100 kHz with the band width of ± 1 kHz (at - 3 dB point). Additional amplification by the operational amplifier yields the total gain of 60 dB. The selectivity at 500 kHz is - 60 dB.

3) Linear Detector: The diode rectifier of a conventional type has linear characteristics for the level range of 60 dB. Due to influence of the diode junction voltage and temperature dependence of the voltage-current characteristics, the linearity more than this dynamic range is impossible. In this circuit system, the operational amplifier with the pair diodes and the integrator is used as a linear detector circuit, the dynamic range of which is 5 mV to 5 V (60 dB).

4) LOG Amplifier and Level Shift Amplifier: In order to obtain a

wide dynamic range for the antenna impedance measurement, the signal should be suppressed logarighmically. The LOG module model 4351 (PHILBRICK/NEXUS) is employed as a logarithmic amplifier. The transfer function is expressed as

$$e_{OUT} = [\ A \log_{10} \frac{\text{Imput Voltage}}{\text{Reference Voltage}}\ ] \qquad (5.2)$$

where the sensitifity A is 1 V/decade. The input - 1 mV to - 10 V is compressed to about - 2 V to + 2 V. This output voltage is transformed to 0 V to 4 V through the level shift amplifier. The transformed signal in 0-4 volts range is used for automatic detection of the upper hybrid resonance (Fh_1) and the admittance values ($Lh_{1\sim3}$). The characteristics of the input versus output level of this system are shown in Fig. 5-15.

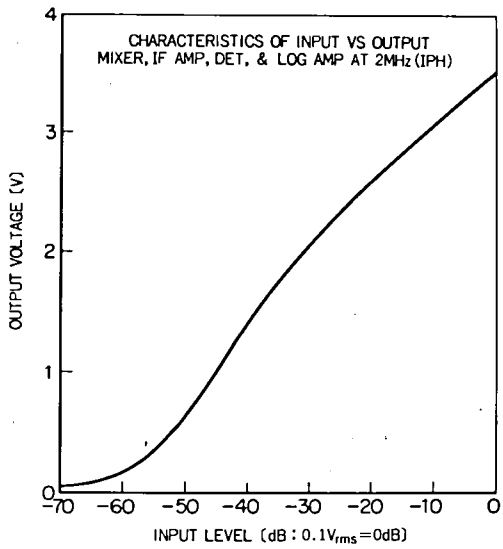

Fig. 5-15 Characteristics of input versus output of IF and logarithmic amplifiers. Dynamic range ≃ 60 dB.

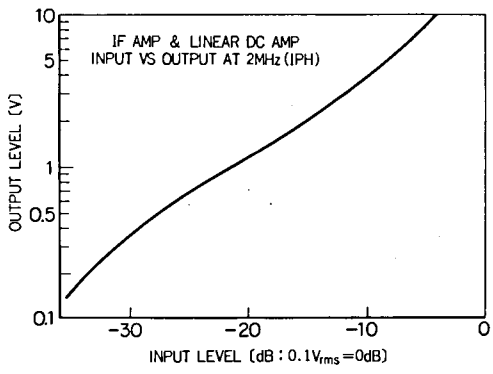

Fig. 5-16 Characteristics of input versus output of IF and linear d.c. amplifiers. Dynamic range ≃ 40 dB.

5) Linear D.C. Amplifier: The logarithmic amplification of the antenna impedance is inconvenient to detect the sheath resonance frequency, because the sheath resonance is characterized by a peak value of the admittance that can be compressed if the logarithmic amplifier is used. The d.c. linear operational amplifier is then employed. The characteristics of input versus output level of this system are shown in Fig. 5-16.

Frequency Detector For the automatic measurement of the antenna admittance value at a given frequency, a control signal is fed to a sampling-hold circuit at the time when the swept frequency coincides with a given frequency. The frequency detector circuit for 0.3 MHz is illustrated in Fig. 5-17. For this purpose the input sweep signal with the frequency f_L is supplied to the L-C tank circuit that are tuned at 0.4 MHz and 13.1 MHz to give the time of detection at 0.3 MHz and 13 MHz respectively. When the sweep signal f_s is fed to the tank circuit, the sweep signal level is changed at the given frequencies due to reaction of the LC resonance circuit. This change is unsuitable for the antenna impedance measurement. The output signals from the tuned circuit indicate r.f. pulse form which is rectified ty a diode that produces a pulse. The wave forms of the output signals from the L-C tank circuits and the monostable multivibrators are illustrated in Fig. 5-18. The produced pulse can be reshaped through a Schmitt trigger circuit. A pulse from the Schmitt trigger circuit induces a transition from the stable state of a monostable multivibrator to the quasi-stable state. The monostable multivibrator may remain in this quasi-stable state for 100 μs which is determined by the RC time constant, and return from the quasi-stable state to the stable state, spontaneously. Thus, the rectangular wave form is obtained; this pulse gates the circuit for the automatic sampling of the Lh_1 and Lh_3 values at the frequencies of 0.3 MHz and 13 MHz, respectively.

Automatic Data Sampling System The signals to the PCM telemetry transmitter should be adapted to the time-shared telemetry channels.

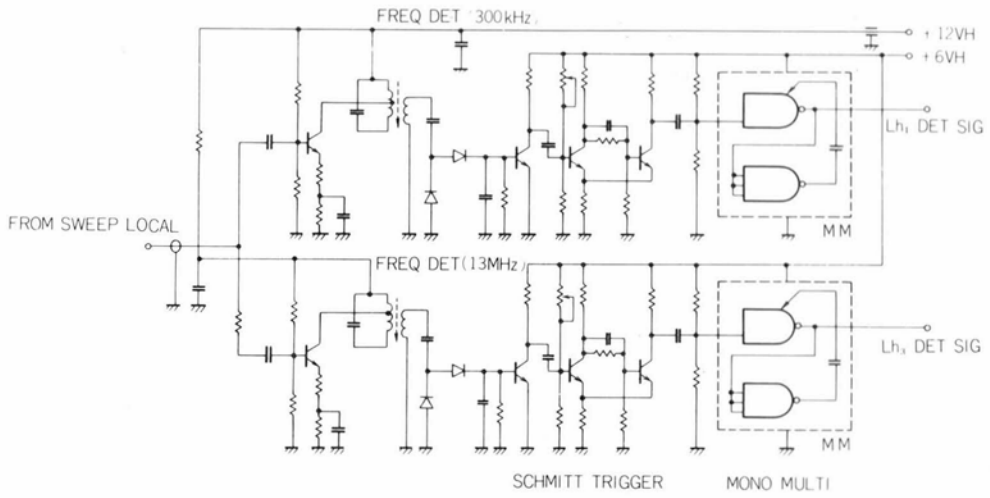

Fig. 5-17 Frequency detector circuits (0.3 MHz and 13 MHz)

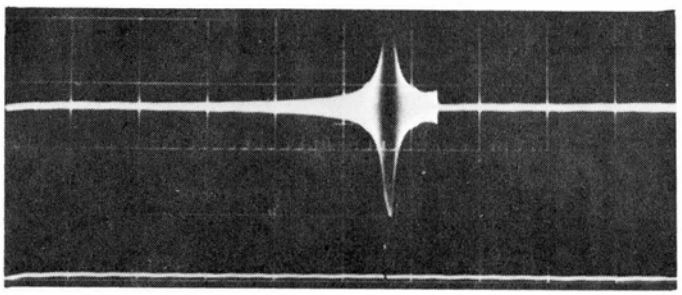

(a) 0.3MHz FREQ DET (20ms/div.)

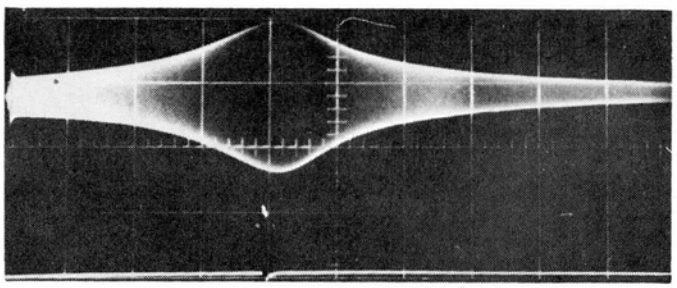

(b) 13MHz FREQ DET (2ms/div.)

Fig. 5-18 Output wave form from the tuned amplifier (upper trace) and frequency detect pulse with pulse width of 100 μsec from the monostable multi-vibrator (lower trace).

The antenna admittance levels at frequencies 0.3 MHz, f_{UHR} and 13 MHz, that are obtained at output points of the logarithmic amplifier, are sampled and stored when frequency detection and resonance detection pulses are submitted to the gate control circuit at the time of swept frequency coincidence at 0.3 MHz, f_{UHR} and 13 MHz. For the identification of upper hybrid resonance, the output signal from the logarithmic amplifier is applied to two circuits; one is a differentiator which produces a gating pulse at the resonance and another is a comparator which excludes the pseudo resonance spikes raised by noise contamination. Since the upper hybrid resonance is characterized by the minimum of the admittance versus applied swept frequency, the reference level of comparator for upper hybrid resonance detection is designed to be the antenna admittance value in free space. The sheath resonance can be detected by differentiating the output signal from linear d.c. amplifier. The detection of sheath resonance is thought to be negligible interference from the small level noise because the resonance is characterized by maximum value of antenna admittance. Therefore the comparator is not used in this system. Both upper hybrid resonance and sheath resonance frequencies (Fh_1 & Fh_2) are measured by a frequency counter that is gated for the pulse counting triggered by these resonance detection pulses. A functional block diagram and electrical circuit of this section are illustrated in Fig. 5-19 and 5-20. The differentiator consists of emitter follower amplifiers, low pass filters, differentiators and Schmitt trigger circuits. The low pass filter with cut-off frequency of 1 kHz is used for the noise screening. The time differentiation of admittance value versus swept frequency at the output point of the logarithmic amplifier is obtained by R-C circuits. At the resonance point, the differenciated signal gives a turn-on signal to the grounded-base junction transistor which drives a Schmitt trigger circuit. The Schmitt trigger circuit produces a gating pulse for the monostable multivibrator. The performance of the comparator circuit is illustrated in Fig. 5-21, and also the output signals of the monostable multivibrators for parallel and series resonances are shown in Fig. 5-22; signals are responsed for the electrical parallel and series resonant

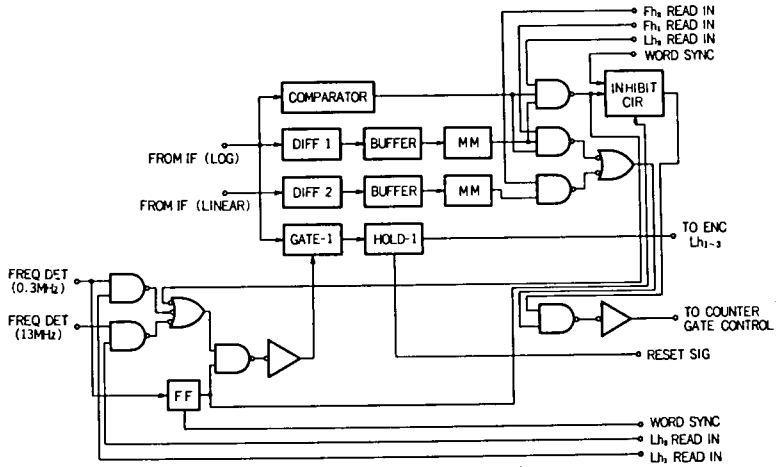

Fig. 5-19 Functional block diagram of resonance detectors for Fh_1 and Fh_2 and sampling-hold circuit for $Lh_{1\sim3}$, including inhibit circuits.

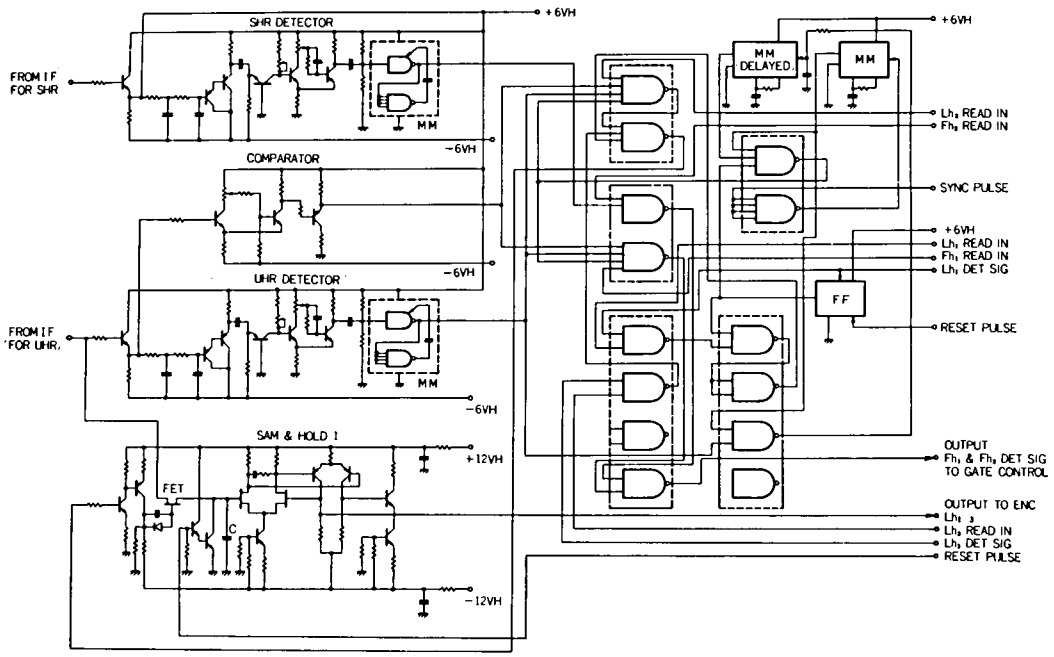

Fig. 5-20 Resonance detectors and sampling-hold circuit.

circuit impedance.

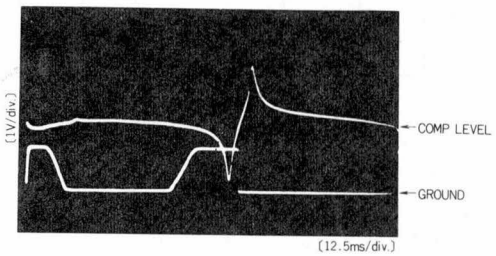

Fig. 5-21 Pulse wave form (lower trace) from the comparator; dummy resonance circuit are used. The wave form of output signal from the logarithmic amplifier is surperimposed (upper trace).

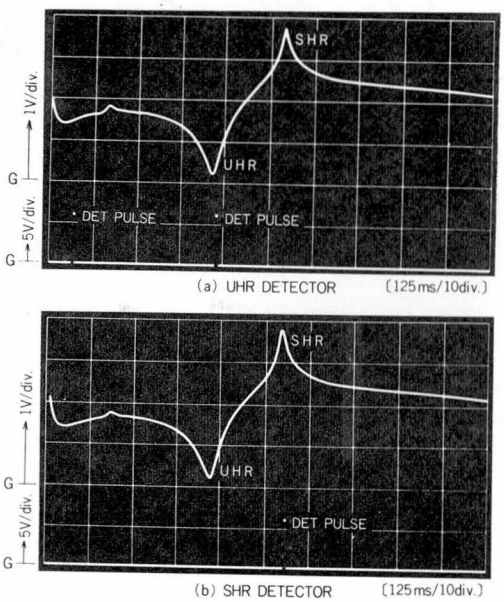

Fig. 5-22 Output pulse of resonance detector; output from logarithmic amplifier is superimposed (upper trace).

1) Sampling-Hold Circuit: The sampling circuit consists of junction type EET's that works as an analog switching elements; these gates are opened by a trigger from the data channel selector as will be discussed later. The sampling gate time is 100 μs, i.e., the same interval with the pulse width of the monostable multivibrator. Sampled potential values are stored in a charging condenser C and discharged to zero value by the reset signal. The potential of C is transmitted to the encoder circuit (ENC) through a negative feedback d.c. amplifier that operates as buffer circuit with a high input impedance. The gain of this amplifier is set to 0 dB. The input versus output characteristics of sampling-hold circuit are given in Fig. 5-23. The operation time sequence for a typical impedance function is illustrated in Fig. 5-24.

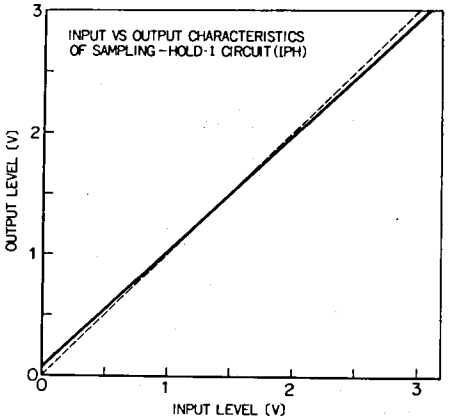

Fig. 5-23 Input versus output characteristics of the sampling-hold circuit.

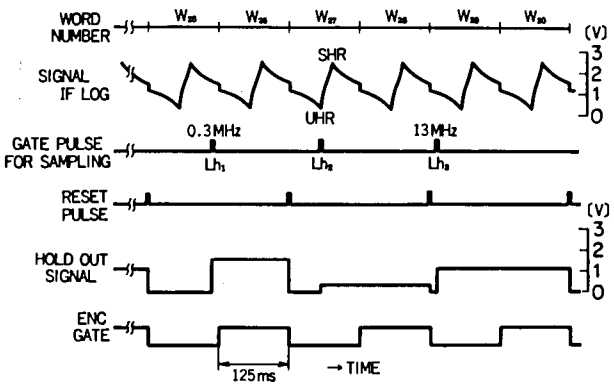

Fig. 5-24 Schematic time sequence of the sampling-hold circuit. Lh_1 whose detect pulse is fed to sampling-hold circuit at W_{25}, is transmitted to ENC at W_{26}, being reset at end of W_{26}.

2) Data Channel Selector Circuit: The mode II_1 ($W_8 \sim W_{31}$) of telemetry time sequence is used for IPH; odd word numbers are for the counted digital frequency of upper hybrid and sheath resonances (Fh_1 and Fh_2); and even word numbers are for the sampled values of admittance levels $Lh_{1\sim3}$. By using the data channel selector circuit, time parallel signals of $Lh_{1\sim2}$ in the hold circuits are rearranged to be the time serial signal for adaption of the time-sharing telemetry sequence. The data are sampled and stored during one word interval of the telemetry sequence before reading out to ENC. Near the starting and ending frequencies of the sweep signal, pseudo pulses are generated due to the circuit characteristics. An active elimination of these pulses are made by using logical inhibit circuit. The operational procedure of the inhibit circuit is shown in Fig. 5-25. The time duration of the inhibit pulses are designed to be 10 ms and τ_0. τ_0 is determined by the set trigger of the first Lh_1 detect pulse and the reset trigger of the word synchronous pulse. The output pulse wave form of the delayed monostable multivibrator is shown in Fig. 5-26.

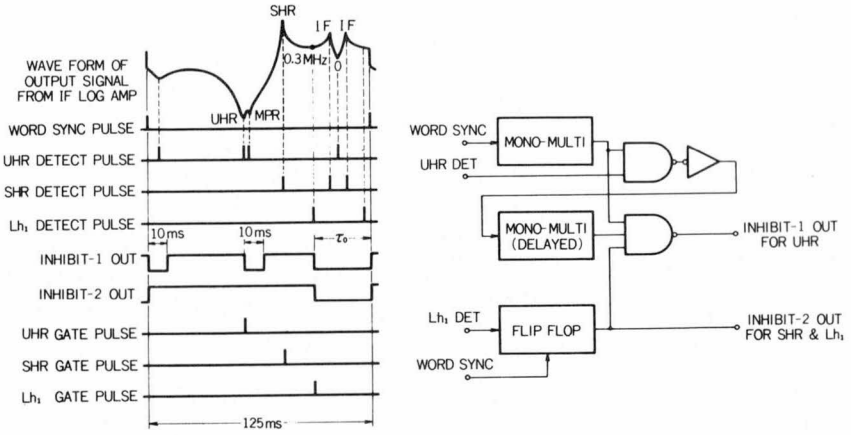

Fig. 5-25 Operational performance of inhibit circuit.

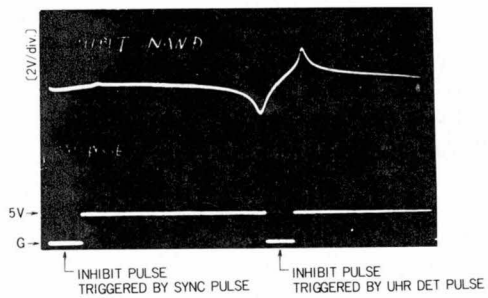

Fig. 5-26 Output pulse (lower trace) of delayed monostable multivibrator of the inhibit circuit. First pulse is triggered by word synchronous pulse and second pulse is triggered by UHR detect pulse. Output curve from logarithmic amplifier is superimposed (upper trace).

Gate-width Control Circuit The gate-width control circuit illustrated in Fig. 5-27 generates a gate pulse to the frequency counter for Fh_1 and Fh_2, and the frequency calibration signal. The crystal controlled oscillator of Pierce-type is used as the standard signal (6.5000 MHz). This standard frequency is demultiplied by 16 through the 8-bit shift resistor coupled to the flip-flop circuit.

The signal of 406.25 kHz (=6.5000 MHz/16) is applied to two circuits; one is the flip-flop circuit which demultiplies the signal by 4 and sends to the frequency calibration circuit, the other is an 8-bit shift resistor. The logical function of the 8-bit shift resistor is given as,

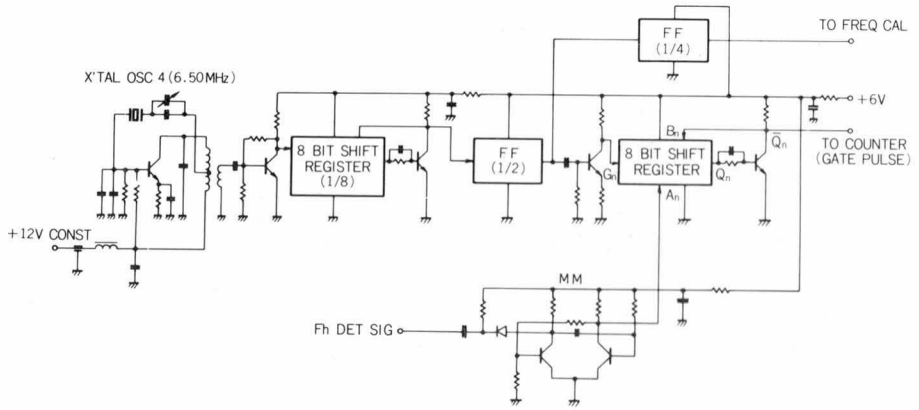

Fig. 5-27 Gate width control circuit.

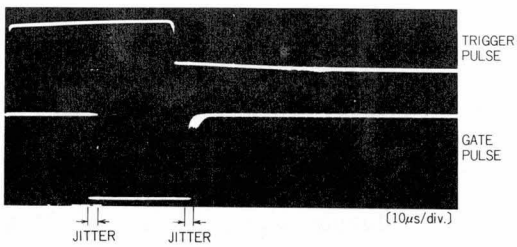

Fig. 5-28 Gate pulse (lower trace) and output pulse of the monostable multivibrator (upper trace). Gate width is 19.692 μsec and jitter of pulse appears because several traces are superimposed.

$$A_n \cdot B_n = Q_{n+8} \qquad (5.3)$$

where A_n is the output of the mono-multivibrator which is triggered (say at n = 1) by the UHR and SHR detect pulses, and B_n is the inverted pulse of Q_n. The clock time τ of pulse G_n is equal to 1/406.25 kHz, i.e., τ = 2.4615 μs. Since the pulse width is less than 16 τ (n = 16) and longer than 8 τ (n = 8), Q_n = 1 ($9 \leq n \leq 16$). Consequently, the output pulse width of the 8-bit shift resistor is just 8 τ (19.692 μs) being controlled accurately by frequency of the crystal controlled oscillator and gated at the time after 8 τ period from triggering of the mono-multivibrator. This pulse is used as a gate pulse to the frequency counter for Fh_1 and Fh_2. The gate pulse and the output pulse of the mono-multivibrator are shown in Fig. 5-28. Jittering is raised by time difference between clock pulse and HUR or SHR detect pulse.

Frequency Counter The swept frequency is counted by the series of 8-bit binary counters during the gating interval, for Fh_1 or Fh_2, that is fed from the gate width control circuit, and transmitted to ENC after time-parallel to time-serial conversion through the data selector. The electrical circuit for this operation is illustrated in Fig. 5-29.

The swept signal is fed to the video amplifier to get 20 dB amplification for triggering the Schmitt circuit. The output wave form at the Schmitt trigger circuit is differentiated and fed to the 8-bit binary counter through the gate circuit. The pulse width of this gate circuit is 19.692 μs, equivalent to the frequency of 50.782 kHz. The available maximum frequency of this counter is 12.949 MHz, i.e., 255 (maximum) counts of the 8-bit binary with the unit of 50.782 kHz for one count.

The parallel output pulses from the 8-bit binary counter are fed to the data selector and read out in time-series form by the Fh_1 or Fh_2 read out pulse from the TIM-ENC circuit. The data selector is a TTL-MSI (Transistor Transistor Logic-Middle Scale Integration) circuit SN 54151 (TEXAS Inst.), the block diagram of which is shown in Fig. 5-30. This circuit element are used to performs the parallel-to-serial conversion. The logical operation of the circuit is expressed as,

$$Y = \overline{S}(\bar{A}\bar{B}\bar{C}D_0 + A\bar{B}\bar{C}D_1 + \bar{A}B\bar{C}D_2 + AB\bar{C}D_3 + \bar{A}\bar{B}CD_4 + A\bar{B}CD_5 + \bar{A}BCD_6 + ABCD_7),$$

and $$W = \overline{Y} \qquad (5.4)$$

where the $D_{0\sim7}$ are the inputs from the binary counter; A, B, and C are the data selecting pulses generated by the 4-bit binary counter using the read out bit pulses from TIM-ENC and $\overline{A}$ shows the inverted pulse of A. S is the reset pulse. The time sequence of the digital read out pulses to ENC is in series of MSB (Most Significant Bit).

The frequency counting is subjected to the relative error that increases as the frequency decreases, when the gate pulse width is constant

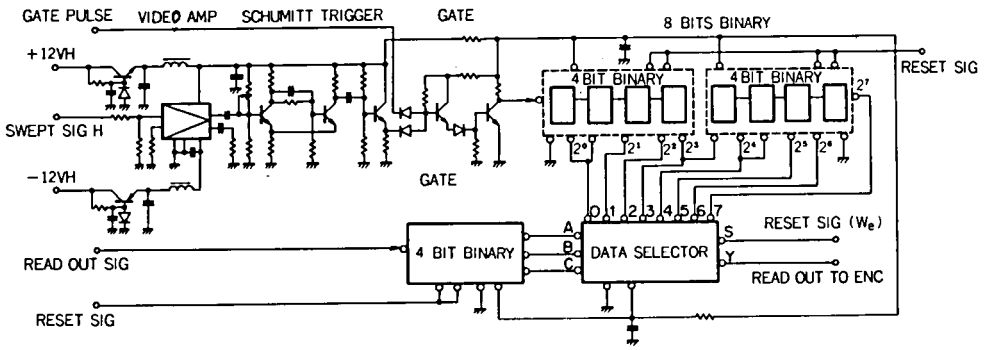

Fig. 5-29 Frequency counter.

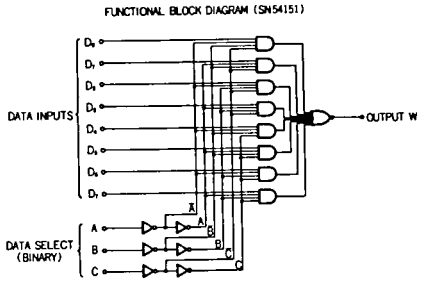

Fig. 5-30 Functional block diagram of data selector, SN 54151

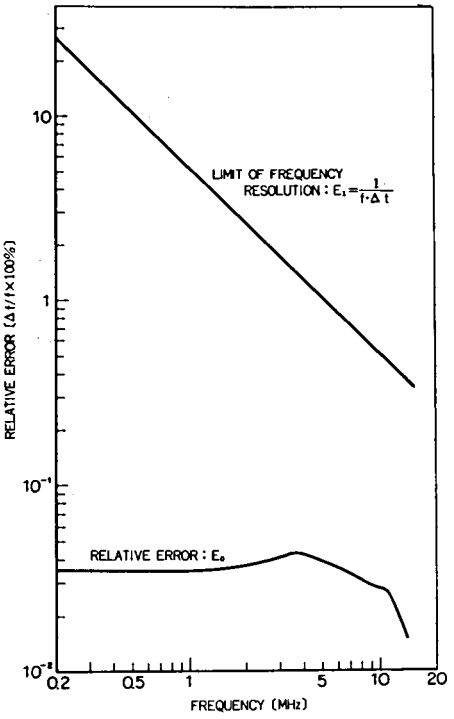

Fig. 5-31 Relative frequency error (E_0 and E_1) of frequency counter system.

while the frequency is swept as linear function of time t. Taking t_1 and t_2 to be the opening and closing times of the gate, the relative error of the frequency E is given by,

$$E = \frac{f(t_1)\Delta\tau - \int_{t_1}^{t_2} f(t)dt}{f(t_1)\Delta\tau} \pm \frac{1}{f(t_1)\Delta\tau} \equiv E_0 \pm E_1 \qquad (5.5)$$

where f(t) is the swept frequency as a function of time t, and $\Delta\tau = t_1 - t_2$ is the gate pulse width. For a constant value of $E(\ll 1)$, the approximate solution of this integral equation is given as

$$f(t) = f_0 \exp(-\frac{2E}{\Delta\tau} t) \mp \frac{1}{\Delta\tau} \qquad (5.6)$$

where $\mp 1/\Delta\tau$ ($\mp$ 50.782 kHz) is the correcting term against the frequency resolution rate of the counter and f_0 is the maximum frequency at $t = 0$. As is shown previously in Fig. 5-9, the time dependence of swept frequency is designed to have an exponential function for f(t), so as to make E_0 independent of t. The estimated relative error E_0 is computed for swept frequency function f(t), shown in Fig. 5-9, as illustrated in Fig. 5-31 with the frequency resolution limit of this counter. E_0 is approximately constant (about 4×10^{-4}) in a range below 10 MHz and negligibly small compared with the frequency resolution limit.

2.2 Low Frequency Gyro-plasma Probe

The antenna impedance as a function of frequency in the low frequency range, including a lower hybrid resonance frequency, can be obtained by the low frequency gyro-plasma probe (IPL). The swept frequency signal is generated by a CR phase shift oscillator, the

frequency of which is controlled by the saw-tooth (serrasoidal) voltage wave form. The frequency is beated down using a crystal oscillator through the mixer, i.e., a kind of beat oscillators is formed. The high frequency side band (65 kHz ~ 79 kHz) of the output signal from the mixer is produced through the high-pass filter and applied to a frequency calibration circuit. The low frequency component (1 kHz ~ 15 kHz) is obtained through the low-pass filter and used as the swept frequency signal that is applied to the antenna and to the frequency detection circuit. The antenna impedance is measured by the capacitance bridge associated with pre-amplifier, the output signal from which is converted to IF signal (32 kHz) and detected through the IF amplifier and linear detector. The frequency and resonance detectors for identification of the time at 1.25 kHz, 3.80 kHz, 10.1 kHz and f_{LHR} associated with the logarithmic amplifier, sampling-hold circuit and data processing circuit are presented.

Swept Frequency Signal Generator The swept frequency signal in a frequency range of 1 kHz to 15 kHz is used for the source signal of the IPL system. The used frequency signal is stepped up from 65 kHz to 79 kHz for the frequency calibration. The block diagram and the electrical circuits which generate these signals are illustrated in Fig. 5-32 and Fig. 5-33.

1) Saw-Tooth Generator: This circuit is a bootstrap sweep circuit that is the same type as is used in IPH saw-tooth generator; but in this circuit the deviation from linearity of the serrasoidal wave form is very small, due to current feedback through the large capacity condenser C_1. The output transistor of the emitter follower circuit are controlled not to saturate at high potential, using three serial diode $D_{1\sim3}$ for the level shift operation. The emitter follower circuit consists of a complementary compound (Darlington) connection of PNP and NPN transistors, in order to set the beginning potential of the saw-tooth to be just 0 volt. The start-end controll of the saw-tooth generation circuit is given by the word synchronous pulse

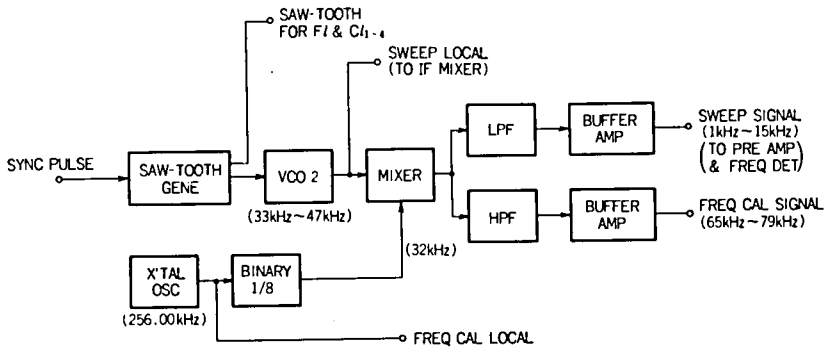

Fig. 5-32 System block diagram of swept frequency signal generator.

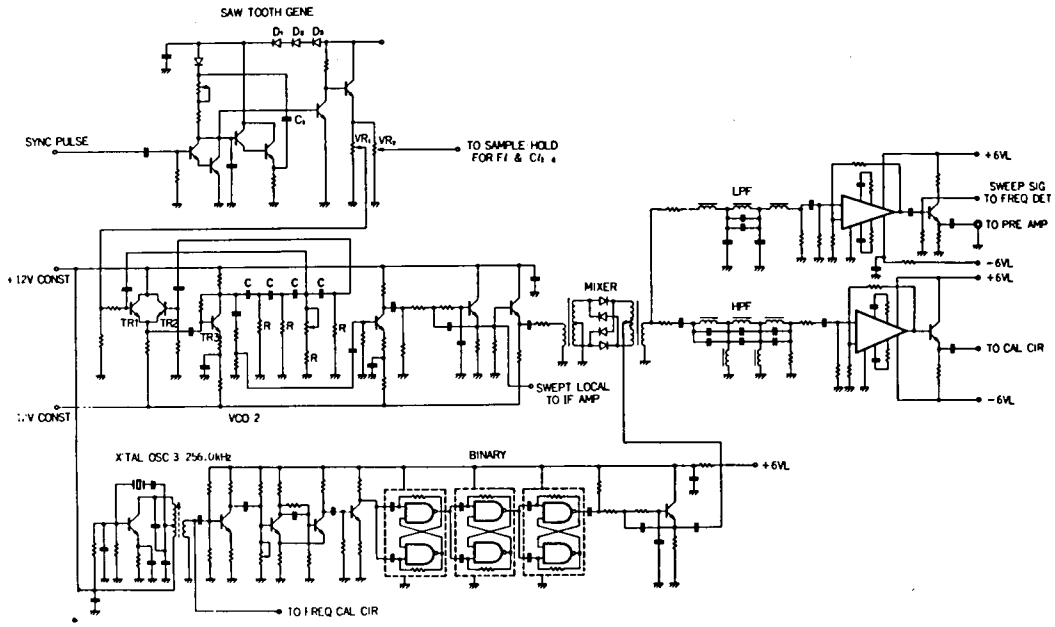

Fig. 5-33 Circuit diagram of swept frequency signal generator.

from TIM-ENC that coincides with a time period of word rate controlling at ENC, i.e., 125 ms. The output signal from the terminal VR_1 is applied to the voltage controlled oscillator and that from VR_2 is used for the reference voltage of $F\ell$ and $C\ell_{1\sim4}$. Wave forms from these terminals are illustrated in Fig. 5-34.

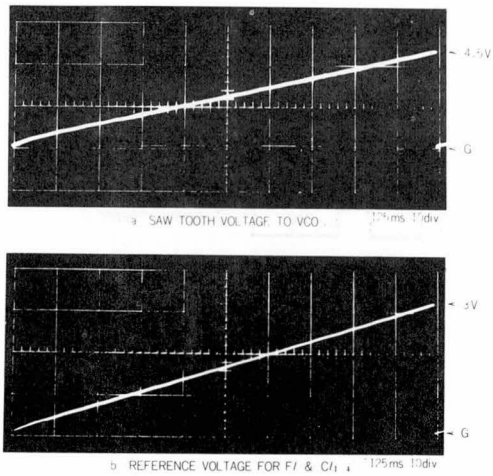

Fig. 5-34 Saw-tooth wave form (0 to 4.5 volts) to voltage controlled oscillator (a), and frequency reference voltage (0 to 3 volts) for Fℓ and $C\ell_{1\sim4}$ (b).

2) Voltage Controlled Oscillator: The voltage controlled oscillator (VCO 2) is the modified high-pass-type phase shift oscillator. The phase of a current is advanced by four CR ladder circuits and the oscillating frequency is selected due to the condition to satisfy that the phase of feedback signal advances by 180° from that of the input signal. In this circuit, the signals having the different phases from 3rd stage and 4th stage of CR ladder circuits are fed back to two inputs of the balanced amplifier (TR_1 and TR_2), and the saw-tooth potential from VR_1 controls the gain of TR_1. The oscillation frequency is determined by the potential ratio of these two feedback signals, that is applied to the input transistor TR_3, as follows,

$$\frac{1}{2\pi RC\sqrt{6}} < f < \frac{1}{2\pi RC\sqrt{10/7}} \qquad (5.7)$$

In this circuit, the oscillation frequency changes from 33 kHz to 47 kHz in accordance with applied saw-tooth potential change of 0 volt to 4.5 volts. This type of a phase shift oscillator is commonly used to generate a signal of frequency at VLF range. An advantage of this circuit is a high operation stability of generating frequency, while

the disadvantage is in the distortion of the wave form to some extent compared with Terman oscillator and other sinusoidal wave oscillators. The output signal from this oscillator is reshaped to be sinusoidal wave form through the active wave filter (12 dB/Oct.).

3) X'tal Oscillator 3: The local oscillator is a Pierce-type crystal controlled oscillator, the generating frequency of which is 256.00 kHz and used for the reference signal of the frequency calibration circuit. The generated signal is also used as a local signal (32.000 kHz), that is fed to a mixer, being devided by 8 through 3-bit binary and the Schmitt trigger circuits.

4) Mixer: The mixer consists of a double balanced modulator which is used in IPH system. As the frequency of the local signal into IF stage from this mixer should be supressed to be - 54 dB, taking the balance of the mixer by the variable resistor that is located at the middle point of the primary coil of output transformer (see Fig. 5-33).

5) LPF, HPF and Buffer Amplifier: The output signal from the mixer contains two side bands. Each side band signal is separated through the low-pass filter and the high-pass filter. The lower side band (1 kHz to 15 kHz) of signal is amplified to apply to the antenna and the frequency detection circuit. The upper side band (65 kHz to 79 kHz) of signal is amplified to use for the frequency calibration. Figure 5-35 shows the frequency characteristics of both low-pass and high-pass filters. The frequency to give maximum attenuation in these filters is designed to be 32 kHz in order to eliminate the leakage signal of local frequency from the mixer. The wave form of swept signal to the pre-amplifier is illustrated in Fig. 5-36 and the characteristics of swept frequency versus time are indicated in Fig. 5-37

Signal Detection System The output swept signal from the pre-amplifier is converted to the intermediate frequency signal (32 kHz) through the mixer. The signal from the mixer is fed to the IF amplifiers; the output signal from the IF amplifier is rectified by the linear detector and compressed logarithmically. The circuit of this section is illustrated in Fig. 5-38. The basic system design of this circuit is the

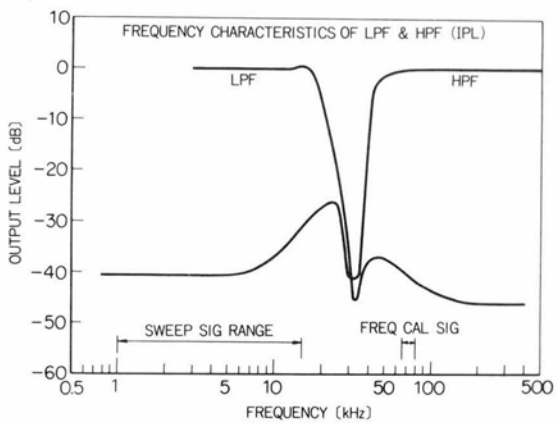

Fig. 5-35 Frequency characteristics of low-pass filter and high-pass filter, maximum attenuation frequency is 32 kHz.

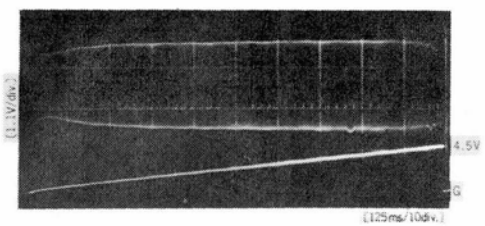

Fig. 5-36 Wave form of sweep signal output applied to antenna. Saw-tooth wave form is supe-imposed (lower trace).

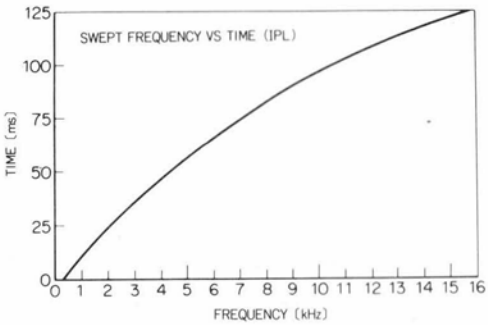

Fig. 5-37 Swept frequency versus time curve.

same as corresponding part of IPH. In this case, the leakage of local swept signal (33 kHz to 47 kHz) should be carefully eliminated by the double balanced modulator. The upper side band of output signal from the mixer should also be depressed by the double tuned selective amplifier with the band-pass filter designed to have the narrow pass-band characteristics (± 600 Hz at - 3dB). This illustrated in Fig. 5-39. The characteristics of input versus output of this circuit are shown in Fig. 5-40. The d.c. signal output from the logarithmic amplifier is applied to the frequency detection circuits for the lower hybrid resonance frequency $F\ell$ and to the sampling hold circuit for absolute values of impedance $L\ell_{1\sim3}$.

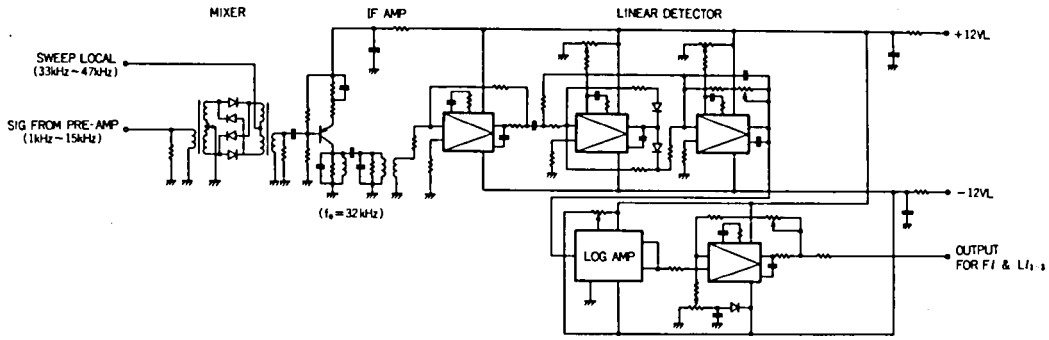

Fig. 5-38 IF amplifier and detector stage.

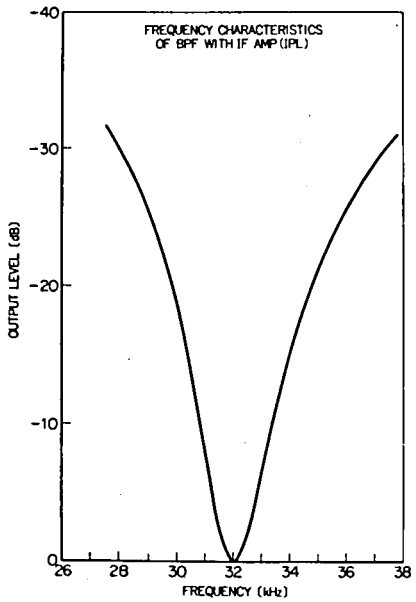

Fig. 5-39 Frequency characteristics of band-pass filter with IF amplifier.

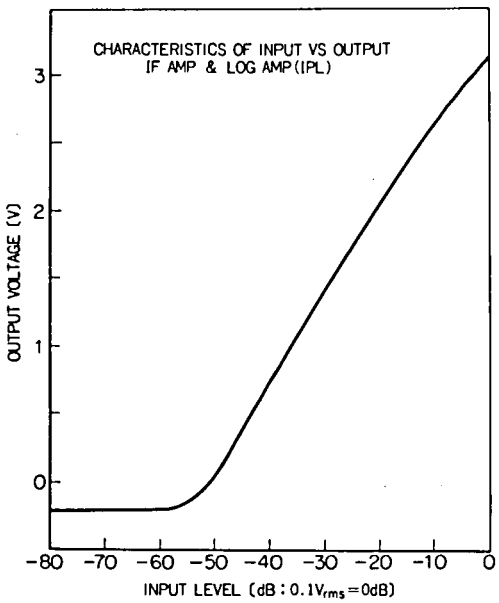

Fig. 5-40 Input versus output characteristics of logarithmic amplifier and IF amplifier. Dynamic range ≈ 60 dB.

Frequency Detector for $L\ell_{1\sim3}$ and $C\ell_{1\sim4}$ To measure the antenna admittance level at fixed frequencies, the control signals to the sampling-hold circuit should be generated at the time when the swept frequency just coincides with a specified frequency. The frequency detector in this circuit, shown in Fig. 5-41, is a super-narrow band selective

amplifier with a RC twin T-section as a feedback circuit, each center frequency ($f_0 = 1/2\pi RC$) of which is designed to be 1.25 kHz, 3.80 kHz, 6.65 kHz and 10.1 kHz. The swept signal is amplified at these frequencies and rectified to give a trigger signal to the monostable multivibrator through the grounded-emitter amplifier. The output pulse width of the monostable multivibrator is 100 μs. Fig. 5-42 shows the resonance wave form at each frequency and the sequence of the output pulses corresponding to frequencies given above.

Lower Hybrid Resonance Detector, Sampling-Hold Circuit and Data Selector The basic concept of the circuit design of resonance detector, sampling-hold circuit, and data selector is the same as corresponding circuits of IPH. For detection of the lower hybrid resonance frequency, the output signal from the logarithmic amplifier is differentiated in terms of time. This signal is formed as a detect pulse, through the monostable multivibrator, to feed to the data selector. The resonance frequency $F\ell$ and frequency calibration levels $C\ell_{1\sim4}$ are expressed in terms of saw-tooth voltage at the sampling time when resonances are detected, or the time when the signal frequency coincides with $C\ell_{1\sim4}$. For the measurement of antenna admittance levels at 1.25 kHz, 3.08 kHz and 6.65 kHz, the output signal from the logarithmic amplifier is sampled at each corresponding frequency; the sampled data are stored until the read-in pulses of $L\ell_{1\sim3}$ are applied to the gate control circuit. The function of data selector is to transform the time-parallel signal to the time-serial signal in accordance with the PCM time-sharing telemetry format for the detected frequency pulses $f_{1\sim4}$ and the resonance pulse. The circuit diagrams of this section are illustrated in Fig. 5-43.

1) Resonance Detector: This circuit is designed to detect the lower hybrid resonance which has equivalent characteristics as a parallel resonant circuit. The circuit is almost the same as the case of the resonance detector used for the upper hybrid resonance detection.
The operation of this resonant detection function is given in Fig. 5-44; this is an example operated by a simulation dummy circuit for the antenna

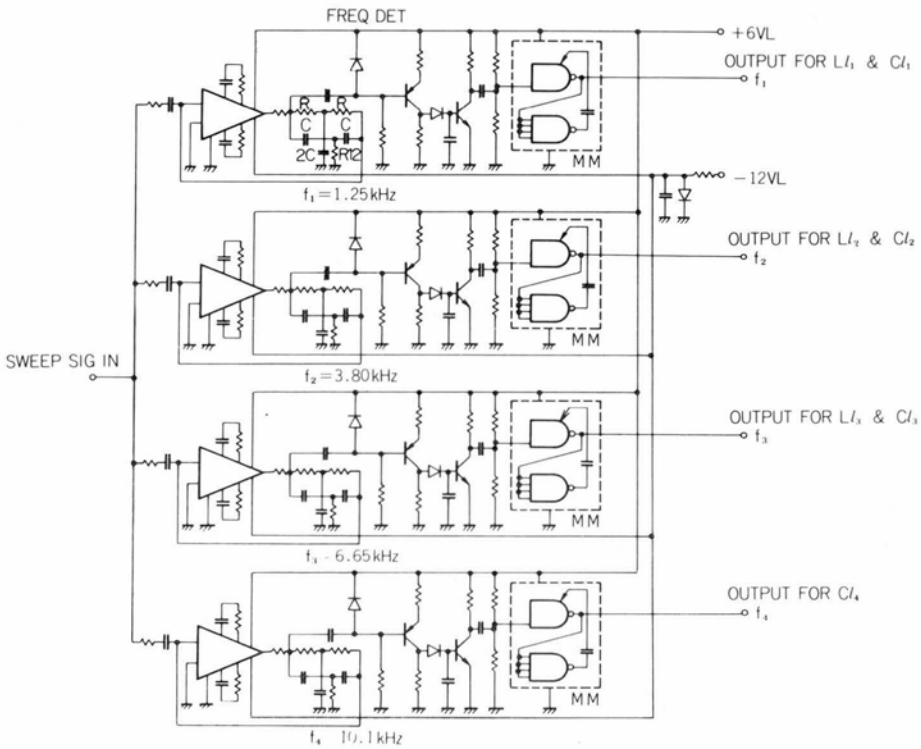

Fig. 5-41 Frequency detector; center frequencies at 1.25 kHz, 3.80 kHz, 6.65 kHz and 10.1 kHz.

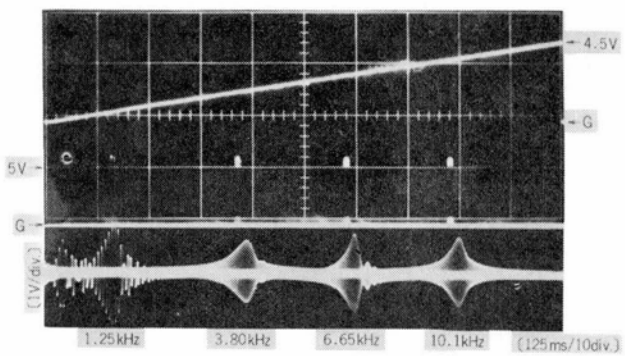

Fig. 5-42 Frequency detect pulse sequence, $f_1 \sim f_4$.; lower trace is resonance wave form of frequency detectors.

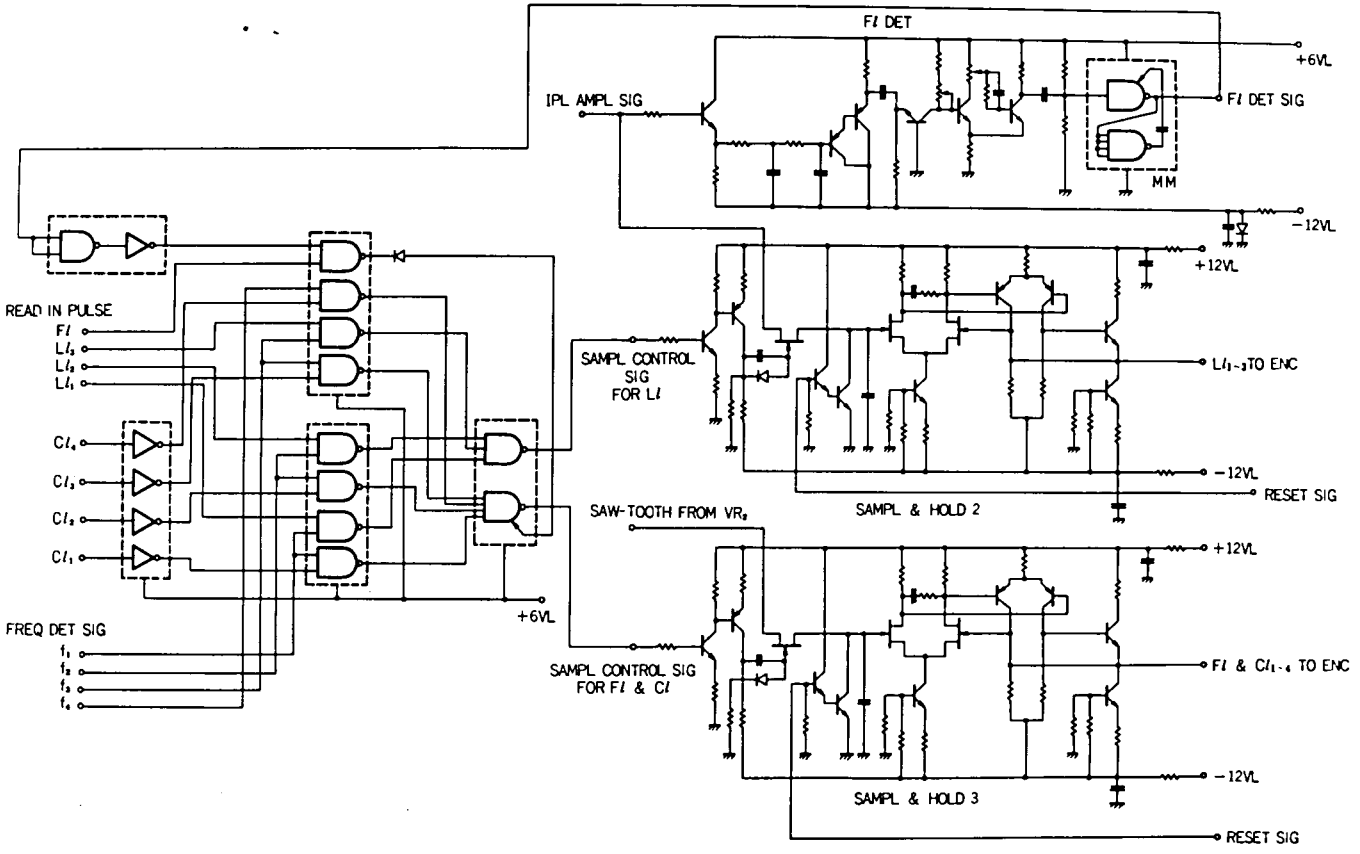

Fig. 5-43 Circuit diagrams of lower hybrid resonance detector, sampling-hold circuit and data selector.

in a plasma, that consists of the parallel and series resonant circuit. The detected pulse at the resonance point is indicated, after reshaped by the monostable multivibrator, with the impedance value obtained from the logarithmic amplifier.

2) Sampling-Hold 2 and 3: The output signal from the logarithmic amplifier gives the absolute admittances; these absolute admittance values are sampled in accordance with the time-sequential gate pulses from the data selector and stored in the charging condenser at frequencies of 1.25 kHz ($L\ell_1$), 3.80 kHz ($L\ell_2$) and 6.65 kHz ($L\ell_3$). The stored data are transmitted to ENC through the d.c. amplifier. The lower hybrid resonance frequency $F\ell$ is transmitted by corresponding potentials of the saw-tooth signal from VR_2. The calibration of this saw-tooth signal is made at frequencies of f_1, f_2, f_3 and f_4 that gives calibration levels $C\ell_1$, $C\ell_2$, $C\ell_3$ and $C\ell_4$. The input versus output characteristics of the sampling-hold circuits (HOLD 2 for $L\ell_{1\sim3}$, and HOLD 3 for $F\ell$ and $C\ell_{1\sim4}$) are given in Fig. 5-45. These function forms of input-output characterictics are used to obtain an accurate input signal level from observed data using the computer.

3) Data Selector: The mode II_2 ($W_8 \sim W_{31}$) of telemetry format is used for the IPL data transmission; odd word numbers are used for the lower hybrid resonance frequency ($F\ell$) and the frequency calibration levels ($C\ell_{1\sim4}$), and even word numbers are used for the admittance levels $L\ell_{1\sim3}$. By using the data selector circuit with read-in signals of $F\ell$, $L\ell_{1\sim3}$ and $C\ell_{1\sim4}$, time-parallel signals of the resonance detect pulse and frequency detect pulses $f_{1\sim4}$ are transformed to time-serial signal in accordance with the time-sharing telemetry format. The data are sampled and stored during one word before the assigned word.

2.3 Capacitance Bridge and Pre-amplifier

As has been previously noted, the gyro-plasma probe system has a capacitance bridge circuit with an antenna. The unbalance potential of the capacitance bridge due to the variation of the antenna

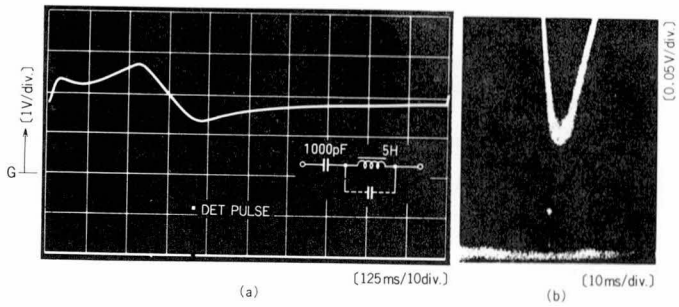

Fig. 5-44 Performance of resonance detector; output wave form from logarithmic amplifier (upper trace) and resonance detect pulse (lower trace). (b) enlarged a part of resonance of (a).

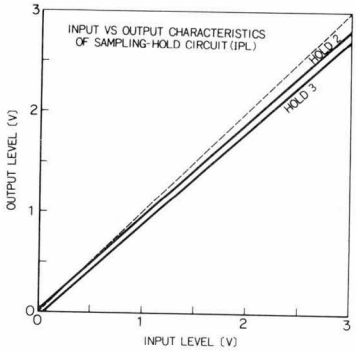

Fig. 5-45 Input versus output characteristics of sampling-hold circuit (HOLD 2 for $L\ell_{1\sim3}$, and HOLD 3 for $F\ell$ and $C\ell_{1\sim4}$).

admittance as a function of operating frequency is detected to give the absolute value of equivalent capacity (admittance value divided by the operating frequency). The rocket-borne gyro-plasma probe includes both amplitude and phase detectors to measure the vector impedance of an antenna. The satellite probe, however, does not include the phase detector circuit for restriction of allowed payload weight and limitation of the PCM telemetry system.

The circuit diagram of the pre-amplifiers is illustrated in Fig. 5-46. The pre-amplifier comprises the emitter follower circuit, the capacitance bridge, the buffer amplifier with high input impedance,

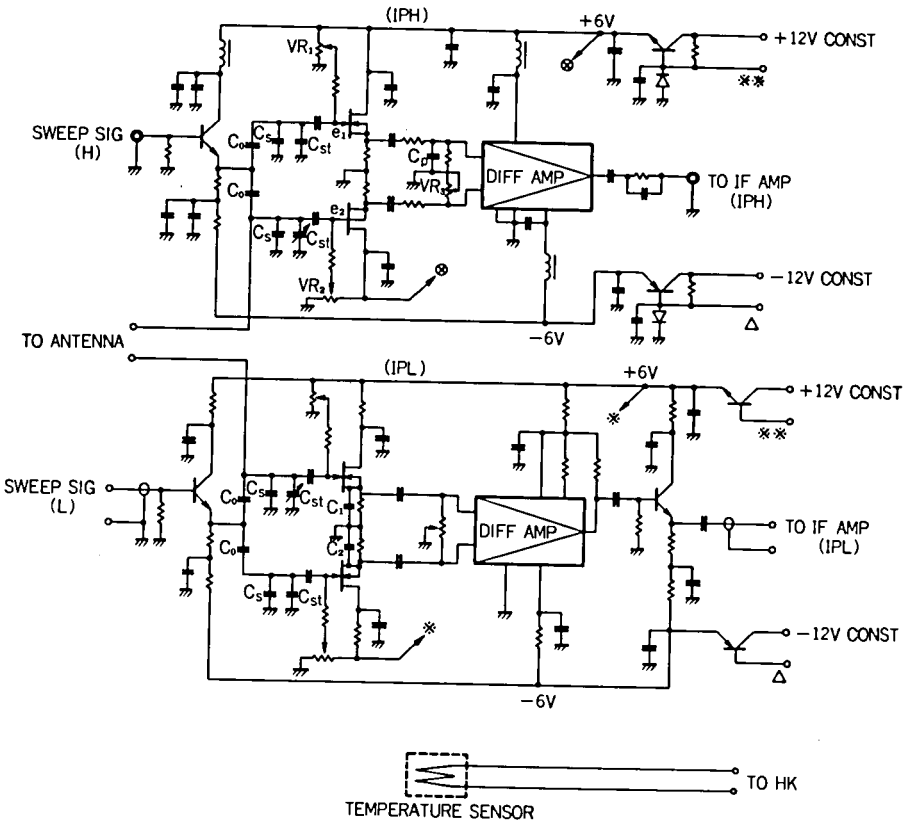

Fig. 5-46 Circuit diagram of pre-amplifiers of both IPH and IPL.

the differential amplifier and the antenna switching circuit (IPH and IPL, and CAL). To measure the temperature at the moment of operation, the temperature sensor of platinum wire is allocated in this pre-amplifier. The detected temperature signal is treated by the house keeping instrument (HK channel #18) and transmitted through telemetry system.

IPH Pre-Amplifier The swept signal from the part of swept signal generator is applied through 50Ω coaxial cable to the emitter follower circuit (buffer amplifier) with the input impedance of 50Ω and the output impedance less than 10Ω. The IPH system is designed to have the dynamic range from 1 pF to 1000 pF for the measurement of the

equivalent capacitance. The value of the capacitor C_0 is 100.0 pF and the stray capacity of the cable is 57 pF, which can be cancelled by adjusting the values of capacitors C_s, C_{st} and C'_{st}. The outputs e_1 and e_2 (as shown in Fig. 5-46) from the capacitance bridge are applied to the source follower EET amplifiers with high input impedances (10 ΩM//12 pF). The balance ratio of the capacitance bridge, that is defined by the difference of the amplification of two EET source followers and the common mode rejection ratio of the differential amplifier should be less than about - 60 dB (1/1000). Adjustment of the amplitude of signal in these two channels is made by the variable capacitor C'_{st} and the variable resistor $VR_{1\sim3}$; and the phase difference through these channels is adjusted by the capacitor Cp. The differential amplifier used in the IPH is the wide band video-amplifier SN5510L (TEXAS Inst.) which has a constant gain and low phase-shift versus from d.c. to 40 MHz as has been illustrated in Fig. 5-47(a). The common mode rejection ratio (CMRR) is given in Fig. 5-47(b).

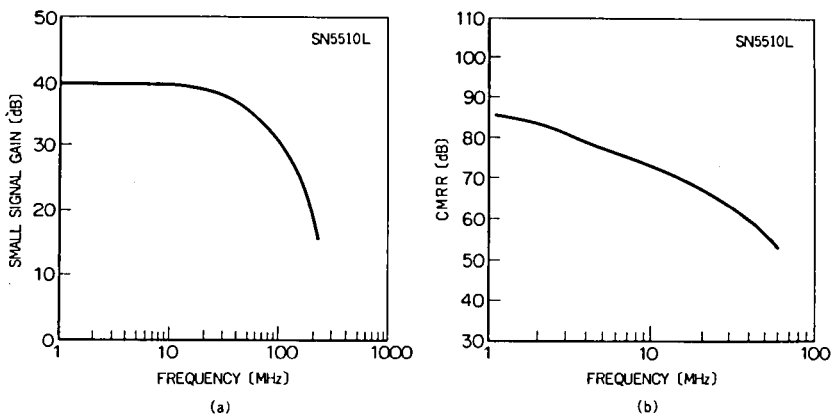

Fig. 5-47 Typical characteristics of wide band video-amplifier, SN5510L; (a) small-signal voltage gain versus frequency, and (b) common-mode rejection ratio versus frequency.

IPL Pre-Amplifier The principle of circuit design is much the same as the case of the IPH pre-amplifier. In this system the values of capacitors C_0 and C_S are chosen to be 10000 pF and 100 pF, to obtain the dynamical range of equivalent capacitance from 30 pF to 10000 pF. The phase difference of two differential amplifier channels is adjusted to be minimum shift angle by the capacitors C_1 and C_2. The differential amplifier used in the IPL is TA7034MJ (TOSHIBA) which has a gain of 16 dB, a low NF (Noise Figure) of 7.8 dB at 100 MHz and CMRR of - 100 dB at 1 kHz.

Switching Circuit A monopole antenna is used for the sensor of high and low frequency gyro-plasma probes, and switched alternately synchronizing with telemetry time-sharing periods. The antenna switching circuit as shown in Fig. 5-48 selects the antenna for IPH and IPL pre-amplifiers (SW 1), and also this circuit comprises the switching operation to earth connecting circuit (SW 3), and the capacitance calibration circuit (SW 2). A trapping circuit to shut the carrier from UHF 400.5 MHz transmitter to avoid the interference has also been included.

The switch SW 1 is operated by the relay RL 1 that is derived by the gate pulse W_{31} and the power supplies of + 6 VH and + 6 VL from the PSW (Power switch of the spacecraft) corresponding to the telemetry mode II_1 and II_2. The gate pulse W_{31} is an end mark of each mode so that SW 1 is switched from IPH to IPL after all the observation of mode II_1 (IPH), and vice versa.

The switches SW 2 and SW 3 are operated by the relay RL 2 that is drived by the gate pulses W_{31} and W_6. When the gate pulse W_6 drives the relay RL 2, both SW 2 and SW 3 connect the line to the antenna. When the gate pulse W_{31} is applied, SW 2 connects the line to the reference capacitor C_{REF} and C_S. The switch SW 3 connects the antenna to the ground. The antenna is connected to the pre-amplifier only during the observation of IPS, i.e., from W_6 to W_{30}, to protect the FET transistors of pre-amplifiers from the damage due to high voltage inputs, that may possibly be transmitted from the cyclotron

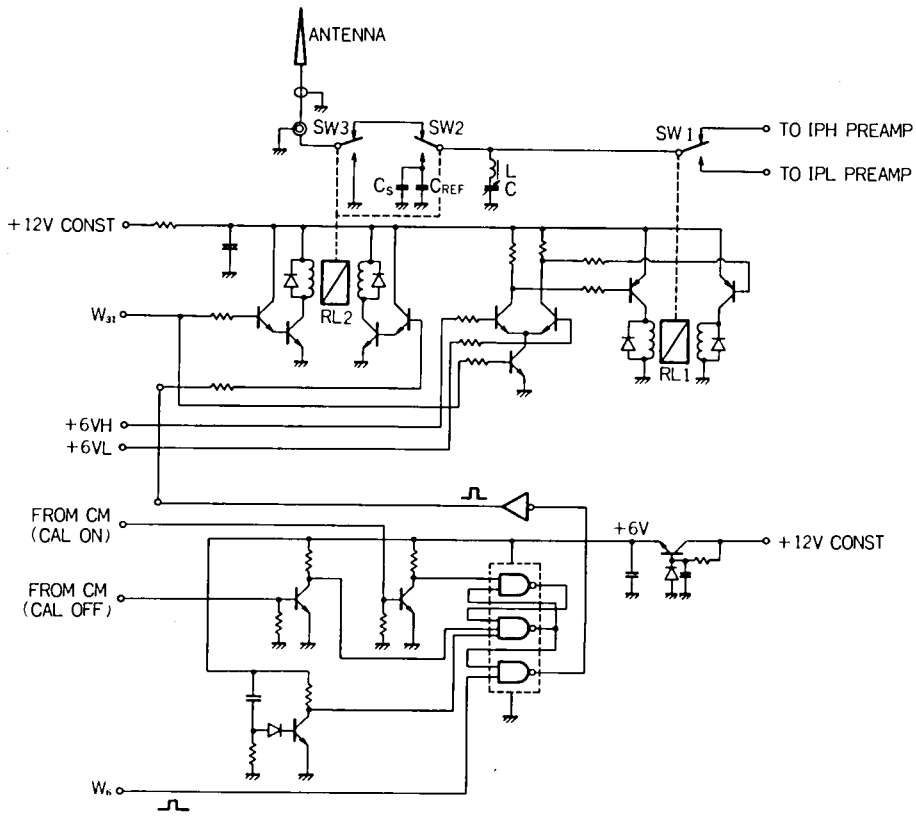

Fig. 5-48 Antenna switching circuit.

instability experiment (CIE). The CIE equipment is designed to radiate the electromagnetic wave with high tension (about 1200 Vpp) at frequencies of 120 kHz to 210 kHz from a horizontal loop antenna (see Fig. 5-57).

The calibration of operating level for the instrument is performed by using the reference capacitor (C_{REF}). The operation to switch C_{REF} by SW 2 is controlled by command (PI CAL ON and OFF). When the "CAL ON" pulse is applied, the gate pulse W_6 is inhibited to drive the relay RL 2. Consequently, SW 2 remains at the side of the reference capacitor, and the pre-amplifier with the capacitance bridge detects the fixed value of C_{FEF} (100 pF). C_S is used to compensate a stray capacitance of the cable that is extended from the position of SW 2

to the antenna.

Since the antenna of the UHF 400.5 MHz transmitter is located just above monopole antennas, the induced potential on the antenna is rectified through the nonlinearity of the circuit and the modulation signal (768 Hz square wave for the real-time mode telemetry transmission) is superimposed on wave form of IPS signal. In order to avoid this interference a trapping circuit is installed. It consists of the LC series resonator which is tuned to the frequency at 400.5 MHz. The admittance of this circuit in the frequency range less than 15 MHz takes capacitive value that is low enough not to disturb the observation value.

2.4 Frequency Calibration and Data Processor

Frequency Calibration Circuit For the purpose of monitoring the circuit operation in orbit, the command system is employed and controls onboard calibration circuits. One of control items is a frequency calibration of IPS; the frequency of the crystal controlled oscillator for the gate width control circuit of IPH and the swept frequency of IPL. These signals are transmitted by a UHF 400.5 MHz telemetry system (IRIG band #10; 5.4 kHz $\pm$ 7.5 %). The circuit of this system is illustrated in Fig. 5-49.

Frequency calibration signals from IPH (101.5625 kHz) and IPL (65 kHz ~ 79 kHz) are switched by the timing signal (+ 12 VH and + 12 VL) that is fed from PSW (Power Switch). Each signal is mixed with the reference signal (256.00 kHz) to convert the signal frequency into the modulation frequency band. The selective amplifier is used to eliminate the lower side band of mixed signals; obtained upper side band frequencies are 357.5625 kHz for IPH, and in a range from 321 kHz to 335 kHz for IPL. These obtained signals are reshaped by a saturation amplifier to be rectangular wave form as shown in Fig. 5-50. The output signal is demultiplied by 64 through binary circuits to obtain final signal frequencies for the telemetry at 5.587 kHz for

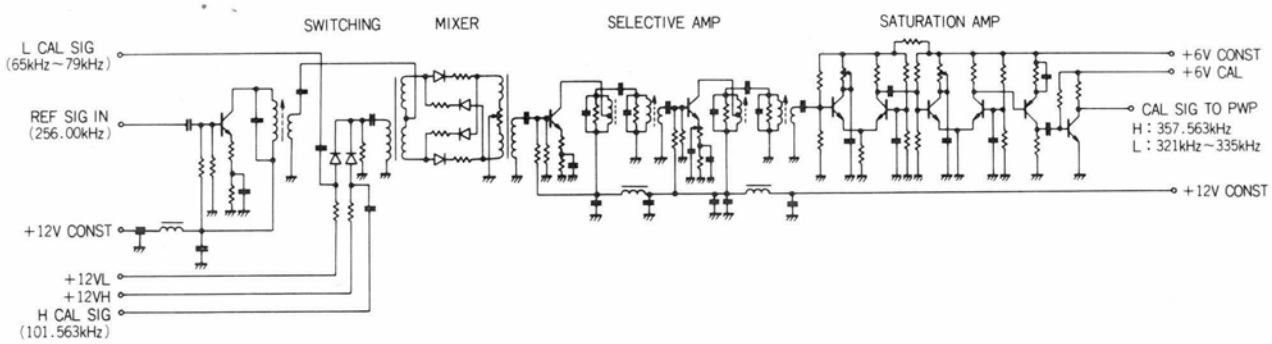

Fig. 5-49 Frequency calibration circuit.

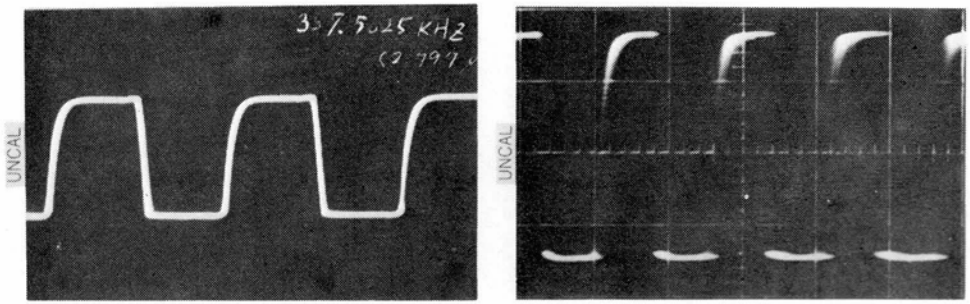

(1μs/div.) (2μs/div.)

(a) IPH (b) IPL

Fig. 5-50 Output wave form of frequency calibration of IPH (a) (fixed frequency of 357.5625 kHz) and IPL (b) (swept frequency of 321 kHz to 335 kHz).

IPH and in a range from 5.016 kHz to 5.234 kHz for IPL.

Data Processor The data processing equipments consist of onboard and ground-based systems. The data processor, onboard the spacecraft, is designed to generate gate control pulses that are required for the data selector which controls the data sample due to time-sharing program of the telemetry. The assembly of functional elements is illustrated in Fig. 5-51; this logical operation circuit is controlled by pulses from the TIM-ENC. The time sequence of input pulses are given in Fig. 5-52. G_0 is a pulse corresponding to frame synchronous word and $G_{1\sim6}$ are used to make 6 groups, for $W_2 \sim W_{31}$, in which 5 words are included. For example, the word pulse W_{13} can be obtained as a result of logical operation, $\overline{G}_3 \cdot \overline{W}_2$. The produced read- in pulses for observation items (Fh_1, Fh_2, Lh_1, Lh_2, Lh_3 for IPH and $F\ell$, $L\ell_1$, $L\ell_2$, $L\ell_3$, $C\ell_{1\sim3}$ for IPL; see Fig. 5-5) are shown in Fig. 5-53. These reading-in pulses are applied to the data selectors of IPH and IPL at the time advancing one-word period before the assigned word number, as has been explained previously in section 2.1 and 2.2. Input pulses SYNC-1 and 2 generated from W_O and W_e produce the timing pulse SYNC-3 which is applied to the saw-tooth generators of IPH and IPL, and these three pulses are used as reset trigger pulses. The pulses for W_6 and W_{31} are used for the set and reset operations of the antenna switching circuit.

The so-called "Quick-Look" instrument is prepared to check demodulated telemetry data quickly on the real-time base. The main quick-look instrument sorts the time-serial PCM signal into the each corresponding frame mode. The sorted PCM signals are converted into the analog signals through the D/A converter. The IPS quick-look sorts the time-serial data of mode II_1 and II_2 into six parallel channels corresponding to observational items, Fh_1 and $F\ell$, Fh_2 and $F\ell$, Lh_1 and $L\ell_1$, Lh_2 and $L\ell_2$, Lh_3 and $L\ell_3$, and $C\ell_{1\sim4}$. The circuit of the gate control signal generator is shown in Fig. 5-54. Input pulses of the frame synchronous, bit and word identification signals are supplied from the main quick-look to this IPS quick-look circuit.

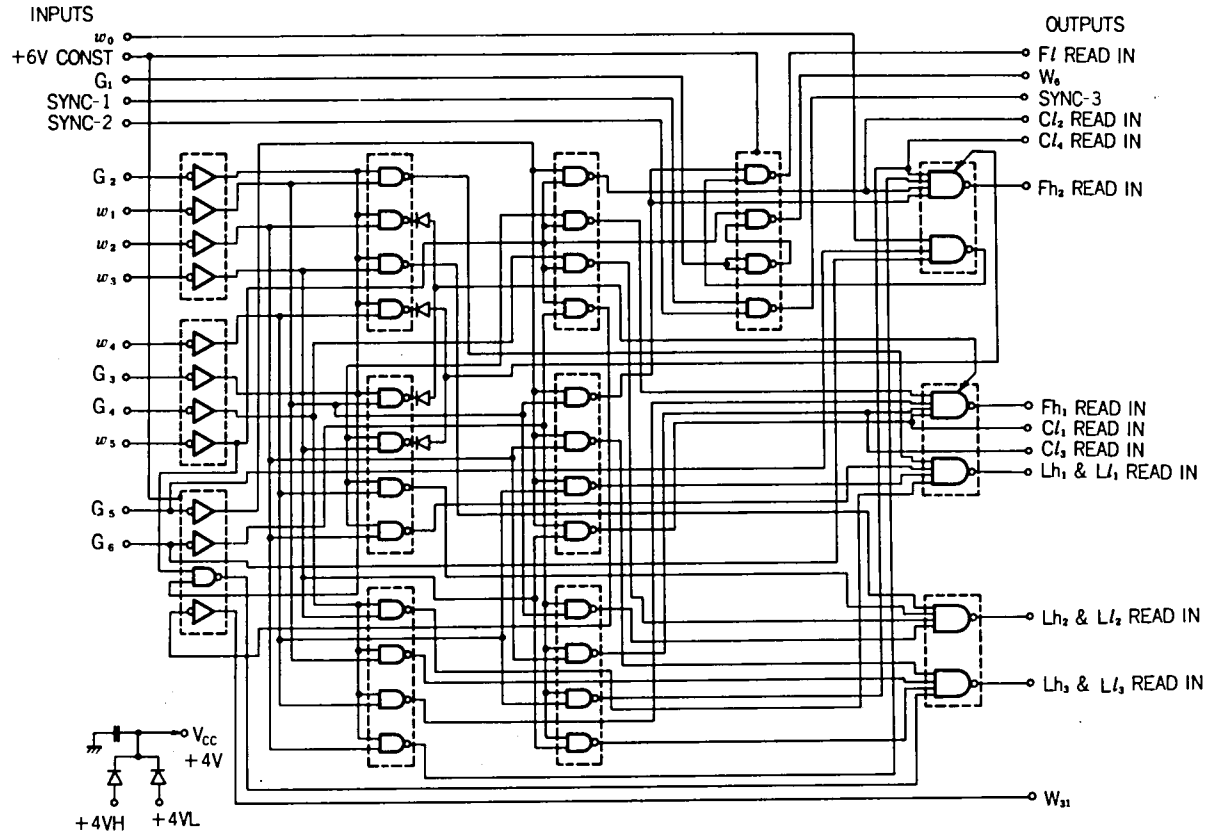

Fig. 5-51 Functional operation diagram of data processor; integrated circuits, HD203F and HD204F, are used.

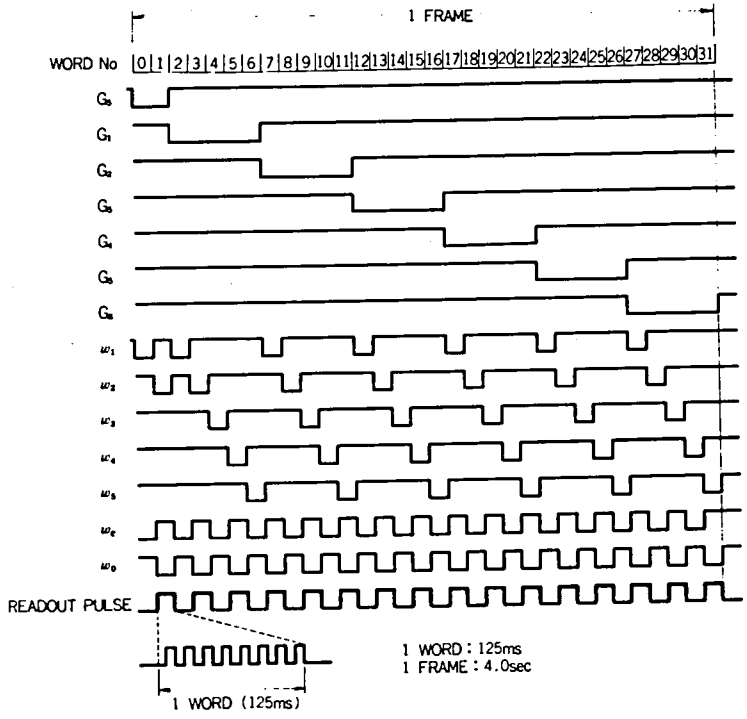

Fig. 5-52 Pulse sequences from TIM-ENC.

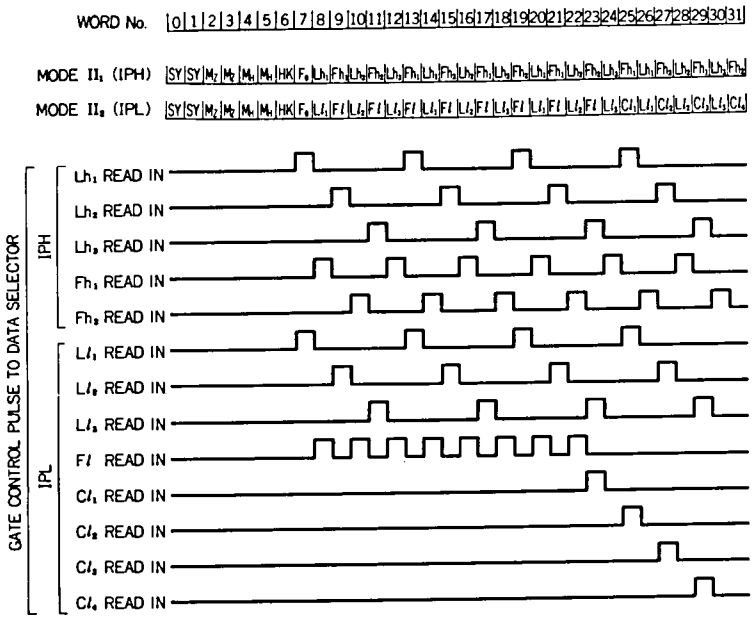

Fig. 5-53 Pulse sequences from data processor.

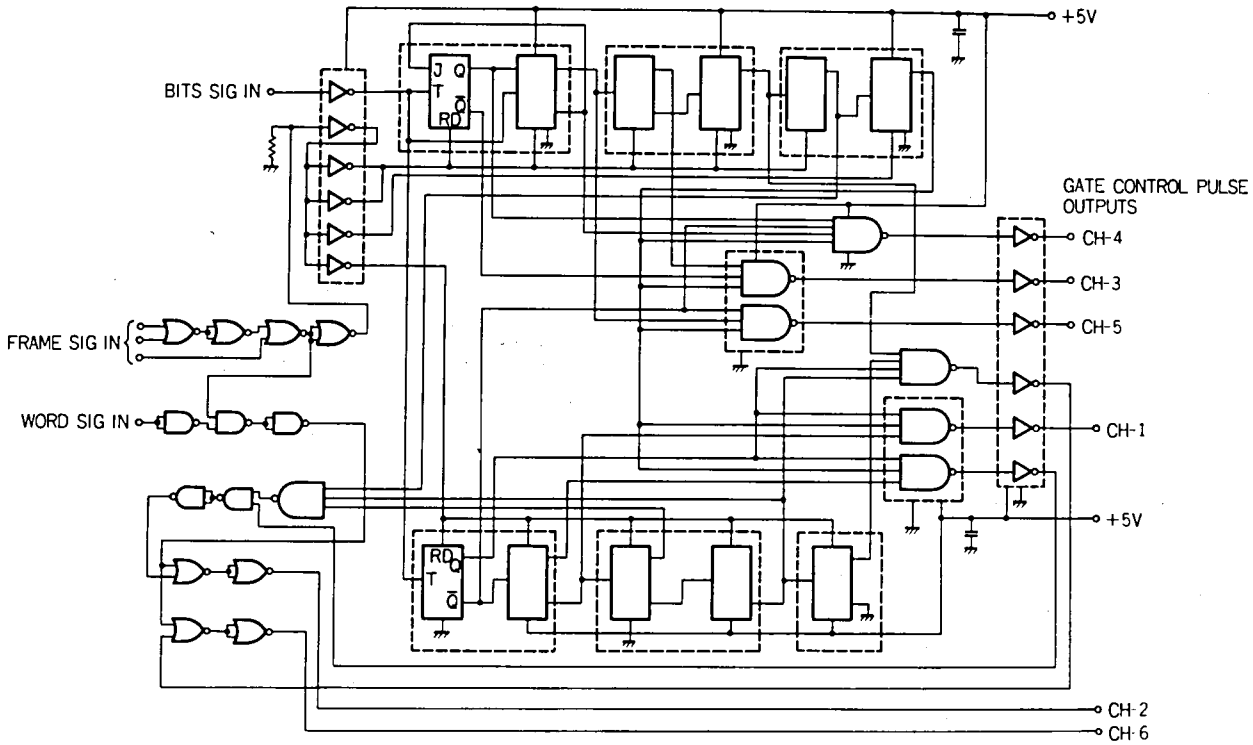

Fig. 5-54 Functional block diagram of ground-based data selector.

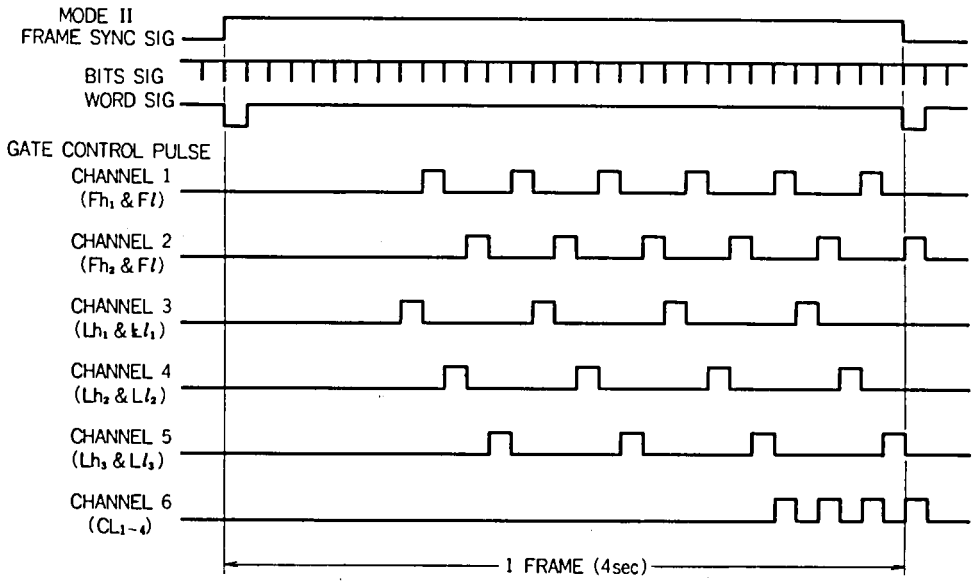

Fig. 5-55 Gate control pulse sequences of ground-based data selector.

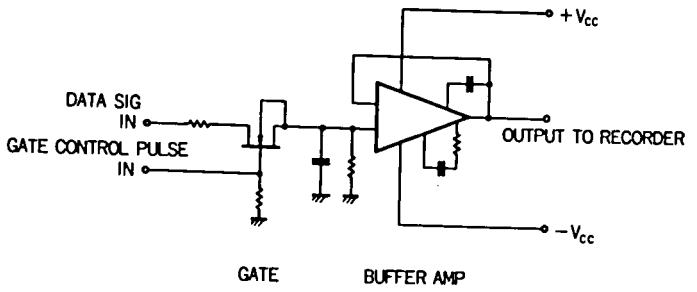

Fig. 5-56 Electrical circuit of gate and buffer amplifier.

Generated pulse sequences to control the gate circuit of IPS quick-look are summarized in Fig. 5-55. These gate pulses are applied with the delay one word period from the assigned word number, because of the time delay of the D/A converter and hold circuits. The signal is sampled by gate control pulses and fed to the pen recorder with six channels through the buffer amplifier and d.c. amplifier. An example of one unit circuit of the gate and buffer amplifier is illustrated in Fig. 5-56.

2.5 Construction of Payload and Antenna

The REXS satellite has three monopole antennas and two orthogonal loop antennas (Fig. 5-57). One of the monopole antennas is used as a sensor of the gyro-plasma probe, which is a thin flat strip of spring steel (beryllium copper) preformed into a cylindrical tube with an overlapping seam. The tube is subsequently opened flat and wound onto a drum for storage purposes. When the strip is released from its storage drum, the strip curls into its preformed shape to form a tube with considerable bending strength. The diameter is 10 mm, and the length from root to tip are movable with three steps of length (60cm, 123cm and 205 cm). When the satellite is separated from the 4th stage rocket motor, the antenna begins to extend with a speed of 5 cm/sec being controlled by a pre-set timer. The command system is able to control the extension and retraction of antennas at every step. The capacitance of fully extended antenna in free space is calculated to be 26 pF, which agrees well with the measured value of the gyro-plasma probe (Lh_3 = 110 decimal counts).

The main package of IPS instrument and its pre-amplifier are shown in Fig. 5-58 (a) and (b). The main package is mounted on the flat aluminium-honeycomb plate of the spacecraft deck. The pre-amplifier is installed in the central tube. To protect from the damage due to vibration, shock, and heat in vacuum condition, all circuits are encapsulated with a polyurethane foam-in-place resin that is called

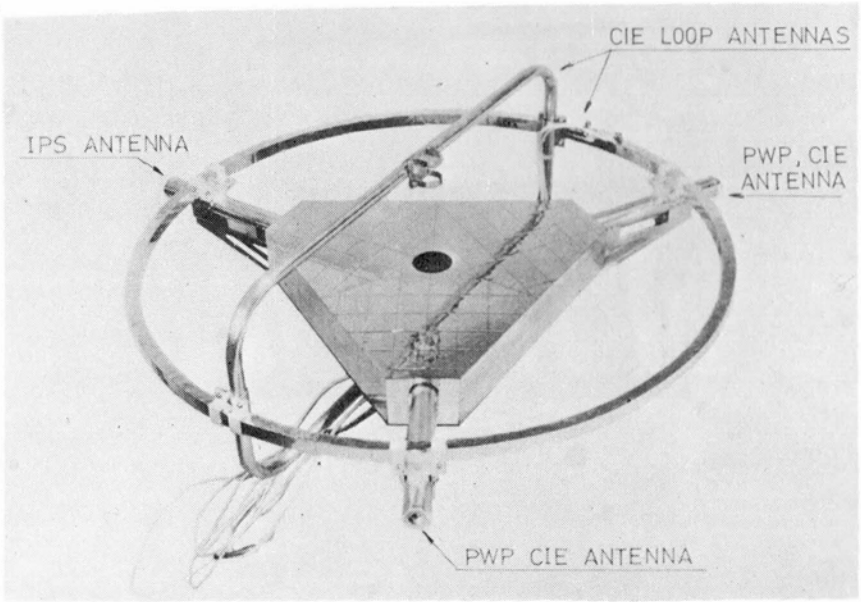

Fig. 5-57 Structure of three monopole antennas and two loop antennas.

Eccofoam FPH. To protect against temperature increment, a thermal barrier of aluminium foils is muffled around the main instrument. The covering-case of the pre-amplifier is painted black for the thermal coupling between the pre-amplifier and instruments of the spacecraft because of its small heat capacity.

Standardized pre-flight test conditions for the mechanical and thermal environment of instruments are summarized in Appendix C.

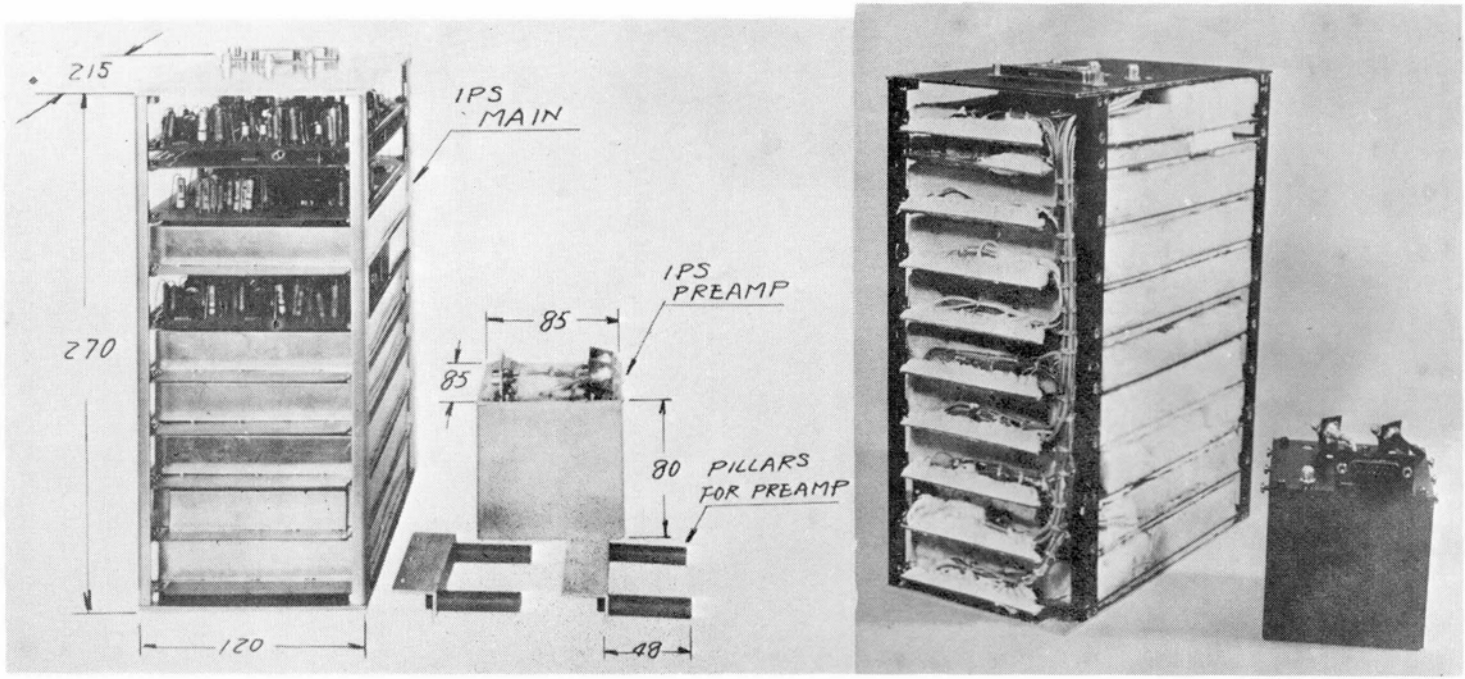

(a) (b)

Fig. 5-58 Main instrument of gyro-plasma probe and its pre-amplifier; (a) before and (b) after encapsulation.

Summary of IPS Instrument The gyro-plasma probe has been designed and developed for the instrument onboard the spacecraft. A number of improvements and re-constructions of electrical circuits and mechanical structures have been made after various operational tests. Adequate operational performances of electrical circuits of both high and low frequency gyro-plasma probes are obtained.

The total weight of the main instrument is 3.642 kg and that of the pre-amplifier is 0.434 kg. The required electrical power is summarized in Table 5-2. As one period of 32 frames contains twelve frames of IPS mode, the use-time ratio of IPH and IPL is 0.1875 (= 6/32). The average electrical power consumption is 2.299 watts for the normal mode and 2.449 watts for the calibration mode (PI CAL ON).

Reliability of the instrument should be studied and considered critically because it is unable to repair or operate the instrument except some controlled items by command after the spacecraft launching. The reliability R is expressed as a function of time t,

$$R = \exp (- k\lambda Nt/10^9), \qquad (5.8)$$

Table 5-2 Electrical power consumption of IPS.

MODE	+ 12 V	+ 6 V	+ 4V	- 12 V	TOTAL	x 0.1875
CONTINUOUS	70 mA	—	—	30 mA	1.20 W	—
IPH	205 mA	150 mA	35 mA	25 mA	3.80 W	0.713 W
IPL	30 mA	120 mA	35 mA	70 mA	2.06 W	0.386 W
CAL	—	25 mA	—	—	0.15 W	—

where k is the coefficient of severity, λ = 1/MTBF in 10^9 fits (MTBF is the mean time between failures), N the total number of the parts, and t the time duration in hour. As the instrument comprises different kinds of parts, λN is written as

$$\lambda N \equiv \sum_i \lambda_i N_i. \tag{5.9}$$

Values of λ_i and N_i are summarized in Appendix D. The total number of parts used in the IPS is 1438 and that of the soldering points is 3969. The summation of products of λ_i and N_i becomes 27007.5. If k might be unity (for the most mild condition), the reliability R of IPS is computed to be 0.9433 for an interest life of three months.

§ 3. Pre-flight Test of Instrument

The instruments onboard the spacecraft should be subjected to pre-flight tests of electrical and mechanical performances under various phase of the spacecraft mission. Pertaining to these tests, operational characteristics of the instrument has been given, using the electrical simulation circuits for the antenna in a plasma. The test for heat effects in vacuum and the space plasma simulation experiment were also carried out. The calibration data for all observational items were obtained.

3.1 Operational Characteristics

The admittance of a combined electrical circuits that consists of the series-parallel resonant circuit shows the similar frequency characteristics with the antenna in a plasma, when the proper values of resistance, inductance and capacitance elements are used (see Fig. 5-61).

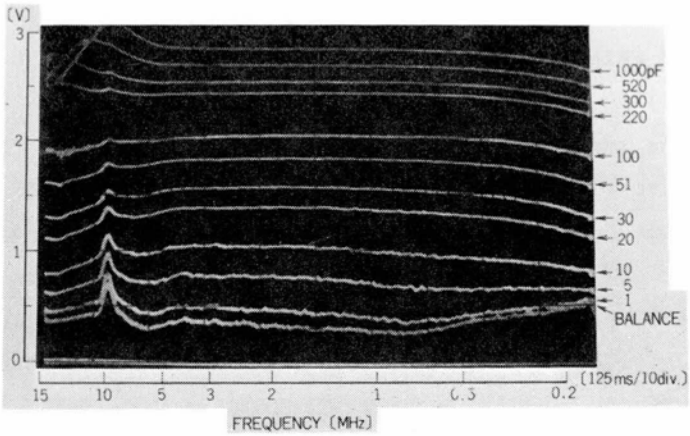

Fig. 5-59 Equivalent capacitance versus frequency characteristics of output from logarithmic amplifier (IPH).

IPH The measured admittance value (output of logarithmic amplifier) versus frequency is illustrated, in Fig. 5-59. In terms of the equivalent capacitance. The peak of the wave form appeared at higher frequency side, is due to a resonance like phase variation in the characteristics of the pre-amplifier circuit. The frequency dependence of amplitude is mainly due to the amplitude variation of the sweep signal versus frequency that is applied to the antenna. The measured values of equivalent capacities at 300 kHz (Lh_1) and 13 MHz (Lh_3) are given in terms of PCM count in Fig. 5-60. These results are obtained

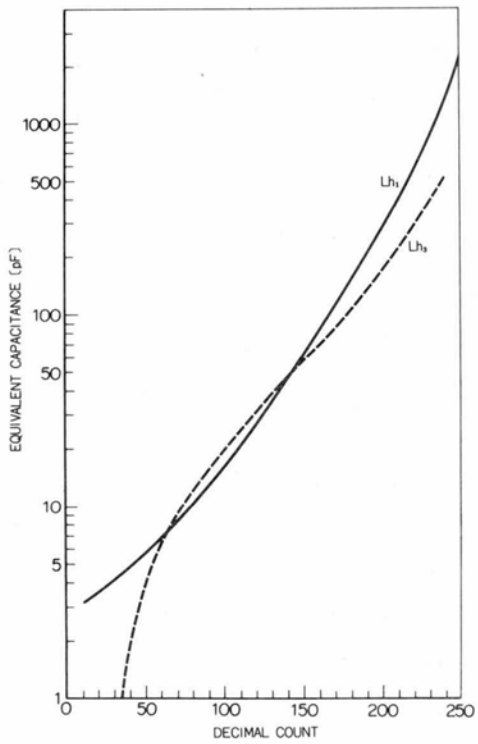

Fig. 5-60 Equivalent capacitance versus output decimal data (Lh_1 and Lh_3) through sampling-hold circuit and A/D converter of telemetry.

through the over all system of instruments. The detection function at $Lh_{1\sim3}$ are examined using a simulation circuit (L = 100 μH, C = 30 pH and C_0 = 100 pF) as given in Fig. 5-61. The output levels Lh_1, Lh_2, and Lh_3 from the sample-hold circuit are compared with the total admittance level from the logarithmic amplifier being superimposed in a dual trace oscilloscope. Detections of resonance point frequencies at Fh_1 and Fh_2, are checked by a simulation circuit with parameters of L = 100 μH, C = 15 pF and C_0 = 100 pF, whose parallel and series resonance frequencies are 2.26 MHz and 1.31 MHz. The output signals from the frequency counter are illustrated in Fig. 5-62. The output admittance level after logarithmic amplifier are given superimposed with the counter output codes. The 8-bit binary counts (MSB) are indicating 00101100 for Fh_1 and 00011010 for Fh_2; these counts correspond to 2.23 MHz and 1.32 MHz, respectively. These agree well with the values of 2.26 MHz and 1.31 MHz, that are indicated by the direct recording of the admittance level, within an error of the frequency resolution of about 50 kHz.

IPL The measured admittance value in terms of the equivalent capacitance that is detected at the output of the logarithmic amplifier is illustrated in Fig. 5-63. A resonance-like behaviour of the admittance value appeared at the low frequency side of the sweep range is produced by leakage of the swept local signal which is allocated near the intermediate frequency and the returning interval of frequency sweep due to the retrace of the saw-tooth. Measured equivalent capacities at 1.25 kHz ($L\ell_1$), 3.80 kHz ($L\ell_2$) and 6.65 kHz ($L\ell_3$) are given in Fig. 5-64. These curves are used for calibration of decimal counts from PCM telemetry to observed antenna admittance values. The detection functions of $L\ell_1$, $L\ell_2$, and $L\ell_3$ are examined in the space plasma simulation chamber; Fig. 5-65 shows the outputs $L\ell_1$, $L\ell_2$, and $L\ell_3$ from the sampling-hold circuit with the admittance level at the output point of logarithmic amplifier being superimposed in a dual trace oscilloscope. A typical response of the low frequency admittance of an antenna in a plasma is simulated by this test. Main contribution to the low frequency admitt-

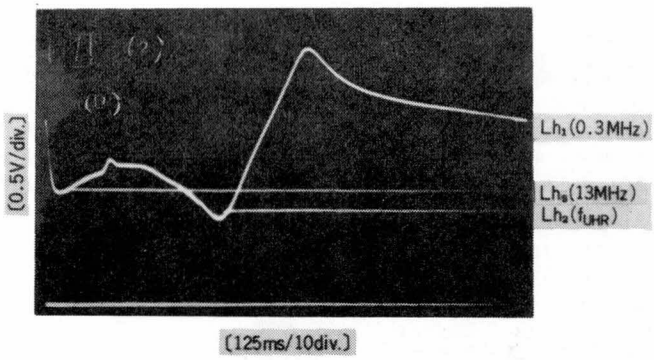

Fig. 5-61 Sampling-hold performance. Corresponding to 0.3 MHz, f_{UHR} and 13 MHz, frequencies are detected and potentials (Lh_1, Lh_2 and Lh_3) are sampled and stored. Output wave form of logarithmic amplifier is superimposed. Dummy antenna circuit of C_0 (L//C) (L = 100 μH, C = 30 pF, C = 100 pF and damping resistor of 5.1 kΩ) are used.

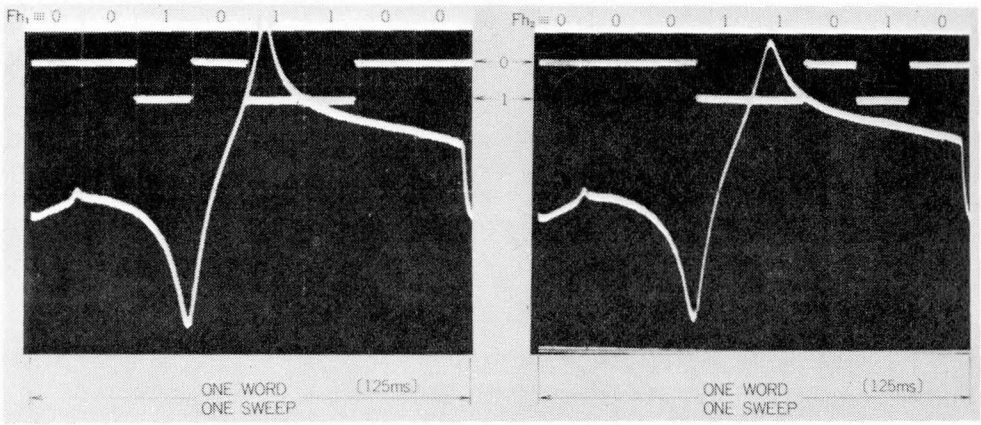

Fig. 5-62 Resonance frequency detection; (a) output of Fh_1 is 00101100 (binary) ≡ 44 (decimal) which is equal to 2.23 MHz, and (b) output of Fh_2 is 0011010 (binary) ≡ 26 (decimal) which is equal to 1.32 MHz. Output wave form of logarithmic amplifier is superimposed (Vertical : 0.5 V/div.). Dummy antenna circuit (L = 100 μH, C = 15 pF and C_0 = 100 pF) are used.

ance of the antenna in a plasma is thought to be represented as RC parallel circuit with an inclination of 6 dB/Oct. The difference

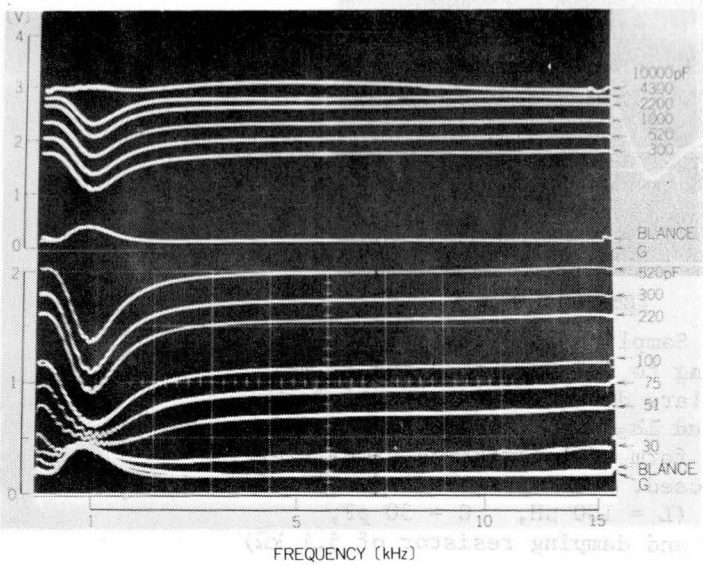

Fig. 5-63 Equivalent capacitance versus frequency characteristics of output from logarithmic amplifier (IPL).

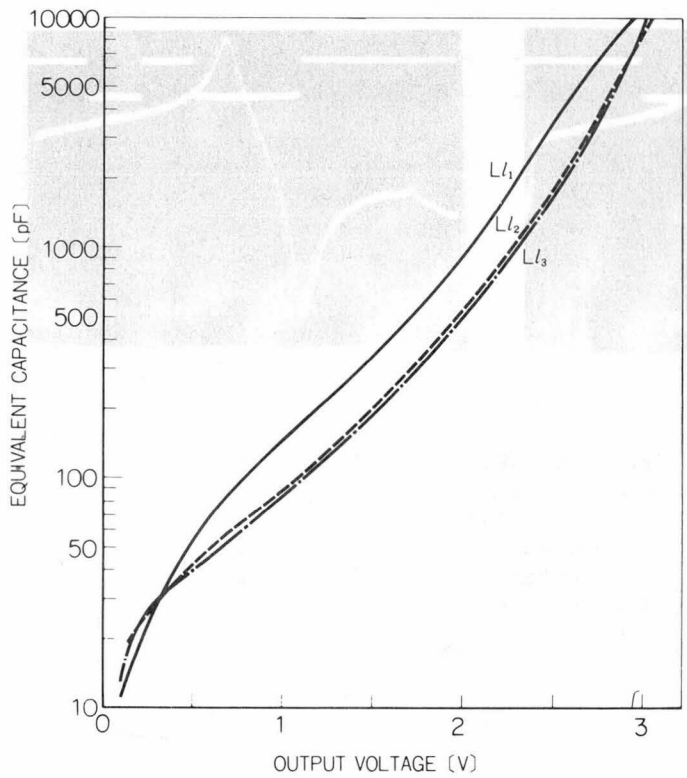

Fig. 5-64 Equivalent capacitance versus output decimal data ($L\ell_1$, $L\ell_2$ and $L\ell_3$) through sampling-hold circuit and A/D converter.

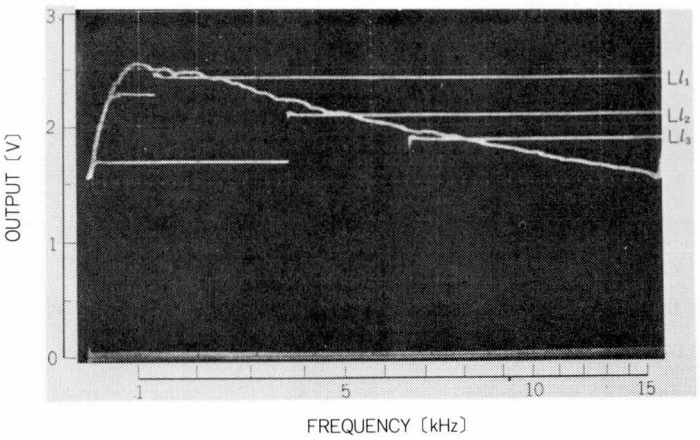

Fig. 5-65 An example of sampled and stored levels of $L\ell_1$, $L\ell_2$ and $L\ell_3$; frequency spectrum of admittance level is superimposed.

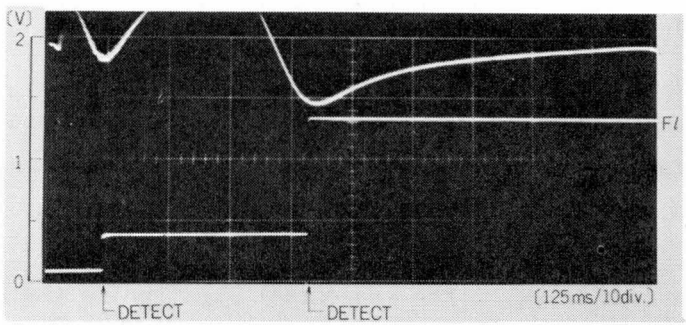

Fig. 5-66 Resonance detect performance. Two resonances are detected and the last one is stored and transmitted as $F\ell$. Output wave form of logarithmic amplifier is superimposed. The dummy antenna circuit with L of 1H, C of 1000 pF is used.

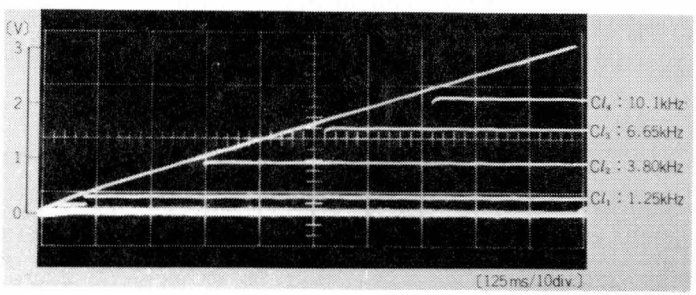

Fig. 5-67 Frequency reference levels $C\ell_{1\sim4}$.; saw-tooth wave form for this reference level is superimposed. Sampled potential is a little less than saw-tooth voltage, due to input-output characteristics of the sampling-hold circuit (HOLD 3, see Fig. 5-45).

between sampled output levels from output potentials of the logarithmic amplifier is due to the variation of stored potential by charge leak at the sample-hold circuit (see Fig. 5-45). $F\ell$ detection function is checked using a simulation circuit, with parameters $L = 1$ H, $C = 1000$ pF and $C_0 = 1000$ pF, whose parallel resonance frequency is calculated to be 5.01 kHz. The measured $F\ell$ is illustrated in Fig. 5-66; the admittance level (equivalent capacity) at the output point of the logarighmic amplifier is superimposed in a dual trace oscilloscope. A pseudo resonance at the low frequency side is also detected. The last sampled data is transmitted to ENC. The data 1.25 V is translated to be 5.00 kHz using reference frequency levels $C\ell_1$, $C\ell_2$, $C\ell_3$, and $C\ell_4$ as shown in Fig. 5-67; this observed frequency $F\ell$ is very close to the calculated value, 5.01 kHz.

3.2 Thermal Test in Vacuum Environment

Operational characteristics of the electrical circuits in space environment largely depends upon the equipment temperature, which varies owing to (i) radiation energy input to the spacecraft due to solar radiation, planetary albedo and infra-red radiation from the earth;[296~299] (ii) radiative heat output through the spacecraft surface to the outer space;[300,301] and (iii) heating of the environment due to energy from its own components, such as resisters, transistors and operational amplifiers. Thermal parameters of each part of the spacecraft,[296,302] such as heat capacity and heat transfer coefficients associated with the thermal contact resistance and the radiation heat exchange of two surfaces are also important thermal controlling factors.

The analytical prediction of the spacecraft and equipment temperatures is impossible because of the number of unknowable variables. Thermal measurement is thus carried out using one of space environmental simulation facilities; a vacuum chamber with liquid nitrogen cooled shroud which can adequately simulate the space environment pertaining to measure of thermal balance characteristics in the spacecraft.[303]

Table 5-3 6 modes of the thermal vacuum test.

Mode	α/ε	θ_s	δ
A	0.730	90°	67 %
B	"	60°	"
C	"	45°	"
D	"	90°	100 %
E	"	60°	"
F	0.846	90°	75 %
G	"	90°	67 %

α/ε is the ratio of solar absorptance to thermal emittance, θ_s sunlit angle, i.e., angle of the spacecraft axis with respect to the direction of the sun, δ the ratio of sunlit time to one period.

Electrical heaters are attached to the spacecraft panels instead of solar simulators to simulate the radiation input energy.

Testing conditions are determined as shown in Table 5-3. These conditions are produced to cover the maximum and also the minimum solar radiation inputs, considering the parameters of the spacecraft aspect on the presumed orbit as well as the parameters of the solar panel on spacecraft surface. The amount of input heat to the panels has been calculated for various geometrical relations between the spacecraft and the sun; cyclic heating and cooling are applied according to the computed sunrise and sunset times at the spacecraft position in orbit. This experiment required 216 hours (the experiment was carried out from June 19 to 29, 1972). Thermo-couples are located in both the pre-amplifier and the main IPS instrument. Temperature values of pre-amplifier are detected by the house keeping instrument (HK) and are transmitted through the telemetry system. To check the operational characteristics of IPS instrument, the simulation electrical circuit is used being replaced by an antenna in a plasma.

Results of this test are shown in Fig. 5-68. Fig. 5-69 is indicating the monitor output of IPH. The temperature of the pre-amplifier is about 35°C at the beginning of mode A and gradually decreases to about 8°C at the end of mode C. Since mode D corresponds to a

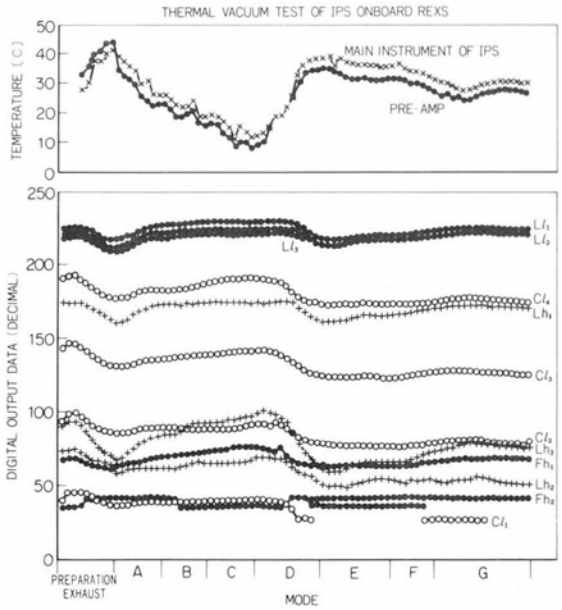

Fig. 5-68 Results of thermal vacuum test; conditions, modes A~G, are listed in Table 5-3.

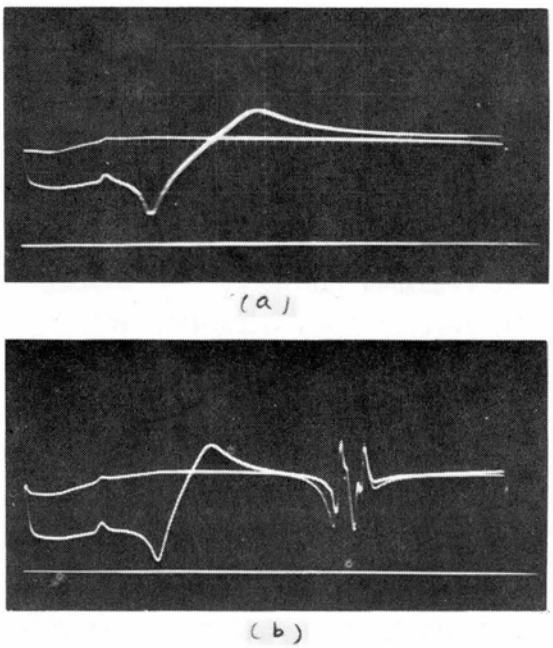

Fig. 5-69 Monitor output of IPH (Horizontal; 125 ms/ 10 div., Vertical; 1 V/div.) (a) Mode C (temperature of 8.5°C). (b) Mode E (temperature of 30.0°C). Antenna is replaced by dummy electrical circuit, i.e., (6.2 kΩ // 100 pF) and (56μH // 4.7 kΩ // 3 pF), and calibration level (100 pF) is superimposed.

period of 100 % sunlight, the equipment temperature increases again. As is obvious from Fig. 5-67, swept range of the high frequency is changed, and Lh_1 (admittance level at 300 kHz) is misdetected below about 10°C. When the spacecraft is in orbit, the temperature is measured at a point in the pre-amplifier. The calibration curve of each measuring value versus temperature at the pre-amplifier has been obtained by this thermal test. In Fig. 5-70, measured values versus temperature at the pre-amplifier are summarized. The temperature calibration data for the value of Fℓ (lower hybrid resonance frequency) are not obtained because the simulator of antenna is selected to have the high frequency resonance during this test. Calibration for Fℓ, can, however, be deduced from the data $C\ell_1 \sim C\ell_4$.

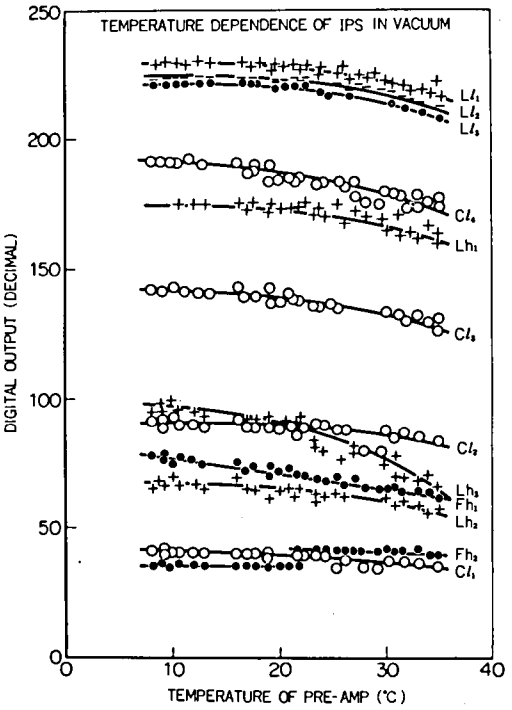

Fig. 5-70 Temperature dependence of gyro-plasma probe characteristics in vacuum.

3.3 Simulation Experiment in Plasma

The test of the gyro-plasma probe operation in a plasma was carried out by using the space plasma simulation chamber to examine output data relating to several parameters of test plasma such as electron density, temperature, ion species and magnetic field intensity. To test the operational performance of the instrument is also important in this pre-flight plasma experiment. Results of the gyro-plasma probe were examined and compared with measurements of the Langmuir

probe method.

The large-scale space chamber was used for the purpose of this experiment; the equipment is described in detail in section 2.1, chapter III. Installed in a frame of the spacecraft, instruments of IPS, CIE, PWP and TEL with a set of antennas are set in the vessel. The antenna of IPS is 1300 mm in length and located at the middle of the vessel. The capacitance bridges of IPH and IPL are balanced to the capacity of cabling and instrumentation in the condition of setup for the space simulation chamber experiment. The Langmuir probe is fixed to the wide range scanning arm. Selected pure gases such as He, N, and Ar can be injected to high vacuum vessel with an arbitrary gas pressure in a range from 10^{-3} torr. to 10^{-6} torr. A pair of hot cathode coated by BaO are used as back diffusion type plasma sources for a plasma with low electron density less than 10^{7} cm^{-3} and electron temperature of 500°K to 4000°K.

Results of IPH and IPL Examples of output data obtained in the space chamber experiment are illustrated in Fig. 5-71 (a) ~ (d). The high frequency gyro-plasma probe (IPH) and the low frequency gyro-plasma probe (IPL) were functioned well to measure the frequency characteristics of antenna impedance. Results are described as follows.

The binary counter output for Fh_1 (HUR) is 01010000 (MSB) which is equal to 80 of decimal count and translated to be 4.063 MHz. Since the magnetic field strength is 0.42 gauss (corresponding electron gyro-frequency is 1.17 MHz), the electron plasma frequency is 3.853 MHz, from which the electron density is calculated to be 1.88×10^{5} cm^{-3}. The output for Fh_2 (SHR) is 00110100 (MSB) which is equal to 54 of decimal count and translated to be 2.742 MHz. These resonance frequencies coincide well with the resonance frequencies obtained from analog data being calibrated by the standard signal generator.

Output voltages of Lh_1 (0.3 MHz), Lh_2 (f_{UHR}) and Lh_3 (13 MHz) are 1.8 V, 1.1 V and 1.2 V corresponding to the equivalent capacitances of 68 pF, 14 pF and 21 pF, respectively. The calculated capacitance value of an antenna (1300 mm in length and 10 mm in diameter) in free space

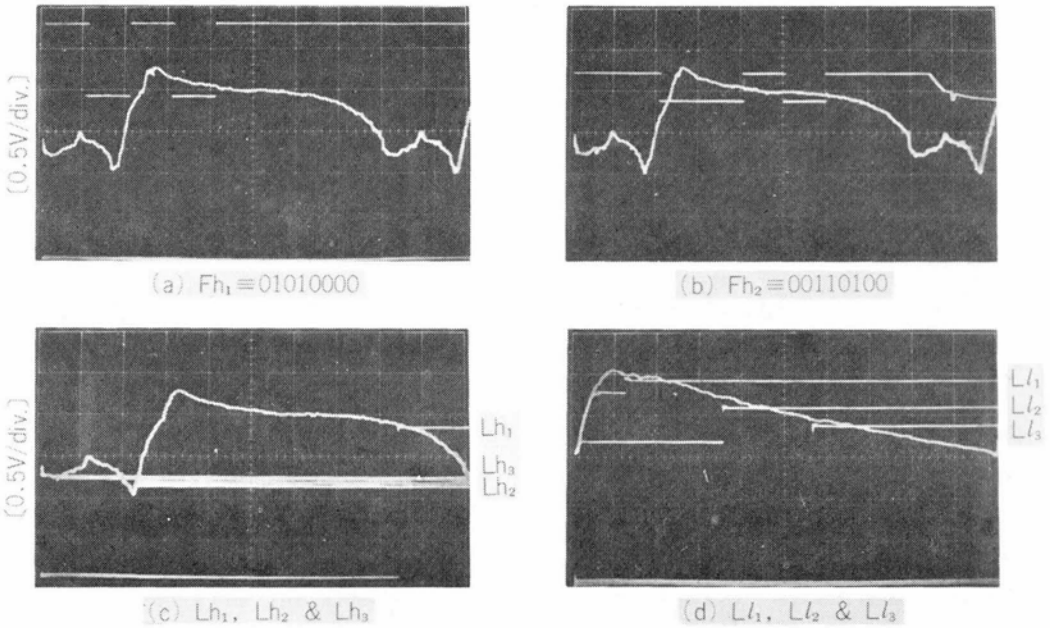

Fig. 5-71 A set of output data obtained in the space chamber experiment.

is 22 pF which coincides well with the measured value of Lh_3. The value of Lh_2 represents the equivalent Q (Quality Factor) of the upper hybrid resonance curve. As the electron-neutral collision frequency increases, the value of Q decreases and also the value of Lh_2 increased. This change of the value of Q is related not only to the collision frequency of electron-neutral particles, but also to the complicated mechanism of an electrostatic wave excitation near the upper hybrid resonance.[107] The value of Lh_1 represents the sheath capacitance of an antenna. As an electron temperature increases while an electron density remains constant, the value of Lh_1 decreases, because of increase of the sheath radius which is controlled by the Debye length.

The output voltages of $L\ell_1$ (1.25 kHz), $L\ell_2$ (3.80 kHz) and $L\ell_3$ (6.65 kHz) are 2.4 V, 2.1 V and 1.86 V. These are translated to the

equivalent capacitances of 4300 pF, 950 pF and 480 pF, respectively, after the correction of characteristics of the sampling-hold circuit (HOLD-2) as shown in Fig. 5-45. The calibration curves of $L\ell_{1\sim3}$ have been shown in Fig. 5-64.

The lower hybrid resonance frequency f_{LHR} is expressed as,[304]

$$f_{LHR} = \left(\frac{1}{f_{Hi}^2 + f_{pe}^2} + \frac{1}{f_{Hi}f_{He}}\right)^{-1/2}$$

$$= f_{He}\left\{\frac{M_p}{m} M_{eff}\left(1 + \frac{f_{He}}{f_{pe}}\right)\right\}^{-1/2} \qquad (5.10)$$

where f_{pe}, f_{pi}, f_{He} and f_{Hi} are electron plasma, ion plasma, electron and ion gyro-frequencies, and M_p/m and M_{eff} are a mass ratio of proton to electron and effective ion mass, respectively. In this experiment, an argon plasma (M_{eff} = 39.948) is used; the electron plasma and electron gyro-frequencies are 3.89 MHz and 1.17 MHz. The lower hybrid resonance frequency is, then, calculated to be 4.15 kHz. The lower hybrid resonance (Fℓ) is not detected as has been seen in the analog data given in Fig. 5-71 (b). This can be attributed to the high collisional frequency due to a partially ionized plasma state; the ionization rate is approximately 10^{-6}. The collision frequency is thought to be larger than the ion plasma and ion gyro-resonance frequencies; i.e., the impedance in the frequency range of 1 kHz to 15 kHz is predominated by the resistance of the sheath region surrounding the antenna in a plasma. The lower hybrid resonance is presumably able to be detected in the magnetosphere where the plasma is fully ionized to make collision frequency less than the ion plasma and ion gyro-frequencies.

Impedance at VLF Range As is shown in Fig. 5-71 (d), the equivalent capacitance value in the frequency range of 1 kHz to 15 kHz decreases as the frequency increases. Three examples of experiments are summarized in Fig. 5-72, corresponding to experimental conditions listed in

Table 5-4. In this frequency range, the impedance can be expressed as parallel circuits consist of resistance and capacitance for each arm. This impedance is mainly controlled by the sheath surrounding the antenna, because the impedance of a plasma becomes very low. Therefore, the equivalent capacitance C_{eq} can be written as

$$C_{eq} = \sqrt{1 + \omega^2 C^2 R^2} \ / R\omega \qquad (5.11)$$

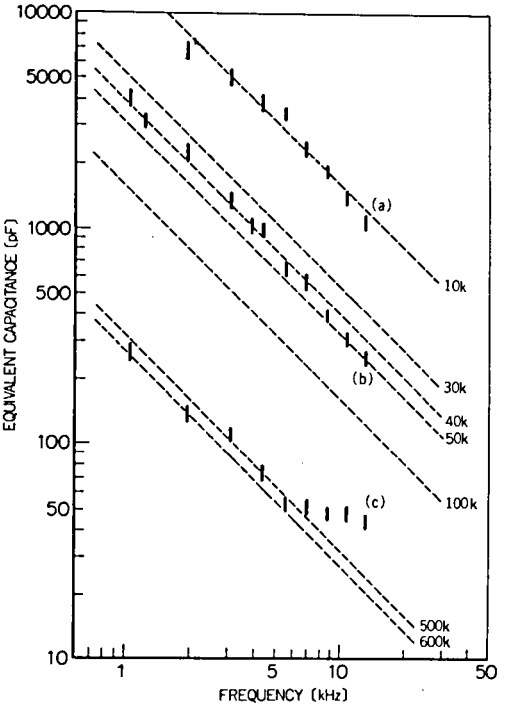

Fig. 5-72 Equivalent capacitance characteristics obtained in the space chamber experiment. Dashed lines show the frequency characteristics of equivalent capacitance corresponding to indicated resistances.

where ω is an operating angular frequency. If the equivalent capacitance due to the resistance is larger than the value of the capacitance C, that is, $(R\omega)^{-1} >> C$, a $\ell n\ C_{eq}$ value is expressed by a linear function of $\ell n\ \omega$. The values of the resistance can be deduced from Fig. 5-72; values are about 10 kΩ, 40 kΩ and 550 kΩ corresponding to the conditions (a), (b) and (c). These values decrease as the electron density increases, as is shown in Fig. 5-73. The conductance of sheath can be deduced from the current-voltage characteristics of the Langmuir probe in the vicinity of floating potential.[305] Namely, the conductance G is calculated as,

$$G = \frac{\partial}{\partial V} \{I_{i0} - I_{e0} \exp(V/V_e)\}\Big|_{V=V_0}$$

$$\fallingdotseq I_e/V_e \qquad (5.12)$$

where I_{io} and I_{eo}, V_o and V_e are ion saturation current, electron saturation current, floating potential and electron thermal energy in volt, respectively. Results of the resistance calculated from Langmuir probe characteristics are plotted in Fig. 5-73, which are indicating a good coincidence with values deduced from the low frequency gyro-plasma probe. In the case of (c), the equivalent capacitance at the higher frequency range in VLF range shows a constant value of the capacitance of sheath, because the resistance value is satisfying the condition that $(R\omega)^{-1} < C$; the constant capacitance value is about 50 pF that coincides with the value of

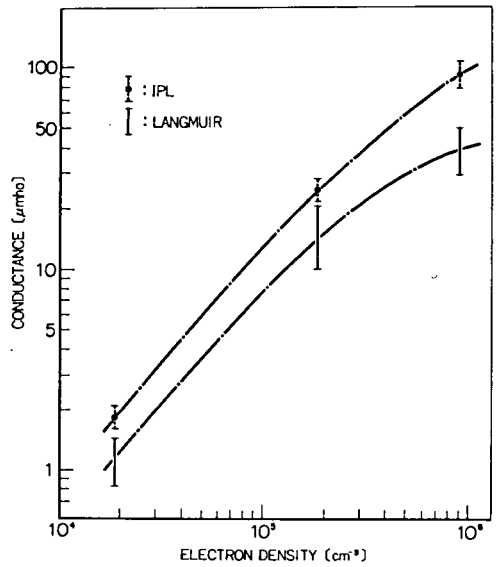

Fig. 5-73 Probe conductance versus electron density value. The values obtained simultaneously by Langmuir probe method are indicated.

Table 5-4 Experimental conditions of the plasma in the space chamber.

		(a)	(b)	(c)
Gas		Ar	Ar	N
Pressure	P mmHg	-	6.8×10^{-5}	2.9×10^{-5}
Electron Density	Ne cm^{-3}	9.1×10^{5}	1.9×10^{5}	1.9×10^{4}
Electron Temperature	T_e °K	(1500)		1000
Debye Length	λ_D cm	0.28	0.62	1.6
Upper Hybrid Frequency	f_{UHR} MHz	8.64	4.06	1.71
Electron Plasma Frequency	f_{pe} MHz	8.56	3.89	1.25
Electron Gyro-frequency	f_{He} MHz	1.17		
Lower Hybrid Frequency	f_{LHR} KHz	4.27	4.15	5.32
Lon Plasma Frequency	f_{pi} KHz	31.6	14.4	8.36
Lon Larmor Radius	r_{Li} m	5.55		2.68
Sheath Capacity	C_{SH} pF	-	-	47
Sheath Conductance by LP	G mho	31-52	10-23	0.85-1.5
Sheath Resistance by LP	R KΩ	19-32	44-96	670-1120
Sheath Conductance by IPL	G mho	100	25	1.8
Sheath Resistance by IPL	R KΩ	10	40	55

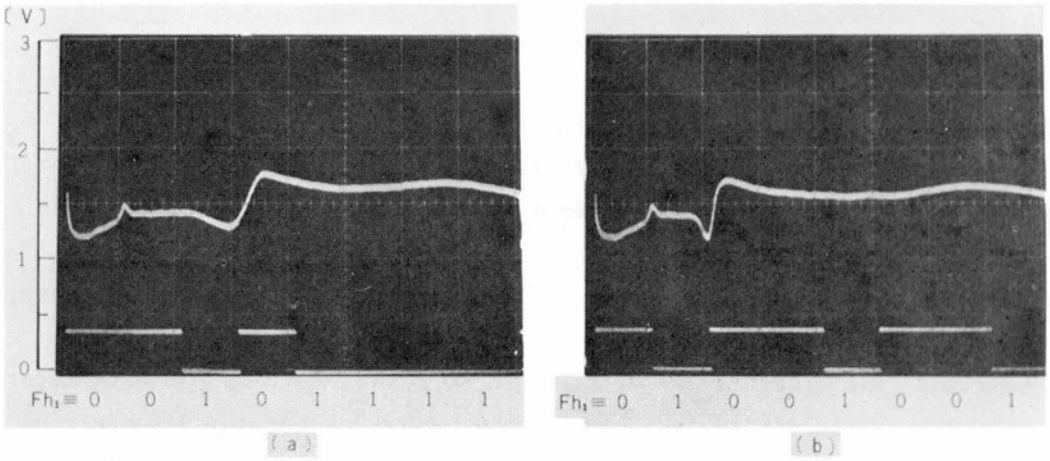

Fig. 5-74 Frequency change of upper hybrid resonance due to applied magnetic field ; (a) 0.57 gauss, (b) 1.14 gauss.

47 pF deduced from Lh_1 (1.65 V) within a measurement error.

Results of Applied Magnetic Field The upper hybrid resonance frequency is a function of a magnetic field intensity. To identify the Fh_1 resonance to be the upper hybrid resonance frequency, an external magnetic field is applied being controlled its field intensity to change the electron gyro-resonance frequency. (see section 3.1, chapter III). Two examples of experimental results in the helium plasma with the gas pressure of 1.4×10^{-4} torr., and the electron density of 4.0×10 cm^{-3} are shown in Fig. 5-74, (a) and (b). The produced magnetic field intensities are 0.5 gauss and 1.14 gauss; outputs of the binary counter for Fh_1 corresponding to these magnetic field intensities are 2.386 MHz and 3.707 MHz, respectively. Calculated values of the upper hybrid resonance frequencies using the observed electron density and the magnetic field strength are 2.41 MHz and 3.66 MHz, which agree well with the observed data of Fh_1 again, within the measurement error.

§ 4. Computer System for Data Analysis

4.1 Data Processing and Analysis System

The large volume of data transmitted from the satellite should be analysed with precise orbit data to fix the time-space of each datum point. For this purpose a systematic usage of a computer system has been carried out.

The data are transmitted to the ground station through the telemetry system from two data sources; one is direct transmission on real-time base and the other is the reading-out of stored-data on the data recorder. The received signals, on the ground, are demodulated to obtain the differential phase shift keying (DPSK) codes. DPSK codes are decoded to obtain digital binary codes. These binary codes are stored in the tape recorder with the frame counter code given in the special portion of telemetry frame that is here called F and F_0 counter. These data are edited by the computer that can be controlled by the FORTRAN IV language, adding the starting time (UT) of data frame. Messages that consists of satellite code number, revolution number, receiving date and time, frame period, data block number, and counter numbers of F and F_0, are also put into the computer with the observation data.

The position of the spacecraft is computed using six elements parameters of the satellite orbit and its secular variations, and the time when data were obtained.[306] Data in binary code on the magnetic tape are rearranged, calibrated, and converted to physical quantities such as electron density, impedance value of an antenna in orbit and so on.

Orbital Analysis The methods to calculate the satellite orbit in an arbitrary coordinate system have been presented by many workers (see P. R. Escobal[307] as a review). A brief summary is given to show the calculation procedure. In the present calculation, following orbital elements at epoch time T_0 are given; semi-major axis a [km], eccentricity e, inclination of the orbital plane i [degree], right ascension of ascending node Ω [degree], argument of perigee ω [degree], mean motion n

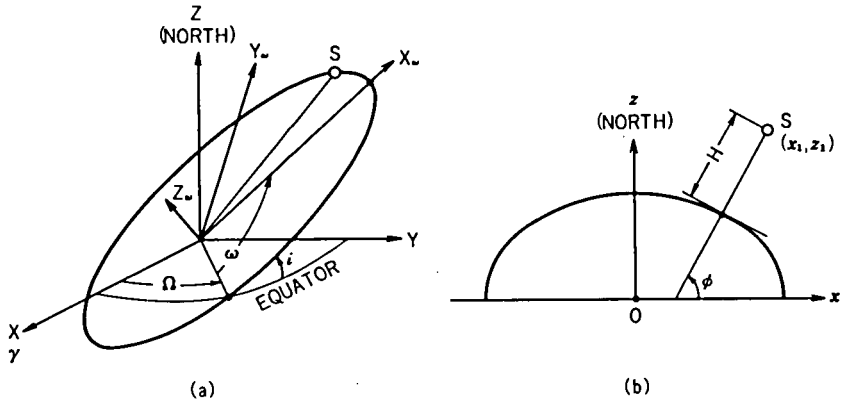

Fig. 5-75 (a) Orbit plane coordinate system (X_ω, Y_ω, Z_ω) and right ascension-declination coordinate system (X, Y, Z). (b) Geodetic coordinate system.

[degree/min], mean anomaly M [degree], and their secular variations due to perturbation around the Keplerian orbit. The eccentric anomaly E is determined from Kepler's equation,

$$E - M = e \sin E. \tag{5.13}$$

In Fig. 5-75 (a), the geometrical relation between the orbit plane coordinate system (X_ω, Y_ω, Z_ω) and the right ascension-declination coordinate system (X, Y, Z) is indicated. The vector γ (see Fig. 5-75 (a)) shows the direction of the mean vernal equinox and Z is the earth's rotation axis. The orthogonal components of the satellite position are obtained as a function of eccentric anomaly angle E, as

$$\begin{aligned} X_\omega &= a\,(\cos E - e), \\ Y_\omega &= a\sqrt{1 - e^2}\,\sin E, \\ Z_\omega &= 0, \end{aligned} \tag{5.14}$$

and these components are transformed into X, Y, and Z components by,

$$\begin{bmatrix} X \\ Y \\ Z \end{bmatrix} = (T) \cdot \begin{bmatrix} X_\omega \\ Y_\omega \\ Z_\omega \end{bmatrix} \tag{5.15}$$

where

$$(T) = \begin{bmatrix} \cos\omega\cos\Omega - \sin\omega\sin\Omega\cos i, & -\sin\omega\cos\Omega - \cos\omega\sin\Omega\cos i, & \sin\Omega\sin i \\ \cos\omega\sin\Omega + \sin\omega\cos\Omega\cos i, & -\sin\omega\sin\Omega + \cos\omega\cos\Omega\cos i, & -\cos\Omega\sin i \\ \sin\omega\sin i, & \cos\omega\sin i, & \cos i \end{bmatrix} \tag{5.16}$$

The position (R, θ, λ_E) in the geocentric coordinate systems is determined from the relations, as

$$R = \sqrt{X^2 + Y^2 + Z^2},$$

$$\theta = \tan^{-1}\left(Z/\sqrt{X^2 + Y^2}\right), \tag{5.17}$$

and $$\lambda_E = \text{mod}\ (360^\circ + \lambda - \lambda_g,\ 360^\circ),$$

where λ_E is the angle measured eastward in the equatorial plane between the inertial X-axis (direction of a mean vernal equinox) and the observer's meridian, and λ_g is the Greenwich angle, that is, the angle between the inertial X-axis and the Greenwich prime meridian. The practical calculation of Greenwich sidereal time at 0 hour U.T. can be accomplished by means of the following formula,[307]

$$\lambda_{g_0} = 99.6909833 + 36000.7689\ T_u + 0.00038708\ T_u^2 \tag{5.18}$$

where the time is measured in centuries as

$$T_u = \frac{JD - 2415020.0}{36525} \tag{5.19}$$

and JD is the Julian Date which is a continuing count of each day elapsed since January 1, 4313 B.C. The Greenwich angle λ_g at any time Δt of day can be obtained if it is known that there is one extra sidereal day for every tropical year, i.e.,

$$\frac{d\lambda}{dt} = 1 + \frac{1}{365.24219879} \quad \text{[revolutions/day]}$$

$$= 0.2506844773 \quad \text{[degrees/minute]} \tag{5.20}$$

then $\lambda_g = \lambda_{g_0} + \Delta t \cdot d\lambda/dt$ (5.21)

The position (H, ϕ, λ_E) in the geodetic coordinate system (see Fig. 5.75 (b)) is determined for the height H from the earth's surface and the geodetic latitude ϕ, as

$$H = \sqrt{(x_0 - x_1)^2 + (z_0 - z_1)^2}, \tag{5.22}$$

and $$\phi = \tan^{-1}\left(\frac{z_0 - z_1}{x_0 - x_1}\right),$$

where $$x_1 = R \cos\theta,$$
$$z_1 = R \sin\theta,$$
$$z_0 = z_1 x_0 (1 - e_E^2)/(x_1 - e_E^2 x_1),$$

and x_0 is one of the roots of the following quartic,

$$x^4 + a_1 x^3 + a_2 x^2 + a_3 x + a_4 = 0, \tag{5.23}$$

with $$a_1 = -2x_1/e_E^2,$$
$$a_2 = -a_E^2 + x_1^2/e_E^4 + (1 - e_E^2) y_1^2/e_E^4,$$
$$a_3 = 2a_E^2 x_1/e_E^2,$$
$$a_4 = -a_E^2 x_1^2/e_E^2.$$

In these equations a_E is the equatorial radius of the earth (6378.160 km) and e_E the eccentricity of the earth (0.08182). The transformation from geocentric coordinates to geodetic coordinates adapted here is to solve the quartic by Newton's method and to determine one of the roots that is located in the same quadrant as the position in the geocentric coordinate system. In this computations, the convergence limit to obtain the root is set ot be 0.1 km which is an adequate resolution for the data sampling of the present observation.

The inverse transformation from geodetic coordinates (H, ϕ, λ_E) to geocentric coordinates (R, θ, λ_E) is easily obtained as

$$R = (x_1^2 + z_1^2)^{1/2}, \tag{5.24}$$

and $$\theta = \tan^{-1}(z_1/x_1), \tag{5.25}$$

where $$x_1 = \left(\frac{a_E}{\sqrt{1 - e_E^2 \sin^2\phi}} + H\right) \cos\phi \tag{5.26}$$

and $$z_1 = \left(\frac{(1 - e_E^2)\, a_E}{\sqrt{1 - e_E^2 \sin^2\phi}} + H\right) \sin\phi \tag{5.27}$$

The geomagnetic coordinate system (θ_m, λ_{Em}) are used extensively in physics of geomagnetic phenomena.[308] The northern and southern points where the axis of the centered dipole, that is set to give the best approximation to the earth's main magnetic field, intersects the surface or the earth are called geomagnetic north and south pole, respectively. The geomagnetic north pole is near Thule, Greenland, at 290.239°E geographic longitude and approximately 11.435° from the geographic north pole on this meridian. Thus, the geomagnetic dipole latitude θ_m and dipole longitude λ_{Em} can be easily obtained from geocentric latitude and longitude as follows.

$$\sin\theta_m = \sin\theta \cos 11.435° + \cos\theta \sin 11.435° \cos(\lambda_E - 290.239),$$

and $$\sin\lambda_{Em} = \cos\theta \sin(\lambda_E - 290.239°)/\cos\theta_m. \tag{5.28}$$

The geomagnetic field intensity can be computed in geocentric spherical coordinates (R, θ, λ_E) as noted in section 2.2, Chapter IV.

The electron density in the ionosphere depends largely on the local time, that is, the solar zenith angle at the observed position. Using the universal time UT[hours] and the east longitude λ_E [degrees], the local time LT [hours] at the observed position is approximately calculated by

$$LT = \text{mod}\,(UT + \lambda_E/15°,\ 24). \tag{5.29}$$

The electron density profiles along the spacecraft orbit are

described with the observed position that is expressed on the geocentric, geodetic and geomagnetic coordinate systems with the local time.

4.2 Calibration Method

The digital data recorded on the magnetic tape at the ground station are rearranged according to observational items listed in Table 5-1. After corrections of equipment characteristics due to temperature variation in the satellite environment, the data are transformed to physical values such as frequencies and the admittance values due to the calibrated data by the equipment for each item.

1) Corrections of the Thermal Shift: As indicated in section 3.2, the operation characteristics of instruments onboard spacecraft depend largely on the operating temperature. The temperature of the IPS preamplifier is measured with the house keeping instrument (HK). Correction function for the data with respect to temperature T is expressed in a form of the series of $\Delta T = T - 20$ using the standard temperature of 20°C as,

$$N_T = N_0 + \sum_{n=1}^{N} C_n(\Delta T)^{n-1} \qquad (5.30)$$

where N_T and N_0 are the data values at T°C (the temperature of preamplifier) and 20°C respectively. The coefficients C_n (n = 1, ..., N) are determined to make the best fit to measured results that have been obtained by the thermal vacuum test as shown in Fig. 5-70.

2) Upper Hybrid and Sheath Resonance Frequencies: Since the gate pulse width of the frequency counter for Fh_1 and Fh_2 is 19.692 μsec, the relation between the digital data N_0 and the resonance frequency f is given by

$$f_{UHR} \text{ or } f_{SHR} = N_0 \times 50.782 \text{ [kHz]}. \qquad (5.31)$$

3) Admittance Values at 0.3 MHz, f_{UHR}, and 13 MHz: Calibration curves

for the admittance values at 0.3 MHz and 13 MHz versus digital data are deduced from Fig. 5-60. The calibration function is given by the expression, as

$$Lh_1 \text{ or } Lh_3 = 10^{**} \sum_{n=1}^{3} C_n N_0^{n-1} \text{ [pF]}. \tag{5.32}$$

There are technical difficulties to obtain the measured calibration function for Lh_2, because Lh_2 is the admittance value at upper hybrid resonance frequency. That is, the calibration data for Lh_2 largely depend on the resonance frequency itself. The calibration is then made using a linear interpolation method as

$$Lh_2 = Lh_3' + \frac{13 - f_{UHR}}{13 - 0.3} (Lh_1' - Lh_3') \tag{5.33}$$

where Lh_1' and Lh_3' are the calibrated values, using eq. (5.32) of the raw data corresponding to Lh_2.

4) Lower Hybrid Resonance Frequency: The lower hybrid resonance frequency $F\ell$ is deduced from $C\ell_{1\sim4}$ which are output values corresponding to frequencies of 1.25, 3.85, 6.65, and 10.1 kHz. The calibration function given as the frequency versus digital data, is given in quadratic equation by least squares using $C\ell_{1\sim4}$ which are obtained in the same period of the telemetry frame. The standard digital data corresponding to $C\ell_{1\sim4}$ are 42, 93, 142, and 187, respectively. These values are used as alternate data when the misdetections on any $C\ell_{1\sim4}$ are revealed in the onboard operations.

5) Admittance Values at 1.25, 3.80, and 6.65 kHz: Admittance values for $L\ell_{1\sim3}$ in IPL channel have been obtained after the three steps of corrections. The first is the correction due to the characteristic of the encoder (ENC), that can be carried out using a function as

$$V_1 = \sum_{n=1}^{3} C_n N_0^{n-1}, \tag{5.34}$$

where N_0 is the obtained digital data for $L\ell_{1\sim3}$. The second correction is for the gate and hold circuits; the characteristics are given by

$$V_0 = \sum_{n=1}^{3} C_n V_1^{n-1} \qquad (5.35)$$

where V_0 and V_1 are input and output voltages. The inputs V_0 versus outputs V_1 characteristics of the gate and hold circuit are given in Fig. 5-45. The third correction is due to the relation of the output voltage from the logarithmic amplifier and the antenna admittance value that is given in Fig. 5-64; the function is here expressed by

$$L\ell_{1\sim3} = 10^{**} \sum_{n=1}^{5} C_n V_0^{n-1} \quad [pF;\ V_0 \text{ in volt}] \qquad (5.36)$$

All the coefficients C_n in eqs. (5.30) to (5.36) including the calibration curve for the temperature of pre-amplifier versus decimal values of HK outputs (word number of W_8 in the telemetry frame whose F counter number is 18) are given in Appendix E.

4.3 Computation of Electron Density

The electron density distribution in global scale are deduced from the measured upper hybrid resonance frequency f_{UHR} with the data of the position where observations were carried out, using eq. (1.45) in which gyro-frequencies f_H were calculated from eq. (4.16). In addition to the upper hybrid resonance frequency, the admittance value at 300 kHz (Lh_1) was also used, that showed the minimum value when the UHR resonance frequency coincided with 300 kHz.

To show electron density profiles as a functions of local time, latitude, and geomagnetic coordinates, the automatic graphical display method is employed using an electronic computer system with a X-Y plotter. The data on spacecraft positions as noted in section 4.1 and the observation data are also stored in the corresponding addresses of the common area of the computer core memory to access quickly due to the program demand. The magnetic tapes are prepared by combining and rearranging these data and the parameters, including operational functions for the X-Y plotter. The flow chart of computing systems for

these data analysis is illustrated in Fig. 5-76.

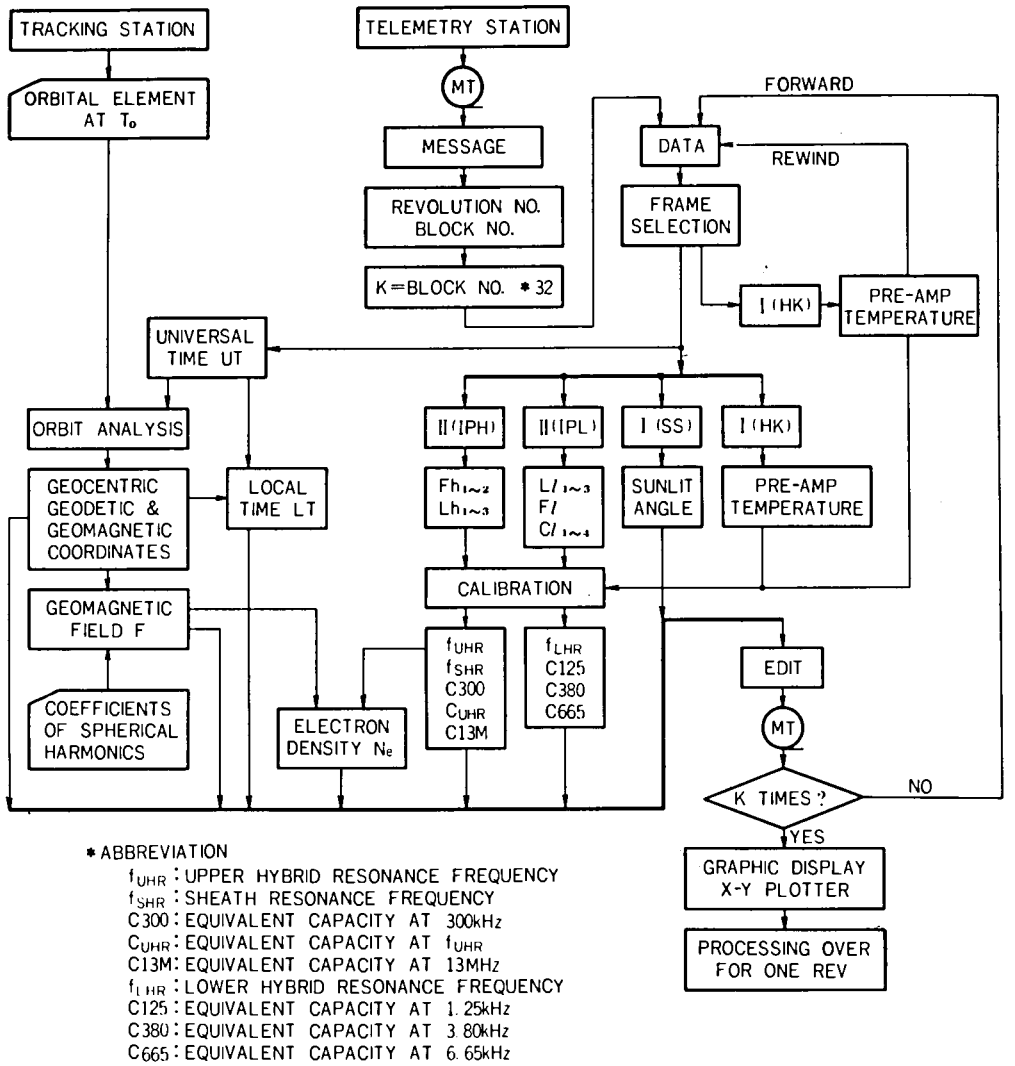

Fig. 5-76 Flow chart of data analysis system.

Chapter VI DISCUSSION OF RESULTS OBTAINED BY THE GYRO-PLASMA PROBE ONBOARD THE SPACECRAFT REXS

§ 1. Introduction

Mu 4S-4 rocket was launched from the Kagoshima Space Center, Uchinoura, Kagoshima, Japan, at 02:40 UT (11:40 JST), August 19, 1972. At 7 min 8 sec after the lift-off, the fourth stage motor injected the spacecraft REXS into orbit at the altitude of 283 km, with the speed of 8.897 km/sec. The satellite was named by "DENPA (Radio Wave)" which bears the international designation "1972-064A".

Mu 4S-4 Launching Mu 4S-4 is a solid propellant four-stage rocket designed as a vehicle for launching the scientific satellite. Total weight of the vehicle is 43,522 kg, the length is 23.698 m, and the diameter of the first and second stages is 1.41 m. Eight strap-on boosters are attached to the first stage in order to augment the thrust at the lift-off time and are jettisoned at 9.5 seconds after lift-off. The first stage flight is stabilized aerodynamically by cruciform fins. After the burnout and the coasting of 20 seconds, the nose covering is jettisoned at the altitude of 50 km, approximately, and then the first stage motor is separated from the upper stage. Ignition of six spin motors, and deployment of six sheets of flares take place to obtain the spin stabilization in the axial direction of the total spacecraft keeping the spin motion of 2.6 rps. The ignition of the second stage motor takes place in series at the interval of 1 second. The third stage motor burns after the separation of the second stage motor. The altitude control system is located between the third and fourth stages. After jettison of the third stage motor, the spinning motion of the upper stage spacecraft is slowed down by a pair of solid despinning motors. The attitude control system starts to operate, then, to direct the vehicle to the local horizontal at the corresponding peak altitude of the rocket

trajectory. The hydrogen-peroxide engine for the attitude control (roll, pitch and yaw) consists of four hydrogen-peroxide reservoirs, two nitrogen gas resorvoirs and eight jet nozzles. When the attitude control is finished, a pair of roll jets give a spin of 0.5 rps to the vehicle. A pair of respin motors are operated to raise the vehicle spin up to 2.7 rps to keep the axial stability again. The fourth stage spherical motor is ignited at the peak of the trajectory. The ignition is designed to make by a programmed timer. A radio command system for the ignition is also prepared for the case of the deviating flight from the planned trajectory. The last stage spherical motor provides a velocity increment to achieve orbital velocity. After the burnout of the last stage motor, the main spacecraft is separated by releasing a marman clamp keeping the spin motion for attitude stabilization. Three retromotors are fired to decelerate the burnout motor to give a safety distance between the main spacecraft.

Detailed descriptions and preliminaly results about the launching phase of Mu 4S-4 have been reported by the rocket launching group.[309]

In this chapter, the results obtained with the gyro-plasma probe onboard the spacecraft REXS are presented. The performance and orbit of the spacecraft including the preliminary experimental data are given in section 2. From the measured upper hybrid resonance frequency, the electron density distribution in the altitude range from about 240 km to 6570 km were obtained and compared with the diffusive equilibrium distribution. The geomagnetic latitude dependence of electron density distribution in the F layer and the field aligned scale height are also deduced. The results are given in section 3.

§ 2. Experiment and Results

2.1 Performance

The instruments in REXS operated satisfactory following the planned programme in the launching phase and the orbital injec-

tion phase. The first step of monopole antenna was deployed by the pre-set timer, and the second and third steps were extended by the radio command at the first and the sixth satellite revolutions, respectively. At the Kagoshima Space Center, all the real-time mode telemetry data as well as the onboard tape-recorder playback mode data were received from August 19 to 22. On August 22, 09:07 JST when the high tension electrical circuit of the electron flux analyser (EBA) was switched on at the first time after the launch, a fatal accident took place. The power supplies of the spacecraft fell in some abnormal condition, and the telemetry encoder ceased to operate normally so that any meaningful data have never been transmitted afterwards. Therefore, the data during the first to 26th revolutions around the earth were available to manipulate.

The attitude of the spacecraft was measured by the flux-gate magnetometer (MGS).[310] This gives the direction of spin axis in the right ascension of 250° ± 5°, declination of - 15° ± 3°, with corning angle of less than 5°. The angle between the spacecraft spin axis and the direction of the sun is estimated to be 108°. The attitude of the spacecraft in the right ascension-declination coordinate system is illustrated in Fig. 6-1. The spin rate was 2.99 rps at the time of injection, decreasing gradually with time at rate of - 0.01 rps/100 revolutions.

The post-launching radio tracking was made by the collaboration of Japanese network, NASA, and CNES tracking stations. The routine radio tracking has been conducted by Orbit Computation Center (Tsukuba) of National Space Development Agency (NASDA), using the data of tracking stations at Katsuura, Okinawa and Uchinoura (KSC). The spacecraft has been injected into an elliptic orbit and the result of orbital elements of REXS on August 21 reported by NASDA are;

Epoch Time	1972,8,21.00.00.00 U.T.		
Semi-major Axis	a	[km]	9784.453
Semi-major Axis Dot	å	[km/day]	0.0
Eccentricity	e		0.3233

Inclination	i	[deg]	31.002
R.A. of Ascending Node	Ω	[deg]	41.392
Motion of Ascending Node	$\dot{\Omega}$	[deg/day]	-2.383
Argument of Perigee	ω	[deg]	127.878
Motion of Perigee	$\dot{\omega}$	[deg/day]	3.717
Mean Motion	n	[deg/min]	2.244
Mean Motion Dot	$\dot{n}$	[deg/min/day]	0.0
Mean Anomaly	M	[deg]	319.170
Anomalistic Period	T_p	[min]	160.533
Period Dot	$\dot{T}_p$	[min/day]	0.0
Height of Perigee	h_p	[km]	242.983
Height of Apogee	h_a	[km]	6569.593

These parameters were used to calculate the spacecraft position where the observation was carried out. The orbit of the spacecraft REXS projected on the earth's surface is illustrated in Fig. 6-2. Since the anomalistic period of this spacecraft was about 24 hours/9, the orbits of revolution numbers of n and n+9 are approximately the same. And, the deviation of the local times at the same phases of the spacecraft positions in orbit is approximately equal to the motion of ascending node and is very small. Fortunately, these facts are very convenient to investigate the physical conditions of the electron density profiles in the ionosphere.

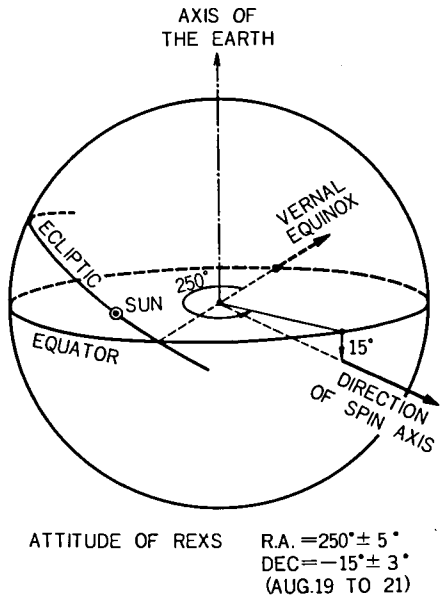

Fig. 6-1 Attitude of the spacecraft in right ascension-declination coordinate system.

2.2 Results and Data Analysis

The IPS instruments onboard the spacecraft REXS has been successfully operated and the

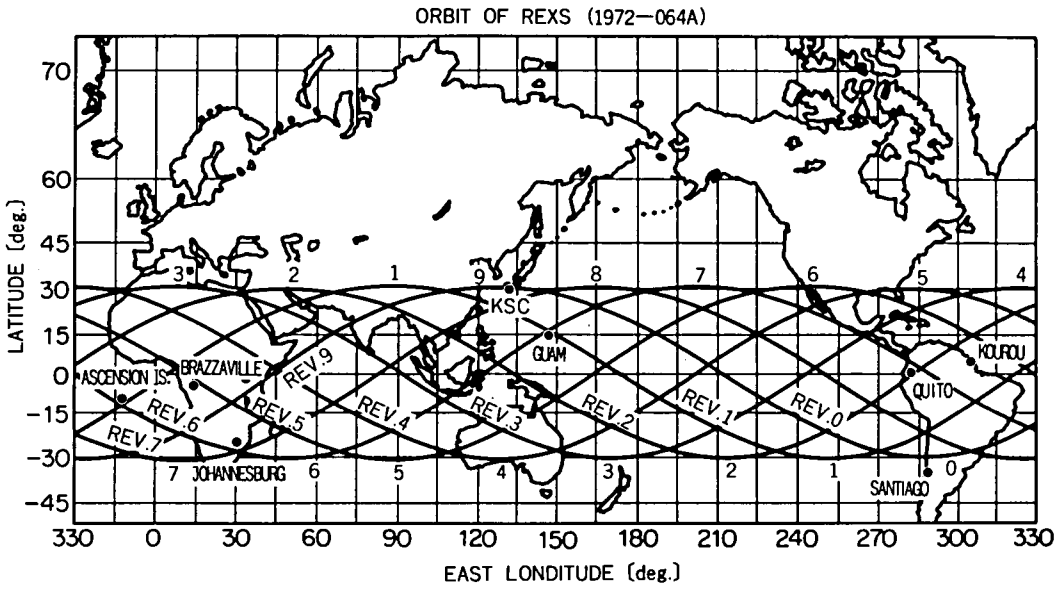

Fig. 6-2 Orbit of REXS Satellite.

measured values of all the observational items have been transmitted through the telemetry system. The real-time telemetry data were recorded on the paper tapes, and the onboard tape-recorder playback data were stored on the magnetic tapes. Both these PCM signals were, also, sent to the main quick-look equipment and converted to analog signals that were diplayed by the pen-recorders. The IPS quick-look sorted these time-serial data of mode II_1 and II_2 into six parallel channels that include two items each as Fh_1 and $F\ell$ in #1, Fh_2 and $F\ell$ in #2, Lh_1 and $L\ell_1$ in #3, Lh_2 and $L\ell_2$ in #4, Lh_3 and $L\ell_3$ in #5, and $C\ell_{1\sim4}$ in #6. In Fig. 6-3, an example of the data displayed by the quick-look system is shown for the case of revolution #23, on Aug. 21, 1972. An overall profile of the measured values of each observational item during one revolution period of the satellite observation can be clearly found from this chart. The upper hybrid and sheath resonance frequencies (Fh_1 and Fh_2) are increasing from the beginning of the record and show the maximum values at the height of about 390 km which corresponds to the height of F2 peak. Above this altitude,

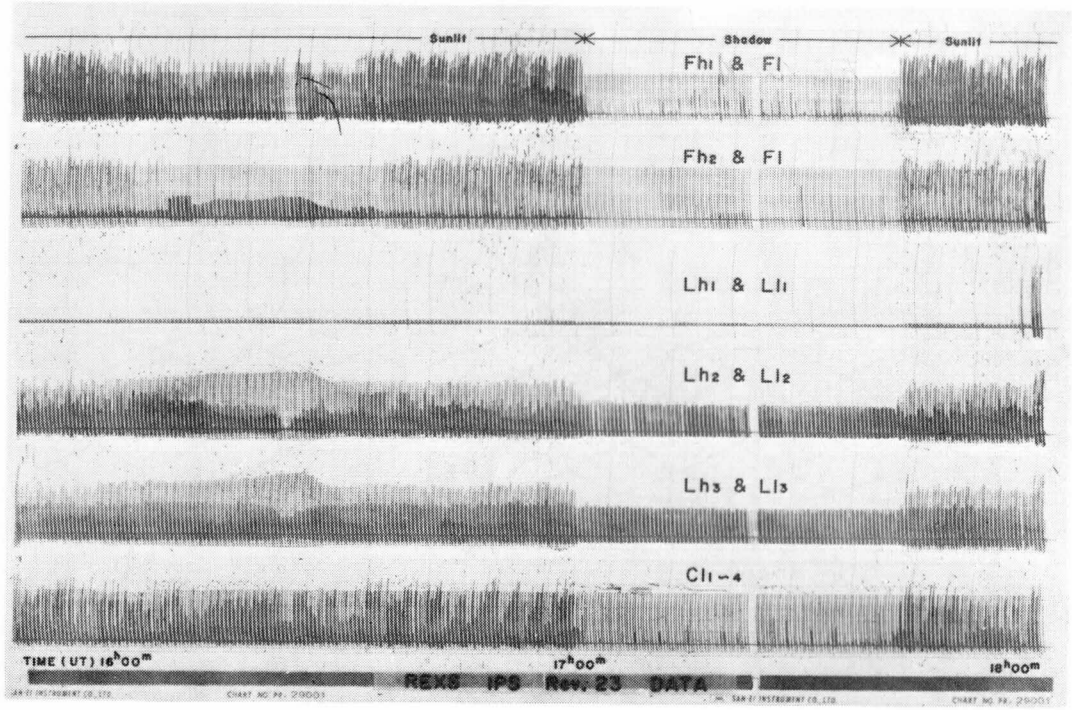

Fig. 6-3 Records of IPS quick-look (rev. #23, Aug. 21, 1972).

the values are gradually decreasing. The admittance value at f_{UHR} (Lh_2) is inversely correlated to the values of Fh_1 and Fh_2. The value of Lh_3 shows the admittance of the antenna in free space, and slightly decreases as Fh_1 increases. Admittance values at VLF range (Lℓ) are abruptly changed when the spacecraft passed through the shadow line due to the earth. The detailed features of the observed data will be given later.

To check the instrument operation, the command signal "PI CAL ON" was transmitted at the revolution #17. The transmitted data of sub-carrier frequency through a 400.5 MHz for the frequency monitor of the crystal controlled oscillator for the gate control circuit of the high frequency gyro-plasma probe was just 5.59 kHz. The swept frequency of the low frequency gyro-plasma probe was from 5.01 kHz to 5.23 kHz, as shown in Fig. 6-4. These calibration data showed quite normal values as noted in section 2.4, Chapter V.

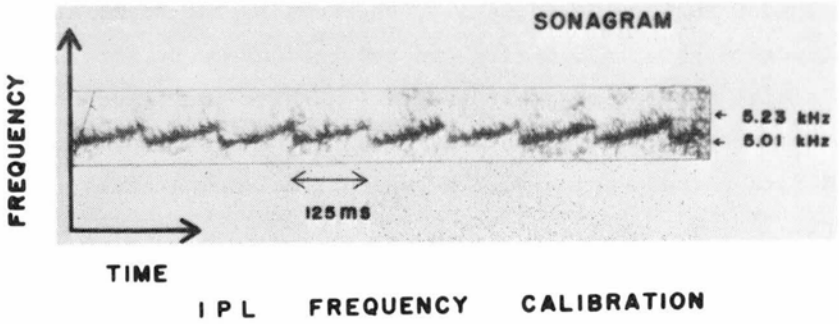

Fig. 6-4 Record for IPL frequency calibration.

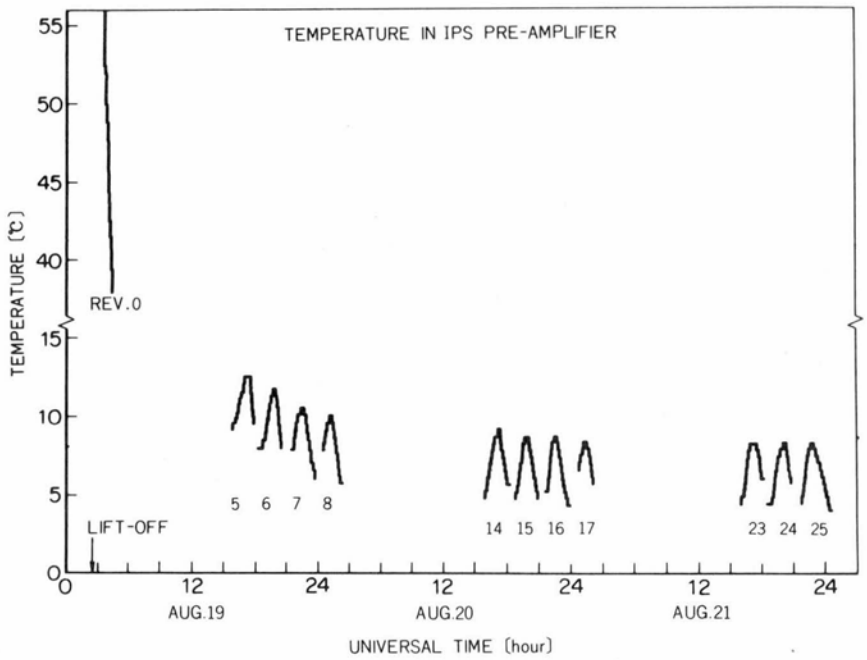

Fig. 6-5 Temperature in IPS pre-amplifier obtained with house keeping equipment.

The temperature in the pre-amplifier was monitored by the house keeping instrument, the data from the revolution #0 to #25 being plotted in Fig. 6-5. The temperature was about 56°C at the beginning phase of the orbiting. As the spacecraft passed through the sunlit

and the shadow regions periodically, the temperature oscillated with an amplitude of about 4°C during one revolution except for the case of the initial revolution that indicate a rapid decrease of the average temperature. These data are used for the corrections of the observed data corresponding to the operational temperature of the equipment.

Examples of the observed data for each observational item as a function of local time are illustrated in Fig. 6-6 to 14, being converted from the binary counts to the corresponding frequencies and the equivalent capacitance values through the calibration method.

2.3 Observation of Ionospheric Plasma Resonance

Upper Hybrid Resonance Frequency, Fh_1 Figure 6-6 shows the typical variation of the upper hybrid resonance frequency during one revolution (Rev. #6). Even though a random scattering of data points is appreciable, the lower boundary of the detected frequency values is indicating a continuous profile versus altitude. The scattering of data can be attributed to a noise that may be impressed on the antenna. The noise frequency could be in audio frequency range. The nonlinear modulation of the impressed r.f. signal can be detected like a resonance points even the frequency is completely independent of the UHR resonance frequency. When the spacecraft was passing through the shadow region, the solar cells and electrical circuits in the spacecraft are connected through the diodes in the power supply circuits, while the diodes are cut off in the shadow region. This point suggests that the noise came from the electrical circuits in the spacecraft itself through the solar cells into the surrounding plasma medium. The noise levels at the antenna can be estimated to be 1 ~ 4 mV/m from the scattering of the admittance values (see Fig. 6-9 ~ 14). Once the resonant point is detected, the automatic detection of the minimum point is stopped during the swept frequency period. This means that UHR resonance becomes the lowest possible frequency for the succeeding trial of the minimum

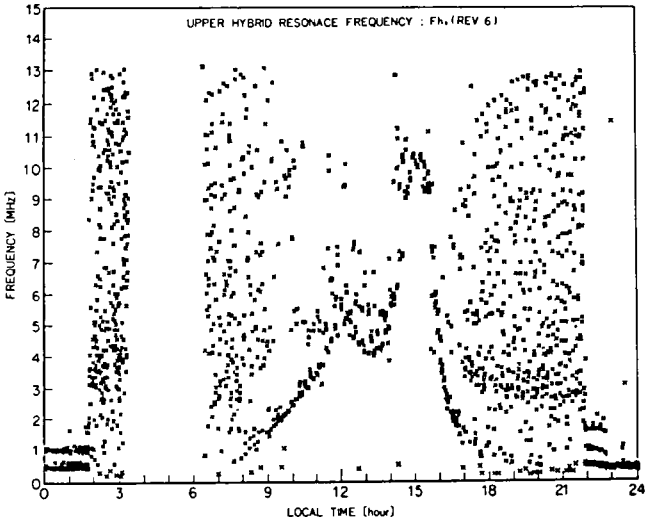

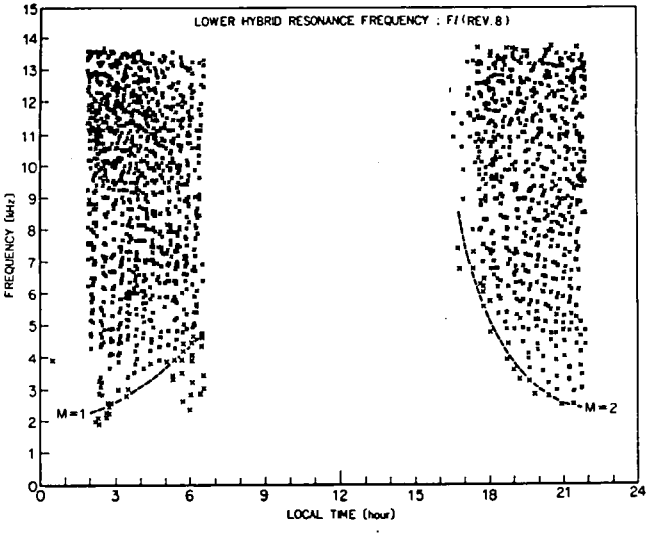

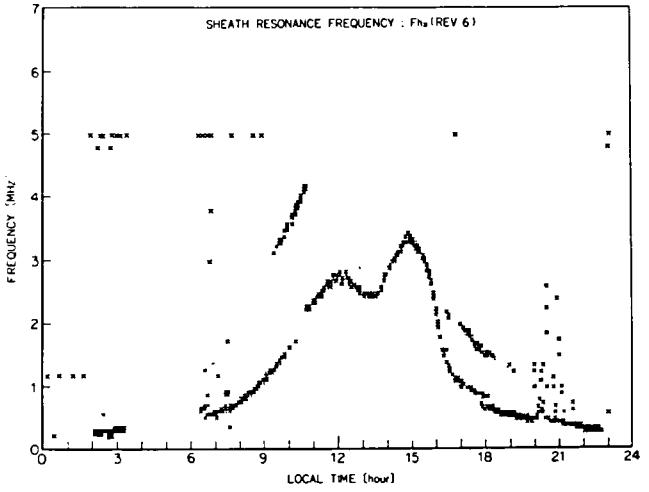

Fig. 6-6 Upper hybrid resonance frequency (Fh_1); rev. #6.

Fig. 6-7 Sheath resonance frequency (Fh_2); rev. #6.

Fig. 6-8 Lower hybrid resonance frequency ($F\ell$); rev. #8.

detection under the superimposed severe noise disturbances.

The electron density values can be deduced from these detected UHR frequencies. The perigee point of the spacecraft orbit is at 13:35 L.T. and its altitude is 247 km. Before arriving and after passing this point, two maxima of the upper hybrid resonance frequencies were appeared. The altitudes and the values of these peaks are corresponding to those of F2 peaks at the different positions.

Sheath Resonance Frequency, Fh_2 . Figure 6-7 shows the measured sheath resonance frequencies at the revolution #6. The admittance value of the antenna near the sheath resonance frequency is high; the noise ratio to the signal is therefore negligibly small to avoid the misdetection of the resonance due to noise. In addition to the usual sheath resonance, the second and higher harmonics of the sheath resonance have been revealed, as was done for the case of the rocket borne gyro-plasma probe experiment (see section 4.3, chapter IV). Assuming the magnetic field is applied perpendicular to the antenna surface, the sheath resonance frequency f_{SHR} is approximately expres-as

$$f_{SHR} = (f_H^2 + \frac{f_p^2}{1 + C_s})^{1/2} \qquad (6.1)$$

where C_s is a sheath capacitance normalized by an antenna capacitance in free space. As is obvious from this equation, the sheath resonance frequency increases as the gyro-resonance and the plasma frequencies increase. Namely, the sheath resonance frequency changes its value correlating with the variation of the upper hybrid resonance frequency as has been shown in Fig. 6-7. Since the sheath capacitance C_s depends largely on the electron temperature, the electron temperature could be deduced from the observed sheath resonance frequency using the electron density and the strength of the geomagnetic field. But more accurate calculation for the sheath resonance frequency as a function

of electron density, temperature, shape of an antenna, etc. should be required.

Lower Hybrid Resonance Frequency, $F\ell$ Figure 6-8 shows the measured lower hybrid resonance frequency during the revolution #8. Since the admittance in the lower frequency region except the resonance can be expressed by the parallel combination of the sheath capacitance and resistance, the admittance value decreases as the frequency increases. And, the measured value is the last sampled and stored data in one frequency sweep. As is mentioned before, the pseudo-resonances (noises) triggered the automatic resonance detection circuit for the lower hybrid resonance and this noises were logarithmically enhanced in the lower admittance values. Therefore, the lower boundary of the obtained data are considered to be the lower hybrid resonance frequency. This resonance detections did not operated in the lower altitude ($<$ 100 km) due to the collisional effect and in the shadow regions where the ion sheath region formed around the antenna increased due to the vehicle's potential drop. Using these data and eq. (5.10), the effective ion mass in the altitude range from 1000 km to 6500 km was computed. Assuming that the effective ion mass M_{eff} is equal to 2.0 along the ascending path (1000 km ~ 4000 km, $\theta_m = +11° \sim -20°$) and equal to 1.0 along the descending path (6400 km ~ 3000 km, $\theta_m = -26° \sim -7°$), the lower hybrid resonance frequencies are computed using the measured electron densities and the calculated geomagnetic field intensities along the spacecraft trajectory, and shown in Fig. 6-8 by dotted lines. This result indicates that the heavy ions such as He^+ exist in the equatorial region up to 4000 km.

2.4 Observation of Antenna Admittance

Admittance Value at 300 kHz, Lh_1 Figure 6-9 shows the variation of admittance values at 300 kHz during the revolution #6. When the upper hybrid resonance frequency is much larger than 300 kHz, this admittance

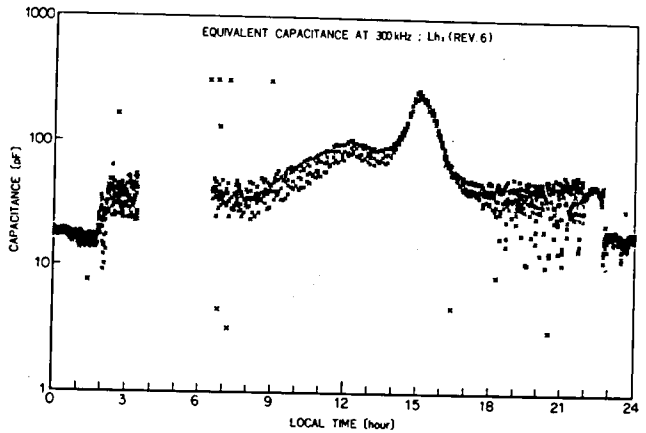

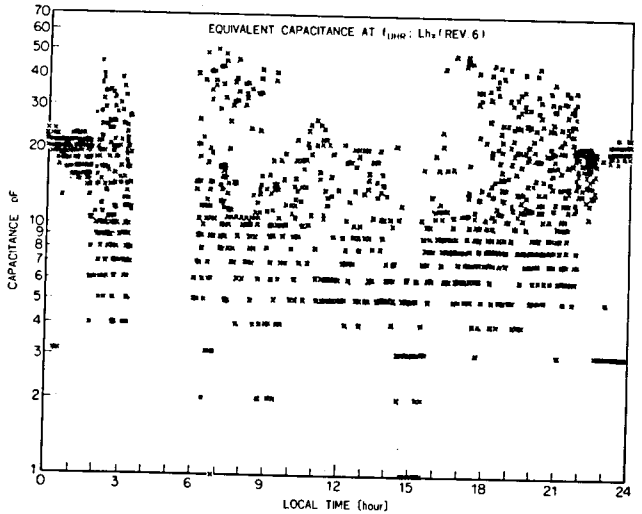

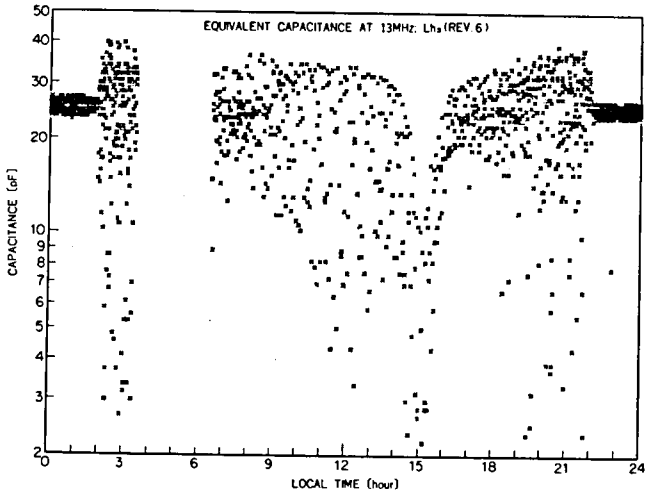

Fig. 6-9 Equivalent capacitance at 300 kHz (Lh_1); rev. #6.

Fig. 6-10 Equivalent capacitance at f_{UHR} (Lh_2); rev. #6.

Fig. 6-11 Equivalent capacitance at 13 MHz (Lh_3); rev. #6.

value represents the admittance of ion sheath surrounding a antenna in a plasma. The formation of the ion sheath is largely controlled by the difference of the thermal velocities between the electrons and ions. Therefore, this admittance value that relates to ion sheath thickness depends on the electron temperature. The sheath resonance frequency is also the function of the sheath thickness. This can be checked using the measured data. For example, f_{SHR} = 3.305 MHz, f_{UHR} = 9.090~ 9.293 MHz at $14^h\ 41^m\ 15.25^s$ (L.T.), and then the sheath capacitance deduced from the sheath resonance frequency using eq. (6.1) is 183 ~ 192 pF, while value at 300 kHz is 185 $\pm$ 7 pF.

When the upper hybrid resonance frequency is close to 300 kHz, to measure the admittance value at 300 kHz is equivalent to a fixed frequency impedance probe. The minimum and maximum points of the values in a certain period across the magnetosphere are identical to the upper hybrid and the sheath resonances, respectively. The equivalent capacitance value can be used to deduce the electron density. In the case of the revolution #6, this minimum point was revealed at the altitude of 5955 km where the geomagnetic field intensity was 0.068 gauss, and then the electron density at that position was calculated to be $8.29 \times 10^2\ cm^{-3}$.

The admittance value were abruptly varied when the spacecraft passed through the sun's shadow line due to the earth. This phenomena were also found clearly in the low frequency side ($L\ell_{1\sim3}$). This is considered to be due to the antenna potential change with respect to the space potential. In the sunlit region, the photoemissions from the antenna surface reduces the accumulation of the excess electron despite of the difference of thermal velocities between electrons and ions. This effect lifts the antenna potential close to the space potential. The admittance value of the sheath increases as a result of the decrease of the sheath radius. The spacecraft or the antenna potential is largely controlled by the photoemission effects as indicated by this result. This suggests that the electron density measurement with any static potential analyser should be carefully

planned to avoid the potential change due to this photoemission effect in the very tenuous plasma regions.

Admittance Value at f_{UHR}, Lh_2 Figure 6-10 shows the measured admittance values at the upper hybrid resonance frequency. This value represents a Q value of the resonance, that is, the values decrease as the Q values increase. The admittance value at the resonance is so small as to be covered with the aforementioned noises in the sunlit region. It is obvious that the values decreased when the spacecraft passed through the F2 layer where the electron density increased. While the collision frequency becomes very low above the F2 layer, the Q value of the resonance decreased. This indicates that the some dissipative mechanisms besides the collision may occur even in a collision free plasma.

Admittance Value at 13 MHz, Lh_3 Figure 6-11 shows the variation of admittance values at 13 MHz during the revolution #6. This admittance value is a monitoring output of the capacitance of an antenna in free space, and the measured admittance indicated the value of 26 pF that is just coincide with the antenna capacitance measured in the preflight operation tests. When the upper hybrid resonance frequency was close to 13 MHz in the F2 layer, the admittance values were affected by the plasma resonance and varied its value like a resonance.

Admittance Values at 1.25 kHz, 3.80 kHz, and 6.65 kHz, $L\ell_1$, $L\ell_2$, $L\ell_3$ Figure 6-12, 13, and 14 shows the admittance values at 1.25 kHz, 3.80 kHz, and 6.65 kHz measured by the low frequency gyro-plasma probe. As noted in section 3.3, chapter V, the admittance value in this frequency range increases as the sheath resistance decreases as a result of the increase of the electron density. The sheath resist ance and capacitance are deduced from eq. (5.11). For example, the admittance values were 8103.5 pF at 1.25 kHz, 3557 pF at 3.80 kHz, and 2678.5 pF at 6.65 kHz at the altitude of 595 km where the electron density was 2.7×10^5 cm^{-3}. Using these values and eq. (5.12), the

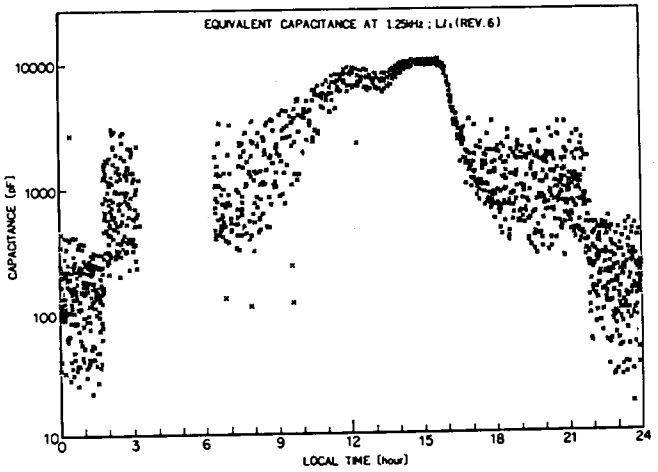

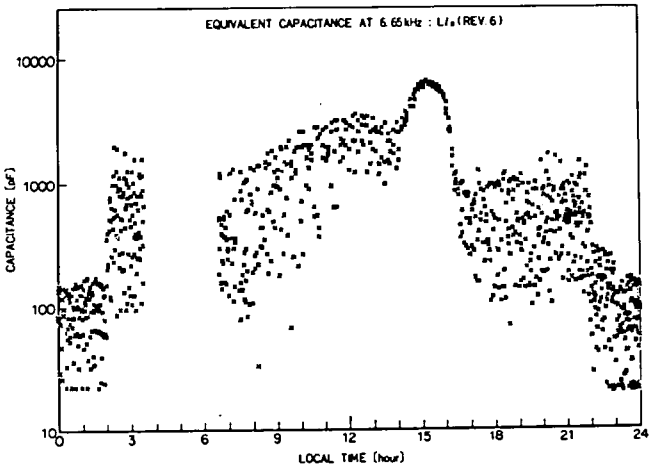

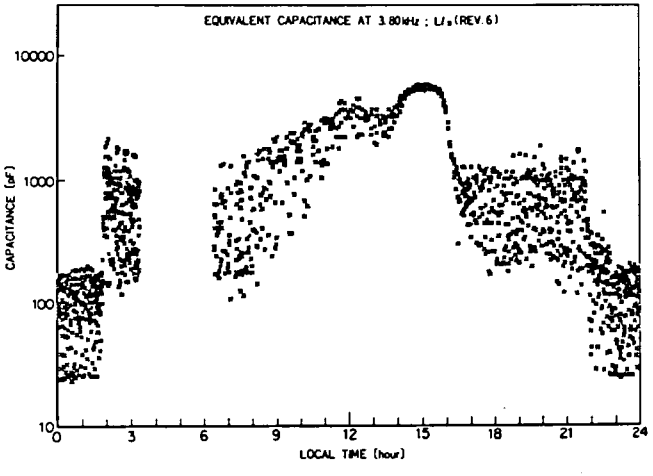

Fig. 6-12 Equivalent capacitance at 1.25 kHz; rev. #6.

Fig. 6-13 Equivalent capacitance at 3.80 kHz; rev. #6.

Fig. 6-14 Equivalent capacitance at 6.65 kHz; rev. #6.

sheath resistance and capacitance are calculated, i.e., R = 600Ω ~ 680Ω and C = 2100 pF ~ 2500 pF, and the condition $(\omega R)^{-1} > C$ is satisfied. The reason for the very low value of the sheath resistance is considered that the photoemission from the antenna metal surface acts to increase the conductivity of the sheath region. In the shadow region where the photoemission is cut off, the sheath resistance abruptly increased to be several hundred kilo-ohms and the sheath capacitance also decreased its value to be several tens pico-farads. As for the potential of the antenna with respect to the space potential in the case of the above example, the value of about - 0.05 volts is calculated from eq. (5.12) if the electron temperature of 1500 ~ 2000°K was assumed. In this case, the computed floating potential of the antenna is about -0.5 volts. This difference of the antenna potential was also caused by the photoemission effect.

All observations were successfully carried out in the experiment with IPS onboard the spacecraft REXS. Operations of the automatic detection systems as the satellite borne instrument were satisfactorily performed and confirmed. The data for resonance frequencies and admittance values of an antenna in a magnetospheric plasma were obtained. Especially the detection of lower hybrid resonance by the impedance measurement method has been made for the first time. From these data, global electron density profiles and the effective ion mass have been calculated. The admittance values as a function of electron density, the electron temperature and the antenna potential have been discussed. The photoemission effects on the antenna potential and its relation to admittance values in a wide frequency range (1 kHz to 13 MHz) have been revealed. Noises from the spacecraft itself disturbed the signal to be detected, but the signal could be clearly discriminated from these noises.

§ 3. Electron Density Profile in the Ionosphere

3.1 Topside Ionosphere

From the measured upper hybrid resonance frequency, the electron density can be deduced, using the gyro-frequency that is computed from the measured local geomagnetic field intensity at the satellite position. Figure 6-15 shows the calculated geomagnetic reference field intensities along the REXS orbit (solid lines) and the measured values with the flux-gate magnetometer (MGS^{310}) onboard the spacecraft at the revolution #6. The geomagnetic field changes its intensity from about 0.039 gauss to 0.43 gauss. Since calculated value is a good approximation of measured value, the geomagnetic reference field was employed to compute the gyro-resonance frequency. Assuming all the detected values (as have been shown in Fig. 6-6) to be the upper hybrid resonance frequency, the electron density values versus the geomagnetic longitude are calculated and one example of the revolution #6 is illustrated in Fig. 6-16.

Figure 6-17 (a) and (b) show the distributions of these values versus altitude along the ascending and descending paths. As demonstrated in the previous section, the lower boundaries of these measured values show electron density profiles along the spacecraft orbit. All measured electron density profiles in the altitude range from 240 km to 6570 km are shown in Fig. 6-18 (a) and (b), corresponding to the ascending paths and the descending paths, respectively. Since the spacecraft trajectories of the revolution numbers of n and n+9 (n; integer) take approximately the same position with respect to the solar coordinate, the groupings of the same orbit (for example, the revolution numbers #6, #15 and #24) are made in these figures. Local times at the spacecraft positions when the measurements were carried out are computed and shown in the figures. From the resonances revealed by fixed frequency admittance values at 300 kHz, electron densities at the altitude of about 6000 km were deduced and shown in the figure by the dotted circles, from which the solid lines are drawn in accordance with R^{-3} and R^{-4} power law

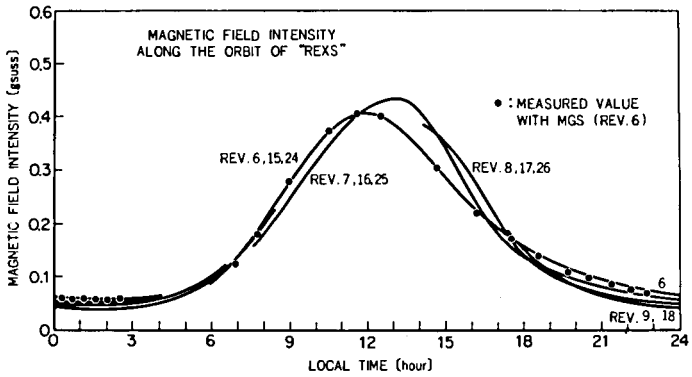

Fig. 6-15 Geomagnetic field intensity along the orbit of "REXS". The dots indicated on the curve are measured values with MGS.

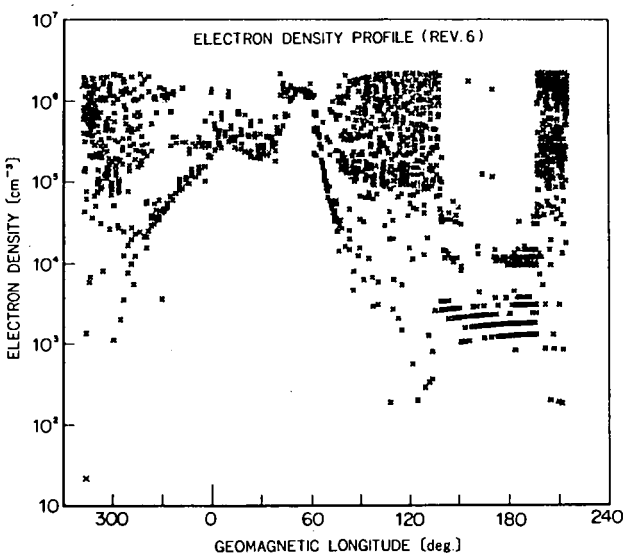

Fig. 6-16 Electron density profile deduced from measured values of f_{UHR} (see Fig. 90) during revolution #6.

models, where R is the radius vector along a geomagnetic field line.

As for the distribution of electrons and ions along the geomagnetic field line, J. J. Angerami and L. O. Thomas[208] gave the theoretical

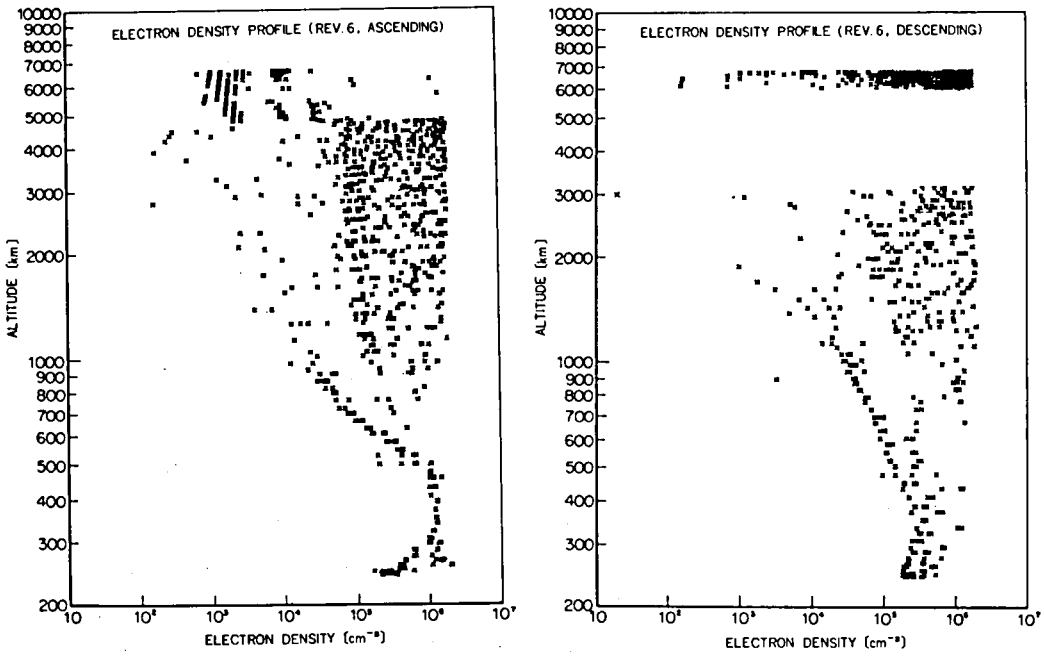

Fig. 6-17 Electron density profile versus altitude.

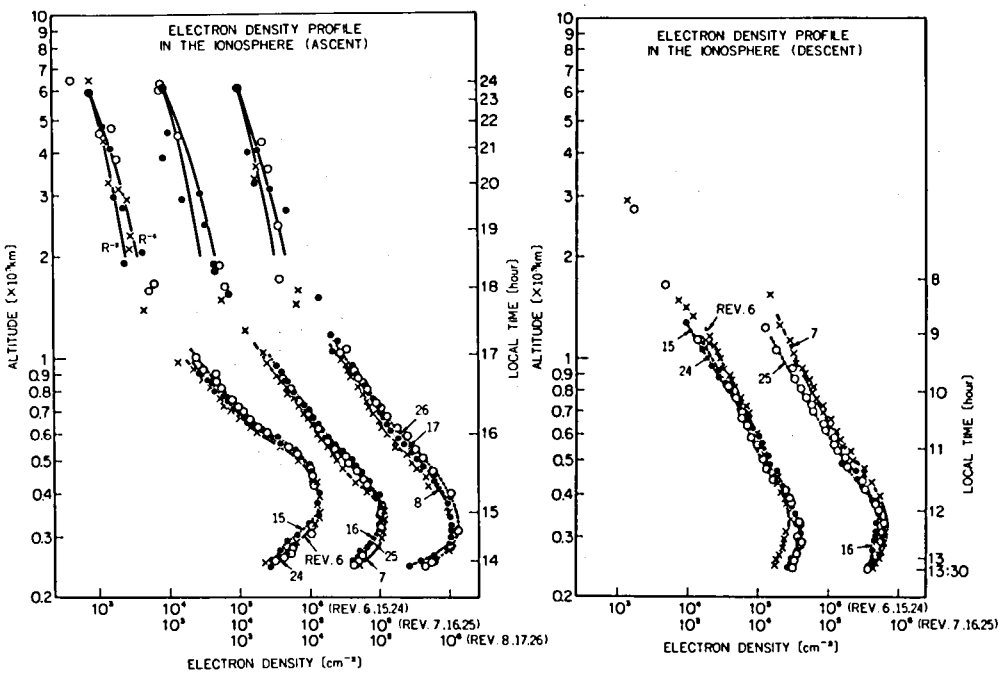

Fig. 6-18 Electron density profiles versus altitude.

consideration about its diffusive equilibrium, taking into account the effect of the electric field that arises from charge separation, the centrifugal force arising from the rotation of the earth, and the effect of the gravitational field. Their calculation is presented in section 2.3, chapter I (see Fig. 1 - 11). The vertical electron distribution up to about 2000 km has been obtained by the gyro-plasma probes in the Lambda 3H-2, 5 and 6 sounding rocket experiments as described in section 3.1, chapter IV. The theory of the diffusive equilibrium has been verified to be a good approximation of the observed electron density distribution. This theory is also applicable to the electron density profiles as shown in Fig. 6-18. Following Bauer,[212] and Eviatar et al.,[231] the electron density profile of ion-exosphere model distribution is given by eq. (1.20). As noted in section 2.3, chapter I, this type of distribution is one which corresponds to a diffusive equilibrium, weighted by a function dependent on the intensity of the geomagnetic field. In this experiment, the distributions of the measured electron density values above about 2000 km fit with the power law models rather than with the diffusive equilibrium distribution.

3.2 Equatorial F Region

As for the electron density profile in the region near the F layer, S. Chandra developed a modified Chapman function with a variable scale height gradient, as noted in section 2.2, chapter I. To give the analytical form for the variable scale height, a modified Chapman function given in eq. (1.17), has been found to be in good agreement with the electron distribution obtained experimentally within the height range from about 100 km below the F2 peak to an altitude of about 700 km.

In this experiment, the five different groups of electron density profiles near the F2 layer in the daytime were obtained. Although the little differences can be found within one group that includes

three observations along the same orbital phase, these distributions mainly controlled by the geomagnetic latitudes. Fig. 6-19 shows the average distribution of the electron density profiles of one group versus the altitude. During these three-day observations, the geomagnetic and solar activities were much the same and were slightly disturbed; the sum of K_p indices (K_p is a geomagnetic planetary three-hour-range index) are 22^+, 23^-, and 24^-, the relative sunspot numbers, R_z, are 54, 48, and 60, and the daily solar flux at 2800 MHz are 116.2, 117.9, and 119.5 ($\times 10^{-22}$ Wm^{-2} Hz^{-1}), corresponding to August 19, 20, and 21, respectively.[311] To refer to the variations due to the geomagnetic latitude, the geomagnetic latitudes at the altitude of 350 km are listed in Fig. 6-19; the value of the group a is 23.7° north and that of the group d is 41.2°. Figure 6-20 (a) and (b) show the geomagnetic latitude dependences of the heights of F2 peak and the maximum electron density values of F2 layer. As is evident from the figures, the maximum electron density and the height of F2 peak increase with the decrease of the geomagnetic latitude. The local time dependence of these values is considered to be negligible because the times when the spacecraft passed through the F2 peak are much the same; at 14:40 to 15:07 (L.T.) in the ascending phases and at

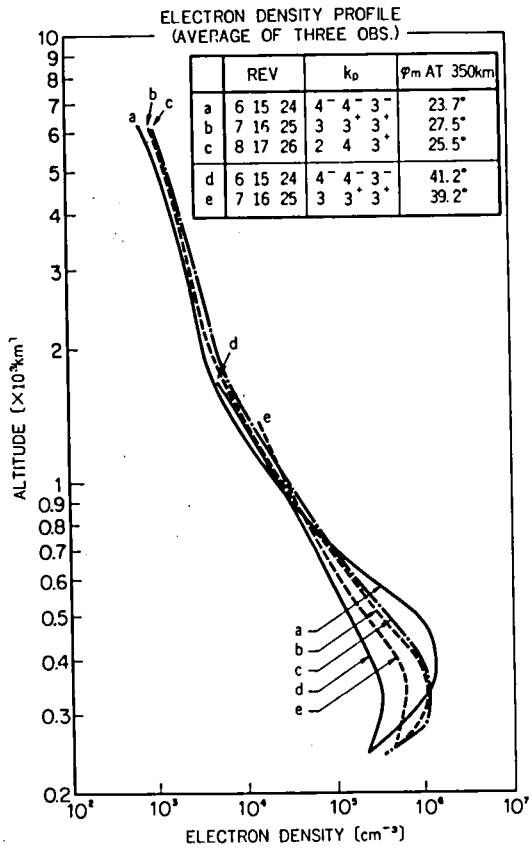

Fig. 6-19 Average electron density profiles of three sets of observations along the same orbital phase.

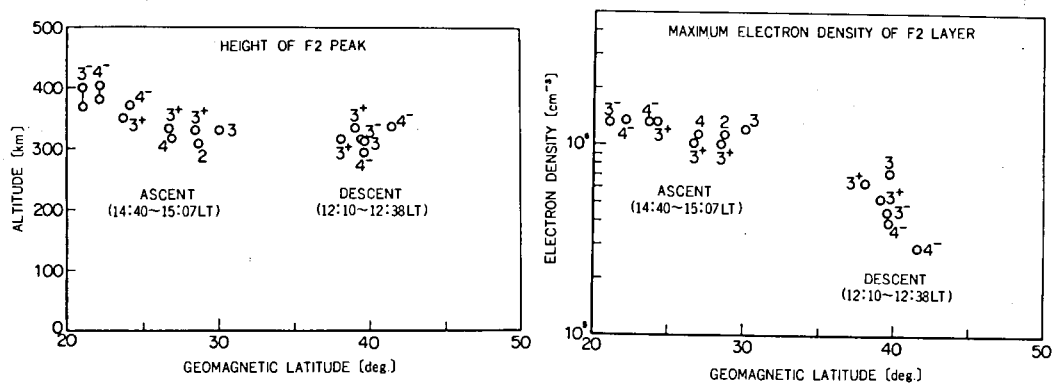

Fig. 6-20 Geomagnetic latitude dependence of F2 peak; (a) height of F2 peak (b) maximum electron density of F2 layer.

12:10 to 12:38 (L.T.) in the descending phases. Consequently, these changes of the electron density and the height of F2 peak are considered to be due to the geomagnetic control.

Figure 6-21 shows the latitudinal variation of electron density at the altitude from 250 km to 900 km, in terms of electron densities at constant altitude versus geomagnetic north latitude. Figure 6-22 represents the contour map of the constant electron density in the altitude-latitude domain. The local time along the spacecraft orbit as given in the same figure, varies from about 10:00 to 13:00 in the descending phase and from about 14:00 to 17:00 in the ascending phase. Since there is no large difference of the local time in the obtained data around the low latitude, enhancements of electron density in the middle latitude towards the equatorial region are due to the well-known equatorial anomaly as discussed in section 2.2, chapter I. The data obtained by the topside sounder satellite Alouette show the remarkable enhancements of electron density above the F2 peak up to the altitude of 700 km. The electron density distributions obtained by the Alouette observation corresponding to Fig. 6-21 is given in Fig. 1-6 (p. 18). The theoretical calculation of contours of electron density as a function of latitude and height given in Fig. 1-8 (p. 20) corresponds to Fig. 6-22. These results indicate the dynamical behaviours of the topside F2 region as discussed in section 2.2,

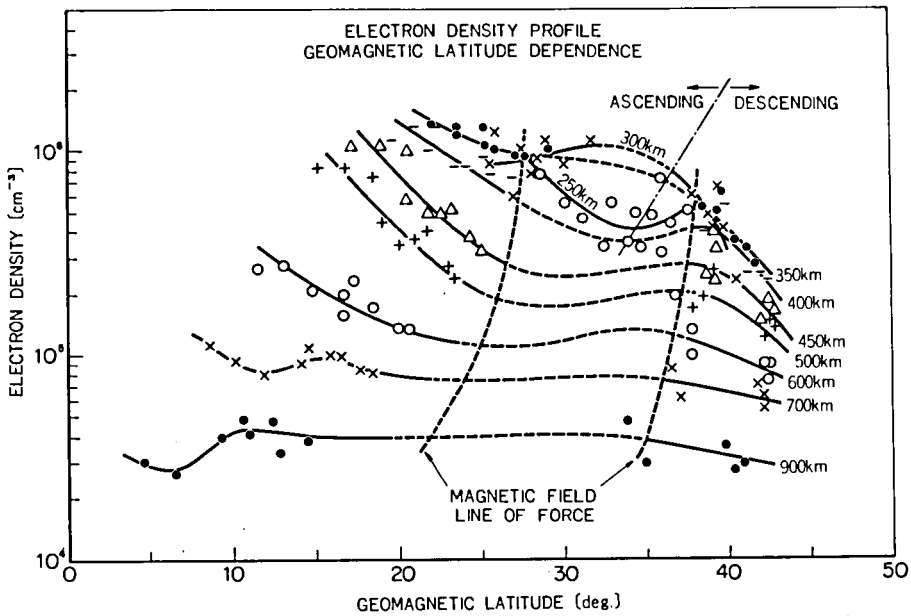

Fig. 6-21 Electron density profile; constant height versus geomagnetic latitude.

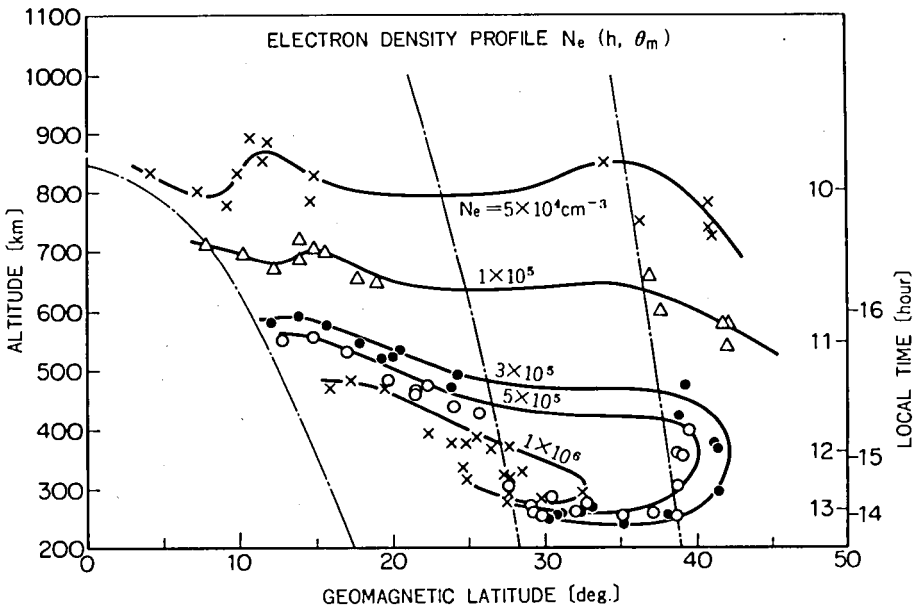

Fig. 6-22 Contour map of constant electron density in altitude-latitude domain.

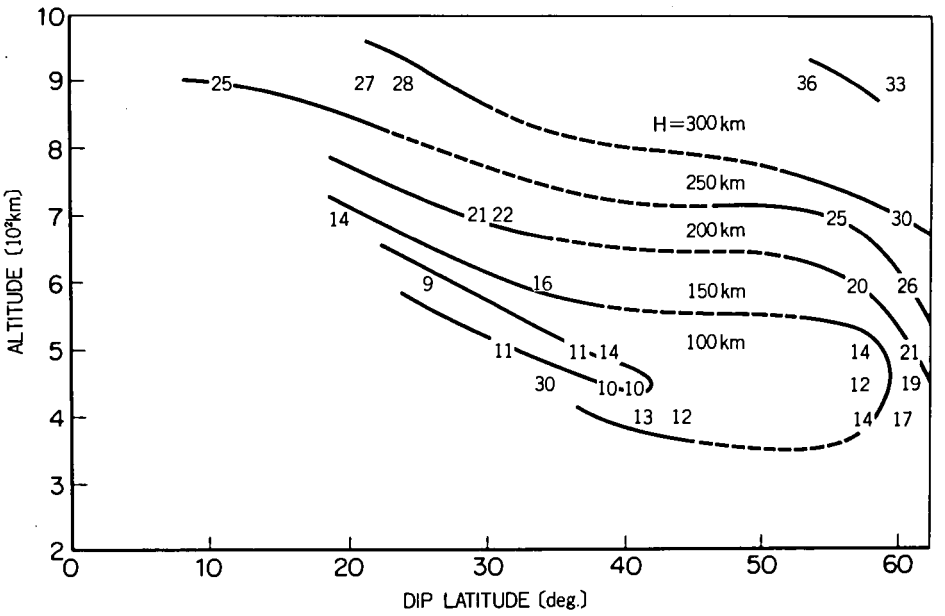

Fig. 6-23 Contour map of field aligned scale height.

chapter I. In the high latitude, the electron density in the F2 region decreases; the high density region exists in the mid-latitude around the magnetic dipole latitude of 20° to 30° (see Fig. 6-22).

Assuming diffusive equilibrium along field lines, that altitudinal and latitudinal gradients of ion temperature T_i and electron temperature T_e are negligible, and that the geomagnetic field can be represented by a dipole field, the scale height along the field lines H_s may be written (S. Chandra and R. A. Goldberg[312]) as

$$\frac{1}{H_s} = -\frac{1}{N}\frac{\partial N}{\partial r} + \frac{\cot \lambda}{2Nr}\frac{\partial N}{\partial \lambda} \qquad (6.2)$$

where r is a geocentric distance, λ a geomagnetic dip latitude. Using above equation, the scale height H_s can be deduced from the measured global electron density distribution. Figure 6-23 shows the

contour map of the field aligned scale height H_S in the altitude-dip latitude domain. This figure is corresponding to the results of the Alouette observation as shown in Fig. 1-7 (p. 19). The effective ion mass can be obtained from the scale height H_S if the ion and electron temperatures may be deduced from the measured admittance values or the sheath resonance frequency.

Although the data were available in only northern hemisphere, it can be concluded that the electron distribution is clearly controlled by the geomagnetic field.

CONCLUDING REMARKS

In this thesis, the r.f. plasma probes, viz., gyro-plasma probe, mutual impedance probe, and high frequency capacitance probe have been studied and applied to the measurements of electron densities in laboratory plasma and space plasma using rocket and satellite.

The historical survey of ionospheric measurements by plasma probes onboard the sounding rockets is made in Chapter I. The existing knowledges of the ionospheric structure are reviewed. An outline of antenna impedance theory is also given as the basis of r.f. plasma probe techniques.

In Chapter II, various r.f. plasma probe systems to measure the probe impedance in cold and warm magnetoplasmas are described. The gyro-plasma probe is designed to measure the antenna impedance versus frequency characteristics, which include various kinds of plasma resonance phenomena, such as higher harmonic gyro-resonances as well as the upper hybrid and sheath resonances. The effects due to electron-neutral collision and density gradient on the antenna impedance measurement are also examined. The mutual impedance probe consists of a transmitter-receiver antenna system, measuring the transmitted signal intensity as a function of frequency. The high frequency capacitance probe is to measure the frequency change of an oscillator due to the ambient electron density variation. The detailed circuit designs of these probes, relevant to the rocket experiment, are given. It is shown that the ion sheath surrounding a body in a plasma is modulated by the potential change due to applied high tension r.f. fields. The analytical expression of floating potential and sheath capacitance of a body affected by such r.f. potential are obtained.

In Chapter III, experimental studies of r.f. plasma probe in laboratory plasma are described. Using an apparatus of the vacuum chamber with back diffusion type plasma sources, the performance of plasma probes has been tested under various conditions. From these experiments, a number of problems have been clarified; the effect of higher harmonics of the gyro-resonance on the antenna impedance, the

excitation of electrostatic wave from an antenna and its propagation characteristics. The Bernstein mode waves are also identified from the observed dispersion characteristics of the wave. The comparison of electron density measurement by r.f. and d.c. plasma probes showed a good agreement of measured electron densities in the range from about 10^4 cm^{-3} to 10^6 cm^{-3}. The model experiment has been performed in a laboratory plasma to simulate the wake produced behind the spacecraft.

In Chapter IV, the results of rocket experiments by r.f. plasma probes are given. The electron density profiles in the ionosphere in the altitude range from about 70 km to 2000 km were obtained using sounding rockets S 210-6 and 8, Kappa 8-15, 9M-35, 38 and 41, and Lambda 3H-2, 5 and 6, launched from the Kagoshima Space Center, in 1969 to 1973. Various plasma resonance effects including the modified plasma resonance have been discovered in these experiments. It has been found that both amplitude and phase of the antenna admittance change its values appreciably near the harmonics of electron gyro-frequency. The comparisons of electron density measurements with gyro-plasma probe, VLF doppler method, two-wire probe, and Langmuir probe have been made using Kappa 9M-35 and 38 sounding rockets. The high frequency capacitance probe, the Langmuir probe, and the gyro-plasma probe have been, also, compared with each other using S 210-6 and 8 sounding rockets. The comparisons of various plasma probes revealed sources of error and gave an increased confidence in their measurements.

The gyro-plasma probe onboard the Radio Exploration Satellite REXS was launched on August, 19, 1972, by the Mu 4S-4 rocket. In Chapter V, the instrumentation of the gyro-plasma probe is described. Since the time-sharing PCM telemetry system was used, onboard data processing circuits including the automatic resonance detection system were required. To detect plasma resonance frequencies unambiguously, an inhibit circuit to eliminate pseudo-resonance signals was installed. Results of the pre-flight operational test and of the thermal vacuum environment test were satisfactory. The laboratory experiment of the instrument in a plasma was also carried out, using the space plasma simulation chamber, to check overall operation of the system in a

plasma. The data processing and analysis systems aided by the digital computer have been developed to get instantaneous spacecraft positions, the geomagnetic reference field, the calibration of the raw data by using thermal data, and the conversion of transmitted PCM data to the physical quantities corresponding to observational items.

In Chapter VI, experimental results are summarized, including the performance of the spacecraft. The gyro-plasma probe operated successfully and very good in-flight data were obtained. The global electron density profiles revealed by this experiment provide an important information to the study of the local time variation and the geomagnetic latitude dependence of the ionosphere. It has been found that, in a tenuous plasma, the admittance of an antenna changes its value in accordance with the potential change due to the photoemission from the metalic antenna surface. From the lower hybrid resonance data, an effective ion mass of about 2 in the altitude of 1000 ~ 4000 km and of about 1 in the altitude of 3000 ~ 6400 km were obtained. The electron density distribution above 2000 km is expressed very well by the power law model, though the field aligned scale height shows a systematic change with geomagnetic latitude.

APPENDICES

A. General Expression of Sheath Capacitance

A body surrounded by an ion sheath is characterized by a dynamic capacitance when the equilibrium potential is allowed to have small variation at a given frequency. The current flowing through this capacitance is the derivative of the charge Q with respect to time,

$$i = \frac{\partial Q_0}{\partial t} = \frac{\partial Q_0}{\partial V_0} \frac{\partial V_0}{\partial t} , \qquad (A.1)$$

where V_0 is the potential of the body. Since $i = C \cdot \partial V_0/\partial t$, the capacitance is,

$$C = \frac{\partial Q_0}{\partial V_0} \qquad (A.2)$$

A common expression of the capacitance is given for a plane surface in rectangular coordinates, a cylinder of revolution in cylindrical coordinates, and a sphere in spherical coordinates. It is assumed respectively planar, cylindrical or spherical symmetry for the electric quantities on the surface of the body and within the sheath, neglecting the edge effect on the borders of the plane surface and at the tips of the cylinder.

From Gauss' theorem the charge borne by each body is,

$$Q_0 = S\varepsilon_0 E_0 \qquad (A.3)$$

where E_0 is the electric field at the surface and S the area.

By definition the electric field in the medium surrounding each body is $E = - \partial V/\partial r$; because of the symmetry in each case, $\Delta V = \partial V/\partial r$, where r is a distance from the body's surface. Consequently, $E_0 = - (\partial V/\partial r)_0$ where $(\partial V/\partial r)_0$ is the value of $\partial V/\partial r$ on the surface. Then, the expression of the capacitance, $C = \partial Q_0/\partial V_0$ becomes

$$C = - S \varepsilon_0 \frac{\partial}{\partial V} \left(\frac{\partial V}{\partial r}\right)\Big|_0 \qquad (A.4)$$

which is also reduced to

$$C = - S \cdot \frac{\varepsilon_0}{\lambda_D} \frac{\partial}{\partial y} \left(\frac{\partial y}{\partial_x}\right)\Big|_0 \qquad (A.5)$$

where $y = \frac{qV}{\kappa T_e}$, $x = \frac{r}{\lambda_D}$, and λ_D is the Debye length.

Using a following dimensionless quantity

$$\Lambda = \frac{C}{S} \frac{\lambda_D}{\varepsilon_0}, \qquad (A.6)$$

the capacitance can be expressed by

$$\Lambda = - \frac{\partial}{\partial y} \left(\frac{\partial y}{x}\right)\Big|_0 . \qquad (A.7)$$

The potential y is found by the Poisson's equation for the symmetrical probe configurations, assuming that the pre-sheath region and the ion sheath are formed around the probe ($y < - \frac{1}{2}$).

$$\frac{1}{x^n} \frac{d}{dx}\left(x^n \frac{dy}{dx}\right) = \exp y - \frac{1}{\sqrt{-2ey}} \left(\frac{x_s}{x}\right)^n \qquad (A.8)$$

where $e = \exp(1) = 2.71828.....$(Napier's number), x_s is the sheath distance or sheath radius normalized by the Debye length, and $n = 0$, 1, and 2 corresponding to a plane, a cylindrical and a sphere probes, respectively (see eq. (2.33)).

B. Vehicle's Horizontal Distance from KSC

The rocket trajectory is, sometimes, described in the altitude versus horizontal distance domain, based on the earth's surface. If the earth is assumed to be a sphere, the horizontal distance is easily calculated as a length of arc of a circle. But, it is more appropriate to assume that the earth can be represented to be an oblate spheroid, i.e., the earth's surface is given by the equation,

$$F(x, y, z) = \frac{x^2}{a_E^2} + \frac{y^2}{a_E^2} + \frac{z^2}{b_E^2} - 1 = 0 \qquad (B.1)$$

where a_E and b_E are the earth's radii at equator and at pole; $a_E = 6378.16$ km, $b_E = 6356.78$ km, and the eccentricity $e_E = 0.081810$. The positions of KSC and the rocket are $A(\lambda_0, \psi_0)$ and $B(\lambda_b, \psi_b)$ where λ is the east longitude and ψ the colatitude. The plane including A, B and the center of the earth 0 is the orbital plane.

Any oblate spheroid and plane may be put into the following general forms, respectively,

$$F(x, y, z) \equiv X_1 \tilde{F}_1 X_1^t = 0 \qquad (B.2)$$

$$f(x, y, z) \equiv X \tilde{f} = 0 \qquad (B.3)$$

where $X = (x, y, z)$ and $X_1 = (x, y, z, 1)$, and t denotes the transposed matrix. $\tilde{F}_1$ and $\tilde{f}$ are the 4×4 matrix and 1×3 matrix. Introducing the transformation matrix T between X and X', $X = X'T$ where $X' = (x', y', z')$. Equations (B.2) and (B.3) are rewritten in the X' coordinates as

$$F'(x', y', z') \equiv X_1' \tilde{F}_1' X_1'^t = 0, \qquad \tilde{F}_1' = T_1 \tilde{F}_1 T_1^t \qquad (B.4)$$

$$f'(x', y', z') \equiv X' \tilde{f}' = 0, \qquad \tilde{f}' = T \tilde{f} \qquad (B.5)$$

where $X_1' = (x', y', z', 1)$ and $T_1 = \begin{pmatrix} T & 0 \\ 0 & 1 \end{pmatrix}$.

If the matrix T is determined so as to $\tilde{f}'^{t} = (0, 0, c)$, eq. (B.5) is equivalent to $z' = 0$. Namely, the plane $z' = 0$ becomes the orbital plane. Therefore, the intersecting line is obtained by the equation

$$F'_{z'=0} \equiv F'(x', y', 0) = 0 \tag{B.6}$$

Let $\vec{OA}$ be x'-axis, and the plane OAB be in x'y' plane. The matrix T is calculated to be

$$T = \begin{bmatrix} \cos\lambda_0\cos\psi_0 & , & \sin\lambda_0\cos\psi_0 & , & \sin\psi_0 \\ -\cos\lambda_0\sin\psi_0\sin\phi_0-\sin\lambda_0\cos\phi_0 & , & -\sin\lambda_0\sin\psi_0\sin\phi_0+\cos\lambda_0\cos\phi_0 & , & \cos\psi_0\sin\phi_0 \\ -\cos\lambda_0\sin\psi_0\cos\phi_0+\sin\lambda_0\sin\phi_0 & , & -\sin\lambda_0\sin\psi_0\cos\phi_0-\cos\lambda_0\sin\phi_0 & , & \cos\psi_0\cos\phi_0 \end{bmatrix} \tag{B.7}$$

where $$\phi_0 = \tan^{-1}\left\{\frac{(\sin\lambda_0\cdot\sin\lambda_b+\cos\lambda_0\cdot\cos\lambda_b)\sin\psi_0\cdot\cos\psi_b-\cos\psi_0\cdot\sin\psi_b}{(\sin\lambda_0\cdot\cos\lambda_b-\cos\lambda_0\cdot\sin\lambda_b)\cos\psi_b}\right\} \tag{B.8}$$

from eqs. (B.1), (B.2), (B.6) and (B.7), the coefficient matrices $\tilde{F}_1$ and $\tilde{F}'_1$ are reduced to be

$$\tilde{F}_1 = \begin{bmatrix} a_E^{-2} & & 0 \\ & a_E^{-2} & b \\ & & b_E^{-2} \\ 0 & & & 1 \end{bmatrix} \qquad \tilde{F}'_1 = \begin{bmatrix} a' & h' & h' & 0 \\ h' & b' & f' & 0 \\ h' & f' & c' & 0 \\ 0 & 0 & 0 & -1 \end{bmatrix}$$

where $a' = a_E^{-2} - (a_E^{-2} - b_E^{-2})\sin^2\psi_0$,

$b' = a_E^{-2} - (a_E^{-2} - b_E^{-2})\cos^2\psi_0\cdot\sin^2\phi_0$,

$c' = a_E^{-2} - (a_E^{-2} - b_E^{-2})\cos^2\psi_0\cdot\cos^2\phi_0$,

$h' = -(a_E^{-2} - b_E^{-2})\cos\psi_0\cdot\sin\psi_0\cdot\sin\phi_0$,

$f' = -(a_E^{-2} - b_E^{-2})\cos^2\psi_0\cdot\sin\phi_0\cdot\cos\phi_0$.

Consequently, eq. (B.6) is obtained as

$$F'_{z'=0} \equiv X'_1 \tilde{F}'_1 X'^{t}_1 \big|_{z'=0} = x'_1 \tilde{A}'_1 x'^{t}_1 = 0 \qquad (B.10)$$

where $x'_1 = (x', y', 1)$, $\tilde{A}' = \begin{pmatrix} A' & 0 \\ 0 & -1 \end{pmatrix}$, and $A' = \begin{pmatrix} a' & h' \\ h' & b' \end{pmatrix}$. The curve of second order given in eq. (B.10) is the elliptic curve because its signature $\sigma = a' + b' > 0$, and the second discriminant $\Delta \equiv \det A' > 0$. Hence, the normal form of this curve is easily found by transformation of coordinates, and the length $\widehat{AB}$ along this arc is also obtained by the curvilinear integral.

C. Standard Pre-flight Test Condition

C.1 The standard test conditions of the each instrument

(1) Thermal Test:

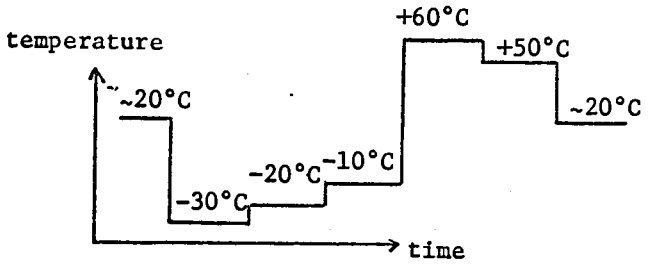

Note; Time interval of 6 hours at each stage of temperature.

(2) Vibration Test:

Frequency	Axial	Lateral	Time
5~35 Hz	± 15 mmp	± 0.5 mmp	3 min
35~200 Hz	7.5 mmp	2.5 Gp	"
200~2000 Hz	15.0 Gp	5.0 Gp	"

(3) Acceleration Test:

Axial	+	30 G	3min
	-	2 G	"
Lateral	±	5 G	"

(4) Shock Test:

Axial	+	25 G , 10 msec	half-wave sinusoidal, twice
Lateral	±	5 G , 10 msec	Sinusoidal, Twice

(5) Vacuum Test:

The pressure is below 10^{-3}mmHg for 6 hours at room temperature.

C.2 The Standard test condition of the spacecraft

(1) Thermal Test:

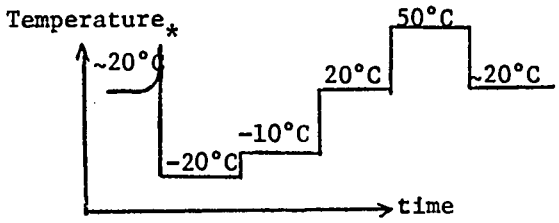

Note; time interval of 6 hours at each stage of temperature. *about 40°C for exclusion of humidity.

(2) Vibration Test:

Frequency	Axial	Lateral	Time
5~35 Hz	0.4 mmp	0.13 mmp	3 min
35~100 Hz	2.0 Gp	0.67 Gp	"
100~400 Hz	2.5 Gp	0.83 Gp	"
200~2000 Hz	5.0 Gp	1.7 Gp	"

(3) Shock Test:

Axial +	25 G , 8 msec	half-wave sinusoidal, Twice

(4) Mechanical Construction (interface) of each part,

(5) Electrical Interference Test,

(6) Dynamical Balance Test,

(7) Moment of Inertia Test,

(8) Thermal Vacuum Test,

(9) Magnetic-moment Test,

(10) Adjustment between spacecraft and launching vehicle.

D. Computation of Reliability of IPS

PARTS		λ_i	n_i	$n_i\lambda_i$
Transistor	(low power)	20	145	2900
"	(")	100	4	400
"	(high power)	45	1	45
FET		100	14	1400
IC	(analog)	50	17	850
"	(")	250	2	500
"	(logarithmic)	250	2	500
"	(digital)	25	31	775
"	(")	150	6	900
Diode	(low power)	3	76	228
"	(zener)	10	11	110
Resistor	(constant)	2	594	1188
"	(variable)	200	46	9200
Condensor	(tantalum)	10	72	720
"	(ceramic)	10	213	2130
"	(mica)	10	109	1090
"	(variable)	150	4	600
Coil		10	24	240
transformer	(signal)	10	51	510
Relay	(latching)	70	2	140
Crystal		150	3	450
DEM connector	(pin)	1	127	127
SMB connector		2	10	20
Soldering point		0.5	3969	1984.5
TOTAL		-----	5407	27007.5

(1) λ(failure rate) of each element is estimated under the condition that the derating ratio is 0.25 at 30°C and the confidence level is 60%.
(2) In the case of the spacecraft REXS, each observational instrument should be designed to have its reliability more than 0.948, in order to keep the reliability of the whole spacecraft system more than 0.9.

E. Calibration Coefficients for IPS

All the values used here are expressed by the floating points data of FORTRAN IV language; E indicates the single precision exponential.

(1) The temperature of pre-amplifier is measured with the house keeping instrument (HK), and the temperature (T°C) versus the output decimal value (N_0) is given in Fig. E-1. This calibration characteristics can be approximated by a following polynomial function selecting C_n values to make the best fit to the measured function as

$$T = \sum_{n=1}^{6} C_n \cdot N^{n-1}$$

where

C_1 = -0.3907810 E + 02,
C_2 = +0.4135541 E + 00,
C_3 = +0.7335699 E - 03,
C_4 = +0.7939580 E - 05,
C_5 = +0.3150700 E - 07,
and C_6 = +0.3742000 E - 10.

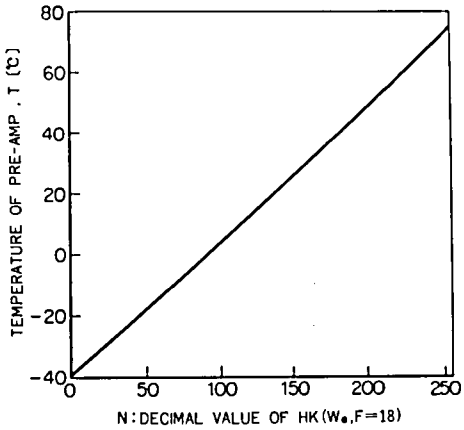

Fig. E-1 Output decimal values vs. temperture in pre-amplifier of IPS.

(2) The coefficients C_n for the temperature correction of Fh_1, Lh_1, and Lh_3 that are given in eq. (5.30), are:

	Fh_1	Lh_1	Lh_3
C_1	+0.5611062E+00	-0.8008370E+00	+0.1700000E-02
C_2	-0.5955836E+00	-0.4531361E+00	-0.1022510E+01
C_3	-0.2533402E-03	-0.3754487E-01	-0.4787000E-01
C_4	+0.6972036E-03	+0.3764375E-04	-0.2730000E-03
C_5			+0.7875000E-04

As for the temperature correction of Fh_2, the following step function is used.

$$N_T = \begin{cases} N_0 & \text{for } T < 21°C, \\ N_0 + 6.0 & \text{for } T \geq 21°C. \end{cases}$$

(3) The coefficients C_n for the calibration of Lh_1 and Lh_3 in eq. (5.32), are:

	Lh_1	Lh_3
C_1	+0.48436849E+00	-0.13788950E+01
C_2	+0.31760218E-02	+0.53816587E-01
C_3	+0.66991901E-04	-0.39311962E-03
C_4	-0.31419130E-06	+0.14225626E-05
C_5	+0.71353541E-09	-0.17612791E-08

(4) The coefficients C_n for the calibration of $L\ell_{1\sim3}$ in eq. (5.36), are:

	$L\ell_1$	$L\ell_2$	$L\ell_3$
C_1	+0.79018545E+00	+0.11921958E+01	+0.11488734E+01
C_2	+0.27178132E+01	+0.87813898E+00	+0.10426516E+01
C_3	-0.21166261E+01	-0.21107455E+00	-0.43391613E+00
C_4	+0.90672745E+00	+0.84797601E-01	+0.18222577E+00
C_5	-0.12740256E+00	-0.37502374E-02	-0.16249358E-01

(5) The coefficients C_n for the V_0 and V_1 in eq. (5.35), and V_1 and N_0 in eq. (5.34), are:

	V_0 and V_1	V_1 and N_0
C_1	-0.13509059E-01	-0.6711605E-01
C_2	+0.10659802E+01	+0.1201142E-01
C_3	+0.47236235E-02	+0.3793714E-06

SYMBOLS AND CONSTANTS

$a_E = 6378.160$ [km]	: Equatorial radius of the earth
α_{eff}	: Effective recombination coefficient
β	: Attachment coefficient
$e = 2.71828.....$	: Napier's number
$\varepsilon_0 = 8.854 \times 10^{-12}$ [F/m]	: Permittivity of free space
$e_E = 0.08182$	: Eccentricity of the earth
$f_P = \Pi_e/2\pi$	: Electron plasma frequency
$f_H = \Omega_e/2\pi$	: Electron gyro-frequency
$f_\nu = \nu/2\pi$	: Collision frequency
f_{UHR}	: Upper hybrid resonance frequency
f_{SHR}	: Sheath resonance frequency
$\kappa = 1.381 \times 10^{-23}$ [Joule/°K]	: Boltzmann constant
$\lambda_D = 6.91 \times \sqrt{T(°K)/N_e(cm^{-3})}$ [cm]	: Debye shielding length
λ_E	: East longitude
$m = 9.107 \times 10^{-31}$ [Kg]	: Electron mass
$M = M_{eff} \times 1.673 \times 10^{-27}$ [Kg]	: Ion mass
$\mu_0 = 1.257 \times 10^{-6}$ [H/m]	: Permeability of free space
$\mu_E = 398{,}603 \times 10^9$ [m^3/sec^2]	: Gravitational constant of the earth
$N_e = 1.24 \times 10^4 f_P^2$ [cm^{-3}]	: Electron density; f_p in MHz
N_i	: Ion density
Q	: Electron production rate
$-q = -1.602 \times 10^{-19}$ [Coulomb]	: Electron charge
R_z	: Relative sun spot number
r_L	: Larmor radius of electron
T_e	: Electron temperature
χ	: Zenith angle
Y	: Admittance
Z	: Impedance

REFERENCES

1. Seddon, J. C., Propagation Measurements in the Ionosphere with the Aid of Rockets, J. Geophys. Res., 58, 323-335 (1953).
2. Jackson, J. E. and J. A. Kane, Measurement of Ionospheric Electron Densities Using an RF Probe Technique, J. Geophys. Res., 64, 1074-1975 (1959).
3. Miyazaki, S., K. Hirao, Y. Aono, T. Takayama, H. Ikegami, and T. Ichimiya, Resonance Probe — A New Probe Method for Electron Density and Electron Temperature in the Ionosphere, Rept. Ionos. Space Res. Japan, 14, No. 2, 148-159 (1960).
4. Haycock, O. C. and K. D. Baker, Measuring Antenna Impedance in the Ionosphere, Electronics, 34, 88-92 (1961).
5. Pfister, W., J. C. Ulwick, and R. P. Vancour, Some Results of Direct Probing in the Ionosphere, J. Geophys. Res., 66, No. 4, 1293-1297 (1961).
6. Haycock, O. C. and K. D. Baker, New Ionosphere Measurement Technique: Plasma Frequency Probe, Electronics, 35, No. 48, 81-83 (1962).
7. Kane, J. A., J. E. Jackson, and H. A. Whale, RF Impedance Probe Measurements of Ionospheric Electron Densities, J. Res. National Bureau of Standards, 66D, No. 6, 641-648 (1962).
8. Ulwick, J. C., W. Pfister, R. P. Vancour, O. C. Haycock, and K. D. Baker, Firing of an Astrobee 200 Rocket with a Multiple Ionospheric Experiment, Proc. IRE, 50, No. 11, 2272-2285 (1962).
9. Herman, J. R., A Method for Determining D-Region Electron Density Profiles Utilizing a Capacitive Impedance Rocket Probe, J. Geophys. Res., 69, No. 11, 2329-2336 (1964).
10. Ulwick, J. C., W. Pfister, O. C. Haycock, and K. D. Baker, Rocket Measurements with Electron and Ion Probes in an Aurora, Air Force Cambridge Res. Lab., AFCRL-64-791 (1964).
11. Haycock, O. C., K. D. Baker, and J. C. Ulwick, Experiences with the Impedance Probe on Satellites, Air Force Cambridge Res. Lab., AFCRL-65-47, 1029-1033 (1965).

12. Oya, H., Effect of Resonances on the Admittance of an RF Plasma Probe Surrounded by an Ion Sheath, Rep. Ionos. Space Res. Japan, 19, No. 3, 243-271 (1965).

13. Ulwick, J. C., W. Pfister, and R. E. McInerney, Direct Satellite Probe Measurements of Ionospheric Irregularities, Space Research, V, North-Holland Pub. Co., Amsterdam, 171-178 (1965).

14. Jacobs, K. G. and K. Rawer, Raketenmessungen mit einer Hochfrequenz-Impedanzsonde, Jb. Wiss. Ges. Luft Raumf., 378-384 (1966).

15. McKenzie, J. F. and J. Sayers, A Radio Frequency Electron Density Probe for Rocket Investigation of the Ionosphere, Planet. Space Sci., 14, No. 8, 731-740 (1966).

16. Oya, H. and T. Obayashi, Measurement of Ionospheric Electron Density by a Gyro-plasma Probe: A Rocket Experiment by a New Impedance Probe, Rept. Ionos. Space Res. Japan, 20, No. 2, 199-213 (1966).

17. Bross, P., K. G. Jacobs, and K. Pawer, Direct Electron Density Measurements in the Ionosphere Below 200 km, Space Research, VII, North-Holland Pub. Co., Amsterdam, 467-476 (1967).

18. Heikkila, W. J., J. A. Fejer, J. Hugill, and W. Calvert, Comparison of Ionospheric Probe Techniques, Space Research, VII, North-Holland Pub. Co., Amsterdam, 397-406 (1967).

19. Holt, O. and G. M. Lerfald, Results From an RF Capacity Probe Experiment in the Auroral Ionosphere, Radio Sci., 2, No. 11, 1283-1294 (1967).

20. Oya, H. and T. Obayashi, Rocket Measurement of the Ionospheric Plasma by Gyro-Plasma Probe, Res. Ionos. Space Res. Japan, 21, No. 1/2, 1-8 (1967).

21. Pfister, W., Auroral Investigation by Means of Rockets, Space Sci. Rev., 7, 642-688 (1967).

22. Storey, O., P. Meyer, and M. Aubry, Ionosphere Sonde de Plasma a Impedance Mutuelle, C. R. Acad. Sci. Paris, 264, 99-101 (1967).

23. Storey, O., P. Meyer, and M. Aubry, Possibilities pour L'etude des Resonances du Plasma Ionospherique a L'aide d'une Sonde a Impedance Mutuelle, C. R. Acad. Sci. Paris, 264, 904-907 (1967).

24. Baguette, J. M. Mesures de Densite Electronique a Bord du Satellite FR-1, GRI/NT/76, (C.N.E.T., C.N.R.S., I.P.G.) Sept. (1968).

25. Kaiser, T. R. and J. K. E. Tunaley, Radio-Frequency Impedance Probes, Space Sci. Rev., 8, 32-73, (1968).

26. Jacobs, K. G., R. Kist, and K. Rawer, The Electron Density Profile of Auroral Layers as Observed with ESRO Rockets at Kiruna, Space Research IX, (North-Holland, Pub. Co., Amsterdam, 246-255 (1969).

27. Ejiri M. and T. Obayashi, Measurement of Ionosphere by the Gyro-plasma Probe, Rept. Ionos, Space Res. Japan, 24, No. 1, 1-12 (1970).

28. Melzner, F. and H. H. Rabben, Electron Density Measurements in the Ionosphere with High Altitude Rockets, Plasma Waves in Space and Laboratory, 2, Edinburgh Univ. Press 77-87 (1970).

29. Melzner, Von F. and H. H. Rabben, Electronendichte-Messungen in der Ionosphare mit einer neuartigen Hochfrequenz-Impedanz-sonde, Zeit. Geophysik, 36, 135-150 (1970).

30. Rao, U. R., S. S. Degaonkar, M. A. ABdu, S. Bansidar, and R. M. Patel, Rocket Based Ionospheric Measurements at Thumba with High-frequency Capacitance Probe, Space Research X, North-Holland, Pub. Co., Amsterdam, 703-706 (1970).

31. Obayashi, T. and M. Ejiri, Ionospheric Plasma Measurements by Gyro-Plasma Probe, Space Research, XI, Akademic Verlag, Berlin, 1067-1070 (1971).

32. Boggess, R. L., L. H. Brace, and N. W. Spencer, Langmuir Probe Measurement in the Ionosphere, J. Geophys. Res., 64, 1627-1630 (1959).

33. Boyd, R. L. F., The Use of Probing Electrodes in the Study of the Ionosphere, J. Brit. I. R. E., 22, No. 5, 405-408 (1961).

34. Boyd, R. L. F., Plasma Probes on Space Vehicles, Proc, 5th Int. Conf. on Ionization Phenomena in Gases, North-Holland Pub. Co., Amsterdam 1388-1396 (1961).

35. Sagalyn, R. C., M. Smiddy, and J. Wisnia, Measurement and Interrelation of Ion Density Distributions in the Daytime F Region, J. Geophys. Res., 68, No. 1, 199-211 (1963).

36. Sagalyn, R. C. and M. Smiddy, Rocket Investigation of the Electrical Structure of the Lower Ionosphere, Proc, 4th Int. Space Sci. Symp. Warsaw 1963, 371-387 (1964).

37. Spencer, N. W. L. H. Brace, G. R. Carignan, D. R. Taeusch, and H. Nieman, Electron and Molecular Nitrogen Temperature and Density in the Thermosphere, J. Geophys. Res., 70 2665-2698 (1965).

38. Aubry, M., M. Blance, R. Clauved, C. Taieb, P. J. Bowen, Some Rocket Results on Sporadic E,Radio Sci., 1, No. 2, 170-177 (1966).

39. Bowhill, S. A., A Rocket Experiment on the Structure of Sporadic E, Radio Sci., 1, No. 2, 187-190 (1966).

40. Bowhill, S. A. and L. G. Smith, Rocket Observations of the Lowest Ionosphere at Sunrise and Sunset, Space Research, VI, Spartan Books, Washington, 511-521 (1966).

41. Smith, L. G., Rocket Observations of Sporadic E and Related Features of the E Region, Radio Sci., 1, No. 2,178-186 (1966).

42. Bragin, I. A., Direct Measurements of Ion and Electron Concentration in the Stratosphere and the Mesosphere, Space Research VII, North-Holland Pub. Co., Amsterdam, 391-394, (1967).

43. Reddy, B. M., L. H. Brace and J. A. Findlay, The Ionosphere at 640 kilometers on Quiet and Disturbed Days, J. Geophys. Res., 72, No. 11, 2709-2726 (1967).

44. Boyd, R. L. F., Langmuir Probes on Spacecraft, Plasma Diagnostics, North-Holland Pub. Co., Amsterdam, 732-776, (1968).

45. Miyazaki, S. and H. Mori, Ionospheric Measuring Probe, Bulletin Space Aeron. Sci. Univ. Tokyo, 4, No. 2(in Japanese),226-236 (1968).

46. Schott, L., Electrical Probes, Plasma Diagnostics, North-Holland Pub. Co., Amsterdam, 668-731 (1968).

47. Smith, L. G. and E. A. Mechtly, Seasonal Variation of the Lower Ionosphere at Wallops Island during the IQSY, J. Atmos. Terr. Phys., 30, 1555-1561 (1968).

48. Donley, J. L., L. H. Brace, J. A. Findlay, J. H. Hoffman, and G. L. Wrenn, Comparison of Results of Explorer XXXI Direct Measurement Probes, Proc. IEEE, 57, No. 6, 1078-1084 (1969).

49. Reddy, C. A. M. M. Rao, S. Matsushita, and L. G. Smith, Rocket Observations of Electron Densities in the Night-time Auroral E-region at Fort Churchill, Canada, Planet. Space Sci., 17, 617-628 (1969).

50. Wrenn, G. L., The Langmuir Plate and Spherical Ion Probe Experiments aboard Explorer XXXI, Proc. IEEE, 57, No. 6, 1072-1077 (1969).

51. Wrenn, G. L. and P. A. Smith, Results Derived from Simultaneous Measurements Using the Langmuir Plate and Spherical Ion Probe on Explorer XXXI and the Ionosonde on Alouette II, Proc. IEEE 57, No. 6 1085-1089 (1969).

52. Smith, L. G. and E. A. Mechtly, Rocket Observations of Sporadic-E Layers, Radio Sci., 7, No. 3, 367-376 (1972).

53. Sayers, J., In-situ Probes for Ionospheric Investigations, J. Atmos. Terr. Phys., 32, 663-691 (1970).

54. Smith, E. K., Electromagnetic Probing of the Upper Atmosphere, URSI, Pergamon Press, Oxford (1970).

55. Lockwood, G. E. K., Plasma and Cyclotron Spike Phenomena Observed in Top-side Ionograms, Can. J. Phys., 41, 190-194 (1963).

56. Thomas, J. O. and D. Westover, The Calculation of Electron Density Profiles from Topside Ionograms Using a Digital Computer, Tech. Ret. No. 5, SEL-63-130, Radiosci. Lab., Stanford Univ. (1963).

57. Bauer, S. J. and L. J. Blumle, Mean Diurnal Variation of the Topside Ionosphere at Mid-Latitude, J. Geophys. Res., 69, No. 17 3613-3618 (1964).

58. Bauer, S. J., L. J. Blumle, J. L. Donley, R. J. Fitzenreiter, and J. E. Jackson, Simultaneous Rocket and Satellite Measurements of the Topside Ionosphere, J. Geophys. Res., 69, No. 1, 186-189 (1964).

59. Fejer, J. A. and W. Calvert, Reasonance Effects of Electrostatic Oscillations in the Ionosphere, J. Geophys. Res., 69, No. 23, 5049-5052 (1964).

60. King, J. W., P. A. Smith, D. Eccles, G. F. Fooks, and H. Helm, Preliminary Investigation of the Structure of the Upper Ionosphere as Observed by the Topside Sounder Satellite, Alouette, Proc. Roy. Soc. London, Ser. A281, No. 1381, 464-487 (1964).

61. Thomas, J. O. and A. Y. Sader, Electron Density at the Alouette Orbit, J. Geophys. Res. 69, No. 21, 4561-4581 (1964).

62. Dayharsh, T. I. and W. W. Farley IV, Electron-Density Variations at 1000 km, J. Geophys. Res., 70, No. 21, 5361-5368 (1965).

63. Chan, K. L., On the Topside Ionosphere over the American Continents, Radio Sci., 1, No. 10, 1158-1162 (1966).

64. Nelms, G. L., R. E. Barrington, J. S. Belrose, T. R. Hartz, I. B. McDiarmid and L. H. Brace, The Alouette II Satellite, Can. J. Phys., 4, 1419-1430 (1966).

65. Benson, R. F., An Analysis of Alouette I Plasma Resonance Observations, NASA Report, X-612-67-287, June (1967).

66. Brace, L. H., B. M. Reddy, and H. G. Mayr, Global Behavior of the Ionosphere at 1000-kilometers Altitude, J. Geophys. Res., 72, No. 1 265-283 (1967).

67. Crawford, F. W., R. S. Harp, and T. D. Mantei, On the Interpretation of Ionospheric Resonances Stimulated by Alouette I, 57-68 (1967).

68. Mayr, H. G., L. H. Brace and G. S. Dunham, Ion Composition and Temperature in the Topside Ionosphere, J. Geophys. Res., 72, No. 17, 4391-4404 (1967).

69. King, J. W., H. G. Rix, and C. Seabrook, The Behaviour of the Topside Ionosphere at Middle Latitudes at Night, J. Atomos. Terr. Phys., 30, 1605-1613 (1968).

70. King, J. W. G. L. Hawkins, and C. Seabrook, The Seasonal Behaviour of the Topside Ionosphere, J. Atmos. Terr. Phys., 30, 1701-1706 (1968).

71. Chapman, J. H. and E. S. Warren, Topside Sounding of the Earth's Ionosphere, Space Sci. Rev., 8, 846-865 (1968).

72. Ondoh, T., NO. Matuura, T. Koseki, R. Nishizaki, and M. Kajiwara, Analysis of the Topside Ionospheric Data from Alouette II over Japan, Part I: Electron Density Distribution in the Topside Ionosphere over Japan, J. Radio Res. Lab., Japan 15, No. 78, 59-68 (1968).

73. Franklin, C. A. and M. A. Maclean, The Design of Swept-Frequency Topside Sounders, Proc. IEEE, 57, No. 6, 897-929 (1969).

74. King, J. W., IQSY Data Review: Ionosphere: 4. The Topside Sounder Satellite Data, Ann. IQSY, MIT. Press, Cambridge, Mass., USA, 6, 167-185 (1969).

75. Hagg, E. L., E. J. Hewens, and G. L. Nelms, The Interpretation of Topside Sounder Ionograms, Rroc. IEEE, 57, No. 6, 949-960 (1969).

76. Hakura, Y., R. Nishizaki, and K. Tao, Analysis of Observation Data Obtained by Alouette II, J. Radio Res. Lab., 16, Nos. 87/88, 215-226 (1969).

77. Jackson, J. E., The Reduction of Topside Ionograms to Electron-Density Profiles, Proc. IEEE, 57, No. 6, 960-976 (1969).

78. Jackson, J. E., Comparisons between Topside and Ground-Based Soundings, Proc. IEEE, 57, No. 6, 976-985 (1969).

79. King, J. W., A Review of the Large-scale Stracture of the Ionospheric F - Layer, Ann. IQSY, M.I.T. Press, Cambridge, Mass., USA, 5, 131-165 (1969).

80. Oya, H., Sequence of Diffuse Plasma Resonances Observed on Alouette II Ionograms, Preprint, X-615-69-542, GSFC, Greenbelt, Mayland, USA (1969).

81. Oya, H., Sequence of Diffuse Plasma Resonances observed on Olouette 2 Ionograms, J. Geophys. Res., 75, No. 22, 4299-4285 (1970).

82. Oya, H., Verification of Theory on Weak Turbulence Relating to the Sequence of Diffuse Plasma Resonances in Space, Phys. Fluids, 14, No. 11, 2487-2499 (1971).

83. Watt, T. M., Topside Ionosphere at Sunrise, J. Geophys. Res., 76, No. 13, 3095-3105 (1971).

84. Becker, W., The Standard Profile of the Mid-latitude F Region of the Ionosphere as deduced from Bottomside and Topside Ionograms, Space Research, XII, Akademie-Verlag, Berlin, 1241-1252 (1972).

85. Takayama, K., H. Ikegami, and S. Miyazaki, Plasma Resonance in a Radio-Frequency probe, Phys. Rev. Letters, 5, 238-240 (1960).

86. Harp, R. S., G. S. Kino, and J. Pavkovich, RF Properties of the Plasma Sheath, Phys. Rev. Letters, 11, No. 7, 310-312, (1963).

87. Uramoto, J., H. Ikegami, and K. Takayama, Resonance Probe in a Magnetic Field, Res. Rept. Inst. Plasma Phys., Nagoya Univ., Japan, No. IPPJ-15, (1963).

88. Uramoto, J., J. Fujita, H. Ikegami, and K. Takayama, RF Current Component in the Resonance Probe, Res. Rept. Inst. Plasma Phys. Nagoya Univ. Japan, No. IPPJ-19 (1963).

89. Harp, R. S., The behavior of the Reaonance Probe in a Plasma, Appl. Phys. Letter, 4, 186-188 (1964).

90. Harp, R. S. and F. W. Crawford, Characteristics of the Plasma Resonance Probe, J. Appl. Phys., 35, No. 12, 3436-3446 (1964).

91. Dote, T. and T. Ichimiya, Characteristic of Resonant Probes, J. Appl. Phys., 36, No. 6, 1866-1872 (1965).

92. Crawford, F. W. and R. S. Harp, The Resonance Probe - A Tool for Ionospheric and Space Research, J. Geophys. Res., 70, 587-596 (1965)

93. Crawford, F. W., Plasma Resonance Probe Characteristics in a Magnetic Field, J. Appl. Phys., 36, 3142-3145 (1965).

94. Crawford, F. W., R. S. Harp, and T. D. Mantei, Resonance Rectification Effects in Warm Magnetoplasmas, J. Appl. Phys., 38, No. 13, 5077-5082 (1967).

95. Buckley, R., Radio Frequency Properties of a Plane Grid Capacitor immersed in a Hot Collision-free plasma, J. Plasma Phys., 2, 339-351 (1968).

96. Aono, Y., K. Hirao, and S. Miyazaki, Rocket Observation of Ion Density, Electron Density and Electron Temperature in the Ionosphere, J. Radio Res. Labs., 9, 407-419 (1962).

97. Hirao, K. and S. Miyazaki, Rocket-borne Ionospheric Direct-Sounding Instruments, J. Radio Res. Labs., 12, No. 64, 357-380 (1965).

98. Hirao, K. and K. Oyama, A Critical Study on the Reliability of Electron Temperature Measurements with Langmuir Probe, J. Geomag. Geoelectr., 24, 415-427 (1972).

99. Bunting, W. D. Jr. and W. J. Heikkila, Observations on the Effect of Surface Conditions on Langmuir Probes, J. Appl. Phys., 41, No. 5, 2263-2264 (1970).

100. Dote, T., H. Amemiya and T. Ichimiya, Effect of a Magnetic Field upon the Saturation Electron Current of an Electrostatic Probe, Japanese J. Appl. Phys., 3, No. 12, 789-796 (1964).

101. Kimura, I., VLF Doppler Experiment for Observation of the Ionosphere by means of Rocket, Rep. Ionos. Space Res. Japan, 21, No. 4, 173-185 (1967).

102. Kimura, I. and R. Nishina, Doppler Shift in an Inhomogeneous Anisotropic Medium, Rept. Ionos. Space Res. Japan, 21, No. 4, 187-192 (1967).

103. Kimura, I. and K. Hirao, Rocket Experiment of Electron Density Measurement by VLF Doppler and Probe Methods, Rept. Ionos. Space Res. Japan, 25, No. 1, 59-64 (1971).

104. H. Oya, Irregular Type Sporadic-E Observed by Roket Borne Gyro-Plasma at a Temperate Latitude, J. Geomagn, Geoele, 19, No. 4, 267-272, (1967).

105. Oya, H. and T. Obayashi, Recombination Coefficient of the Upper-E and F. Regions Deduced from the Electron Density Profile at Sunset Measured by Rocket Borne Gyro-Plasma Probe, Rept. Ionos. Space Res. Japan 21, No. 1/2, 9-16 (1967).

106. Ejiri, M., H. Oya and T. Obayashi, A Modified Plasma Resonances Observed by a Rocket-borne Gyro-plasma Probe, Rept. Ionos. Space Res. Japan, 22, No. 3, 201-203 (1968).

107. Oya, H., Effects of Electron Acoustic Waves on a Cylindrical Dipole Type RF Magneto-Plasma Probe, Preprint, X-615-69-272 GSFC, Greenbelt, Mayland, USA, (1969).

108. Oya, H. and T. Aso, Ionospheric Electron Temperature Measured by a Gyro-plasma Probe, Space Research, IX, North-Holland Pub. Co., Amsterdam, 287-296 (1969).

109. Oya, H., Ionospheric Plasma Disturbances due to a Moving Space Vehicle, Planet. Space Sci., 18, 793-802 (1970).

110. Hirao, K., S. Miyazaki, and N. Fugono, Electron Density Measurement in the Ionosphere; the Results of the Spacecraft SINSEI, Proc, Symp. Space Sci. Obs. (in Japanese), ISAS, Univ. Tokyo, 30-33(1971).

111. Chapman, S., The Absorption and Dissociative or Ionizing Effect of Monochromatic Radiation in an Atmosphere on Rotating Earth, Proc. Phys. Soc., 43, Part 1, 26-45 (1931).

112. Hanson, W. B., Structure of the Ionosphere, Satellite Environment Handbook, Edited by F. S. Johnson, Stanford Univ. Press, Stanford, California, USA, 24(1965).

113. Nicolet, M. and A. C. Aikin, The formation of the D region of the Ionosphere, J. Geophys. Res., 65, 1469-1483 (1960).

114. Reid, G. C. and C. Collins, Observations of Abnormal VHF Radio Wave Absorption at Medium and High Latitudes, J. Atmos. Terr. Phys. 14, 63-81 (1959).

115. Bourdeau, R. E., Research Within the Ionosphere, Science, 148, 585-594 (1965).

116. Belrose, J. S. and E. Centiner, Measurement of Electron Densities in the Ionospheric D-Region at the Time of A 2^+ Solar Flare, Nature, 195, 688-690 (1962).

117. Titheridge, J. E., The Electron Density in the Lower Ionosphere, J. Atmos. Terr. Phys. 24, 269-282 (1962).

118. Bailey, D. K., Abnormal Ionization in the Lower Ionosphere Associated with Cosmic-Ray Flux Enhancements, Proc. I.R.E., 47, 255-266 (1959).

119. Davies, K., Ionospheric Radio Propagation, National Bureau of Standards Mon-graph 80, U.S. Department of Commerce (1965).

120. McKiarmid, I. B., D. C. Rose, and E. Budzinski, Direct Measurement of Charged Particles associated with Auroral Zone Radio Absorption, Can. J. Phys., 39, 1888-1900 (1961).

121. Heikkila, W. J. and S. R. Penstone, Rocket Measurement of Auroral Radio Absorption, Can. J. Phys., 39, 1875-1881 (1961).

122. Ziauddin, S. and P. A. Forsyth, Three-frequency Measurement of Auroral Absorption, J. Geophys. Res., 66, 2315-2319 (1961).

123. Hartz, T. R., L. E. Montbriand, and E. L. Vogan, A Study of Auroral Absorption at 30 Mc/s, Can. J. Phys., 41, 581-595 (1963).

124. Bourdeau, R. E., Ionospheric Research from Space Vehicles, Space Sci, Rev., 1, 683-728 (1963).

125. Thomas, L., The Winter Anomaly in Ionospheric Absorption, J. Atmos. Terr. Phys., 23, 301-317 (1961).

126. Sechrist, C. F. Jr., A Theory of the Winter Absorption Anomaly at Middle Latitudes, J. Atmos. Terr. Phys., 29, 113-136 (1967).

127. Maeda, K., Study on Electron Density Profile in the Lower Ionosphere, J. Geomag. Geoele., 23, No. 2, 133-159 (1971).

128. Wakai, N., C. Ouchi, and C. Nemoto, Winter Anomaly of Ionospheric Absorption as Observed in Loran-A Signals, J. Radio Res. Labs., Japan 17, No. 91, 185-198 (1970).

129. Mitchell, J. D. and L. C. Hale, Positive Ions and the Winter Anomaly, Radio Sci., 7, No. 1, 175-179 (1972).

130. Thomas, L., The Electron Density Distribution in the D- and E-regions During Days of Anomalous Radio Wave Absorption in Winter, J. Atmos. Terr. Phys., 30, 1211-1217 (1968).

131. Watanabe, K. and H. E. Hinteregger, Photoionization Rates in the E and F Regions, J. Geophys. Res., 67, 999-1006 (1962).

132. Yonezawa, T., Theory of the Formation of the Ionosphere, Space Sci. Rev., V, No. 1, 3-56 (1966).

133. Bates, D. R., Chage Transfer and Ion-Atom Interchange Collisions, Proc. Phys. Soc. London, A68, 344-345 (1955).

134. Allen, C. W., Critical frequencies, sunspots, and the sun's ultra-violet radiation, Terr. Mag. Atm. Electr., 53, 443-448 (1948).

135. Maeda, K. and S. Fukao, Study on the Solar Active Dependence of the E Region Peak Electron Density and Some Atmospheric Parameters, J. Geomag. Geoele., 24, No. 3, 289-302 (1972).

136. Maeda, K., Mid-Latitude Electron Density Profile as Revealed by Rocket Experiments, J. Geomag. Geoele., 21, No. 2, 557-567 (1969).

137. Maeda, K., Mid-Latitude Electron Density Profile in the Low Solar Activity, J. Geomag. Geoele., 22, No. 4, 551-558 (1970).

138. Ogawa, T. and T. Tohmatsu, Photoelectric Processes in the Upper Atmosphere. II. The Hydrogen and Helium Ultraviolet Glow as an Origin of the Nighttime Ionosphere, Rept. Ionos. Space Res. Japan, 20, 395-417 (1966).

139. Sagalyn, R. C., M. Smiddy, and W. P. Sullivan, Experimental Investigation of the Nighttime E region, Space Research, VII, North-Holland Pub. Co., Amsterdam, 448-463 (1967).

140. Tohmatsu, T. and N. Wakai, An Investigation of Nighttime Ionizing Sources in Low- and Mid-latitudes, Ann. Geophys., 26, 209-211 (1970).

141. Wakai, N., Quiet and Disturbed Structure and Variations of the Nithtime E Region, J. Geophys. Res., 72, 4507-4517 (1967).

142. Matsushita, S., Intense Es Ionization near the Magnetic Equator, J. Geomag. Geoele., 3, 44-46 (1951).

143. Bowles, K. L., R. Cohen, G. R. Ochs, and B. B. Balsley, Radio Echoes from Eifle-Aligned Ionization Above the Magnetic Equator and Their Resemblance to Auroral Echoes, J. Geophys. Res., 65, 1853-1855 (1960).

144. Farley, D. T., A Plasma Instability Resulting in Field-Aligned Irregularities in the Ionosphere, J. Geophys. Res., 68, 6085-6097 (1963).

145. Sato, T. and T. Tsuda, Computer Study of Nonlinear Cross-Field Instability, Phys. Fluids, 10, No. 6, 1262-1268 (1967).

146. Tsuda, T. and T. Sato, Structure of Plasma Turbulence due to Nonlinear Cross-Field Instability, Phys. Fluids, 11, 676-678 (1968).

147. Sato, T. and T. Tsuda, Three-dimensional Analysis of the Cross-field Instability in the Ionosphere, Radio Sci., 7, No. 3, 429-432 (1972).

148. Kato, S., Cross-field Instability for the Formation of Sporadic E, Radio Sci., 7, No. 3, 417-423 (1972).

149. Bowles, K. L., Doppler Shifted Radio Echoes from Aurora, J. Geophys. Res., 59, 553-555 (1954).

150. Whitehead, J. D., The Formation of the Sporadic-E Layer in the Temperate Zones, J. Atmos. Terr. Phys., 20, No. 1, 49-58 (1961).

151. Axford, W. I., Note on Mechanism for the Vertical Transport of Ionization in the Ionosphere, Can. J. Phys., 39, 1393-1396 (1961).

152. Axford, W. I., The Formation and Vertical Movement of Dense Ionized Layers in the Ionosphere Due to Neutral Wind Shears, J. Geophys. Res., 68, 769-779 (1963).

153. Whitehead, J. D., Survey of Sporadic E Processes, Space Research, VII, North-Holland Pub. Co., Amsterdam 89-99, (1967).

154. Kato, S., T. Aso, T. Horiuchi, J. Nakamura, and T. Matsuoka, Sporadic-E Formation by Wind Shear, Comparison Between Observation and Theory, Radio Sci., 7, No. 3, 359-362 (1972).

155. Sato, T., Nonlinear Study of Cross-Field Plasma Instability and its Applications to Ionospheric Irregularities, Doctorial Thesis, Kyoto Univ. (1969).

156. Hinteregger, H. E., K. R. Damon, L. Heroux, and L. A. Hall, Telemetring Monochromator Measurements of Solar 304 Å Radiation and its Attenuation in the Upper Atmosphere, Space Research, North-Holland Pub. Co., Amsterdam, 615-627 (1960).

157. Spencer, N. W., L. H. Brace, and G. R. Carignan, El-ctron Temperature Evidnece for Non-Thermal Equilibrium in the Lonosphere, J. Geophys. Res., 67, 157-175 (1962).

158. Maeda, K., Study on the Electron Density Profile in the F1 Region, J. Geomag. Geoele., 24, No. 3, 303-316 (1972).

159. Rishbeth, H. and O. K. Garriott, Introduction to Ionospheric Physics, Academic Press, New York (1969).

160. Yonezawa, T. and H. Takahashi, On the Electron and Ion Density Distributions from the Lower up to the Uppermost Part of the F Region, J. Radio Res. Lab. Japan, 7, No. 32, 335-378 (1960).

161. Wright, J. W., A Model of the F Region Above hmax F2, J. Geophys. Res., 65, No. 1, 185-191 (1960).

162. Chandra, S., Electron Density Distribution in the Upper F Region, J. Geophys. Res., 68, No. 7, 1937-1942 (1963).

163. Thomas, J. O. , J. Haselgrove, and A. Robbins, The Electron Distribution in the Ionosphere over Slough. I. Quet Days, J. Atmos. Terr. Phys., 12, 46-56 (1958).

164. Thomas, J. O. and A. Robbins, The Electron Distribution in the Ionosphere over Slough II. Disturbed Days, J. Atmos. Terr. Phys., 13, 131-139 (1958).

165. Evans, J. V., Cause of the Mid-Latitude Evening Increase in f_0F_2, J. Geophys. Res., 70, No. 5, 1175-1185 (1965).

166. Hohl, H. and J. W. King, Atomospheric Winds between 100 and 700 km and their Effects on the Ionosphere, J. Atomos. Terr. Phys., 29, 1045-1062 (1967).

167. Kohl, H., J. W. King, and D. Eccles, Some Effects of Neutral Air Winds on the Ionospheric F-layer, J. Atmos. Terr. Phys., 30, 1733-1744 (1968).

168. Berkner, L. V., H. W. Wells, and S. L. Seaton, Characteristics of the Upper Region of the Ionosphere, Terr. Mag. Atm. Elec., 41, 173-184 (1936).

169. Yonezawa, T. and Y. Arima, On the Seasonal and Nonseasonal Annual Variations and the Semiannual Variation in the Noon and Midnight Electron Densities of the F2 Layer in Middle Latitudes, J. Radio Res. Labs. Japan, 6, 293-309 (1959).

170. Yonezawa, T., On the Seasonal and Non-seasonal Annual Variations and the Semi-annual Variation in the Noon and Midnight Densities of the F2 Layer in Middle Latitudes. II, J. Radio Res. Labs. Japan, 6, 651-668 (1959).

171. King, J. W. and P. A. Smith, The Seasonal Anormaly in the Behaviour of the F2-layer Critical Frequency, J. Atomos. Terr. Phys., 30, 1707-1713 (1968).

172. Evans, J. V., Cause of the Mid-latitude Winter Night Increase in f_0F_2,J. Geophys. Res., 70, 4331-4345 (1965).

173. Carlson, H. C., Ionospheric Heating by Magnetic Conjugate-point Photoelectrons, J. Geophys. Res., 71, 195-199 (1966).

174. Antonova, L. A. and G. S. Ivanov-kholodnii, Corpuscular Hypothesis for the Ionization of the Night Ionosphere, Geomag. Aeronomy (English Transl.), 1, 149-156 (1961).

175. Yonezawa, T., Maintenance of Ionization in the Night-time F2 Region, J. Radio Res. Lab. Japan, 12, No. 60, 65-88 (1965).

176. Knecht, R. W., Observations of the Ionosphere over the South Geographic Pole, J. Geophys. Res., 64, 1243-1250 (1959).

177. Duncan, R. A., Universal Time Control of the Arctic and Antarctic F Region, J. Geophys. Res., 67, 1823-1830 (1962).

178. Sato, T. and G. F. Rourke, F-region Enhancements in the Antarctic, J. Geophys. Res., 69, 4591-4607 (1964).

179. King, J. W., H. Kohl, and R. Pratt, The Effect of Atmospheric Winds on the Height of the F2-layer Peak at Middle and High Latitude, J. Atmos. Terr. Phys., 29, 1529-1539 (1967).

180. Hirono, M. and H. Maeda, Geomagnetic Distortion of the F2 Region on the Magnetic Equator, J. Geophys. Res., 60, 241-255 (1955).

181. Duncan, R. A., The Equatorial F-region of the Ionosphere, J. Atmos. Terr. Phys., 18, 89-100 (1960).

182. Kendal, P. C., Geomagnetic Control of Diffusion in the F2-region of the Ionosphere-I, The Form of the Diffusion Operator, J. Atmos. Terr. Phys., 24, 805-811 (1962).

183. Kendal, P. C., Geomagnetic Control of Diffusion in the F2-region of the Ionosphere-II, Numerical Results, J. Atmos. Terr. Phys., 25, 87-91 (1963).

184. Goldberg, R. A., The Effect of Diffusion on the Equilibrium Electron Density Distribution in the F Region near the Magnetic Equator, J. Geophys. Res., 68, No. 7, 1927-1936 (1963).

185. Goldberg, R. A., P. C. Kendall, and E. R. Schmerling,Geomagnetic Control of the Electron Density in the F Region of the Ionosphere, J. Geophys. Res., 69, 417-427 (1964).

186. Bramley, E. N. and M. Peart, Diffusion and Electromagnetic Drift in the Equatorial F2 Region, J. Atmos. Terr. Phys., 27, 1201-1211 (1965).

187. Hanson, W. B. and R. J. Moffett, Ionization Transport Effects in the Equatorial F Region, J. Geophys. Res., 71, 5559-5572 (1966).

188. Goldberg, R. A., A Review of the Theories Concerning the Equatorial F2 Region Ionosphere, Proc. IEEE, 57, No. 6, 1119-1126 (1969).

189. Thomas, J. O., The Electron Density Distribution in the F2 Layer of the Ionosphere in Winter, J. Geophys. Res., 68, No. 9, 2707-2718 (1963).

190. Lyon, A. J. and L. Thomas, The F2-region Equatorial Anomaly in the African, American and East Asian Sectors during Sunspot Maximum, J. Atmos. Terr. Phys., 25, 373-386 (1963).

191. Lockwood, G. E. K. and G. L. Nelms, Topside Sounder Observations of the Equatorial Anormaly in the 75°W Longitude Zone, J. Atmos. Terr. Phys., 26, No. 5, 569-580 (1964).

192. Croom, S. A., A. R. Robbins, and J. O. Thomas, Two Anomalies in the behaviour of the F2 Layer of the Ionosphere, Nature, 184, 2003-2004 (1959).

193. Mitra, S. K., Geomagnetic Control of Region F2 of the Ionosphere, Nature, 158, 668-669 (1946).

194. Baxter, R. G., A Numerical Solution of the Time-varing Diffusion Equation for the F2-layer, Plane. Space Sci., 15, 701-713 (1967).

195. Woodman, R. F. and H. Hagfors, Methods for the Measurement of Vertical Ionospheric Motions near the Magnetic Equator by Incoherent Scatter, J. Geophys. Res., 74, 1205-1212 (1968).

196. Balsley, B. B. and E. F. Woodman, On the Control of the F-region Drift Velocity by the E-region Electric Field: Experimental Evidence, J. Atmos. Terr. Phys., 31, 865-867 (1969).

197. Rastogi, R. G., The Morphology of Lunar Semi-Diurnal Variation in f_0F_2 near Solar Noon, J. Atmos. Terr. Phys., 22, 290-297 (1961).

198. Obayashi, T., Morphology of Storms in the Ionosphere, Research in Geophysics, Vol. 1, MIT Press, New York, 335-366 (1964).

199. Obayashi, T., Morphology of Storms in the Ionosphere, J. Geomag. Geoele., XVI, No. 1, 1-30 (1964).

200. Obayashi, T., World-wide Electron Density Changes and Associated Thermospheric Winds during an Ionospheric Storm, Planet. Space Sci., 20, 511-520 (1972).

201. Warren, E. S., The Topside Ionosphere during Geomagnetic Storms, Proc. IEEE, 57, 1029-1036 (1969).

202. Chan, K. L. and L. Colin, Global Electron Density Distributions from Topside Soundings, Proc. IEEE, 57, 990-1004 (1969).

203. Obayashi, T. and N. Matuura, Theoretical Model of F-region Storms, Solar-Terr. Phys., IV, 199-211 (1970).

204. Wright, R. W., J. R. Koster, and N. J. Skinner, Spread F Layer Echoes and Radio-Star Scintillation, J. Atmos. Terr. Phys., 8, 240-246 (1956).

205. Newman, P., Spread F and its Effects upon Radio Wave Propagation and Communication, Technivision, Mainhead, England (1966).

206. Johnson, F. S., The Ion Distribution above the F2 Maximum, J. Geophys. Res., 65, 577-578 (1960).

207. Hanson, W. B., Electron Temperatures in the Upper Atmosphere, Space Research, III, North-Holland Pub. Co., Amsterdam, 282-302 (1963).

208. Angerami, J. J. and J. O. Thomas, Studies of Planetary Atmospheres, 1. The Distribution of Electrons and Ions in the Earth's Exosphere, J. Geophys. Res., 69, No. 21, 4537-4560 (1964).

209. Bourdeau, R. E., J. L. Donley, E. C. Whipple, and S. J. Bauer, Experimental Evidence for the Presence of Helium Ions Based on Explorer VIII Satellite Data, J. Geophys. Res., 67, 467-475 (1962).

210. Willmore, A. P., R. L. F. Boyd, and P. J. Bowen, Some Preliminary Results of the Plasma Probe Experiments on the Satellite Ariel, Proc. Inst. Conf. Ionos. 1962, Inst. Phys. Soc. London, 517-522 (1963).

211. Taylor, H. A. Jr., L. H. Brace, H. C. Brinton, and C. R. Smith, Direct Measurements of Helium and Hydrogen Ion Concentration and Total Ion Density to an Altitude of 940 Kilometers, J. Geophys. Res., 68, 5339-5347 (1963).

212. Bauer, S. J., Diffusive Equilibrium in the Topside Ionosphere, Proc. IEEE, 57, No. 6 1114-1118 (1969).

213. Eviatar, A., A. M. Lenchek, and S. F. Singer, Distribution of Density in an Ion-Exosphere of a Nonrotating Planet, Phys. Fluids, 7, No. 11, 1775-1779 (1964).

214. Carpenter, D. L., Whistler Evidence of a 'Knee' in the Magnetospheric Ionization Density Profile, J. Geophys. Res., 68, No. 6, 1675-1682 (1963).

215. Angerami, J. J. and D. J. Carpenter, Whistler Studies of the Plasmapause in the Magnetosphere Electron Density and Total Tube Electron Content near the Knee in Magnetospheric Ionization, J. Geophys. Res., 71, No. 3, 711-725 (1966).

216. Marubashi, K., Structure of Topside Ionosphere in High Latitudes, J. Radio Res. Lab. Japan, 17, Nos. 93/94, 335-416 (1970).

217. Nelms, G. L. and J. H. Chapman, The High Latitude Ionosphere: Results from the Alouette/ISIS Topside Sounders, The Polar Ionosphere and Magnetospheric Processes (ed. by Gunnarskovli), Gordon and Breach, New York, 233-269 (1970).

218. Thomas, J. O. and M. K. Andrews, The Polar Exospheric Plasma, The Polar Ionosphere and Magnetospheric Processes (ed. by Gunnarskovli), Gordon and Breach, New York, 225-231 (1970).

219. Holzer, T. E., Effects of Plasma Flow on Density and Velocity Profiles in the Polar Ionosphere, The Polar Ionosphere and Magnetospheric Processes (ed. by Gunnarskovli), Gordon and Breach, New York, 209-223 (1970).

220. Banks, P. M., Plasma Transport in the Topside Polar Ionosphere, The Polar Ionosphere and Magnetospheric Processes (ed. by Gunnarskovli), Gordon and Breach, New York, 193-208 (1970).

221. Shaw, R. R. and D. A. Gurnett, Magnetospheric Electron Density Measurements from Upper Hybrid Resonance Noise Observed by IMP-6, Rept. U. of Iowa/72-37, Department Phys. Astonomy, Univ. Iowa, (1972).

222. McIlwain, C. E., Coordinates for Mapping the Distribution of Magnetically Tra-ped Particles, J. Geophys. Res., 66, No. 11, 3681-3691 (1961).

223. Stix, T. H.,The Theory of Plasma Waves, McGraw-Hill Books Co., New York,(1962).

224. Kaiser, T. R., The Admittance of an Electric Dipole in a Magneto-ionic Environment, Planet. Space Sci., 19, 639-657 (1962).

225. Balmain, K. G., The Impedance of a Short Dipole Antenna in a Magnetoplasma, IEEE Trans. AP-12, 605-619 (1964).

226. Langmuir, I. and H. Mott-Smith, Studies of Electric Discharges in Gases at Low Pressure, Part I GE Rev., 27, No. 7, 449-455 (1924). Part II ibid, No. 8, 538-548 (1924). Part III ibid, No. 9, 616-623 (1924). Part IV ibid, No. 11, 762-711 (1924). Part V ibid, No. 12, 816-820 (1924).

227. Schiff, M. L. and J. A. Fejer, Impedance of Antennas in a Warm Isotropic Plasma: A Comparison of Different Models, Radio Sci., 5, No. 5, 811-819 (1970).

228. Lafon, J. P. and H. Weil, Impedance of Cylindrical and Helical Antennas in Lossy Magnetoplasma including Conditions of Refractive Index Resonance, Radio Sci. 6, No. 1, 99-111 (1971).

229. Oya, H., Study on Boundary Value Problems of Magneto Active Plasma and Their Applications to Space Observation, Doctorial Thesis, Kyoto Univ. (1966).

230. Miller, E. K., The Admittance of an Infinite Cylindrical Antenna in a Lossy Incompressible, Anisotropic Plasma, Can. J. Phys. 45, 4019-4038, (1967).

231. Tunaley, J. K. E. and R. J. L. Grard, The Impedance of a Probe in a Warm Plasma, Ann. Geophys., 25, No. 1, 55-65 (1969).

232. Balmain, K. G., Impedance of a Short Dipole in a Compressible Plasma, Radio Sci., 69D, No. 4, 559-566 (1965).

233. Oya, H., Radiation of Electro Acoustic Wave in a Magnetoplasma, Rept. Society for Study of Ant. Propag. (in Japanese), Inst. Elec. Comm. Eng. Japan, A.P. 67-39 (1967).

234. Wait, J. R., On Radiation of Electromagnetic and Electroacoustic Waves in a Plasma, Appl. Sci. Res., 11B, 423-432 (1964).

235. Monroe, R. L., Admittance of an Infinite Cylindrical Antenna immersed in a Lossy, Compressible Plasma, Can. J. Phys., 47, No. 20, 2129-2135 (1969).

236. Schiff, M. L., Current Distribution on a Grid Type Dipole Antenna Immersed in a Warm Isotropic Plasma, Radio Sci-, 6, No. 6, 665-671 (1971).

237. Whale, H. A., The Excitation of Electroacoustic Waves by Antenna in the Ionosphere, J. Geophys. Res., 68, No. 2, 415-422 (1963).

238. Grard, R. J. L., Coupling Between Two Electric Aerials in a Warm Plasma, URSI Symp. on Elecromagnetic Waves, Stresa, Italy, June (1968).

239. Rooy, B., M. R. Feix et L. R. O. Storey, Theorie de la Sonde Quadripolaire en Plasma Chaud Isotrope, Plasma Phys., 14, 275-300 (1972).

240. Cohen, M. H., Radiation in a Plasma I. Cerenkov Effect Phys. Rev., 123, No. 3, 711-721 (1961), Radiation in a Plasma II. Equivalent Sources, Phys. Rev., 126, No. 2, 389-397 (1962), Radiation in a Plasma III. Metal Boundaries,ibid. 398-404 (1962).

241. Balmain, K. G., Impedance of a Radio-Frequency Plasma Probe with an Absorptive Surface, Radio Sci., 1, No. 1, 1-12 (1966).

242. Fejer, J. A., Interaction of an Antenna with a Hot Plasma and the Theory of Resonance Probes, J. RES. N.B.S., 68D, 1171-1176 (1964).

243. Holt, O. and J. Trim, Impedance of a Radio Frequency Plasma Probe in a Static Magnetic Field, Plasma Waves in Space and Laboratory, 1, Edinburgh Univ. Press, 263-284 (1969).

244. Wunsch, A. D., The finite Tubular Antenna in a Warm Plasma, Radio Sci., 3, 901-920 (1968).

245. Cook, K. R. and B. C. Edgar, Current Distribution and Impedance of a Cylindrical Antenna in an Isotropic Compressible Plasma, Radio Sci., 1, 13-19 (1966).

246. Lin, S-H. and K. K. Mei, Numerical Solution of Dipole Radiation in a Compressible Plasma, IEEE Trans. AP-16, No. 2, 235-241 (1968).

247. Lin, S-H. and Mei, K. K., On the Effect of Sheath Collision and Absorptive Surface on the Performance of a Linear Antenna in a Compressible Plasma, IEEE Trans. AP-18, No. 5, 672-679 (1970).

248. Maxam, G. L. and K. M. Chen, An Experimental and Theoretical Study on the Circuit Properties of a Cylindrical Antenna in a Hot Lossy Plasma, IEEE Trans. AP-20, No. 3, 347-353 (1972).

249. Preis, D. H., The Integral Equation and Boundary Conditions for a Cylindrical Antenna in a Warm Plasma, Radio Sci., 7, No. 12, 1143-1149 (1972).

250. Tarstrup, J. and W. J. Heikkila, The Impedance Characteristic of a Spherical Probe in an Isotropic Plasma, Radio Sci., 7, No. 4, 493-502 (1972).

251. Bernstein, I. B., Waves in a Plasma in a Magnetic Field, Phys. Rev., 109, No. 1, 10-12 (1958).

252. Kuehl, H. H., The Kinetic Theory of Waves in a Warm Plasma Excited by a Current Source, J. Math. Phys., 43, 218-226 (1964).

253. Kuehl, H. H., Resistance of a Short Antenna in a Warm Plasma, Radio Sci., 1, 971-976 (1966).

254. Kuehl, H. H., Computations of the Resistance of a Short Antenna in a Warm Plasma, Radio Sci., 2, 73-76 (1967).

255. Schiff, M. L., Impedance of a Short Dipole Antenna in a Warm Isotropic Plasma, Radio Sci., 5, No. 12, 1489-1496 (1970).

256. Baenziger, G. and H. H. Kuehl, Imput Resistance of a Short Dipole Antenna in a Warm Uniaxial Plasma, Radio Sci., 7, No. 12, 1117-1129 (1972).

257. Crawford, F. W., T. D. Mantei, and J. A. Tataronis, The Plasma Capacitor in a Magnetic Field, Int. J. Electronics, 21, No. 4, 341-351 (1966).

258. Buckley, R., RF Characteristics of a Plane-grid Capacitor immersed in a Hot Collision-free Plasma with Uniform Magnetic Field parallel to the Grid Plates, Plasma Waves in Space and Laboratory 2, Edinburgh Univ. Press 129-158 (1970).

259. Pavkovich, J. and G.S. Kino, RF behavior of the Plasma Sheath, ARL Rept. 64-15, Stanford Univ. (1964).

260. Buckley, R., A Theory of Resonance Rectification, The Response of a Spherical Plasma Probe to Alternating Potentials, Proc. Rayal Soc. London, A290, 186-219 (1966).

261. Bernstein, I. B. and I. N. Rabinowitz, Theory of Electrostatic Probes in a Low-density Plasma, Phys. Fluids, 2(2), 121 (1959).

262. Shure, F. C., Boundary Value Problems in Plasma Oscillation; The Plasma Capacitor, Plasma Phys., 6, 1-14 (1964).

263. Spitzer, L. Jr., Physics of Fully Ionized Gases, John Wiley & Sons, New York (1962).

264. Itatani, R., Lecture on "Plasma and Magnetic Field", (in Japanese), Summer School For Plasma Scientist, Aug. (1964).

265. Dote, T. and T. Ichimiya, Characteristics of Plasma Resonance Probe and RF Impedance Probe in a Magnetic Field, J. Phys. Soc. Japan, 22, No. 5, 1266-1273 (1967).

266. Miyazaki, S., Radio Frequency Characteristics of Electrode Immersed in Magnetoplasma and its Application to Plasma Diagnostic Techniques (I), J. Radio Res. Lab. Japan, 15, No. 78, 81-103 (1968).

267. Butler, H. S. and G. S. Kino, Plasma Sheath Formation by Radio-Frequency Fields, Phys. Fluids, 6, No. 9, 1346-1355 (1963).

268. Belrose, J. S. and I. A. Bourne, The Electron Distribution and Collision Frequency height profile for the Lower Part of the Ionosphere (The D and Lower E Regions), Proc. Conf. Ground-based Radio Wave Propagation Studies of the Lower Ionosphere, Ottawa, Canada, 80-96 (1969).

269. Bohm, D., E. H. S. Burhop, and H. S. W. Massey, The Characteristics of Electrical Discharges in Magnetic Fields, McGraw-Hill Co. New York (1949).

270. Hirao, K., Electron Temperature Probe, COSPAR Tech. Manual Series, Electron Density and Temperature Measurement in the Ionosphere, 58-65 (1967).

271. Hirao, K., and K. Oyama, An Improved Type of Electron Temperature Prove, J. Geomag. Geoele., 22, No. 4, 393-402 (1970).

272. Tominaga, G., K. Hirao, T. Ito, and C. Hayashi, Caracteristique D'une chambre a ultra-vide, Le Vide, 132, 355-360 (1967).

273. Dote, T., A Method for Determination of the Plasma Potential by an RF Probe, J. Phys. Soc. Japan, 24, 224, (1968).

274. Rand, S., Wake of a Satellite Traversing the Ionosphere, Phys. Fluids, 3, No. 2, 265-273 (1960).

275. Henry, B. G., A Local Reduction of F-Region Ionization Due to Missil Transit, J. Geophys. Res., 66, No. 4, 1073-1079 (1961).

276. Getmantsev, C. G. and N. G. Denisov, Concerning an Effect During Measurement of Electron Concentration in the Ionosphere by the Antenna Probe Method, Geomag. aeronomy, 4, 575-577 (1962).

277. Al'Pert, Ja. L., A. U. Gurevic, and L. P. Pitaevskiy, Effect due to an artificial earth satellite in rapid motion through the ionosphere or the interplanetary medium, Space Sci. Rev., 2, 680-748 (1963).

278. Gurevich, A. V. and L. P. Pitayevskiy, Supersonic Motion of a Body in Plasma, Geomag. aeronomy, 4, No. 5, 637-642 (1964).

279. Kawashima, N., Laboratory Experiment on the Disturbance of Environmental Conditions by Presence of Sounding Rockets, J. Geophys. Res., 70, No. 13, 3203-3210 (1965).

280. Al'pert, Ya, L., A. V. Gurevich, and L. P. Pitaevskii, Space Physics with Artificial Satellites, Consultants Bureau, New York (1965).

281. Gurevich, A. V. and L. P. Pitayevskiy, Scattering of Radio Waves on the Trail of a Body Moving in Plasma, Geomag. Aeronomy, 5, 650-658 (1966).

282. Gurevich, A. V., L. P. Pitaevskii, and V. V. Smirnova, Ionospheric Aerodynamics, Space Sci. Reviews, 9, 805-871 (1969).

283. Crawford, F. W., J. C. Lee, and J. A. Tataronic, Some Studies of Whistler Instability, Plasma Waves in Space and Laboratory 2, Edinburgh Univ. Press, 447-470 (1970).

284. O'Malley, T. F., Extrapolation of Electron-Rare Gas Atom Cross Sections to Zero Energy, Phys. Res., 130, No. 3, 1020-1029 (1963).

285. Miyazaki, S., H. Mori, K. Hirao, and S. Mitome, Measurement of Electron and Ion Currents by Faraday Cup, Proc. Symp. Space Plasma, ISAS, Univ. Tokyo (in Japanese) 1-6 (1970).

286. Fugono, N. and T. Ito, Design Manual of Solar Wind Simulator, Pre-print (in Japanese) (1969).

287. Ejiri, M., T. Aso, N. Yokobori, H. Oya, and T. Obayashi, Rocket Experiment with Impedance Probe - L-3H-5, L-3H-6 -, Bulletin of ISAS, Univ. Tokyo, 1, No. 1 (B), (in Japanese) 117-129 (1971).

288. Ejiri, M. and T. Obayashi, Magnetospheric and Ionospheric Observation with Impedance Probe, Bulletin of ISAS, Univ. Tokyo, 6, No. 1 (B), (in Japanese) 176-189 (1970).

289. Ejiri, M. and T. Aso. R. F. Probes, Study on Discharge, No. 46, JRED (in Japanese) 47-64 (1972).

290. Cain, J. C. and R. E. Sweeney, Magnetic Field Mapping of the Inner Magnetosphere, J. Geophys. Res., 75, No. 22, 4360-4362 (1970).

291. Oya, H., Theoretical Prediction on Discrimination of Mofified and Hybrid Plasma Resonances, Rept. Ionos. Space Res. Japan, 22, No.1/2, 119-122 (1968).

292. Toyama, H., Private Communication (1969).

293. Miyazaki, S. and H. Mori, Electron Temperature Profile by Grid Current Characteristic of Retarding Potential Trap (Ascent), Sounding Rocket Data in Japan, 1, ISAS, Univ. Tokyo (1972).

294. Bauer, S. T., Helium Ion Belt in the Upper Atmosphere, Nature, 197, 36-37 (1963).

295. Hiraishi, K., VLF Doppler Experiment, Master thesis, Kyoto Univ. March (1971).

296. Heller, G. B., Thermophysics and temperature control of spacecraft and entry vehicles, Academic Press, New York. (1966).

297. Hrycak, P., Thermal Design of Telstar, Astro. Aero. Eng., 44-49 (1963).

298. Hammerdinger, L. H., Thermal Design of the Orbiting Astronautical Observatory, J. Spacecraft, 1, 477-483 (1964).

299. Millard, J. P. and C. B. Neel, Measurements of Albedo and Earth Radiation from OSO-1, AIAA Journal, 3, 1317-1329 (1965).

300. Gordon, G. D., Measurement of Ratio of Absorptivity of Sunlit to Thermal Emissivity, Rev. Sci. Inst., 31, 1204-1208 (1960).

301. Hoke, M. G., A Thermal Vacuum Technique for Measuring the Solar Absorptance of Satellite Coatings as a Function of Angle of Incidence, AIAA Journal, 3, 947-951 (1965).

302. Charnes, A. and S. Paynor, Solar Heating of a Rotating Cylindrical Space Vehicle, ARS Journal, 479-484 (1960).

303. John, J. E. A. and W. F. Hardgrove, Design of an Ultrahigh-Vacuum Space Simulator, J. Spacecraft, 3, 427-428 (1966).

304. Smith R. L. and N. Brice, Propagation in Multicomponent Plasmas, J. Geophys. Res., 69, No. 23, 5029-5040 (1964).

305. Mlodnosky, R. F. and O. K. Garriott, The v.l.f. Admittance of a Dipole in the Lower Ionosphere, Proc. Inter. Conf. on the Ionosphere, Inst. Phys. and Phys. Soc., London, 484-491 (1962).

306. Kozai, Y., The Motion of a Close Earth Satellite, Astronomical J., 64, No. 9, 367-377 (1959).

307. Escobal, P. R., Methods of Orbit Determination, John Wiley & Sons, Inc., New York (1965).

308. Matsushita, S. and W. H. Campbell, Physics of Geomagnetic Phenomena, Akademic Press, New York (1967).

309. Results of Experiment of Mu-4S-4 and Denpa (1972-064A), Inst. Space Aeronaut. Sci., Univ. Tokyo, Oct. (1972).

310. Aoyama, I. and F. Toyama, Private Communication (1972).

311. Solar-Geophysical Data (Prompt Report) No. 341-PART 1, Published by National Geophys. Solar-Terr. Data Center, Boulder colo. (1973).

312. Chandra, S., and R. A. Goldberg, Geomagnetic Control of Diffusion in the Upper Atmosphere, J. Geophys. Res., 69, No. 15, 3187-3197 (1964).